

MARCH 1, 2023



University of
Nottingham

UK | CHINA | MALAYSIA

ORIENTATION CONTROL DURING 2D-3D COMPOSITE PREFORMING

THESIS IN ADVANCED MANUFACTURING OF COMPOSITE MATERIALS
FOR THE DEGREE OF DOCTOR OF PHILOSOPHY

ALBERT GIBBS
THE UNIVERSITY OF NOTTINGHAM

Abstract

Non-crimp fabrics (NCFs) are employed in composite structures as an alternative to woven fabrics when there is a requirement for improved tensile strength and modulus. To exploit NCF properties, components are designed with optimised fibre directions that reinforce the predicted load paths. 2D to 3D composite forming is a manufacturing method that has been developed for automation, to improve the labour economy of components and reduce per unit costs. Currently it is difficult to maintain accurate fibre orientation control due to the constraints of the 2D pre-form and the lack of interaction with the fabric during its transition from a 2D to a 3D form.

This thesis explores process alterations that improve fibre orientation control in 2D-3D forming through the introduction of multiple forming stages. Thus enabling the implementation of optimised NCF layups in formed components. The approach has been broken down into the following research areas:

1. Analysis of fibre angle distribution

A robust method for the full field measurement of fibre angle distribution has been created and validated to ± 0.5 degrees for in-plane testing and ± 3 degrees on double curvature surfaces. It has been shown that the theoretical calculation of shear angle from the bias extension test for an NCF is incorrect above shear angle values of 15 degrees. Whereas, theoretical shear angle calculations for NCFs in the picture frame test are accurate to within ± 1 degree. It was found that shearing causes a non-linear variation in the tensile properties of an NCF due to fibre misalignment that has previously been unmeasured. NCFs can experience an undesirable reduction in tensile properties at shear angles that are commonly found in 2D-3D formed components.

2. Analysis of fibre misalignment due to inter-stitch buckling defects.

It was found that a deformation mode occurs in NCFs at very low shear angles (0 degrees to 1 degree) where frictional interactions between the yarns prevents slippage at the stitch points. This causes a non-linear shear region at low shear angles observed for many NCF shear force/angle graphs. An analytical model was

created to show the link between the initial non-linear shear region and the inter-stitch buckling defects that has been proved to impact fibre misalignment at higher shear angles. To improve fibre alignment, two buckling defect reduction strategies were developed as a result of the modelling and applied to 2D and 3D samples. During in-plane testing localised stitch removal showed a 51% reduction in fibre misalignment and resin lubrication presented a 57% reduction. These strategies combat the undesirable reduction in properties due to fibre misalignment, enabling multiple forming cycles to be conducted without negatively impacting the fabric structure.

3. Modelling multiple forming cycles.

A novel multi-cycle finite element material model was created, that accurately captures the previously undocumented hysteresis phenomenon found in NCFs when subjected to multiple shear cycles. This was validated to within 8% of experimental values during in-plane testing. A multi-stage double diaphragm forming process has been developed that locally induces regions of high shear with the objective of taking advantage of the multi-cycle hysteresis in the fabric. The process alteration generated a 25% reduction in the maximum defect size found on a double curvature component, highlighting the formability benefits of a multiple stage processes and validating the model.

4. Fibre continuity control during forming.

A process alteration has been developed to show that plies running longitudinally along a formed component can be successfully pre-sheared before the forming operation to locally align fibres in the desired orientation. A structural simulation was created that combined the multi-cyclic material model and the non-linear structural behaviour of sheared fabrics. The results for a simple beam showed that a pre-sheared laminate has a higher peak stress under all the tested load cases and an improvement to mechanical stiffness which was shown to be transferable to a component weight reduction of 17% through ply removal. The pre-shearing process also generated a reduction in the wastage from trimming fabrics. The overall fabric area needed for simple beam like geometries was

reduced by 15.5%-34.5%. A complex beamlike demonstrator was modelled and showed a 31% improvement to material utilisation and 11% improvement to mechanical stiffness.

The thesis chapters progress the idea of fibre alignment control in 2D-3D forming from: measurement), to understanding, into modelling, and finally a demonstration of the application. Ideas from each chapter can be applied to current industrial processes and improve the capabilities of components made using 2D-3D forming.

Acknowledgments

The author gives his utmost gratitude to the academic supervision of Dr Lee Harper and Professor Nicholas Warrior. Their guidance and support, both educationally and pastorally created a wonderful environment to explore ideas and develop this research.

Special thanks goes to Dr Shuai Chen for his knowledge during the development of the multi-cyclic material model (Chapter 5). Thanks also goes to the outstanding technical support of Paul Johns and Liam Sprake.

The author gratefully acknowledges the financial support of the EPSRC Future Composite Manufacturing Research Hub as well as the invaluable discussions with its participating researchers: Guy Lawrence, Ángela Lendínez, George Street, Dr Adam Joesbury and James Mortimer, with a special mention to Matthew Thompson and Dr Joe Eastwood.

As a final thanks, my eternal gratitude goes to my family and partner Dr Elizabeth Poxon for the bottomless love, support and encouragement.

CONTENTS

Abstract.....	2
Acknowledgments.....	5
1 Introduction	13
1.1 Carbon fibre composites	13
1.2 Mass produced continuous carbon components.....	14
1.3 Fibre alignment control in 2D-3D forming	15
1.4 Research Areas	16
1.4.1 Chapter 3: Analysis of fibre angle distribution in biaxial non-crimp fabric: Measurement of formed fibre angle distribution (measurement)	18
1.4.2 Chapter 4: Characterisation of non-linear shear behaviour and inter-stitch buckling defects in biaxial non-crimp fabrics: Fibre misalignment during forming (understanding/modelling)	18
1.4.3 Chapter 5: Modelling the multi-cycle shear behaviour of biaxial non-crimp fabrics: Lack of modelling capability for consecutive forming processes (understanding/modelling/application)	19
1.4.4 Chapter 6: Maintaining fibre continuity over formed composite components using biaxial non-crimp-fabrics: Understand the structural benefits of fibre alignment control (measurement/modelling/application).....	20
1.5 Chapter summary	21
2 Literature review.....	22
2.1 Introduction.....	22
2.2 Material architecture	22
2.2.1 Woven Fabrics.....	23
2.2.2 Non-Crimp Fabrics.....	25
2.2.3 Unidirectional Fabrics	26
2.2.4 Pre-impregnated fabrics	26

2.3	2D-3D Forming	27
2.3.1	Initial non-linear shear region – yarn sliding	28
2.3.2	Steady-state Shear – yarn rotation	30
2.3.3	Yarn locking – lateral yarn compression	32
2.3.4	Out-of-plane bending.....	32
2.3.5	Defects caused by 2D-3D forming.....	33
2.4	Material characterisation	34
2.4.1	In-plane shear tests.....	35
2.4.2	Comparison of tests	40
2.4.3	Bending tests.....	42
2.5	Full field fibre angle measurement.	43
2.5.1	Manual image analysis	43
2.5.2	Algorithm based analysis	44
2.5.3	Discrete dot tracking method	45
2.5.4	Digital image correlation (DIC).....	46
2.6	Forming and pre-forming techniques	49
2.6.1	Hand Layup.....	49
2.6.2	Matched tool 2D-3D Press forming	49
2.6.3	Diaphragm forming	50
2.6.4	Double diaphragm press forming	52
2.6.5	Unidirectional tape laid preform	53
2.7	Composite Forming Simulations	54
2.7.1	Kinematic models.....	54
2.7.2	Finite element models	55
2.7.3	Ply Meshing	63
2.7.4	Diaphragm simulation.....	63

2.7.5	Friction	64
2.8	Conclusion of literature	65
3	Analysis of fibre angle distribution in biaxial non-crimp fabrics.....	67
	Abstract	67
3.1	Introduction.....	67
3.1.1	Objectives:.....	67
3.1.2	Fibre misalignment during shearing	67
3.1.3	Fibre angle measurement	68
3.1.4	Current work	69
3.2	Methodology for analysing local fibre orientations.....	70
3.2.1	Optical scanning methodology	70
3.2.2	Custom shear angle analysis	71
3.2.3	In-plane shear test optical scanning	73
3.2.4	2D-3D punch forming.....	74
3.3	Results:	76
3.3.1	Optical Scanning methodology validation	76
3.3.2	Non-crimp fabric optical scanning.....	82
3.3.3	Tensile properties of sheared fabrics.....	93
3.4	Chapter summary	103
4	Characterisation of non-linear shear behaviour and inter-stitch buckling defects in biaxial non-crimp fabrics	105
4.1	Introduction.....	105
4.1.1	Objectives:.....	105
4.1.2	2D to 3D fabric forming.....	105
4.1.3	Initial non-linear shear region.....	105
4.1.4	Inter-stitch buckling defect	107

4.1.5	Current work	109
4.2	Methodology	109
4.2.1	Initial non-linear shear behaviour modelling.....	109
4.2.2	Yarn buckling defect measurement	114
4.2.3	Defect reduction strategies.....	117
4.3	Results	118
4.3.1	Yarn slippage during shearing.....	118
4.3.2	Verification of initial non-linear shear behaviour	119
4.3.3	Initial non-linear shear region model.....	122
4.3.4	Identifying buckling defect reduction strategies from the initial non-linear shear region model	124
4.3.5	Inter-stitch buckling model	126
4.3.6	Inter-stitch yarn buckling defect reduction	127
4.4	Chapter summary	137
5	Modelling the multi-cycle shear behaviour of biaxial non-crimp fabrics	140
	Abstract	140
5.1	Introduction.....	140
5.1.1	Objectives:.....	140
5.1.2	Non-crimp fabrics.....	140
5.1.3	2D-3D Forming	140
5.1.4	Finite element forming models.....	142
5.1.5	Current work	142
5.2	Experimental Methodology.....	142
5.2.1	Materials	142
5.2.2	Multi-cycle in-plane shear testing methodology	144
5.2.3	Multi-stage double diaphragm forming.....	147

5.2.4	Multi-cycle stitch extension methodology	152
5.3	Multi-cycle non-orthogonal material model.....	155
5.3.1	Homogenisation	155
5.3.2	Non-crimp fabric material model.....	155
5.3.3	Non-linear cycle dependant shear modulus	157
5.3.4	Multi-cycle picture frame model	161
5.3.5	Multi-stage diaphragm forming model.....	163
5.4	Experimental results.....	166
5.4.1	Multi-cycle picture frame results.....	166
5.4.2	Multi-cycle stitch and yarn deformation	168
5.4.3	Stitch extension results	171
5.5	Multi-cycle modelling results	174
5.5.1	Multi-cycle picture frame simulation results.....	174
5.5.2	Multi-cycle diaphragm forming results.....	176
5.6	Chapter summary	182
6	Maintaining fibre continuity over formed composite components using biaxial non-crimp-fabrics.....	183
	Abstract	183
6.1	Introduction.....	183
6.1.1	Chapter Objectives:.....	183
6.1.2	Local fibre alignment.....	184
6.1.3	2D-3D forming.....	184
6.1.4	Current work	186
6.2	Methodology:	187
6.2.1	Non-uniform shearing across a fabric length.....	187
6.2.2	Diaphragm forming pre-sheared fabrics.....	191

6.2.3	Finite element forming model	192
6.2.4	Finite element mechanical model.....	198
6.2.5	Experimental forming of L-Beam	203
6.2.6	Experimental forming – Sill section	204
6.3	Results:	205
6.3.1	Simulating pre-sheared fabric forming	205
6.3.2	Stress analysis of L-Beam	209
6.3.3	Experimental forming of L-Beam	213
6.3.4	Wastage reduction, L-beam	216
6.3.5	Stress analysis of demonstrator sill section	218
6.3.6	Experimental forming – Sill section	222
6.4	Chapter summary	226
7	Conclusions	228
7.1	Fibre angle measurement	228
7.2	Initial non-linear shear region and inter-stitch yarn buckling.....	229
7.3	Modelling of consecutive forming processes.....	230
7.4	Fibre alignment control during forming processes.	232
7.5	Discussion of pre shearing in 2D-3D composite forming.....	233
8	Appendix A	235
8.1	Apodius scanning methodology.	235
8.1.1	Laser scanning	235
8.1.2	Optical imaging	235
9	Appendix B	237
9.1	Shear angle calculation and export to Abaqus, Matlab code	237
9.1.1	Single sided scanning	237
9.2	Doubled sided scanning	244

10	Appendix C	255
10.1	In-plane testing	255
10.1.1	Picture frame shear testing.....	255
10.1.2	Bias extension shear testing	256
10.1.3	Tensile testing	258
11	Appendix D	261
11.1	Mutli-cycle picture frame testing	261
11.1.1	Extended multi-cyclic methodology.....	261
11.1.2	Results	261
11.1.3	Discussion.....	264
11.1.4	Conclusion	265
12	Appendix E	266
12.1	Fabric stabilisation and spring back.....	266
12.1.1	Methodology.....	266
12.1.2	Fabric Spring Back Results.....	267
12.1.3	Conclusion	268
13	References.....	280

1 Introduction

1.1 Carbon fibre composites

Carbon fibre reinforced polymers (CFRPs) are lightweight materials that have seen extensive use in automotive, aerospace and sporting applications over the last 20 years. CFRPs offer significant performance advantages over other materials. Their high specific stiffness and strength enable the creation of innovative engineering structures and can lead to environmental benefits, such as fuel savings via reduced mass for transport applications. In addition, their construction enables the creation of multi-functional structures, delivering transformative design opportunities. Material costs have steadily declined over recent years, but manufacturing challenges continue to be the major barrier preventing wider adoption, particularly in high volume applications.

A composite material consists of two or more constituents, typically a stiff, brittle fibre surrounded by a matrix. The arrangement and type of reinforcement dominate the mechanical properties of the composite, with the matrix material responsible for transferring stress from fibre to fibre whilst maintaining the fibre spacing and orientations. The matrix also provides vital protection to the fibres from abrasion and the environment. The combination of the two constituents results in a new material with remarkable anisotropy, sometimes with mechanical properties (e.g., tensile strength) that vary by orders of magnitude depending on the orientation and volume content of the reinforcement. Engineering composites are typically built up from individual fibre plies at different orientations, which are laminated layer by layer to create the final structure.

When designing fibre-reinforced composite structures, the material is often created at the same stage as the component. The properties are therefore dependent on the manufacturing process, which controls the placement of the fibres. This makes computer-based design somewhat challenging for the beginner who may be more familiar with designing with metals, where material properties are similar in all directions. Consequently, inexperienced designers can often be too conservative, opting for composite layups with lower, quasi-isotropic properties to offer a greater factor of safety. This approach negates one major advantage of composite structures,

as the strong, stiff fibres are not primarily aligned in the direction of the applied loads, therefore producing a suboptimal layup.

Currently the most popular method of composite manufacture involves a laminator placing fibre reinforcement, pre-impregnated with a polymer matrix, into a mould tool of the desired geometry. Heat and pressure are then used to cure the resin to form a solid composite structure. This thesis focuses on the production of carbon fibre composites for high volume applications (10,000ppa +) products through novel manufacturing techniques, without compromising on the specific properties. There is a gap in current industry at the medium-large scale where there is a lack of methodology for scaling up composite production from batches of 25-50 up to multiple hundreds and thousands of units. Bridging this gap would then open up enough demand for extremely high production rate technologies and advancement into automation.

1.2 Mass produced continuous carbon components

With the environmental drive towards electrification for passenger vehicles, energy saving measures are becoming increasingly important to maximise efficiency, due to the low energy density of current electrical storage methods. Light weighting is an effective way to improve efficiency and carbon fibre reinforced polymers (CFRP) can have the highest specific stiffness of all engineering materials when implemented correctly. Increasing CFRP production from batch production for structural components is currently limited by the requirement of highly skilled fabric laminators or high cost automated fibre placement machines. The aim of the current research is to overcome these limitations by provide an alternative production method to produce consistent structural components in high volumes at low cost.

Labour makes up 65% of the component cost when using a hand laminating approach. Within that cost, 75% of the man hours are associated with the lay down of plies to produce a monolithic component. New technologies attempting to reduce Takt time must tackle laminating time or remove the step entirely. 2D-3D forming is the high volume manufacturing route explored in this study. The methods that have been researched stem from current high output composite manufacturing methods, which use matched tool press forming with pre-preg (fibres pre impregnated with a

partially cured resin). Current aerospace components such as console panels and ejector seats are manufactured this way. Production rate is limited by the preforming operation which requires the fabric to be laminated into a shape that can be dropped onto the press tool for moulding. Due to this, a single laminator can only produce 5-10 components a week (dependent on complexity) and production is limited despite the much higher capacity of the press moulding operation. 2D-3D forming requires a ply layup to be kit-cut and constructed via pick and place, followed by immediate deposition into a press or alternative forming process without the need for an intermediate hand laminating stage. Removal of the laminating stage reduces overall cycle time, shifting the process bottleneck to the curing stage. Removal of manual tasks improves component consistency, which previously depended on the skill of the laminator. This also yields an overall reduction in component cost, as there is a reduction in labour.

1.3 Fibre alignment control in 2D-3D forming

CFRPs are anisotropic materials and the orientation of each ply is used to control the mechanical properties and optimise a laminate for its intended use case. This is because each reinforcement material has up to 3 (longitudinal, transverse and through-thickness) reinforcement directions, which align with the directions of the yarns running through them. A difficulty with 2D-3D forming is that yarns are reorientated during the forming process (Figure 1-1) and the yarn orientation controls both the mechanical properties (needed for component optimisation) and the formability (needed to achieve defect free components). Structural CFRP components are tested with a designated orientation for each of the plies in the laminate. Deviation from these values could cause the part to fail in-service. Formability is a crucial characteristic for creating defect free components, which is a combination of yarn orientation, fabric shear properties and bending properties. Reorientation of the yarns can be easily achieved during hand laminating, as each ply is manually placed according to a work instruction telling the laminator to bend or align the yarns to fit the tool geometry. Hand layup is currently being used to manufacture even the simplest structures, such as flat plates, as accurate orientation control is crucial. 2D-3D forming is a hands-off process as once the flat laminate is

placed in the press/diaphragm system, there is no way of interacting with it. The low level of forming control means that fibre alignment can currently only be controlled in the 2D ply layup stage. Further restrictions are placed on the orientations of the 2D ply-stack, as it must be able conform to the tooling and a trade-off is often required between preferred fibre orientation for structural purposes and for formability purposes. This thesis looks into a gap in the research around fibre alignment control during forming operations, focussing on structural benefits rather than formability improvements. There is a push from industry to understand the impact of forming on the mechanical performance of the final component and to maximise those properties.

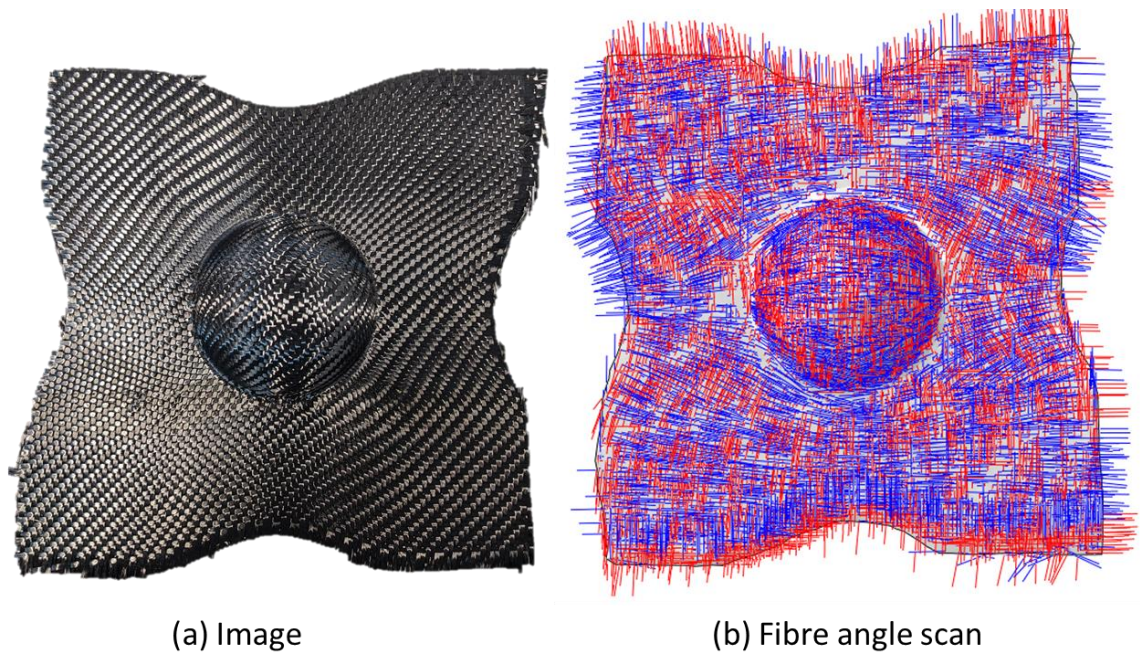


Figure 1-1 (a) Photo of 2D-3D formed hemisphere using a twill weave fabric. (b) Fibre angle plot of 2D-3D formed hemisphere.

1.4 Research Areas

Current research has highlighted a non-optimised usage of fibre angle alignment when forming composites. It raises the question of why there is not the same level of attention paid to optimised fibre angles when forming a composite as when using other manufacturing methods such as automated fibre placement (AFP). The research areas outlined in Figure 1-2 explore reasons why this is the case and each

chapter goes on to study the solutions that can be implemented using the novel ideas form this work.

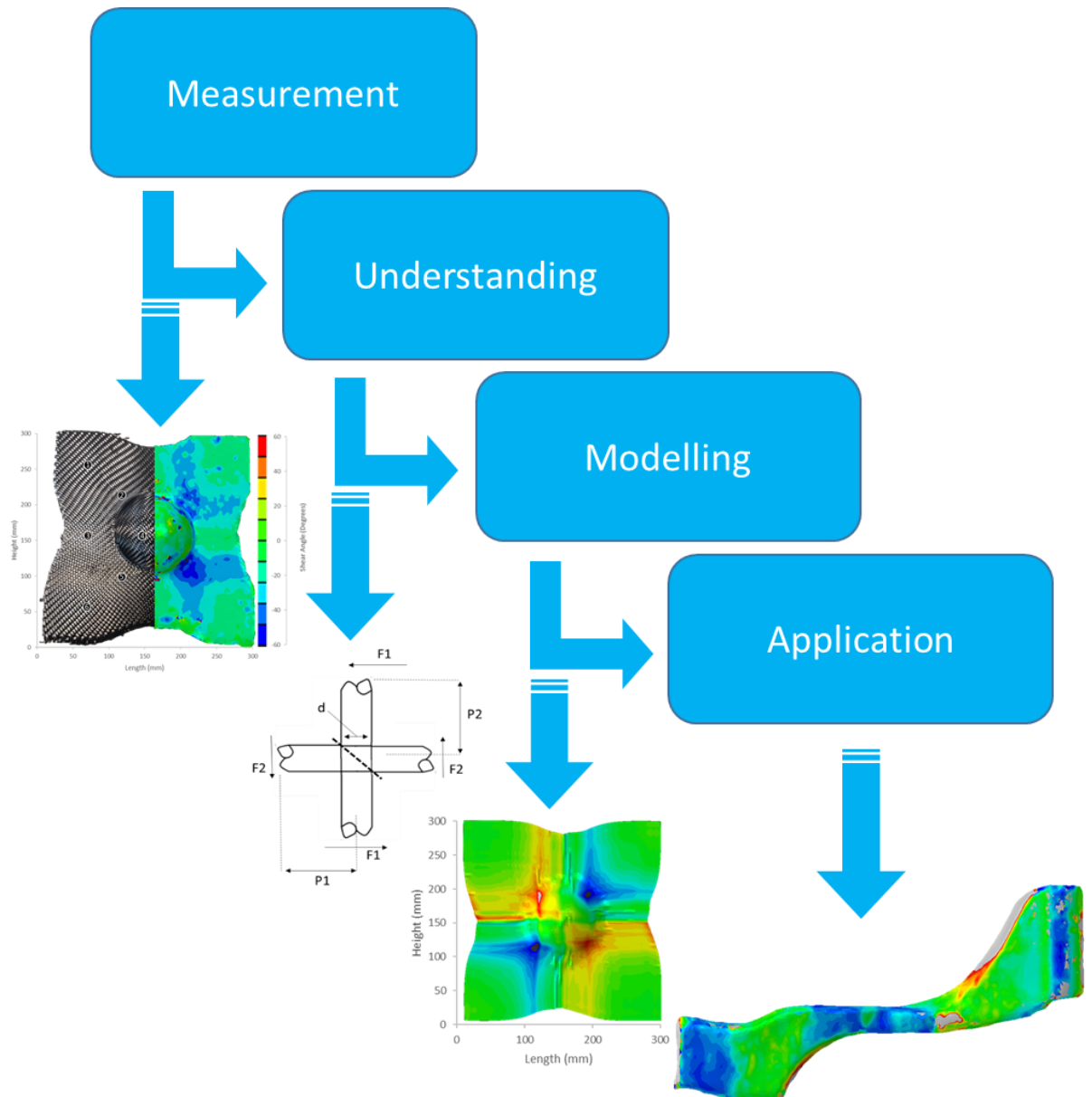


Figure 1-2 the four areas addressed by the research sections of this thesis.

For the sections of this thesis a selection of critical matters surrounding current fibre alignment methods have been identified, with aims to address each matter. Outputs from each of the chapters fall within at least one of the 4 areas outlined in Figure 1-2. The subsequent chapter synopses show the placement of each chapter within the aforementioned research areas, thereby providing a comprehensive overview of the interdependence observed between the chapters.

1.4.1 Chapter 3: Analysis of fibre angle distribution in biaxial non-crimp fabric: Measurement of formed fibre angle distribution (measurement)

Criteria for determining fibre alignment cannot be established without accurate measurement of the fibre angle distribution on a formed component. An improvement in commercial optical scanning technology has enhanced full-field angle measurements, which can be used to validate simulations and inform design.

The aim of this chapter is to generate a methodology for accurately measuring full-field fibre angle information from complex components and implementing that information into finite element material models.

The industrial application is to enable companies to start designing composite components with non-standard fibre angles. This chapter outlines a robust method for modelling and measuring fibre angles to remove the need to rely on quasi-isotropic layups.

Objectives:

- To create a methodology for using an optical scanning system for high resolution measurement of shear angles in formed non-crimp fabric (NCF) parts.
- To measure the fibre misalignment generated during the forming process of biaxial NCFs.
- To characterise the effect of fibre misalignment on the tensile stiffness of formed NCF components for use in finite element simulations.

1.4.2 Chapter 4: Non-linear shear behaviour & inter-stitch defects in non-crimp fabrics: Fibre misalignment during forming (understanding/modelling)

Understanding mesoscale fibre misalignment generated during forming is crucial as a change in fabric structure directly impacts the macroscale mechanical properties. This understanding can be used to implement strategies to control fibre misalignment and improve post forming mechanical properties. The focus of this chapter is on understanding the causes of fibre misalignment and implementing defect reduction strategies.

Results from this chapter can be applied to inspections that are performed on all parts in industry. During the prove-out process for a formed part, the appearance of inter stitch buckling can be identified up by a trained inspector and mitigation strategies can be applied without the need for expensive physical testing.

Objectives:

- To explore the link between non-linear shear behaviour of non-crimp fabric plies at the onset of shearing and the development of inter-stitch yarn buckling. An analytical model of the initial non-linear shear behaviour will be developed, which will be used to predict the likelihood of inter-stitch yarn buckling.
- To understand how inter-stitch yarn buckling generates a difference in fibre misalignment between positive and negative shear directions.
- To propose methodologies for inter-stitch yarn buckling reduction strategies.

1.4.3 Chapter 5: Modelling the multi-cycle shear behaviour of biaxial non-crimp fabrics: Lack of modelling capability for consecutive forming processes (understanding/modelling/application)

The cyclic behaviour studied in this work describes the shearing, un-shearing and re-shearing of fabrics that occurs during the forming process. By adding the ability to accurately model cyclic behaviour in forming processes, the design space can be

opened up to add more novel fibre alignment strategies into current operations. The aim is to generate a novel material model that captures the multi-cyclic nature of consecutive forming operations and accurately outputs fibre angle.

Accurate forming models will enable industry to increase the uptake of 2D-3D preforming as a mass manufacturing method. An accurate and robust forming model will reduce the prove-out cost by eliminating the need for testing dozens of laminate kits in the pursuit of defect free parts. In many cases, machining multiple mould geometries requires a huge capital outlay, in which case an accurate model will save tens of thousands of pounds worth of tooling cost.

Objectives:

- Explore the effect of multiple shear cycles on the shear modulus of biaxial non-crimp fabrics (NCFs).
- Generate a finite element (FE) material model that encompasses the multi-cycle shear properties of a biaxial NCF and accurately captures the shear angle distribution during a multi-stage forming process.
- Propose and simulate a modified forming process that utilises multiple shear cycles to improve formability.

1.4.4 Chapter 6: Maintaining fibre continuity over formed composite components: Understand the structural benefits of fibre alignment control (measurement/modelling/application)

Maintaining fibre continuity is vital for maximising mechanical properties in components. Darting of fabric plies is common to ensure plies conform to complex tooling, but these discontinuities in the fibre architecture can cause unwanted stress concentrations. During hand layup, these darts can form a triangular gap in the ply, which is typically plugged by a small patch. Automated forming processes are unable

to facilitate this, so a local thinning is experienced as a hole forms, which reduces the local fibre content in the part. The focus of this chapter is on creating a fibre alignment strategy for 2D-3D forming. Using the tools generated in previous sections a novel simulation has been created that models the output of the alignment strategy. After generating an optimised fibre path, the structural improvements have been outlined by incorporating the methodologies and data from the previous chapter findings.

The industrial use case for this adaptation to the current 2D-3D forming methodology is an example of the design freedom that can be achieved by utilising the findings of this thesis. A distinct structural improvement can be achieved with a minor change to the layup step that mimics the alignment control that is currently afforded by hand layup.

Objectives:

- Develop a methodology to locally control fibre orientations in a 2D blank, to follow key geometric features within the component, using pre-sheared fabrics.
- Create a finite element model that can accurately plot the fibre orientation of pre-sheared fabrics.
- To model the structural effect of localised pre-shearing on formed components

1.5 Chapter summary

This chapter contextualises the structure of the thesis and outlines how each chapter fits in to the greater narrative of improving fibre orientation control in formed composite components. The rationale behind the research has been outlined and a path has been defined to contextualise the results and gain a thorough understanding of fibre alignment control in 2D-3D forming. The final research chapter (Chapter 7) presents an example of a use case that incorporates results from the previous 3 chapters. Each chapter contains outputs that align with the objectives stated above.

2 Literature review

2.1 Introduction

A review of the common reinforcement formats used to produce structural components within the automotive and aerospace industries has been conducted, with a view to understanding the material requirements to facilitate an automated 2D-3D forming process.

Various material characterisation tests have been investigated that focus on quantifying fabric drape characteristics which are sensitive in 2D-3D forming. Industrially prevalent 2D-3D forming techniques have been noted alongside some novel forming processes to identify current and future technologies that could benefit from an improved understanding of the material characteristics. . Methods of scanning composite components for topology and fibre orientation information are compared to identify a robust method of for measuring properties around formability. The section concludes with a look into current computer modelling of composite forming and the insights that can be gained with improved material modelling capability. Finally, the aims and objectives for the work conducted to date are compared to gaps in current knowledge.

2.2 Material architecture

This thesis focuses on carbon fibre reinforced composites, specifically dry biaxial carbon fabrics. Continuous fabrics are produced from individual yarns as a flat sheet and need further processing to generate complex 3D geometries. These fabrics are used with thermoset and thermoplastic resin systems and a range of infusion processes that require a forming procedures to create a 3D component. The principal composite architectures used in engineering applications are woven fabrics, non-crimp fabrics and unidirectional fabrics. Shorthand for these general architectures are: Woven, NCF and UD respectively. Each type of fabric binds the yarns together in a different manner, giving different inter-yarn properties which manifest as contrasting macro scale fabric properties. Woven fabrics rely on inter-yarn friction generated by a crimp to hold the fabric together, whilst NCFs and UD fabrics use a

stitch or a polymer binder. The benefits and disadvantages of each method in forming operations have been explored.

2.2.1 Woven Fabrics

Woven materials generally consist solely of reinforcement yarns and are the original method for generating fabric materials from structural fibre. These fibres can consist of glass, aramid, carbon or a host of exotic fibre types used to suit specific needs. A fabric material is obtained by orthogonally interweaving yarns about each other, forming an out-of-plane undulation known as a crimp. A woven fabric relies on the normal force created at the crimp due to the bending of the yarns to create a frictional resistance. This resistance holds the yarns in place and resists unwanted sliding and subsequent degradation of the structure [1]. Weaving as a method has been around for thousands of years and a vast array of different weave patterns exist. The most common weave in the composite industry is a twill weave which consists of a distinct diagonal pattern or texture created by the interlacing of warp and weft threads. It is named after the twill line, which refers to the diagonal lines formed by the pattern and is used by laminator to distinguish between ply angles. Some less common weaves found in engineering applications are shown in figure (1).

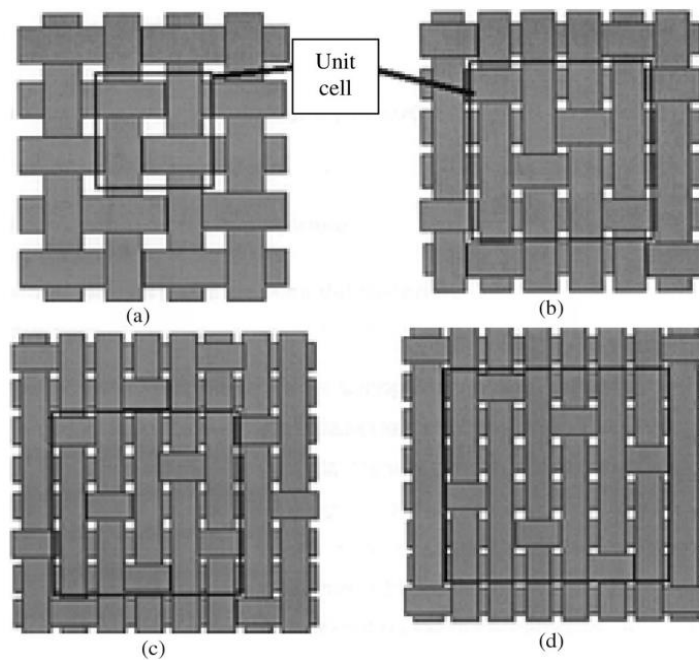


Figure 2-1 Weave architectures: (a) plain weave, (b) crow-foot satin weave, (c) five-harness satin weave, (d) eight-harness satin weave. [2]

Weaving structural fabrics is a well proved out process leading to consistent and widely available fabrics with a variety of fibre types. The woven fabrics properties are inherent to its architecture with different weave patterns generating different properties. The weave is the only thing constraining the local fibre slippage at low load, which can lead to internal local defects caused during manufacture or handling. The stability is reduced at the boundary where tension in the interlaced yarns is low and free movement of transverse yarns can occur at the edges of woven blanks or in low weight fabrics. This is known as yarn slippage. The weave provides an ideal structure for shearing, as each crimp in the material is assumed to act as a friction dependent pin around which the yarns can rotate [3]. Shearing is the dominant deformation mode in 2D-3D forming processes as the yarns are relatively inextensible. All fabrics experience non-linear in-plane shear and the aim of characterisation is to understand how the function for shear modulus influences defects generated during forming. The architecture of a material greatly influences the shear function. Woven fabrics experience locking at very high shear where the yarns compress up against one another and there is an increase in the fabric modulus. The specific shear angle value for locking depends on the yarn dimensions, weave tightness and pattern. At lower shear angles the weave tension is the most important property as tension is directly related to the inter-yarn frictional forces being generated. A loose weave gives much greater formability [4] . However, it may then be susceptible to increased yarn slippage.

The biggest drawback of a woven fabric also comes from the crimp. The crimp bends the fibre out-of-plane resulting in a marked reduction in the in-plane final failure strength. This is up to 50% in 3D woven fabrics [5] and 20% in comparison to UD fabrics. Particularly detrimental is the accompanied reduction in stiffness. Structural composite components are not just designed for failure, but are used to maximise component modulus in high end applications such as F1 chassis, rotor blades and wing spas. A lower stiffness fabric requires a thicker composite sheet to be used which lowers the weight saving benefit of using the composite. The reduction in final part mechanical properties is enough for new materials with lower formability but no crimp to be explored as an alternative.

2.2.2 Non-Crimp Fabrics

Non-crimp fabrics will be the material focused on in this thesis. Non-crimp fabrics (NCFs) do not rely on interweaving to join yarns. Instead rows of polymer stitches are placed across aligned reinforcement yarns. This method can be used to stitch one, two or three plies together in uniaxial, biaxial or triaxial NCF fabrics. In biaxial NCFs the stitches join a second layer of aligned UD carbon yarns perpendicular to the first, with each stitch acting as a pin joint for the accompanying 2 yarns. This gives shear deformation properties similar to a woven architecture and allows for some crossover of the assumptions when attempting to characterise the in-plane shear properties [6]. Polypropylene and Nylon are popular stitch materials and lock stitching and pillar stitching are examples of common stitch patterns shown in figure (2) [7].

Stitch patterns can differ on each face of the NCF and different combinations of stitch types give different fabric properties. Stitch width, density, pattern and material properties all have an effect on the fabric shear whilst only having a marginal impact on the strength [8] and stiffness of the final composite once it is infused [9]. There is a gap in research around how the combination of stitch parameters affect the fabric draping properties and defect formation during forming. NCFs also have stability that is dependent on the stitch tension and architecture used. Low tension NCFs with wide stitch spacing are very difficult to handle, whereas high tension fabrics have better handleability due to the stitch having equal tension across the fabric, holding it together. Damage to the stitch is an issue unique to NCFs, with stitch pull out and breakage being a cause of non-uniformity over a fabric length. The mechanical performance improvements caused by removing the crimp makes NCFs appealing for structural use and as biaxial NCFs provide more forming challenges than woven architectures, there is an opportunity to investigate defects specific to them.

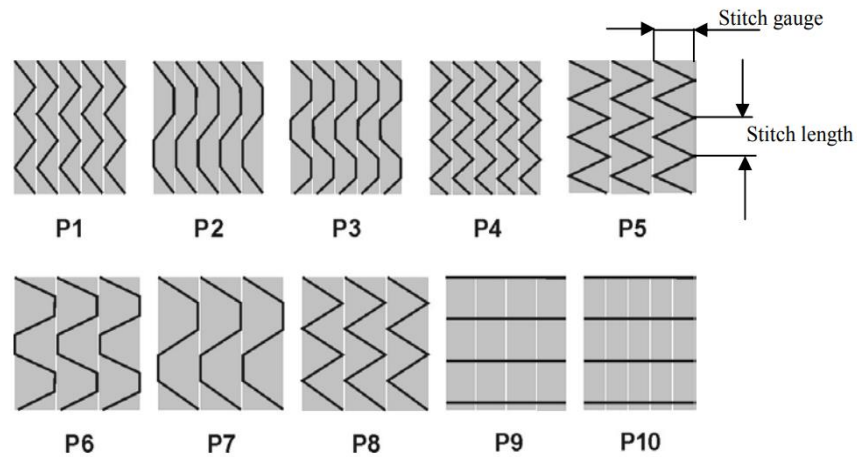


Figure 2-2 Various stitch pattern types (P1, 4, 5, 8) zig-zag/tricot, (P2, 3, 6, 7) mixed zig-zag/half tricot, (P9, 10) straight (Pillar).

2.2.3 Unidirectional Fabrics

UD NCF fabrics have a binder applied that adheres parallel fibre yarns together creating a fabric with no crimp and no stitch. These yarns can then be bound to another set perpendicular to the first in a similar manner to biaxial and triaxial NFCs. However, the pin jointed shearing approximation cannot be used. In some cases UD without stitches of binder can be used and comes fixed to thin veil or grid material. UD is particularly difficult to handle as yarns are loosely bound and can separate easily when moving the fabric and during manufacture. UD has a low formability due to the lack of pinned yarn cross-over points found in the other fabrics discussed. The major benefit of UD fabrics is in the consistency of in-plane properties which gives high confidence in the failure point of UD components. Automated forming is a challenge as the poor handling of many UD fabrics means that it requires a complex quality assessment system and a methodology that is able to achieve proper ply-tool conformity.

2.2.4 Pre-impregnated fabrics

Pre-impregnated fabrics (pre-

pregs) have a controlled amount of resin coating the fibres. During shear dominated deformation, the resin gives the fabric viscoelastic properties which adds a rate dependency to the uncured mechanical properties [10]. Pre-pregs can have the same

architectures as dry fibre fabrics and the same mechanical benefits are gained with pre-preg NCFs and dry fabric NCFs. Rate dependency is an aspect that is not considered in this thesis, but could be expanded in further research. The similarities between the fabric types mean that many of the proposed methodologies are transferable between dry and pre-preg fabrics.

2.3 2D-3D Forming

Flat sheets of fabric must deform significantly to conform to 3D shapes. The mechanisms for this are unique to textiles and are a result of the multi scale interaction of fibres and yarns within the fabrics. In-plane shear is the dominant deformation mode in biaxial fabrics as the fabric shear modulus is significantly lower than the tensile stiffness in all engineering fabrics [11]. Fabric shear modulus is not constant and generally increases as the shear increases and relative angle of the yarns is increased. There are three identifiable regions in most shear stiffness curves that are each dominated by differing deformation modes.

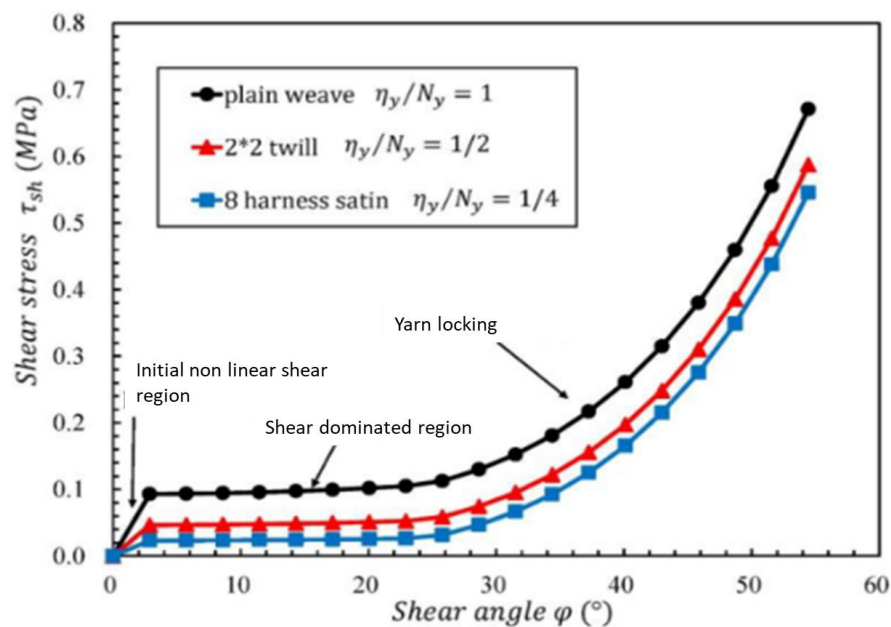


Figure 2-3 [12] Example woven fabric shear force, shear angle graphs with the three identifiable different deformation mode regions added.

2.3.1 Initial non-linear shear region – yarn sliding

At the onset of shearing up to 5 degrees (in some fabrics), there is an initial non-linear shear region. The existence of this particular region is subject to ongoing debate, with one perspective attributing it to an artifact of the picture frame shear test, while another perspective suggests its origin as a result of inter yarn forces preceding the onset of shear. Supporters of the inter yarn forces theory have presented papers explaining the potential mechanisms underlying this phenomenon. Before the force applied to the yarns is enough to overcome the frictional interactions between them and initiate slippage, there is a region where zero shear occurs and the forming is controlled by other mechanisms. The dominant mechanism is reasonably well understood in woven fabrics [13]. There is a small amount of yarn tension inherent to the crimped fabric which causes a small normal force and frictional inter-yarn interaction at each crimp. This is due to the geometry of the crimp and the tension needed to weave the yarn into that structure. Inter-yarn slippage must occur to generate fabric shearing. However, at very low loads the applied shear force cannot exceed the inter yarn friction, so the fabric deforms as an elastic grid structure instead. The total angle for shear is the sum of the angles in the two beam sections of the grid (Figure 2-4): $\theta = \theta_1 + \theta_2$.

$$\frac{1}{G} = \frac{\theta}{F} = \frac{1}{12BL} \left[\frac{P_1}{P_2} (l_2 - d)^3 + \frac{P_2}{P_1} (l_1 - d)^3 \right] \quad [13] \quad \textbf{Equation 2-1}$$

where θ is the total shear angle with θ_1 and θ_2 being the shear angles in the arms. F is the total shear force and B is the in-plane bending stiffness of the yarn. L is the sample width and P1 and P2 are the respective yarn spacing in the warp and weft directions. D is the contact length and G the shear modulus.

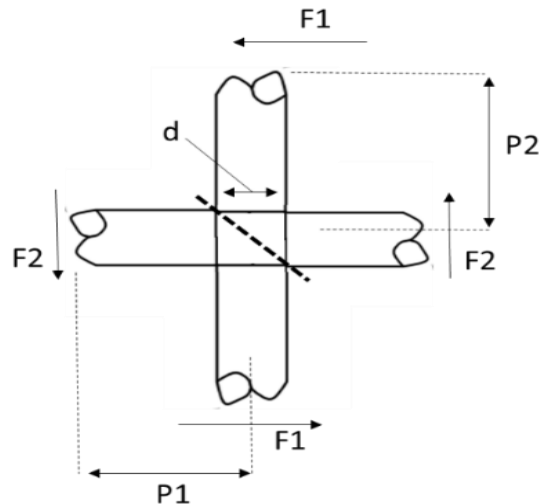


Figure 2-4 Diagram of the stitch at a yarn on yarn crossover point (NCF). θ_1 and θ_2 are shear angles of each arm.

There is a high initial shear modulus at low load as there is no shearing occurring between the yarns. Instead the apparent shear in the fabric is due to in-plane bending of the fibres and rigid rotation of each yarn crossover point. Inter-yarn shearing begins in conjunction with the in-plane yarn bending as slippage begins to occur at each yarn crossover point. As the inter-yarn friction is overcome the modulus reduces as inter-yarn shear takes over as the dominant deformation mode. A full transition occurs at 0.2 - 0.5 degrees depending on the fabric architecture.

This mechanism is essential for understanding the initial deformation of fabrics during forming. All draping in the fabric starts from this initial deformation, and a fabric that is sheared multiple times during forming will pass back and forth through this region. Without full understanding of the consequence of that any predictive drape models will be incomplete and predicted fibre orientations used for structural simulated testing could be incorrect. This could lead to reduced performance or premature failure of a component.

A similar process could also occur in biaxial NCFs as a similar low shear region is seen in the modulus function of some NCF materials. There is no crimp, but there is a similarity between the yarn deformation modes. However, a major difference between woven fabrics and stitched NCFs is the generation of a normal force at each

yarn crossover point. The inclusion of a stitch adds new parameters that could dictate the shape of the low shear region, which are not currently understood.

The majority of constitutive material models remove data at the low shear region to improve model stability. This creates a jump between the positive and negative shear stiffness data across the zero point, which is removed by translating the entire function and interpolating between the negative and positive regions [14]. It is not known what impact this has on the validity of NCF material models when assessing defect generation. The initial non-linear shear region requires further investigation as any shearing of a fabric must start and go through this region. This becomes increasingly important in multi-step forming processes where a fabric may transition through this region many times. Understanding the significance of this region will become more valuable for NCFs as forming operations become more complex.

2.3.2 Steady-state Shear – yarn rotation

In-plane shear is the dominant deformation mode for the majority of the 2D-3D fabric forming process. This means that shearing prevails over stretching when the fabric needs to conform to complex double curvature surfaces. A sheet material with similar tensile properties, but without the ability to shear would experience wrinkling and poor conformity. The low shear modulus is due to the weak stitch fixation, enabling the fibres to rotate about the pin joint, as shown in Figure 2-5 [14]. Many biaxial non-crimp fabrics have non-symmetrical positive and negative shear curves due to the orientation of the stitch (although some maintain symmetry with mirrored stitch directions). The stitch provides resistance to shear in one axis called the positive direction, but has very little interaction in the opposing negative direction. This is due to the stitch being in tension in the positive direction and compression in the negative direction. The shear stiffness is generally much higher in a positively sheared NCF than a woven fabric (with similar yarn properties) and contains a characteristic drop in force at a high shear angle which relates to the point at which the stitch tension exceeds the breaking point of the stitch, as shown in Figure 2-6. This tends to occur before the locking angle but is dependent on the tension and the type of stitch used. The stitches have a negligible effect on the final in-plane strength and stiffness properties of the composite, relative to the primary reinforcing yarns,

but broken stitches allow for deformation of individual unconstrained yarns rather than the ply deforming uniformly as a continuum [7]. Consequently there is no resistance to yarn spreading and bunching, so forming at an angle beyond the stitch breakage point can create unwanted defects. There is an opportunity to utilise the breakage or removal of stitches to free the fabric in local regions as a method of defect removal as discussed by Chen et al [ref]. The material depicted in Figure 2-6 deviates slightly from the norm, exhibiting a notable presence of loose stitching that conceals the initial non-linear shear region. Conversely, all fabrics examined in the subsequent chapters manifest the emergence of an initial non-linear shear zone.

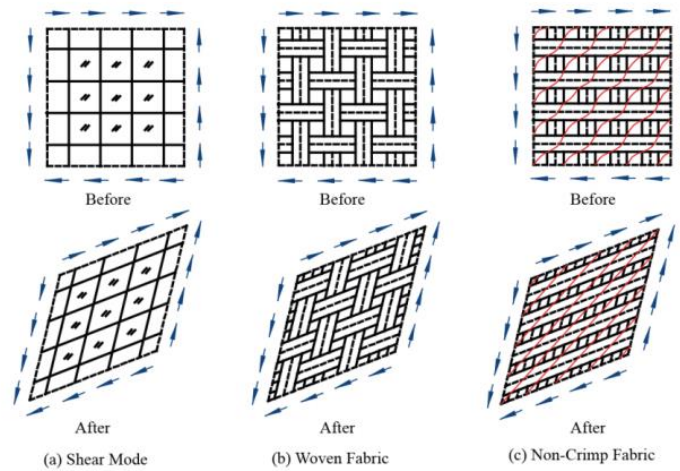


Figure 2-5 In-plane shear diagram (a) general modes, (b) woven fabrics, (c) NCF fabrics.

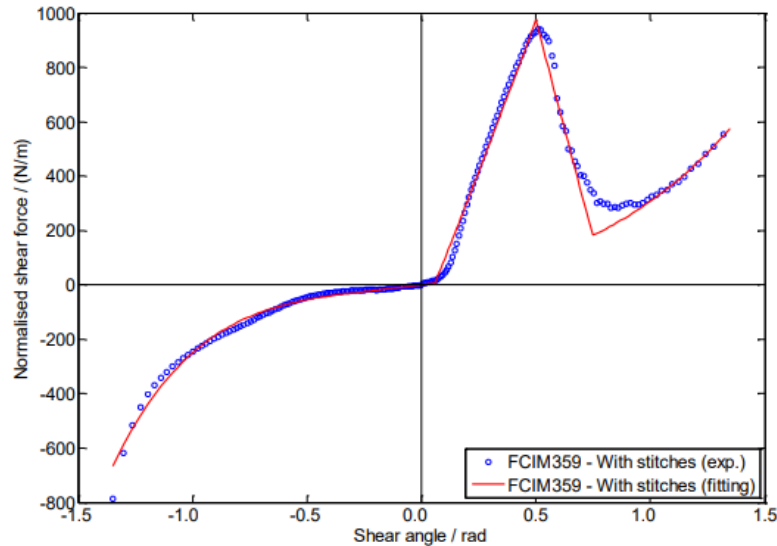


Figure 2-6 Difference in force, shear angle response of a pillar stitched non-crimp fabric (FCIM359) between positive and negative shear directions. [14]

2.3.3 Yarn locking – lateral yarn compression

Yarn locking describes the rise in shear stiffness seen at the end of the shear function. It occurs when the reduction in the yarn spacing generated by the deformation compresses neighbouring yarns against one another. In a woven fabric this region is important for understanding defect generation and an angle range is denoted as the locking angle of the fabric. The compressed yarns require more force to shear as the yarn bundle deforms which can lead to out-of-plane buckling. This phenomenon is seen in woven fabrics as a sharp rise in shear modulus as shear angle increases. In NCF fabrics it looks like a recovery of shear stiffness after the drop caused by stitch breakage. Not all NCFs experience stitch breakage before yarn locking in which case there is no plateau or drop in modulus and instead the modulus continues to rise non-linearly.

2.3.4 Out-of-plane bending

Dry fabrics have poor compressive properties when unconstrained due to the tendency for the yarns to buckle. Buckling is related to the fabric bending stiffness, which is generally very low in comparison to the tensile stiffness along the direction of the yarns. It is likely that an unconstrained fabric under compression will experience some form of in-plane or out-of-plane buckling. Knowledge of the bending stiffness is necessary to measure any out-of-plane movement correctly. For

example large out-of-plane deformation occurs once the in-plane shear in a fabric surpasses the locking angle [15], or if complex shearing is seen with multiple regions of positive and negative shear. This causes wrinkles in the fabric, which are a type of defect that are governed by the bending stiffness of the fabric [16]. Material bending stiffness is a material property that is incorporated into finite element forming models for its impact at high shear when wrinkling occurs. The property is also significant at low shear before frictional forces are overcome and shearing begins.

2.3.5 Defects caused by 2D-3D forming

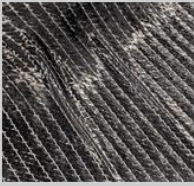


Defect mode	Macro scale wrinkling	Meso scale wrinkling	Yarn spreading (gapping)
Image			
Mechanism	Shear locking	Yarn compression and buckling	Intra ply slippage

Figure 2-7 types of common defect generated during 2d-3d forming processes.

2.3.5.1 Wrinkling

Wrinkling is the most common defect seen in components that have been formed from a 2D blank into a 3D shape [17] due to the low bending stiffness relative to the tensile stiffness of the yarns. Wrinkling is due to buckling of the fibres at the macro- and mesoscale, where a different wrinkle type is generated at each scale. As previously mentioned, macroscale wrinkles are attributed to the compression of yarns producing an out of plane wrinkle. Mesoscale wrinkles are due to uneven compressive and tensile forces across the face of the fabric sheet, causing individual yarns to buckle. This can be observed as fibre waviness on the surface of the ply. Both types of wrinkle are defects in the final formed piece that affect the final properties once resin is introduced. In addition, macroscopic wrinkles can also cause geometric tolerance issues which may stop a part from conforming correctly to tools and other parts at bond lines.

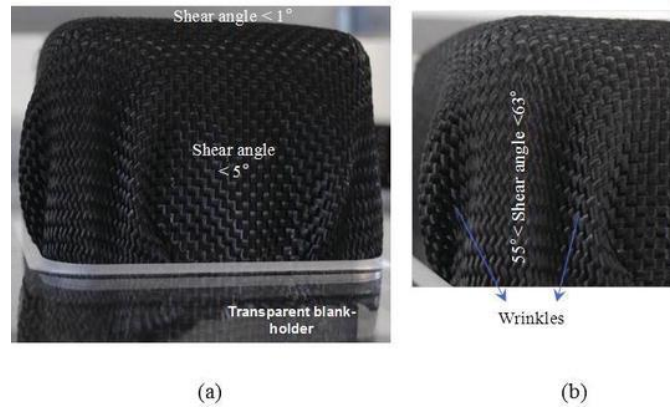


Figure 2-8 Example of out-of-plane macro scale wrinkling on a formed component. [17]

2.3.5.2 Yarn spreading

Yarns spread and bunching are the two defects stemming from fibre slippage. Yarn spread refers to where there is uneven slippage of the yarns, leading to areas devoid of warp or weft yarns. These cause resin rich areas in the final composite which lead to onset points for crack propagation during matrix failure [18]. A lower tension NCF is more likely to experience yarn spreading as the yarns have less constraints. The occurrence of this in the middle of a 2D-3D formed laminate would be difficult to detect and potentially catastrophic for the component mechanical properties.

2.3.5.3 Yarn buckling

Out-of-plane buckling occurs in two ways: the fabric level (macro scale), and at the yarn level (mesoscale). Both are classed as defects. The fabric level defect is a wrinkle as discussed above. The yarn level buckling defect occurs when varied compressive and tensile stresses are seen across the fabric. This could occur in a forming process because of differing blank holder forces or diaphragm forces. These small buckles in individual yarn or sets of yarns are observed as out-of-plane buckles and in-plane buckles once they have been flattened by a tool. This defect is related to the initial non-linear shear region and is sensitive to the bending properties of the yarn.

2.4 Material characterisation

Isolating and fully understanding individual deformation modes is necessary for gathering a thorough understanding of a fabric material. By testing for individual properties separately the most important forming modes can be focussed upon such

as the in-plane shear modulus. Less sensitive deformation modes have been explored to improve the understanding of the holistic material and give a better understanding of drape response and defect formation.

2.4.1 In-plane shear tests

The literature gives two widely accepted methods for measuring in-plane fabric shear, with both methods presenting positive and negative attributes and neither method being preferred over the other.

2.4.1.1 *(Uniaxial) Bias extension test (UBE)*

Bias extension of a material sample can give the shear properties from a simple tensile test. A single rectangular sheet of fabric is clamped into a tensile extension machine with the primary axis of the fibres orientated at 45° to the extension direction. Elongating the sample causes non-uniform shear across the fabric which can be split into three deformation zones. A central zone (zone A) that experiences pure shear forms on the sample away from the clamped boundary, a combined deformation zone (zone B) and a zero deformation zone (zone C). Assumptions in the bias extension test are as follows [19] :

- Fibres are inextensible.
- Inter-fibre slippage is 0.
- Fibres are pinned at the cross over points and shear occurs by the rotation about these points.
- Bending stiffness of fibre is neglected.

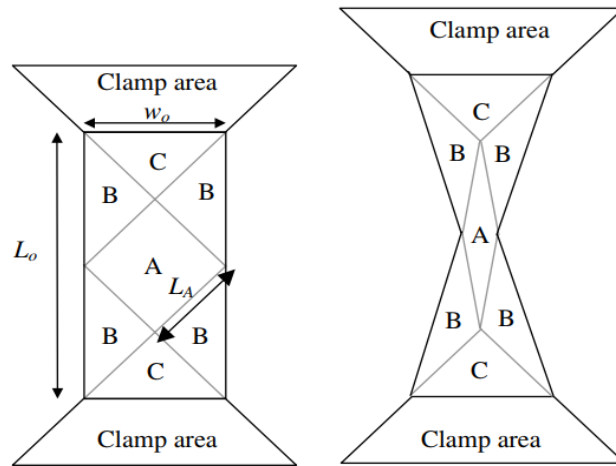


Figure 2-9 Bias extension test with deformation zones identified

At the fabric level the material deforms under pure kinematic conditions with shear angle (α) being a function of the angle between fibre directions (θ).

$$\alpha = \frac{\pi}{2} - \theta \quad \text{Equation 2-2}$$

The shear angle in a zone of pure shear can be determined by the crosshead displacement (D) and the initial length (L_0) and width (l_0).

$$D = \frac{\pi}{2} - 2 * \cos^{-1} \left(\frac{\sqrt{2}}{2} * \left(1 + \frac{D}{(L_0 - l_0)} \right) \right) \quad \text{Equation 2-3}$$

The pure shear zone is identified as zone A and is surrounded by zone B consisting of combined deformation methods and zone C which experiences no deformation. Biaxial NCFs can be measured with the UBE test by assuming that the fabric is a stack of UD fibre layers which are modelled using the simple shear kinematic. Applying simple shear kinematic to zone A of the UBE test gives a simplified equation where (w) is the angle from the vertical axis of zone A.

$$A = \frac{\sqrt{2}}{2} * \left(1 + \frac{D}{(L_0 - l_0)} \right) \quad \text{Equation 2-4}$$

$$w = \sin^{-1} A \quad \text{Equation 2-5}$$

$$D = \frac{\pi}{2} - w - \sin^{-1} \left(\frac{\sin w}{\sqrt{1 + \frac{1}{\sin^2 w} - \frac{2}{\tan w}}} \right) \quad \text{Equation 2-6}$$

This equation has to be used for simple shear processing of NCF materials. At large extension values, buckling can be seen across the centre of the sample at which point the test is no longer an accurate approximation of simple shear. A laddering effect can also be seen on the boundary of the sample during testing where yarns have clearly begun to slide relative to one another invalidating the pin jointed assumption used during shear angle calculation.

The Bias extension test can be conducted at elevated temperatures. This is useful for characterising thermoplastics which require testing up to and above the matrix melting point. Additional difficulties can occur at high temperature, including inconsistent clamping force due to matrix flow [20].

Advantages of bias extension test

- Consistent tension in the yarns.
- Simplicity in setup and execution.
- Simple sample preparation.

Disadvantages of bias extension test

- Involved calculation for the measured area of pure stress.
- Lack of simple shear with NCFs.

2.4.1.2 Picture frame test (PF)

The picture frame test measures the in-plane shear of a square fabric sample. It is one of the standards for characterization of shear resistance and is an alternative to the bias extension test, especially for the case of NCFs [6]. A cross shaped sample with a square central section is clamped (variable clamping conditions) at its boundaries to a pin jointed rigid beam frame. The yarns in the sample are at 45 degrees to the direction of extension and sit perpendicular to two sides of the frame and parallel to the others. The test setup approximates an orthogonal trellis in the frame where each yarn is a bar that is allowed to rotate at the sides of the frame. The

crosshead is extended vertically and the frame is extended with each beam pivoting about one another to produce shear over the entirety of the sample. (Figure 6) [21]

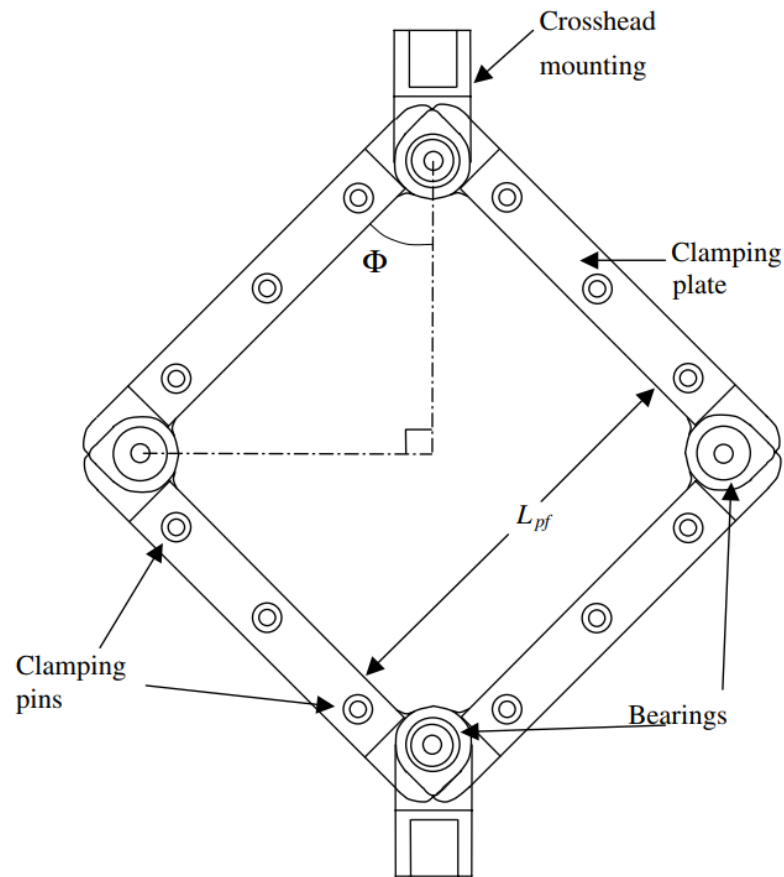


Figure 2-10 Picture frame in-plane shear test and example clamping setup.

The relationship between force and shear angle is below:

$$F_S = \frac{F_p}{2 * w * \cos \frac{\alpha}{2}} \quad \text{Equation 2-7}$$

$$\gamma = \frac{\pi}{2} - \alpha \quad \text{Equation 2-8}$$

Where (F_S) is the force required to shear the fabric as a function of the extension load (F_p) and the frame angle (α). The frame angle can be used to directly measure the shear angle (γ) from the crosshead displacement.

A clamped boundary condition with free edge rotation is difficult to achieve and in a number frames the boundary fibres are fully clamped and bend at the edge to conform to the imposed strain [22]. This is a known testing parameter where the

edges of the picture frame are considered not to be under pure shear conditions. The edge deviation can be reduced by lowering the bending stiffness of the material which is achieved in woven fabrics by removing the transverse yarns at the edges of the sample. In NCFs removing the transverse yarns has an impact on stitch tension, so the edge yarn removal alters the fabric properties in the pure shear zone.

Yarn tension must be at a minimum across the sample otherwise the high tensile stiffness changes the force used to extend the crosshead [23]. It is assumed that all forces in the sample are homogenous so uneven tensioning of the fibres influences the measured shear force with tensile force component. Misalignment of fibres in the frame will also cause an uneven tension to be seen across the fabric. Even a small misalignment will generate large tensile forces in the picture frame sample due to the fully constrained boundaries. It is currently unknown how large this effect is on the shear curve for NCFs, or what the allowable ^{error} on fibre misalignment is.

Yarn slippage within the sample alters the shear properties between cycles of picture frame tests. Slippage is lower in the picture frame test than the bias extension test due to the boundary constraints keeping the fibres in place. Slippage of the yarns within the central region of the picture frame particularly occurs in loosely woven fabrics. Shearing and un-shearing the fabric multiple times before conducting the picture frame test has a permanent effect on the measured shear modulus. This is because the yarns are compressed during shearing [24] and the yarn width and yarn spacing are altered [1]. There is an argument to pre-shear fabrics multiple times before testing because more consistent results are seen, but this is not representative of a real draping process where the fabric will be formed from a flat un-sheared sheet.

Alternative clamping methods for the picture frame test exist to help reduce the setup complexity and the inconsistencies in the test. Individually clamping and tensioning of each yarn assures that all fibre yarns in a sample are completely aligned with the frame. Alternatively, only securing the yarns at small sections near the pivot points of the frame reduces the boundary bending effect [22]. This method greatly reduces the number of yarns that must be aligned and provides zero tension in the rest [25]. Only clamping some yarns raises questions as to how the force can be

evenly distributed when shearing the fabric and the new free edges created by this method must experience some fibre slippage (similar to the bias extension test).

Advantages of picture frame test

- Easy to see and measure pure shear region

Disadvantages of picture frame test

- Careful setup to ensure each yarn is clamped with equal tension.
- Unknown boundary clamping effect.

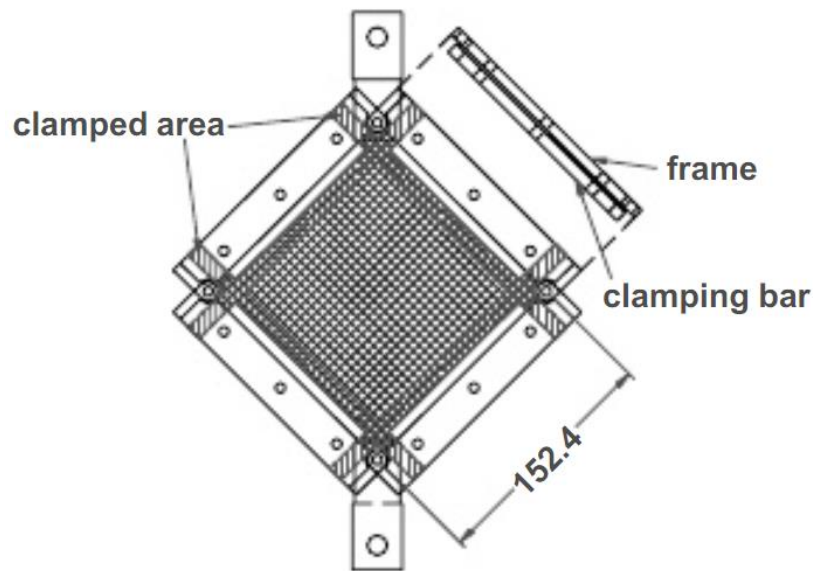


Figure 2-11 Picture frame with free edge boundary condition, created by extended fabric clamps.

2.4.2 Comparison of tests

Benchmark tests have been carried out for both the bias extension test and the picture frame test. The benchmarks controlled for material, but allowed for a difference in setup between each facility. As a result each facility presents varied data with no two facilities having entirely matching results. It also showed that standardisation is needed for both tests as disparity in setup causes major variability in the output data.

Comparison of the two in-plane shear tests has been inconclusive as a set of unified assumptions proving that both tests measure the same trellis shear has not been achieved. Hivet and Duong [26] suggested that the picture frame and bias extension

test do not load the sample in the same way, and therefore cannot be directly compared. However Pasco[27] equated the rate of extension in both tests and normalises the data to give a comparison where it is assumed that samples in both tests are loaded in pure shear. The study focused on a woven pre-preg where rate dependency is important, but the comparison of loading methods is applicable to dry NCFs.

A Comparison of the two tests was conducted by Pasco [27]. It compared that to the shear angle measured from the surface of the sample using digital image correlation and a discrete dot tracking method. A full comparison of the theoretical values and measured values in both tests showed that: in the bias extension test the theory accurately calculates the shear angle up to 40 degrees after which the calculated shear modulus experiences an exponential rise which is not representative of the measured fibre angle. The picture frame test maintains an excellent conformity between the theoretical values and the measure values throughout the entirety of the test.

The comparison of tests show that the measured shear angle is different between the two tests until 45 degrees where they both converge (Figure 2-12). Both tests follow a similar shape but with the bias extension test having a distinct plateau in the force during the middle of the test, whereas the picture frame maintained a more progressive curve. The presented theoretical shear angles from the bias extension test are far higher than the real values.

The picture frame test is the most viable method for NCFs for measuring shear angle over the range of values seen in forming operations. The boundary laddering in the bias extension test makes NCF testing inconsistent. The difference between measured and theoretical shear angle is much larger in the bias extension test than the picture frame test. Calculation of the shear angle is much simpler in the picture frame test and does not rely on the creation of multi deformation mode regions. For low shear the bias extension test may still provide accurate results and could be used as a tool for comparison however the picture frame test will be used for in-plane testing in this thesis.

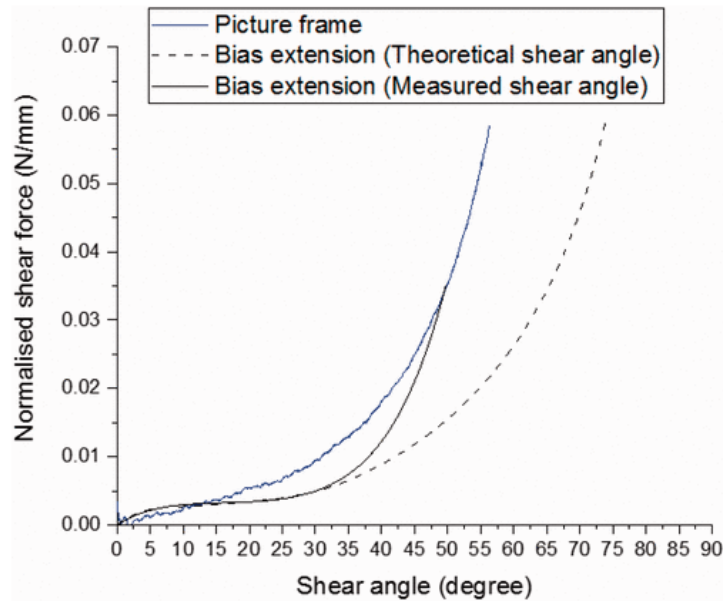


Figure 2-12 Comparison of bias extension and picture frame test for a woven pre-preg [1]

2.4.3 Bending tests

In-plane and out-of-plane bending are not well understood in composite forming. The influence of bending tends to be ignored in forming models because the effects have previously been assumed to be small compared to in-plane shear. Because of this, far less characterisation work has gone into understanding the effects of bending. Recently an effort to understand the effects of bending stiffness has been made and a deeper look has been taken at methods for characterising bending stiffness. Currently a single value is typically quoted for the bending stiffness of a piece of fabric. However, it is known that fabrics tend to have a non-linear bending stiffness that is a function of increasing out-of-plane curvature [28]. These tests have been conducted on woven fabrics and conclude that the bending function is partially determined by the properties of the crimp. The bending function for Non-crimp fabrics is currently being investigated and may vary significantly from a woven material with the influence of stitching. The bias direction has a significantly lower out-of-plane bending stiffness than the two fibre directions [29]. By working to the assumption that there is no intra-ply slip via a modified bias extension test, the wrinkle response of the fabric was used to characterise the out-of-plane properties

alongside a simple cantilever bending test [30]. Incorporating a linear bending coefficient has proven to greatly improve the accuracy of modelled wrinkle generation when combined with a shell based material model. The addition of a non-linear bending model presents even greater accuracy during wrinkle prediction [30]

2.5 Full field fibre angle measurement.

It has been found that the theoretical calculations used to measure shear angle from crosshead displacement in both the bias extension test and the picture frame test do not fully capture the correct shear response in all types of fabric [6, 27]. A complete understanding can be gained by measuring the full-field fabric strain during the test to infer the fibre angle. There is also a need to look at the boundary conditions and how they differ between tests, which is only possible through direct measurement.

There are several ways to measure fibre angle which can be applied to both tests. Three general methods are covered in detail here: manual analysis, algorithmic analysis, and a selection of optical measurement methods [31]. All are non-contact methods but still require modification of the sample with either a thin coating or markings. Any coating to the fabric will have an effect on the initial shear region, as the adhesive is absorbed into the fibres and binds them. The low shear region is dominated by frictional effects so any influence on the friction coefficient or stick-slip properties will give unrepresentative results. In the shear dominated region the significance of thin coatings will be reduced due to the higher forces involved. It may be possible to isolate the effect of a coating on the shear modulus function and use a reduction curve to extract accurate data.

2.5.1 Manual image analysis

The simplest method is to measure the difference between warp and weft yarns manually. By taking images or micrographs at specific time intervals during the test, the visual state of the sample can be captured and imported into image analysis software where the fibre angle can be measured and shear can be calculated [1]. With a biaxial NCF there is no visual indication of the weft yarns from the front face of the sample. A second camera could be employed to capture both the front and the back of the sample, but software would be needed to stitch the images together for an accurate angular measurement to be made. Manual image analysis is subject

to human error and can only give the shear angle at a discrete number of the points measured by the user. This makes obtaining a full field value for shear angle time consuming. An advantage of manual measurement is that the high resolution images lets the user measure very small variation in fibre angle. A user can also filter out outliers that can be generated through measurement error in the other scanning methods. However, this is subject to user bias.

2.5.2 Algorithm based analysis

A logical step forward from manual measurement is the use of line tracking algorithms to map the fibre angle. MATLAB and Python scripts utilising the Hough transform to identify and track yarn edges on the picture frame test have been created for this [32]. These have also been built into dedicated edge vector tracking software packages. The scripts still involve analysing images of the test at multiple time frames and comparing fibre angle between frames to get the shear. They convert the image into greyscale, then into a binary image so that high contrast lines can be seen. At this point an edge detection algorithm is used, such as the Hough transform or Canny edge detection. On some fabrics the yarn spacing is too detailed to be picked up by the algorithm, so the sample must be coated to reduce the reflectivity. Alternatively a contrasting grid pattern can be drawn on the surface and measured instead of the fibres. The algorithm then gives the distance and angle between each line and the origin where shear angle can be obtained at each intersection point.

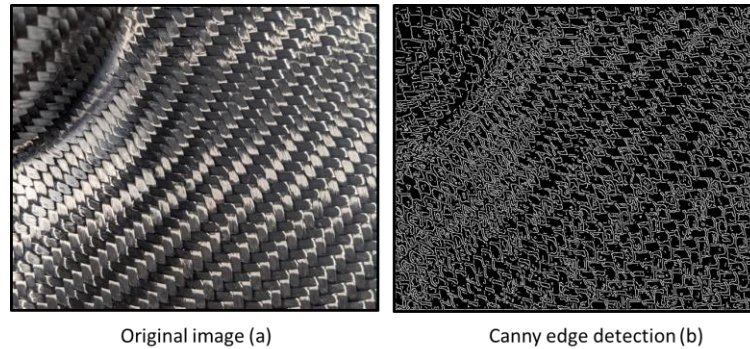


Figure 2-13 Original image of a woven hemisphere (a) and image after Canny edge detection algorithm (b) The edges of the yarns have been highlighted in a black and white image which contains much less information can be processed for structural analysis (measuring angles).

2.5.3 Discrete dot tracking method

An alternative to plotting and tracking a grid pattern on the sample is to track singular points. A method has been developed by Pasco [27] that utilises a plugin for the FIGI image analysis software which tracks bright spots contrasting a dark background. Application of a light dot pattern on the surface of the fabric can be performed with paint, or point-tracking adhesive targets. A series of images taken at discrete intervals during a test are imported into the software where any bright points are identified using a linear assignment problem (LAP) algorithm. The images must be the same size and colour depth and contain high contrast greyscale images similarly to the Hough based algorithm analysis. The point coordinates from the targets are mapped across each frame to give a trajectory that is plotted against the test time. The target information can be imported into MATLAB and run through a custom algorithm that meshes the dots and uses the law of cosines to give shear angle from the elements.

The benefit of this method over edge detection is that a coating is not needed for the fabric. The natural black colouring on carbon fibre means that white dots can be applied straight to the surface giving high contrast without first spray painting the face. The dot tracking method can output the full field shear for the bias extension test across the full range of shear angles, or conduct small scale tracking using a telocentric lens. A telocentric lens is a compound lens that has an exit pupil at the infinity, causing images to be taken with an orthographic view (and is used on video

gauge cameras). The view provides zero magnification at differing distances, so any tracking will remain consistent even with large out-of-plane deformation. This is useful for getting very precise measurements where out-of-plane buckling is present such as in the bias extension test. An issue with the use of a telocentric lens is that due to the lack of magnification at distance, images can only be captured with size equal to the lens diameter. This makes full field capture of a shear test impossible, as the samples for both the picture frame and bias extension test are far larger than the lens diameter. In these cases a standard convex lens can be used. However, if significant out-of-plane distortion occurs, there will be inaccuracy in the tracking data.

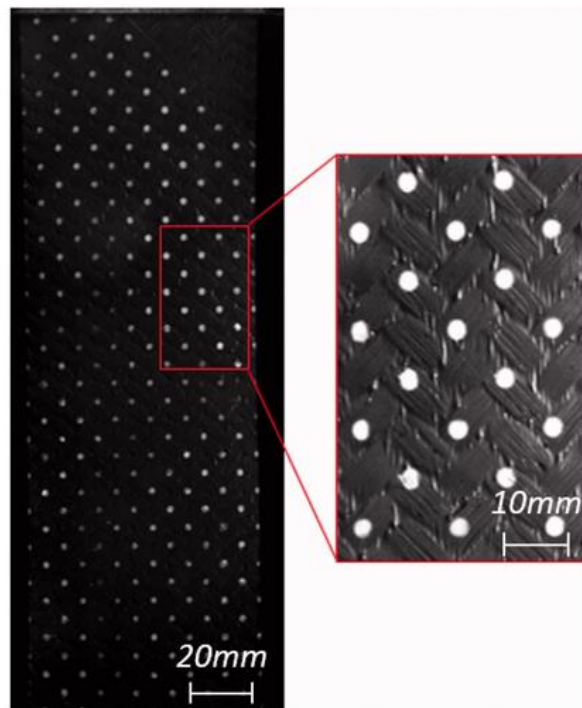


Figure 2-14 Example dot pattern used for discrete dot tracking shear angle measurement method [27]

2.5.4 Digital image correlation (DIC)

Digital image correlation (DIC) maps the strain in an object by optically scanning it then splitting the image into groups of pixels with a unique grey scale value and using that to track the group over multiple frames. A single camera can be used for 2D scans or two offset cameras can be used to simultaneously give out-of-plane

deformation. The method requires a sample to be spray painted with a matt finish and a speckling pattern to be applied which has heavy contrast to the background. The speckling provides the unique greyscale needed for high fidelity mapping.

Applying DIC to the picture frame and the bias extension test has been conducted with woven fabrics [25]. Most of the issues found with DIC have been identified and stem from the large strains generated during the testing. DIC relies on each pixel group maintaining a similar greyscale value from frame to frame, but the large strains and fibrous nature of the fabric deforms the pixel groups beyond recognition of the DIC software. The drop in quality is found to begin at 20 degrees of shear and major loss of tracking occurs at 35 degrees [25, 27]. This highlights the biggest flaw in employing DIC for shear tests and is the reason why alternative methods that can maintain measurement beyond 35 degrees are needed.

Applying the required speckle pattern onto the surface of the fabric is difficult, as tracking must not be lost during fibre slippage and the counting cannot interfere with the output. Both a low reflectivity surface and a speckle pattern are needed for DIC measurements. Graphite powder brushed onto the fabric face has been found to reduce the glare from the surface [29]. This has been combined with a high viscosity paint for contrast dotting and has been proven to give a pattern that can be recognised by the DIC. Carbon is also black and highly reflective so achieving a matt finish on which speckling can be applied requires a full coating of the sample. Spray paint entering the yarns will influence the shear stiffness, as even paint without binding agents may instead cause a lubrication effect that will influence the force. This makes DIC of in-plane shear tests very difficult to set up and work with.

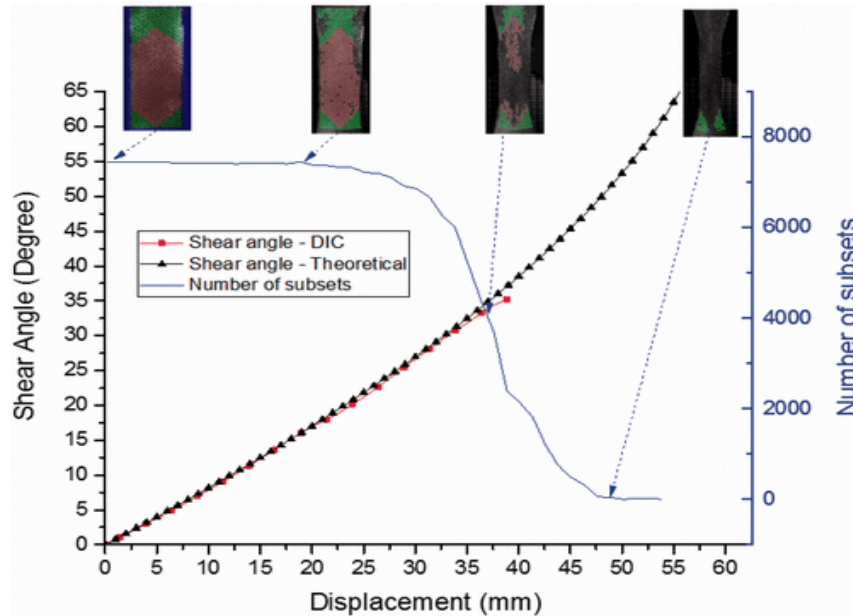


Figure 2-15 DIC of a bias extension test shear angle graph with accompanying subset (number of measurement points) measurement for data quality assessment.[27]

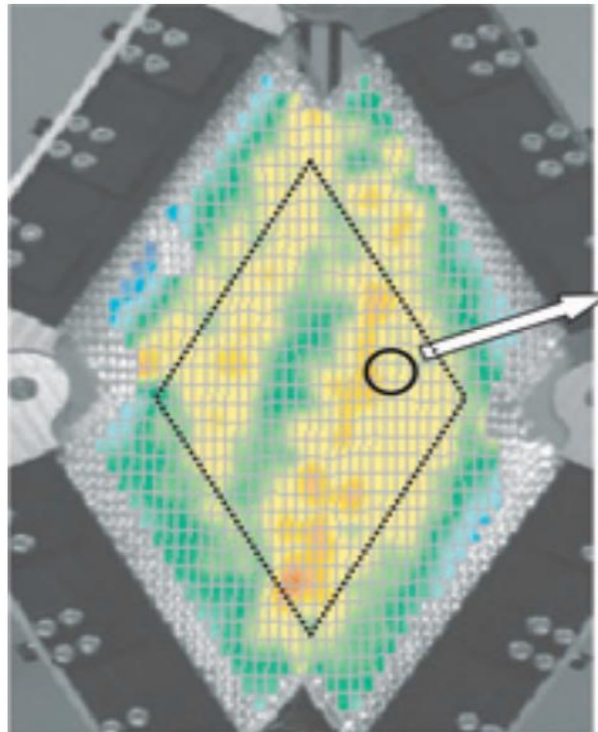


Figure 2-16 Fibre angle contour plot of a picture frame test, using DIC [25]

2.6 Forming and pre-forming techniques

2.6.1 Hand Layup

The most common and oldest form of shaping composite fabric sheets is by hand layup. An operator or a robot will cut the flat fabric sheet into templates which are then stacked onto a 3D form by a skilled worker until the full part has been built [33]. This method gives good conformity to the tool and high quality final parts, but is difficult to automate [34]. Workers must have training and experience and the process is time consuming, taking multiple people many hours to lay up complex forms. There is also an A and B face on components which are laid up using a single sided tool and vacuum bag. This is the standard method for processing in an autoclave, so it is common to only have one face of the component with a high surface quality.

Hand layup is the preferred method for small batch production runs, as it gives consistently high quality results. Efficiently scaling the process for high production levels is an ongoing challenge so other methods of 2D-3D forming composite components are being explored.

2.6.2 Matched tool 2D-3D Press forming

Matched tool forming uses a pair of opposing steel dies clamped together under high pressure over a flat fabric sheet to give a 3D shape[35]. The shape is set by using heated dies and setting binders placed in the fabric sheet, or by infusing the part within the dies. The method has been developed from thermoplastic composite compression moulding which is used for both sheet moulding compounds and continuous fibre fabrics [36]. The forming process is quick with snap cure resins such as PRF RP570 series giving 5 minute cure times. The high pressures means that the final part is forced into conforming to the required shape without bridging [37]. The part also has 2 "A" faces as both sides of the component contact the tool.

Process benefits:

- High rate manufacturing. Optimised to 5 minute cure times, rates can match injection moulded components.
- High consistency. Removing the hand laminating step.

- Single operator overseeing multiple machine improves LEAN manufacturing capabilities.

The process is limited in a few ways:

The parts that can be manufactured must not have any undercuts and generally must have a minimum draft angle to 2 degrees to allow for the top and bottom tool to marry successfully. This limits the design space as the part must be split to achieve this requirement and bonded post moulding. There are currently small scale industrial application of multi part press tooling however further research could be conducted into developing this area.

The amount that a sheet can deform to the desired shape limits part complexity. Over shearing leads to structural defects (wrinkles) that are squashed under the high pressures of the tool leading to failure points that are difficult to visually identify [38]. There is also the risk of bruising to the tool if the fabric will no match the cavity size. Formability is the focus research in this area with non-public studies conducted by companies such as Solvay, Aston martin and BMW. Publically novel material characterisation research is ongoing in areas such as sustainable materials [39] and structural materials such as NCFs [40]. The blank holder force is an aspect that is unique to 2D-3D press forming. This is a plate that holds the flat laminate before the tool halves close and constrain it. Developments have been made from globally varying the blank holder force, to implementing local changes [40].

2.6.3 Diaphragm forming

Diaphragm forming employs the use of one or more thin polymer sheets to constrain a flat pre-form prior to forming. The diaphragm is formed alongside the pre-form using vacuum pressure. Double diaphragm forming sandwiches the pre-form in between two sheets by drawing a vacuum between the diaphragms and relying on the ply diaphragm static friction. This eliminates the need for a blank holder to apply pressure and opens more options for automation [41]. The double diaphragm process can be easily scaled for mass manufacture. A pick and place cell can load the pre-form onto the diaphragm and then the entire assembly can be moved onto the pre-form press. The diaphragm then acts as a release agent for any moulds after forming.

The compaction of the diaphragms does have an effect on the in-plane properties of the pre-form [42]. A bias extension sample under normal test conditions was compared to one done under varying degrees of compaction. The diaphragm compression created a 44% reduction in the shear angle seen during the test and significantly restricted the fibre movement. This was attributed to compression of the crimp, increasing the normal force between the yarns and increasing the force needed to cause inter-ply slippage. High vacuum pressure is necessary to reduce any yarn buckling during forming that may cause wrinkles, but increases intra-ply and inter-ply frictional resistance. It is not known whether the same or a reduced effect is seen for a non-crimp fabric, as there is no yarn on yarn overlap.

Using diaphragm friction over a traditional blank holder to apply pressure to the pre-form opens the risk of large inter-ply slippage as the maximum pressure that can be applied is 1bar vacuum pressure. This can potentially generate inconsistent cross-sectional thickness where unwanted slippage occurs [41]. Bridging is a defect prevalent in diaphragm forming and is where the composite cannot conform to the tool shape. As the diaphragm deforms to the tool shape it first contacts the fabric at raised points, which therefore experience a very high normal force. This traps those points stopping all slippage and all forming must propagate from these peaks. If two peaks are trapped simultaneously then the fabric in between them will be suspended and unable to conform to the tool shape due to the inextensibility of the fibres causing a defect called bridging. Areas subject to bridging are seen in both matched tool and single tool vacuum formed parts but in matched tool forming the pressure is sometimes high enough to force these areas to conform [37]. If the diaphragm slips in relation to the pre-form, then it may wrinkle independently and form lines on the surface of the part [43]. However this is only a concern if the part is to be cured in situ. This can be solved by using thicker and stiffer diaphragms, which are also required when forming multiple sets of plies in one pre-form to reduce diaphragm breakage.

The choice to use diaphragms over a blank holder opens up more possibilities for automation and process flexibility, but has a significant level of added complexity. Potential automation benefits available with diaphragm are:

- Improved pick and place capabilities as a laminate kit can be built on top of the lower diaphragm, whereas the central opening needed in a blank holder for the press tool does not allow this.
- Movement of the laminate from pick and place to press moulding and out of the press within the same cell.

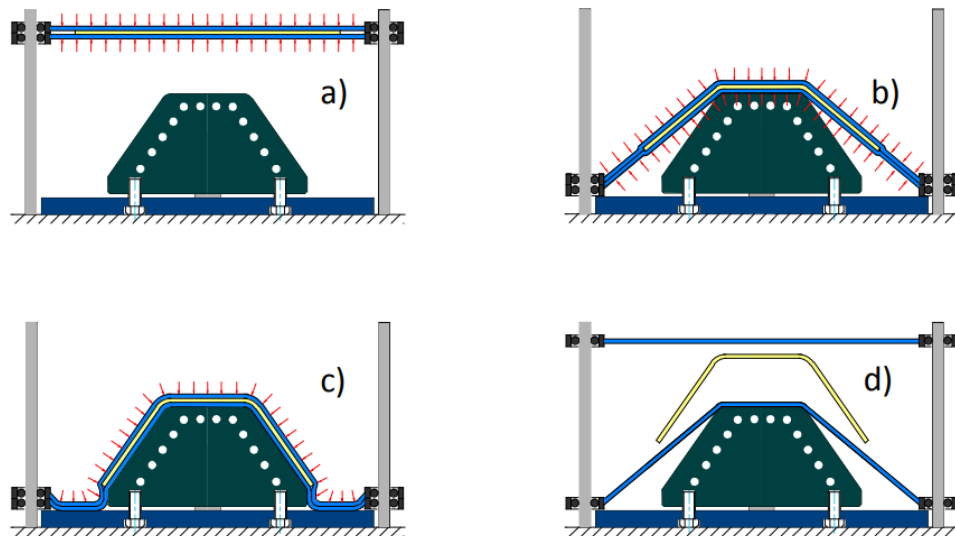


Figure 2-17 Four stages of diaphragm forming. (a) Vacuum compaction between the two polymer diaphragms. (b) Lowering of the compacted diaphragm ply stack over the tooling. (c) Vacuum compaction of the diaphragm ply stack over the mould tool. (d) Releasing of the moulded component.

2.6.4 Double diaphragm press forming

Double diaphragm press forming of pre-pregs gives the automation benefit of the diaphragms, with the final form accuracy of using matched tooling. Solvay have created a system that uses pre-preg carbon preforms with heated diaphragms and tools to give a “1 hit” forming process. The preform can be pick and placed onto the diaphragms then automatically moved off the tooling once it is formed without the need of release agent, allowing for very quick cycle times. One of the drawbacks of press forming is still present here, which is that any fabric wrinkling becomes squashed by the high pressure. This allows for accurate part geometry, but unseen defects to be present in parts.

2.6.5 Unidirectional tape laid preform

This is a process developed to combine the tailored properties of tape layup with the speed and low cost of forming a 2D pre-form [44]. The process involves laying down thick UD carbon tapes as a flat pre-form. Areas within the tape pre-form can be tailored to run in specific directions, to meet specialised loading conditions. Neue Materialien Bayreuth has developed a combined tape laid pre-form process named FORCE. The multiaxial layup machine can place a tape every 2 seconds giving pre-form creation times of 120-180 seconds [45]. After cutting the tape, a pick and place vacuum head moves and stacks the tape. Benefits of this methods are easy creation of tailored pre-forms which can give specific improvements in forming or mechanical benefits. Pre-forms can also be moved away from square perimeters to fit the tool shape, thus reducing trimming and scrap created. The pre-form can then be used in conjunction with any press or diaphragm forming process. The FORCE system uses thermoplastic binder to hold yarns together, whereas alternative systems stitch the yarns together allowing for dry fibres to be placed. Relying on stitching alone to hold a pre-form in place during forming raises questions about whether any yarn separation is seen. Even so, the ability to selectively control the primary direction of each section of the pre-form opens up the design space.

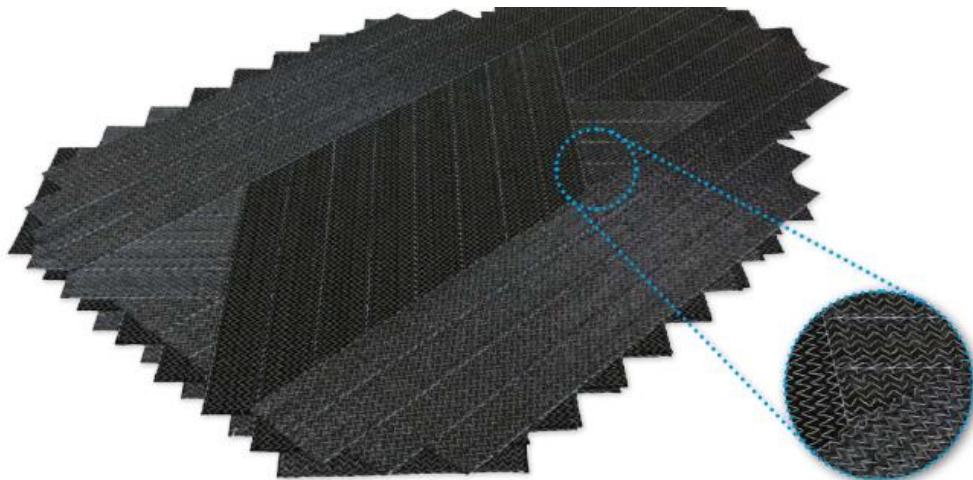


Figure 2-18 Unidirectional tape laid, stitched variable angle yarn (VAT) pre-form. A variation of VAT laminates that is designed for high speed creation of the VAT blank.

2.7 Composite Forming Simulations

The following section outlines the difference between kinematic and finite element modelling methods. It then gives a timeline of the current progression of finite element forming models and the significant model developments.

2.7.1 Kinematic models

Kinetic models use geometric approximations to model the draping of a fabric with no incorporation of mechanical properties [46]. A pin jointed net of rigid bars represents the fabric and the assumption is that all of the deformation comes from the trellis shearing. The models also do not incorporate friction and only uses ideal tool-ply and ply-ply interactions [47]. Yarns in either direction are modelled as inextensible fibre families and varied algorithms can be applied to simulate draping. The most common currently is the fishnet algorithm, as it is optimised to determine topology very quickly and can be used in optimization studies. The algorithm takes the geodesic curves which traverse a curvature and place an interlocked fibre net over them with each fibre on a geodesic edge. The fishnet is draped over the surface by interpolating the geometry of each element over the surface element nodes. Other algorithms include an energy based approach, which minimises elastic energy numerically. It is very efficient but overestimates the Young's modulus. Output values are quadratic with two solutions, so there is a chance of spurious results especially with large structures. There is also the mosaic approach, which approximates a curved surface to a series of flat triangles, which turns the geodesic curves into flat lines. The minimisation interpolation is the same as the fishnet, but using the corner angle and edge length. This gives a constant error due to the flat triangle approximation, though the solution output is close to analytical values. Overall the fishnet algorithm, though the most computationally expensive, gives the greatest detail for a kinematic model. With the large increase in computing power since these algorithms were first created, kinematic algorithms have given way to finite element models in many scenarios. The methods can still be used for comparing shear angle to locking angle and deciding whether a 3D shape is formable or not. They however lack the information to predict non-shear locking based defects or wrinkle shape accurately [48].

2.7.2 Finite element models

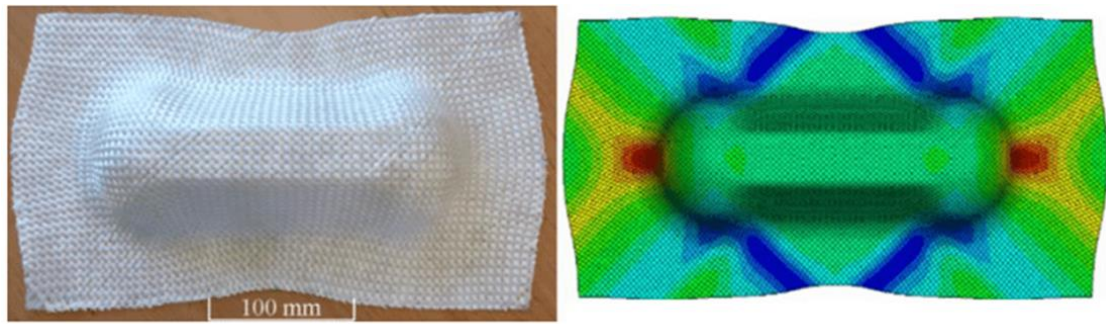
2.7.2.1 *Benefit over kinematic models*

The kinematic model has a very high calculation speed when simulating, making it appropriate for very large simulations and attractive to industries. However, it becomes increasingly inaccurate for surfaces with varied curvature and increasing complexity as all fabric properties are ignored. Membrane forces, normal forces between composite plies and tool interaction are known to play a large role in determining the final formed shape. Incorporating these effects requires a finite element analysis model (FEA) [49]. A finite element model is a numerical model built up of individual elements used to approximate the solution to physical interactions described by partial differential equations.

2.7.2.2 *Model scales*

Fabrics are multi-scaled materials, as the microstructure affects the mesoscale interaction which in turn controls the macroscopic properties. Fabrics can be modelled at each of these scales, but due to computation restrictions when modelling large objects a macroscale model must be used. At the macroscale a fabric is approximated as a continuous material with specific properties that define it as a fabric, rather than having individual yarns modelled. This ignores the fibre architecture or any specifics in the composite structure and is defined purely through the mechanical properties of the fabric. This is done to eliminate the need to consider contact properties between yarns within the fabric. This is known as a meso scale approach and is considerably more computationally expensive. Currently, a continuum macro scale model is preferred, although work has been conducted into a semi-discrete model that incorporates some meso scale properties. The limiting factor for large scale modelling is the run time and computing power needed for large forming models. The aim is to create a representative model that runs in a relatively short period of time so it can be used to influence design [50].

2.7.2.2.1 Macro scale



Experimental form (a)

Macro scale continuum material model (b)

Figure 2-19 Experimental and simulated double dome form, using a continuum finite element material model [51].

Macro scale models centre on treating the entire fabric as a single continuum and approximating the properties of that continuum based on empirical. They are computationally the simplest model scale to run and are therefore the quickest. Because of the usefulness to industry, many efforts have been made to improve the accuracy and further increase the computational speed of these models. While this timeline is not exhaustive, it provides a comprehensive overview of the historical and present state of modelling.

Macro scale model development timeline:

1990 [15] – shear required for double curvature formation over a mould in a kinematic model (kinematic). Initial usable forming models.

With the deformation mode of fabric composites being principally down to transverse shear, many approximations can be made. An ideal composite can be made that only deforms via in-plane shear and bending. Large strain equations are incorporated which do not ignore the rigid rotation component of shearing.

1998 [50, 52] – hypoelastic forming model. First finite element models that incorporated material properties

The hypoelastic approach was formed for high strain materials such as forming metals. It calculates the objective derivative of the stress tensor, from the rotation

of the orthogonal frame. The most common objective derivatives are from Green-Naghdi and Jaumann and it has been shown that in a material with a fibre direction, the objective rotational derivative is based off the rotation of the fibre [53]. Two orthogonal frames g and h based on the two fibre directions of a fabric are defined in Green-Naghdi and the components of strain increment in the two frames are considered. Fibre stretch and shear strain are calculated so that an axial stress and shear stress component can be calculated for each frame. The in-plane shear stiffness is not a constant and strongly depends on the in-plane shear demonstrated by the fabric at each time step. The stress at each time step is calculated by the addition of the stress in each frame

2006 [54] – new method of displaying kinematic models to aid layup. Critical for ply flattening and generating kits using CAD data. Before this templates were created off of the physical mould tool.

2008 [55] – hyperelastic method of forming (FE continuum) .

This hyperelastic approach assumes that the tensile strain and shear strain are uncoupled, giving three energy terms. This allows for the elastic properties to be established with non-linear properties at high strain.

The structural tensors $\underline{\underline{L}}_{\alpha\beta}$ are defined from the direct and transverse directions and \bar{W}_1 and \bar{W}_2 are energies due to tension in the yarns. The accompanying invariants are dependent on the Cauchy Green strain tensor $\underline{\underline{C}} = \underline{\underline{F}}^T \cdot \underline{\underline{F}}$ and structural tensor $\underline{\underline{L}}_{\alpha\alpha}$ with the deformed length of a unit fibre being λ_α . The shear term is a function of the second mixed invariants of $\underline{\underline{C}}$

$$I_1 = Tr(\underline{\underline{C}} \cdot \underline{\underline{L}}_{11}) = \lambda_1^2 \quad \text{Equation 2-9}$$

$$I_2 = Tr(\underline{\underline{C}} \cdot \underline{\underline{L}}_{22}) = \lambda_2^2 \quad \text{Equation 2-10}$$

$$I_{12} = \frac{I}{I_1 I_2} Tr(\underline{\underline{C}} \cdot \underline{\underline{L}}_{11} \cdot \underline{\underline{C}} \cdot \underline{\underline{L}}_{22}) = \cos^2 \theta \quad \text{Equation 2-11}$$

because the in-plane shear and the two tensions are independent the potential $\underline{\underline{S}}$ has to vanish in a stress-free situation.

$$\underline{\underline{S}} = 2 \frac{\partial W}{\partial \underline{\underline{C}}} \quad \text{Equation 2-12}$$

Creating global versions of the potential energy and resulting Piola Kirchhoff tensor shows the necessity for three material constants $A_i B_j C_k$ to be found. These come from two tensile tests in the direct and transverse directions and one in-plane pure shear test. For strain to equate, a condition must be imposed to make stress equate

$$\sum_{i=0}^r A_i = 0 \quad \sum_{j=0}^s B_j = 0 \quad \text{Equation 2-13}$$

This hyperelastic model can be applied to membrane elements in Abaqus/Explicit through a sub-routine VUMAT/VFABRIC.

2013 [56]– single ply membrane stress model for macroscopic forming (FE continuum). A step away from laminate modelling, allowing for the interaction between individual plies to be simulated.

2016 Modelling stitched NCF (FE continuum).

2.7.2.2.2 Meso scale

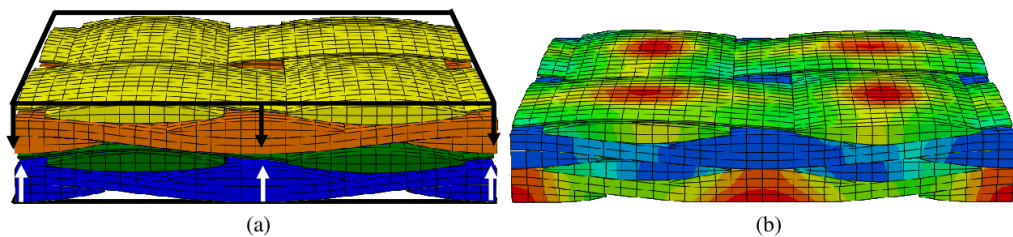


Figure 2-20 Meso scale yarn model of crimped fabric geometry (a) and example yarn stresses (b) [57].

Many attempts at a meso scale model have been proposed but none have made it to industry as a viable alternative to the hyperelastic or hypoelastic model. Although a meso scale model looks to balance computational time with increased model accuracy, all current attempts do not give enough accuracy benefit for the required increase in time. All developments in the area look to find a method of keeping computational time similar to a macroscopic model whilst pulling away from the

continuum approximation and incorporating features that are more representative of a fabric.

Semi Discrete model development timeline:

2001 [50, 58] – The semi discrete unit cell model for mesoscopic approach (FE Meso).

This approach takes into account the difficulties of a continuous and the difficulties of a fibre-based approach. The material is modelled as a set of unit cells under membrane loading and bending. Each unit cell in a displacement field has a prescribed load at its boundary and the internal and external accelerations are related.

$$W_{ext}(\underline{\eta}) - W_{int}(\underline{\eta}) = W_{acc}(\underline{\eta}) \quad \text{Equation 2-14}$$

$$W_{int}(\underline{\eta}) = W_{int}^t(\underline{\eta}) + W_{int}^s(\underline{\eta}) + W_{int}^b(\underline{\eta}) \quad \text{Equation 2-15}$$

Where $W_{int}^t(\underline{\eta})$, $W_{int}^s(\underline{\eta})$, $W_{int}^b(\underline{\eta})$ are the internal virtual biaxial tension, in-plane shear and bending in the unit cell respectively. The virtual strains can be related to virtual modal displacements of an element, considering the neighbouring elements. The semi discrete approach has given very promising results and has been used to model turbine fan blades [59].

2006 [10] – Truss and membrane model used to give viscoelastic properties needed for strain rate dependency (FE continuum).

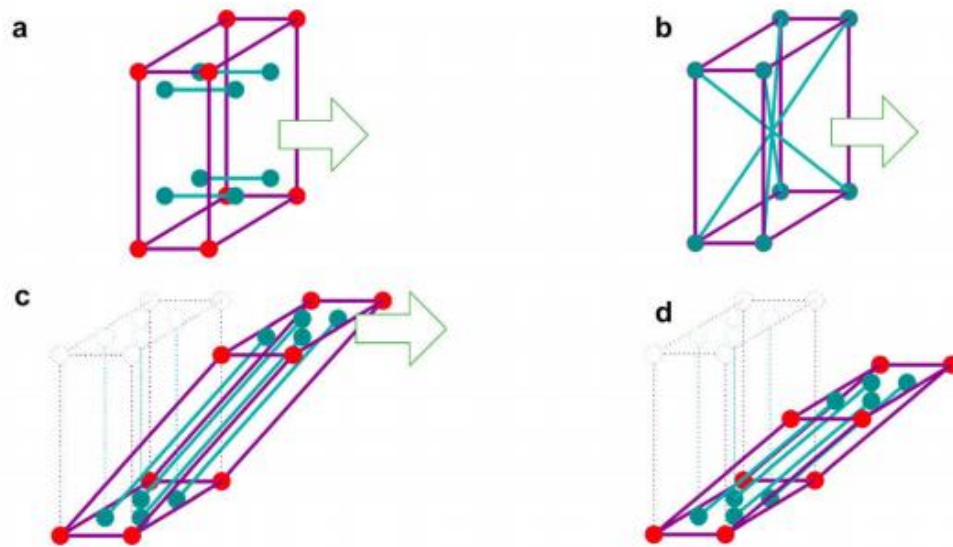


Figure 2-21 Visualizing an element with truss and membrane elements. Elementary tests of semi-discrete element method (a) tension; (b) tension disoriented yarns; (c) simple shear; (d) pure shear.

2013 [60] – Shell sandwich method.

An approach that stemmed from the meso scale properties of the fibre yarns has been further explored by M.Nishi [60]. It sandwiches a membrane element with two shells. The in-plane shear is held by the membrane which is coupled to the two shells that control bending stiffness, giving uncoupled out-of-plane and in-plane properties. This meso scale model can capture the change in fibre direction during forming and the shape of wrinkling, but is not sensitive enough to show fibre yarn buckling.

2014 [61] – Shell sandwich method of incorporating bending (FE continuum) re-explored.

The model from M.Nishi has been extended to thermoplastic composite pre-pregs as bending stiffness is an important part of thermoplastic forming [61]. An isotropic elasto-plastic model is added that accounts for the addition of the thermoplastic resin. Closer attention is paid to the temperature sensitivity and how that affects the forming, as a pre-consolidated thermoplastic sheet can only be formed above the glass transition point of the resin. The model is accurate in predicting in-plane shear

properties, even at high temperature and with a non-isothermal process. This is an area that could be further explored to optimise the non-isothermal forming process.

2016 [62] – Beam constrained membrane method of incorporating bending (FE continuum).

This model has been explored as a method of combining the mechanical properties and high run speeds of a 1D element (beam element), with the frictional and contact benefits of a 2D element (membrane element). This method was developed in Abaqus CAE and constrains a membrane element with a hinged frame of beam elements to create a new combined element type. The membrane carries the in-plane shear properties and the beams give additional in-plane and out-of-plane bending characteristics. This gives independent control of the associated properties and greater control over characterisation inputs. The results are comparable to alternative incorporated bending methods such as shell element or kinematic beam models but with a much lower run time to the shell element method and better frictional properties to the 1D model. This method requires an external mesh generator which adds a level of complexity and makes iterative optimisation very difficult. However, as an analysis tool for bending, this method is very interesting. The in-plane bending properties of a fabric at low shear could be incorporated via this method and be controlled separately to the shear. This may allow for simulation of the bending that occurs at the clamped boundary of the picture frame test, and may provide insight into the low shear region. As forming in this region is dominated by the bending of fibres at the boundary, it may enable the analysis of the contribution that this initial fibre bending has on the output shear curve from the picture frame. An option could be to remove the membrane elements and see if the initial curve section can be re-produced, purely from the bending of boundary fibres and rigid body rotation of the rest of the fabric.

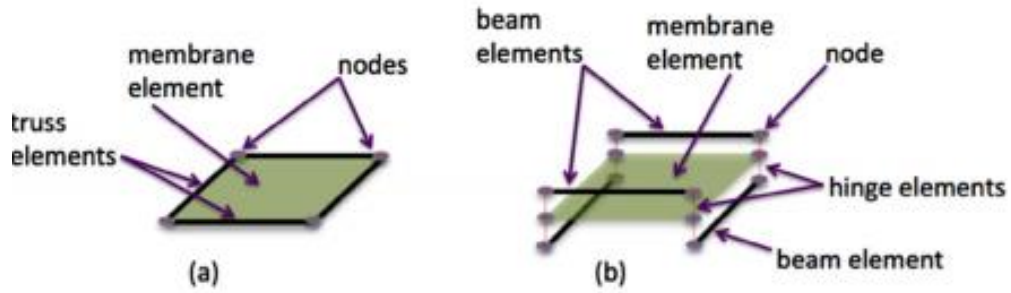


Figure 2-22 (a) Beam and membrane element (b) Exploded view of beam and membrane element [3]

Micro scale

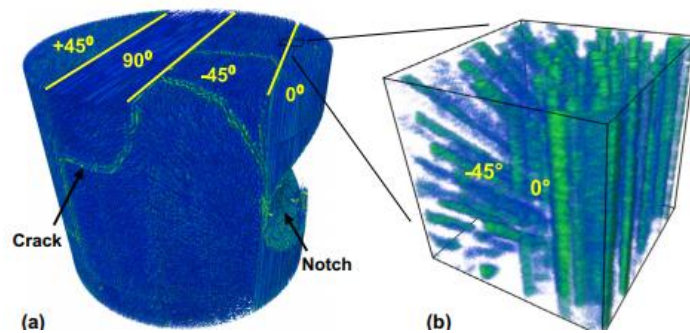


Figure 2-23 (a) X-ray CT render of CFRP sample (b) X-ray CT render of CFRP sample intensity thresholds filtered to view fibres [4]

The micro scale fibre interactions are essential for fully understanding the relationship between fibre architecture and final macro scale mechanical properties. X-ray computer tomography (X-ray CT) is a common way of scanning a composite with the goal of creating a 3D model for analysis [63]. These models incorporate any small-scale defects that have been scanned such as fibre discontinuities and the matrix fibre interface. Sencu and Yang [63] scanned a sample and applied a Bayesian inference algorithm to identify the fibre centrelines and build an FE mesh around them in ABAQUS. This type of FE model is incredibly detailed but the large data fields produced by X-ray CT make it very computationally expensive for tiny sample sizes and impractical for forming simulations where that level of precision is not needed.

2.7.3 Ply Meshing

Forming simulation in industry focusses on using a continuum-based approach, but there are still issues directly related to the complexity of forming which has benefits and drawbacks that have been previously discussed.

Issues with the continuum method arise when multiple plies are being formed as each ply must be modelled separately and adds a level of complexity to the numerical calculation. Inappropriate meshing in this case can cause intra-ply locking where unrealistic fibre stresses are seen and spurious wrinkling forms [64]. The problem can be solved by increasing the number of elements involved in the simulation, but there are more computationally efficient ways to achieve the same effect. Aligning the mesh to the fibre direction is the preferred solution, although this becomes difficult to implement at curved boundaries. Using reduced integration elements removes the problem, as the fibres can stretch to relieve locking at the integration points that are not used. However this causes a zero energy mode which can lead to element hourglassing, and applying hourglass control equations brings back the locking problem. Reduced integration cannot be used on triangular elements and yet triangular elements are preferred for meshing complex shapes because the mesh solvers are more robust than quadratic ones. A triangular multi-field element with quadratic in-plane and linear out-of-plane properties has been developed [65] to give the most accurate shear angle values without the need to have an aligned mesh. This element is accurate for large shear simulations and avoids contact problems in 3D models and is available in Abaqus/Explicit which is the solver used in this thesis.

2.7.4 Diaphragm simulation

Diaphragms are thin sheets of polymer used to suspend a pre-form in some forming methods. They form alongside and in contact with the pre-form and this brings with it a set of challenges unique to diaphragm forming.

Introducing diaphragms imposes the need for two new layers of material using a different material model. Common diaphragm materials include silicone, which can be modelled using a strain energy density function in terms of the principal elongation. The Ogden hyperelastic model has been shown to accurately capture the

response of a silicone sheet in pure shear and can be implemented and stability checked in Abaqus explicit [37].

Stability issues can arise if diaphragm shell thickness is very small relative to the fabric thickness and adequate mass scaling is not implemented. ESI PAMFORM shows this as an error where forming material can pass through the diaphragm. Abaqus has an inbuilt error system that states when the nodal displacement is too large and cancels the calculations.

Interaction between the diaphragms and the material can also be problematic during simulation. A contact must be stated to implement diaphragm interaction and a frictional coefficient must be imposed.

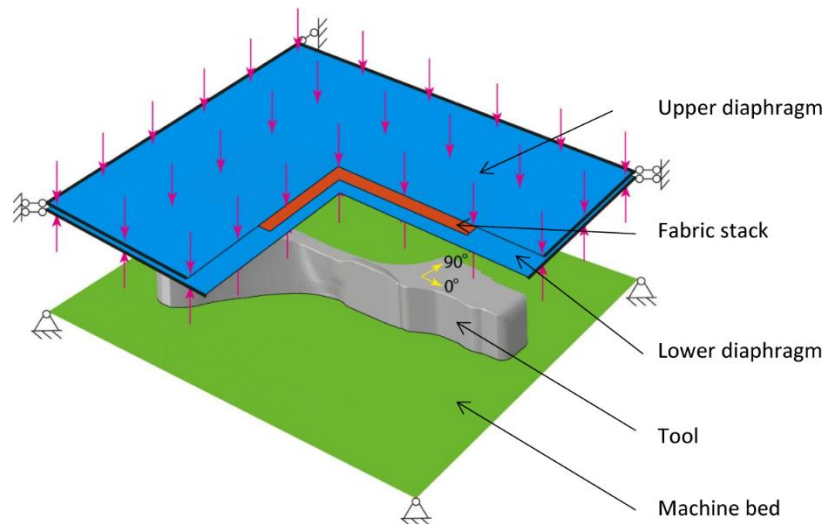


Figure 2-24 Double diaphragm forming simulation [37].

2.7.5 Friction

Introducing friction into a simulation has a large impact on computational time. The double diaphragm model must approximate the pressure differential created between the diaphragms and the subsequent clamping forces. The intricacies of inter-ply contact are not fully understood and relative sliding between plies is one of the main forming modes when multiply plies are being used or if there is a ply-diaphragm interaction. NCF experience a higher level of slip than interwoven yarns in woven fabrics, as the stitches provide lower surface roughness than the crimp found in a woven fabric [66]. The nature of fabric friction is still not clear and although multiple studies have been published there is no true consensus on how to model it

[67]. It is generally accepted that the Coulomb friction model is the most appropriate for dry fibre forming interactions at the macroscopic level [68]. Howell's equation has been used to define frictional coefficient with K and m (proportionality constant and fitting parameter) replacing the normal force and proportional friction coefficient of the Coulomb law. Here issues arise as the directionality of the material is not incorporated and further studies have shown this to have an effect [69].

Incorporating a viscous layer, such as resin or binder, adds further complication and as such no predictive model of interply slip conditions exists, due to the massive number of process dependant factors [70]. Phenomenological models have been developed that approximate a viscous layer that controls ply-ply and ply-tool slippage [70]. The viscous layer thickness is determined by the process conditions and expressed through Newton's law of viscosity. Sensitive conditions are pressure, temperature and velocity. The Hersey number is a function of the velocity, normal force and viscosity which are controlled in the process by the press velocity, pressure and temperature respectively. An increase in Hersey number gives an increased frictional coefficient. A custom VFRIC can be implemented into Abaqus to incorporate this type of interaction without needing to implement resin flow properties. This gives a significantly reduced computation time, although it is still more complex than a frictionless contact. Similar models could be introduced for modelling dry fibres with a binder, as the binder will have very little resin flow, but may create a viscous layer that needs to be accounted for in the simulation.

2.8 Conclusion of literature

The current materials and processes used during automated composite forming have been explored. An overview has been given of methods used for material characterisation and subsequent simulation of these processes, with the benefits and drawbacks of each method stated. The research here will be used as a framework for process changes, material characterisation and simulation development.

Gaps in the literature

- There is no explanation of the initial low shear region in NCFs as there is for woven fabrics. The lack of understanding presents itself as a lack of understanding of the yarn buckling defect that is comment found in NCFs.

- Aim: To fully understand the yarn interactions occurring during the initial low shear region and allow for future material characterisations to include or ignore the region.
 - Aim: To investigate the relationship between the initial non-linear shear regions in NCFs and the yarn buckling defect.
- There are gaps surrounding the measurement of fibre angles in the literature. The inability to collect accurate fibre angle data across an entire component during forming makes simulation validation difficult. During characterisation it also requires a set of assumptions to be made about the entire sample fibre angle from a calculated data point.
 - Aim: Generate a robust methodology for measuring the full field fibre angle and shear angle of formed components.
 - Aim: Measure the full field shear angle during characterisation tests and affirm the assumptions currently being made.
- Looking into novel forming processes there is no material characterisation information about the response of NCFs past the first forming cycle.
 - Aim: collect data on NCFs for shear and formability during multiple cycles.
 - Aim: develop a finite element model that could be applied to novel forming techniques that have a need for multiple forming cycles.
- There is development to be made on the layup of the initial flat blank for 2D-3D forming. A combination of yarn steering and tape laid pre-forms would allow for control over fibre direction whilst maintaining fibre continuity.
 - Aim: Develop a process that incorporates yarn steering into 2D-3D forming.
 - Aim: Asses the structural benefits of maintaining fibre continuity using this method using the models developed in previous chapters.
 -

3 Analysis of fibre angle distribution in biaxial non-crimp fabrics

Abstract

3.1 Introduction

3.1.1 Objectives:

- To create a methodology for using an optical scanning system for high resolution measurement of shear angles in formed non-crimp fabric (NCF) parts.
- To measure the fibre misalignment generated during the forming process of biaxial NCFs.
- To characterise the effect of fibre misalignment on the tensile stiffness of formed NCF components for use in finite element simulations.

3.1.2 Fibre misalignment during shearing

Full field measurement of fibre angles during in-plane shear testing shows local discrepancies between measured and theoretical shear, which can be attributed to non-uniformity in the strain across the sample [27, 71, 72] (Figure 3-1). Non-uniform shear over the sample indicates that yarns are locally deformed to different levels generating fibre misalignment that has not been identified. Change in the alignment structure of the fabric through shearing was shown to considerably affect damage initiation in a consolidated composite [73] and as such, it is necessary to incorporate the relative fibre angles of the post-formed shape into structural models when predicting the mechanical response.

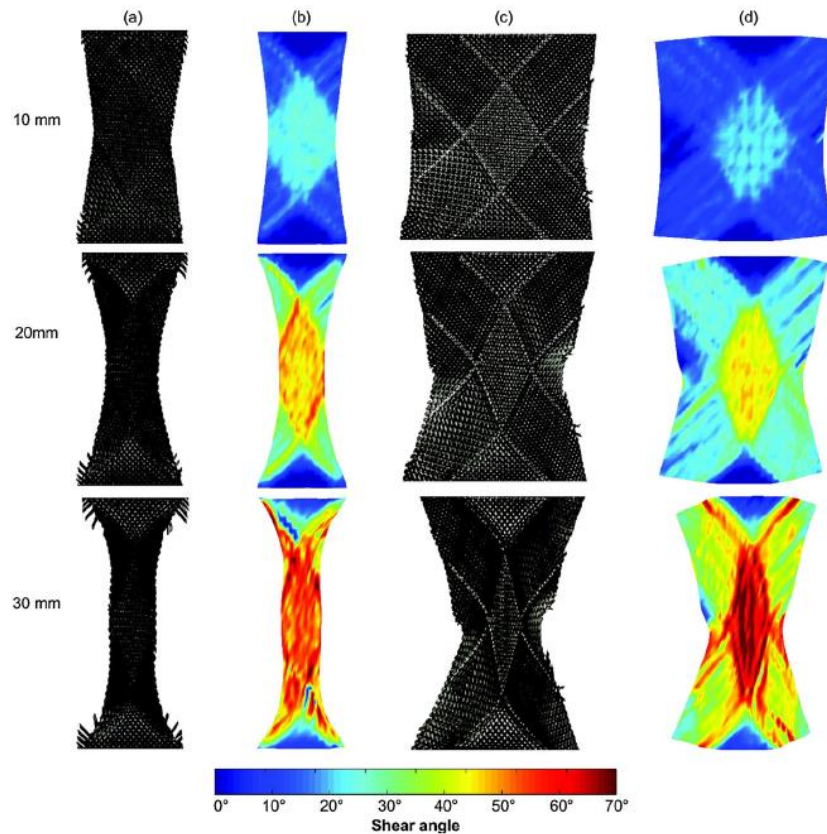


Figure 3-1 Increasing levels of extensions for (a-b) a narrow bias extension specimen and (c-d) a wide bias extension specimen. DIC images indicate regions of heterogeneous shear. Image reproduced from Pierce [72].

3.1.3 Fibre angle measurement

Accurate full-field measurement of the fibre angle distribution on a 2D-3D formed component is required to capture large levels of fibre reorientation caused by shearing [74]. A number of methods exist for measuring the topology and fibre angle distribution of 2D and 3D parts, and a selection of common optical based scanning methods is given here. Painting orthogonal lines onto samples provides distinct edges that have commonly been used to measure shear angle by hand or through the use of assisted algorithms (e.g. Canny edge detection). Digital image correlation has been used with moderate success for 2D samples [72]. Measurement of the strain during in-plane testing enables the degree of in-plane fabric shear to be determined. Issues stem from the speckle patterns that must be applied to the surface of the sample. Coating the sample creates a unique pattern that can be discretised into regions, enabling strains to be established from the movement of the regions. Coatings can

cause undesirable changes to the fabric stiffness and large strains can deform the pattern beyond recognition of the DIC software. These issues were addressed with the creation of discrete dot tracking methodology (DDT).

In DDT small dots are placed on the sample at the yarn crossover points and the strain is measured from their movement [27] removing the need for a full coating on the sample. Grid tracking uses a similar approach with shear angles calculated from the initial fibre angle and the deformation of the grid lines. These methodologies are designed for continuous measurement throughout a test rather than for post process inspection. Recently polarising imaging technologies have been tested for their suitability for measuring fibre angle with an accuracy of 0.2 degrees [75]. The system uses the reflection from the surface to distinguish between yarns, but only qualitative analyses have currently been conducted on non-planar components. Each currently used optical method requires some form of coating or marking of the sample.

3.1.4 Current work

Current optical methods for measuring and analysing shear angle require the sample to be marked/coated and are subject to data loss if that coating is damaged. The resolution of the data is also linked to the marking/coating, so small deviations in shear angle are often lost, making it difficult to use these methods to validate high fidelity finite element forming simulations.

A Hexagon Apodius Vision Sensor has been used in the current work to capture high resolution fibre angle data without the need for any sample coatings. A custom script was developed to calculate local shear angle, which can be exported into Abaqus CAE for direct comparison to simulation results. This has been conducted for 2D and 3D components using both 1-sided and 2-sided scanning methodologies for both woven and non-crimp fabrics. The high resolution data has enabled an in depth analysis of fibre misalignment caused by shearing and the creation of a function to predict changes in elastic properties due to fibre misalignment.

3.2 Methodology for analysing local fibre orientations

3.2.1 Optical scanning methodology

The Apodius Vision System 3D by Hexagon was used for assessment of samples during this study. This is a 2-part system comprising an RS5 laser scanner and an HP-C-V3D Vision sensor unit. Both of these are paired with the Hexagon Absolute Arm and a point placement and meshing software that enables combined topological and image based analyses to be run on the collected data. During scanning a 3D reconstruction of the component topology is created and measurements for the local fibre orientation are mapped onto the surface. Building of the digital reconstruction is carried out in two operations. Firstly, the laser line scanner is used to map a point cloud of the required component (Figure 3-2), alternatively this stage can be replaced by importing CAD data of the component giving the option to apply surface images to the idealised form or the real component.

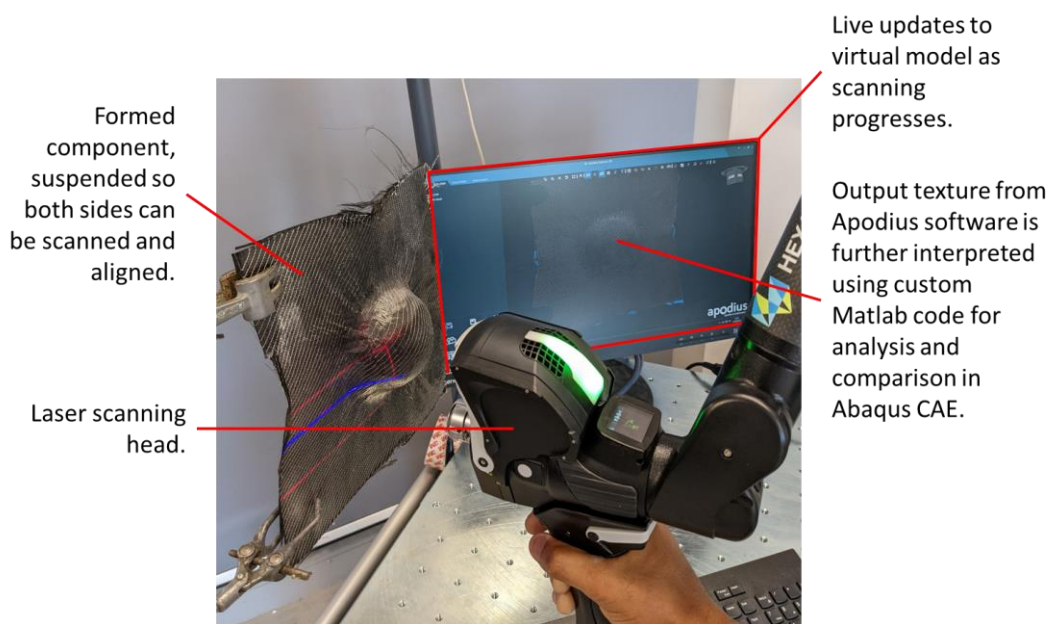


Figure 3-2 First stage of optical scanning methodology. Laser scanning and concurrent building of the virtual points cloud.

The second stage uses the Vision sensor camera to take multiple images from the surface of the fibre preform, which are subsequently stitched together to form a surface map of the fibre architecture (Figure 3-3). A more detailed explanation of the Apodius scanning system can be found in Appendix (B).

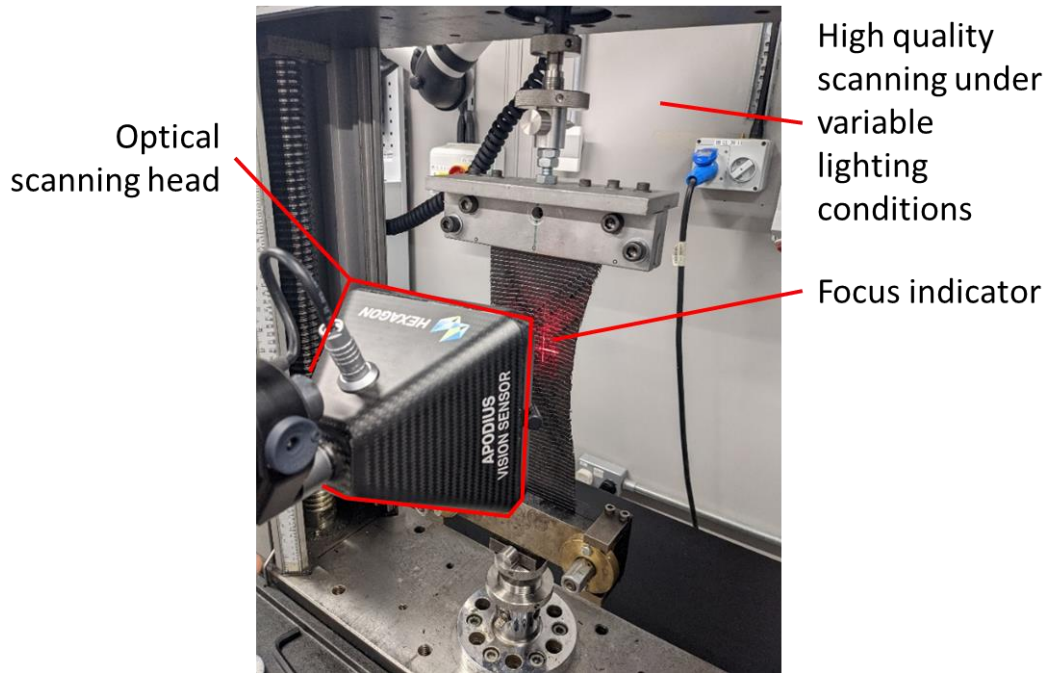


Figure 3-3 Second stage, Apodius scanning of NCF bias extension sample using optical sensor.

3.2.2 Custom shear angle analysis

3.2.2.1 Shear angle calculation

The Output inside the user interface for the Apodius software is limited and could not generate the data needed for this study. There was no ability to output local selection of fibre angle regions, shear angle calculation or local fibre angle standard deviation. The shear angle calculation was processed using a custom Matlab script that structured the .xml output from the Apodius software into variables that could be processed. It then imported the processed data into Abaqus CAE for comparison with the simulation results. Only the front facing surface of an NCF can be easily scanned for multi-layer laminates, so shear angle was calculated using the fibre angle on the front surface and the initial stitch direction. The assumptions made were as follows:

- Shearing occurs evenly across both in-plane faces of an NCF
- The stitch can be used as a reference direction from which shear can be calculated.

The assumptions used above were validated by comparing the measured values for shear angle with the theoretical and expected values from in-plane fabric shear testing. In Matlab A tetrahedral mesh was used with a 3mm edge length to match

the highest resolution capability of the Vision sensor. Elements were imported into Matlab along with the orientation data at each integration point and a coordinate system was established from the home position of the scanning unit. A vector was established for the stitch direction and a new coordinate system was created for the orientation information. This used the stitch direction as a reference, with a normal directed away from the scanned surface. The difference between the reference vector and the orientation data was calculated for each element (α):

$$\alpha = \cos^{-1} \frac{\vec{V}_f \cdot \vec{V}_s}{\|\vec{V}_f\| \|\vec{V}_s\|} \quad \text{Equation 3-1}$$

with \vec{V}_f and \vec{V}_s representing the fibre and stitch orientation vectors respectively.

The shear angle was then calculated by using the assumptions above to calculate the shear increment from the initial orientation difference.

$$\theta = 2 \left(\alpha - \frac{\pi}{4} \right) \quad \text{Equation 3-2}$$

3.2.2.2 Fibre misalignment probability density

Shearing between yarn directions in a biaxial fabric is necessary for forming over double curvature geometries and requires the yarns to slide within the fabric, as well as the fibres to redistribute within the yarn. The movement of yarns from the stitched orientation can cause fibre misalignment, as factors such as stitching and geometric boundary conditions impact the yarns non-uniformly [76]. Local fibre misalignment is very apparent in NCFs when an applied shear angle reaches the stitch breakage point in the fabric. At this point, stitches rupture in a random manner over the ply surface and local regions experience reduced constraints. The yarns in these regions are unbound from the adjacent biaxial ply and are free to accommodate strain via methods other than shear. This causes an increase in fibre misalignment as fibres become free from yarns, and yarns are seen to buckle in and out of the plane.

Micromechanical analysis provides effective properties of a composites laminate from the constituent properties, but must incorporate process induced material defects to be accurate. The optical scanning methodology was used to measure the mean fibre angle μ of a sheared sample and to calculate the standard deviation from

the measured regions. Work by Yurgartis [77] and Fleck [78] showed that a normal distribution can be used to determine the shear angle probability density function. From this, the standard deviation was used as a measure of fibre misalignment with a larger standard deviation indicating that a larger number of yarns have strayed from the mean value.

$$P(x) = \frac{1}{s\sqrt{2\pi}} \exp \left[-\frac{1}{2} \left(\frac{x - \mu}{s} \right)^2 \right] \quad \text{Equation 3-3}$$

Using the standard distribution, the range of values found across a sheared sample has been collated into a range using Equation 3-3. This distribution has been compared at various levels of shear during in-plane testing to identify points at which the homogeneity assumption breaks down.

3.2.3 In-plane shear test optical scanning

Optical scanning was conducted using a similar methodology for both the picture frame and bias extension test. Each sample was extended in 5mm increments, pausing in between increments so that a scan could be taken. Ten scans were taken for the bias extension test over a range of 0-50mm in both the positive and negative shear directions to give a set of 20 scans over the full range of theoretical shear angles. 32 scans were taken for the picture frame test to cover the entire shear curve using the same 5mm extension increment size. The scans were analysed using a customised Matlab script found in Appendix (B), which enabled the data to be visualised in Abaqus CAE and contour plots to be generated.

A set of 15 random elements were taken across the pure shear zones on each sample and the shear angle was noted. These data points were collected manually to allow for elements containing poor data to be filtered. This also enabled data to be collected from Zone C of the bias extension test without including any information from zones A or B (zones visible in Figure 3-1). The average shear angle and standard deviation values were calculated from the set of points in zone C. The average shear angle was used for comparison against predicted shear angle derived from the crosshead extension of the universal testing machine.

3.2.3.1 Single face scanning

Single face scanning was used in tests measuring pure shear or where both fibre orientations could be gathered from a single-sided scan (woven materials). Only the top layer of yarns could be seen and scanned with this method so calculation of the shear angle in the A and B regions does not fully capture the strain occurring in the back face yarns for NCFs (Figure 3-4). Observations of the samples show that that the original B region is split into: an A/B region where the scan data from the top face is insufficient for capturing the shearing of the back face; and a B/C region where the scanned values are correct. The C region is in a state of pure shear so both sets of yarns are equally sheared and is captured properly.

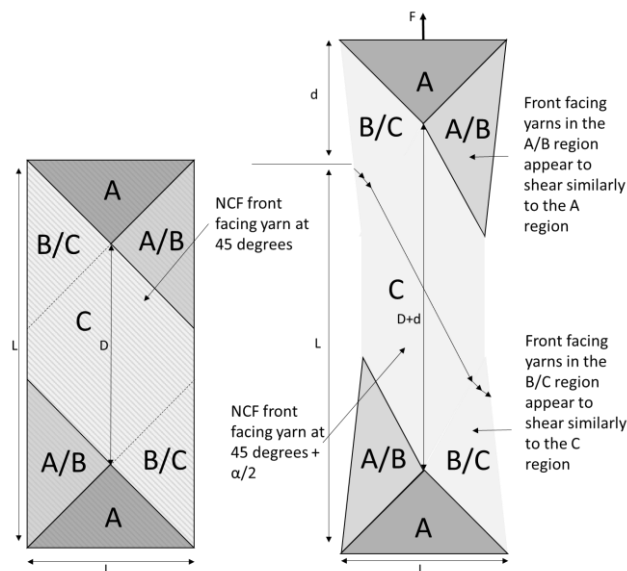


Figure 3-4 Observed deformation distribution in NCFs in the bias extension test

3.2.4 2D-3D punch forming

A hemisphere punch forming tool was used to create highly sheared fabric preforms to validate the scanning and post-processing methodologies (Figure 3-5). The tool consisted of a 50mm radius hemisphere punch that pressed into a cavity with a 5mm edge fillet. A 300mm by 300mm square blank was placed over the cavity and was constrained by a blank holder that provided 0.15 bar of static pressure. The tool and blank holder surfaces were tool steel and the relative coefficient of friction between the tool and the preform was 0.23 [14]. For NCF testing, 2 layers of biaxial NCF with matching fibre orientations were placed on top of one another. Epoxy binder

(20g/sqm) was placed in between the plies so the formed shape could be stabilised after pre-forming. Using 2 plies at the same orientation is assumed to produce equal amounts of shear deformation in each ply, ensuring the two plies shear together and effectively act as a single ply [40]. This enables binder to be applied at the inter-ply boundary and not on the outer surfaces of the preform, ensuring no binder comes into contact with the tool faces for quick demoulding.

The NCF material chosen for the testing in this chapter is Hexcel FCIM789 and the woven is Hexcel 282 which are both 200gsm materials representative of commonly sheared fabrics (as is shown in comparative cyclic shear testing in chapter 5).

The punch was placed in an Instron 5581 testing machine using a 50kN load cell and displacement rate of 100mm/min, giving an overall punching time of 30 seconds. The tool, cavity surface and blank holder were each heated to 120°C before testing. The blank holder was heated for a further 10 minutes after testing. This enabled the binder to cure before a 2 hour cool down period with the punch displacement still applied. Following the cool down period the tool was returned to its original position and the blank holder pressure was removed, enabling the preform to be extracted and scanned.

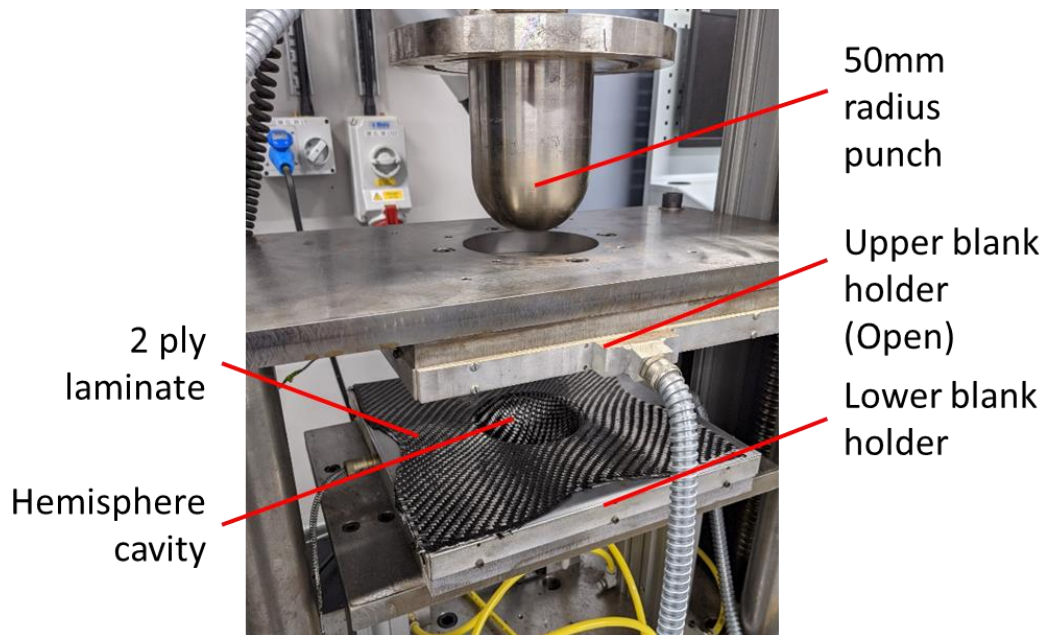


Figure 3-5: Heated punch rig for hemisphere preforming

3.2.4.1 *Double face scanning*

Each stabilised hemispherical sample was mounted vertically in a set of clamps, so that both sides of the preform could face the scanning head without moving or rotating the part. Scans were taken from the front and back face and meshed individually. Equation 3-1 and Equation 3-2 were used to calculate the shear angle for each face, based on the individual face mesh and the stitch angle, using a custom Matlab script. This created two sets of orientation data, one for each of the two meshes. Since both scans were taken without moving the component, mesh alignment was not necessary and a nearest node [79] algorithm was used to pair the central integration point of each element in the top face mesh with the bottom face. This single point allows for a smaller data set to be used when aligning the meshes and avoids spurious edge nodes. This algorithm used a k-dimensional tree to organise points, as this enabled the nearest neighbour search to efficiently eliminate large portions of the search space.

Since the maximum edge length of each element was 3mm from the Apodius output, the paired integration points sat in-plane within 1.5mm of each other giving very little distortion to the positioning of the data. Each paired integration point contained 2 points of shear angle data, which were combined to give the overall shear. For simplicity, the integrated data was applied to the mesh of the top surface to create a point cloud for visualisation.

3.3 Results:

3.3.1 Optical Scanning methodology validation

3.3.1.1 *Woven fabric picture frame shear analysis*

The optical scanning methodology was applied to a picture frame test using a 450g 2x2 twill woven fabric to compare the theoretically calculated shear angles to the measured values. The global shear angle for plain weave and twill weave fabrics calculated from the crosshead displacement has been shown to match local measured values in the literature through DIC, point tracking and grid tracking methodologies [25, 27]. To validate the Apodius scanning, a similar comparative test was conducted to compare measured and calculated shear angles.

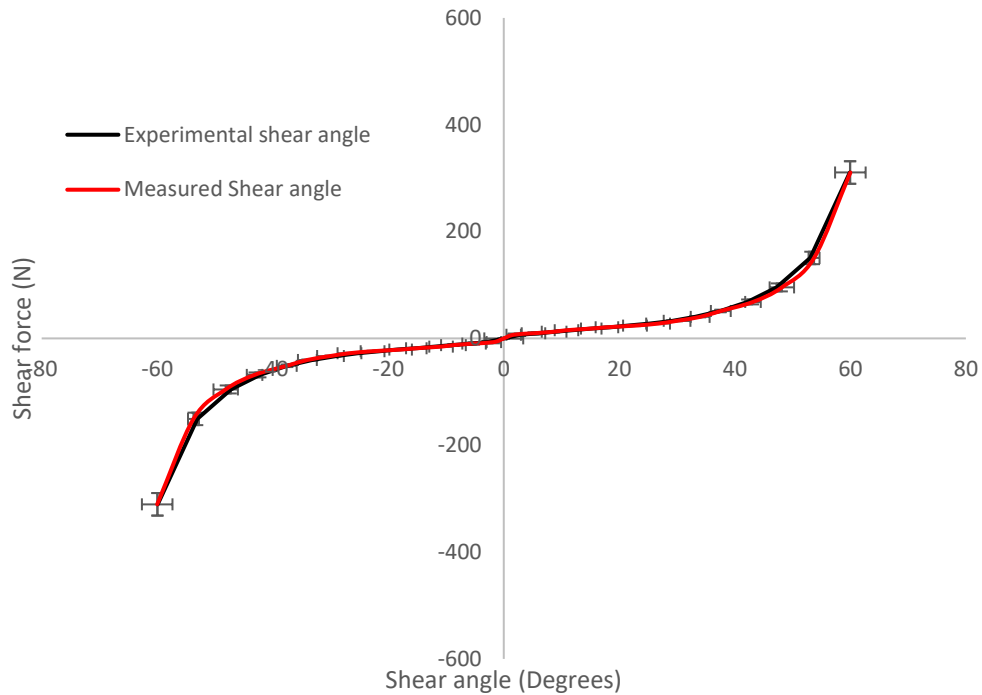


Figure 3-6 Shear force versus shear angle curve produced from a picture frame test with a woven fabric. The experimental shear angle is calculated from the crosshead displacement and the measured shear angle is taken from optical measurements of the fabric. Error in the y-axis shows the shear force variation over multiple samples. Error in the x-axis shows deviation in the measured fibre angles.

It was shown that the measured shear angle was within 2 degrees of the theoretical values across the full range of positive and negative shear angles. The average deviation across the range of shear angles was 0.5 degrees (measured from the mean value of the randomly selected points on the sample). Peak deviation of 1 degree occurs symmetrically about the 0 degree mark at 50 degrees and -50 degrees, after which the two curves converge back to a deviation of 0.5 degrees. The cause for this peak deviation point could be a difference between the calculated and the true shear angle at which yarn locking takes effect. It indicates non-uniformity in yarn locking over the sample. Woven fabrics are shown to experience variable tension at the boundary of the frame, which causes non-uniform shearing.

The overall error in the measured shear angle captures the standard deviation found across the sample. This remains constant at values between 1.5 degrees and 3.2 degrees and is explored further in a later section. This methodology enables for the

high accuracy scanning of picture frame samples to very large shear angles without the need to mark or coat the sample.

3.3.1.2 Woven fabric bias extension shear analysis

The optical scanning methodology has been applied to a uniaxial bias extension test and the results have been compared to trends found in the literature. It has been previously shown in the literature that during the uniaxial bias extension test there is a deviation between the measured shear angle and the theoretical values that occurs as the fabric locking angle is approached. This is attributed to slippage at the yarn crossover points and a breakdown of the pure shear zone from which the shear angle is calculated. During picture frame testing of the 450g 2x2 twill weave fabric the locking angle was found to occur between 45 and 52 degrees. Due to this, it is expected that there will be a deviation between measured and calculated shear angle values in this range.

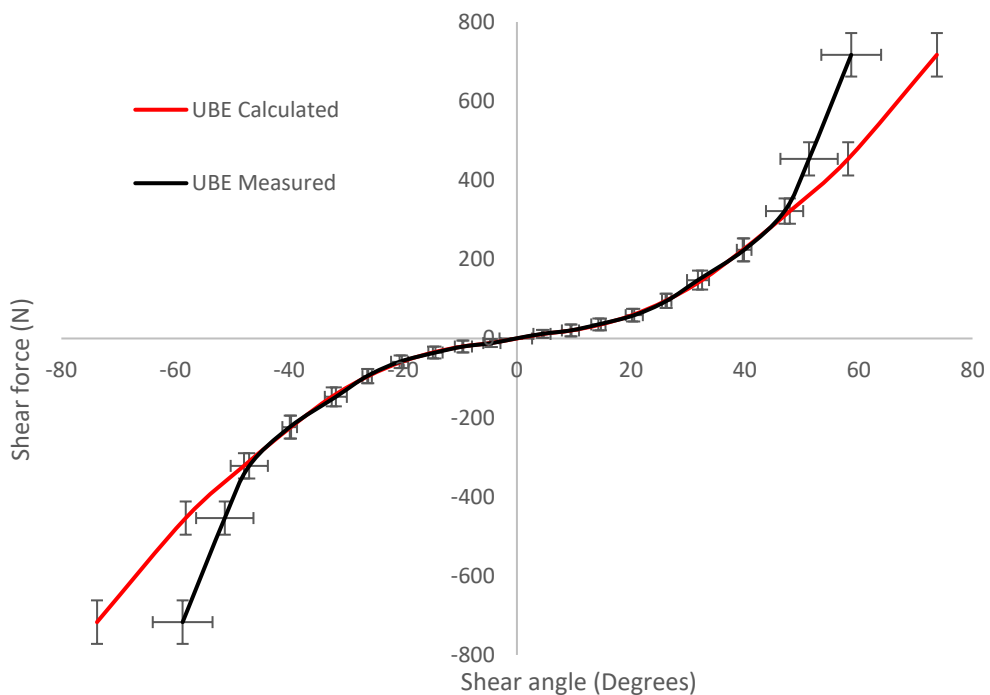


Figure 3-7 Shear force versus shear angle curve for a woven fabric using a bias extension test. The experimental shear angle is calculated from the crosshead displacement and the measured shear angle is taken from optical measurements of the fabric. Error in the y-axis shows the shear force variation over multiple samples. Error in the x-axis shows deviation in the fibre angle from the measured results.

Figure 3-7 shows the scanning results from the bias extension test. There is very good agreement between the measured and calculated shear angle values between 0 degrees and 50 degrees, with a mean deviation of 0.2 degrees (0.4% of peak shear angle). Beyond the fabric locking angle of 50 degrees the two curves diverge. This trend agrees with data presented in the literature [20, 27], as the yarns become compacted in-plane as they rotate. The experimental shear angles calculated from the crosshead displacement should not be used cautiously as input data for material modelling if derived from a uniaxial bias extension test. The comparison between the literature and current results is shown in Figure 3-8.

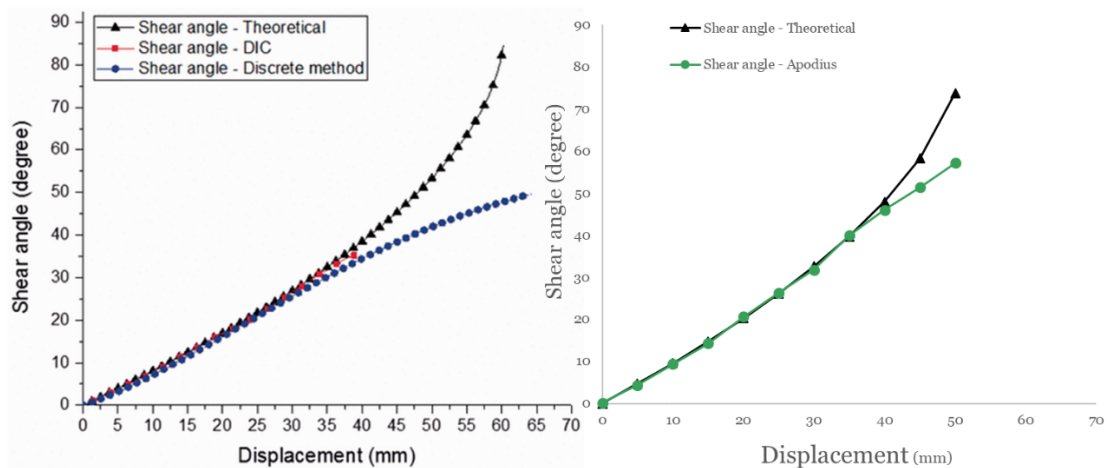


Figure 3-8 (a) shear angle values derived from crosshead displacement measurements for a bias extension test on a woven fabric [27]. (b) Shear angle values derived from Apodius scans for bias extension tests conducted on a woven fabric in this study. Woven fabric 3D forming analysis

3.3.1.3 Woven fabric hemisphere forming analysis

This optical scanning method was extended to a 2D-3D formed component to assess the measurement accuracy on a more complex geometry. A pneumatic punch was used to create a woven hemisphere, using the Apodius scanner to evaluate the local shear angles on both sides of the geometry using the code presented in Appendix B. This was compared at discrete points to measurements taken using an algorithm assisted edge detection and measurement method. The Canny edge detection

method was chosen, which was coupled with a custom Matlab script to align the location of the discrete measurement points between the scanning techniques. 12 points were measured on each of the three hemispheres located symmetrically about the central plane and encompassing each dome and the surrounding material. This gave a sufficiently wide range of values from which to validate the scanning methodology on a formed component.

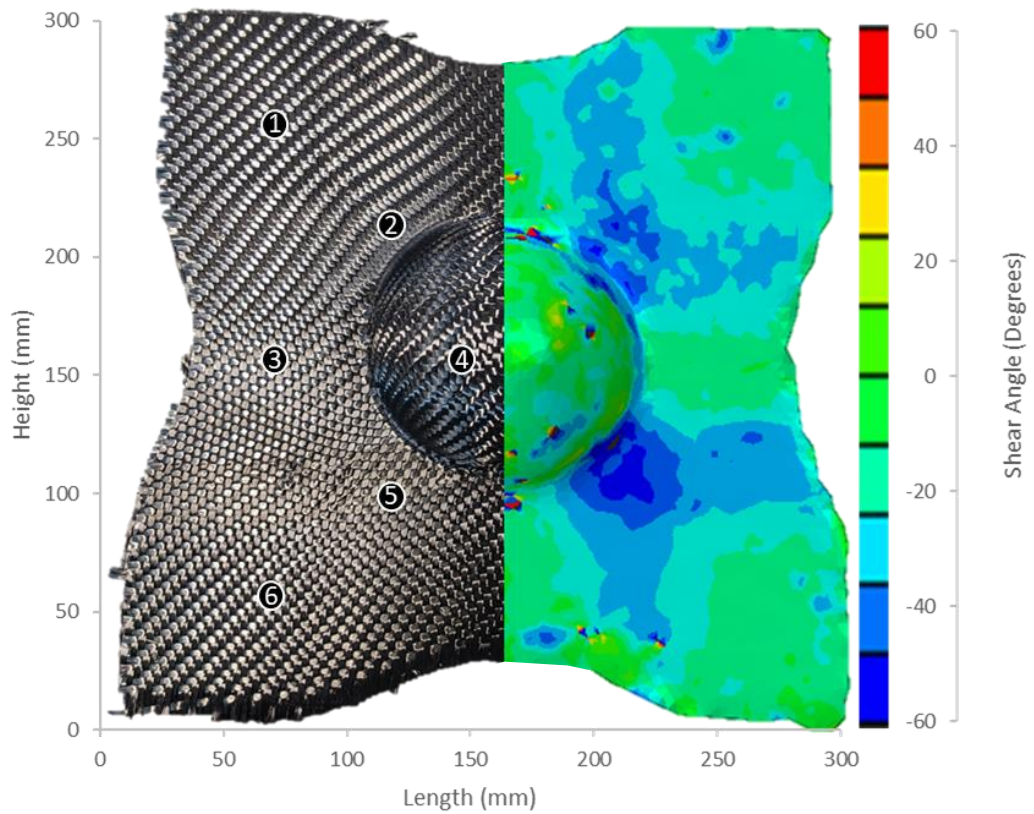


Figure 3-9 Woven hemisphere form, scanned using the Apodius optical scanning methodology. The right side shows the shear angle distribution and the left shows the fabric with discrete measurement positions noted.

Table 3-1 Comparison of shear angle at 12 discrete points on a formed woven hemisphere. Measurements taken using the Canny edge detection method and optical scanning methodology.

Point Label	Shear angle (degrees)				Difference
	Optical Scanning	Error \pm	Edge detection	Error \pm	
1	1	1	3	1	2
2	-33	5	-31	4	2
3	2	2	3	1	1
4	-12	4	-10	2	2
5	-50	6	-47	7	3
6	1	2	1	3	0
7	2	1	0	1	2
8	-30	4	-32	4	2
9	3	1	4	2	1
10	-14	2	-13	1	1
11	-44	3	-40	5	4
12	0	1	0	3	0

Figure 3-9 shows a contour plot of shear angle on a woven hemisphere alongside the discrete point locations from the edge detection analysis. The selected point locations align with areas of interest on the hemisphere. Points 1, 3, 7, 6, 9 and 12 show the extremities of the preform, points 2, 5, 8 and 11 show areas with high levels of shearing, and points 4 and 10 are on the dome. Table 3-1 shows the shear angle for each of the 12 discrete points on the hemisphere from Figure 3-9. The average difference between scanning methods was 1.7 degrees. The Canny edge detection method has been proven in the literature to provide an accurate assessment of fibre angle. On simple geometries or a small sample size such as this, the Canny edge detection method can be used to validate shear angle values. However there is little scope for expanding the point cloud or improving detection without a full optical system such as the Apodius arm. An agreement between the methods within 1.7 degrees over a shear angle range of ± 50 degrees gives confidence in the validity of the results from the optical scanning methodology.

3.3.2 Non-crimp fabric optical scanning

3.3.2.1 NCF picture frame shear analysis

By using the scanning methodology and custom code on the picture frame test it was possible to output the full field shear of NCFs at discrete times during the test and analyse the homogeneity of test samples and assess the accuracy of crosshead displacement calculated shear angle. The fibre angle has been noted across the central region and arms of the sample and the standard deviation of the central region was calculated to define the fibre misalignment. Particular attention was given to the stitch breakage point where peak fibre misalignment was expected. The results are presented for both positive and negative shearing with the stitches aligned parallel (positive) and perpendicular (negative) to the displacement direction in Figure 3-10 and Figure 3-11 respectively.

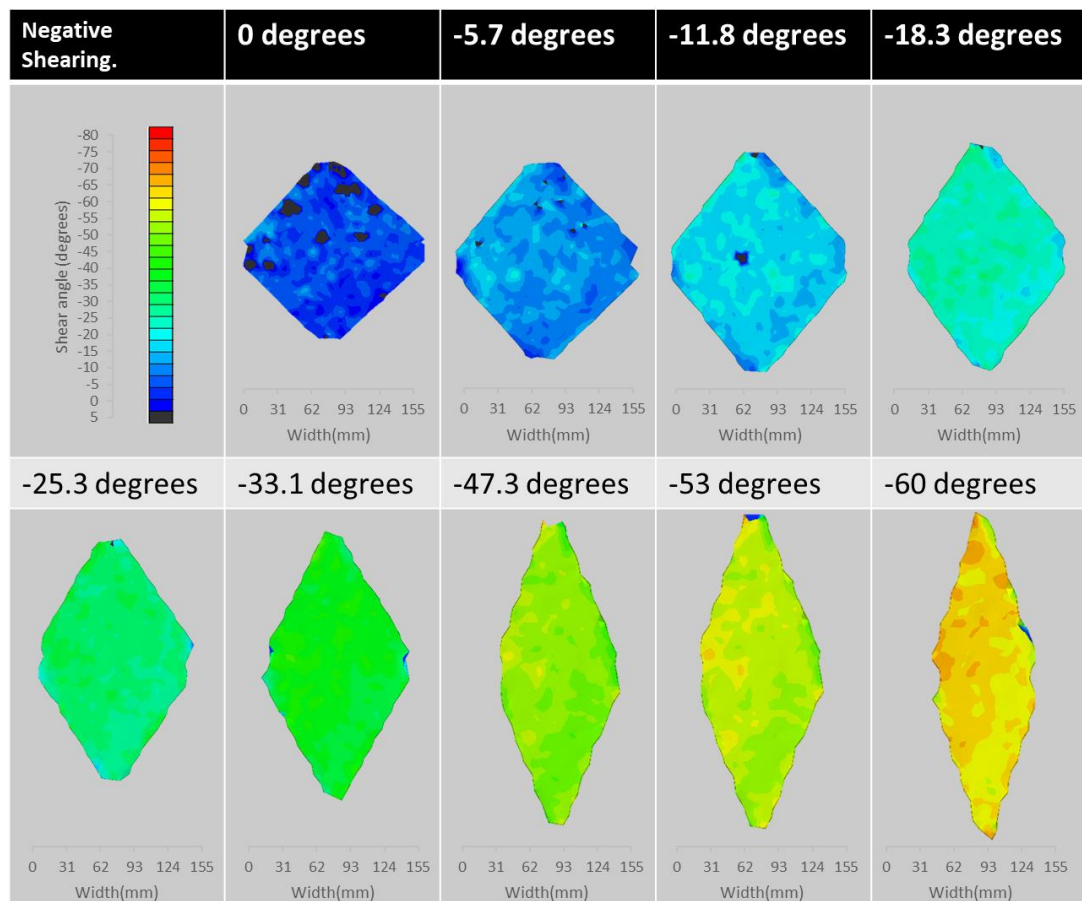


Figure 3-10 Full field shear angle distribution of the NCF FCIM379 at 9 discrete displacements during the picture frame test. Shear is in the negative direction, therefore stitching is perpendicular to the crosshead displacement.

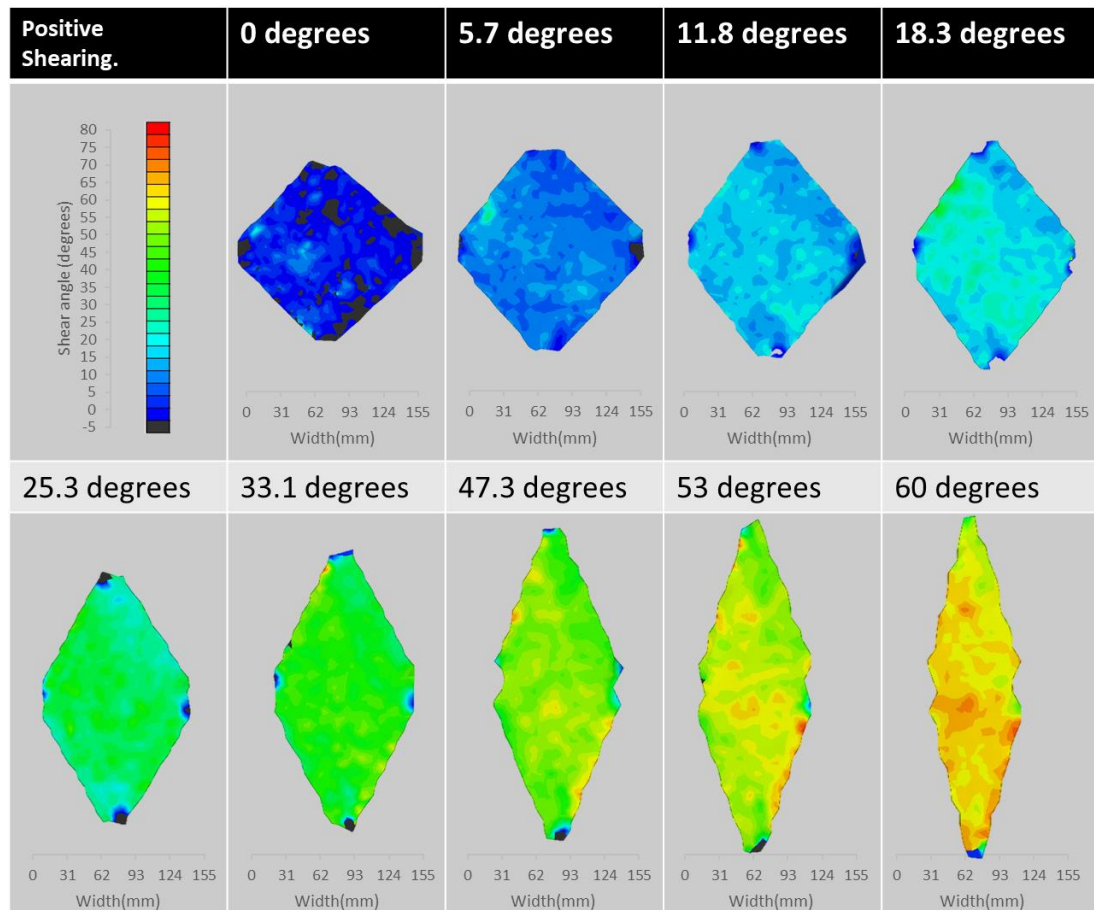


Figure 3-11 Full field shear angle distribution of the NCF FCIM379 at 9 discrete points in the picture frame test. Shear is in the positive direction and the stitching is parallel to the direction of the crosshead displacement.

Assessment of the homogeneity of the contour plots qualitatively showed a difference between the positive and negative shear direction when 33.1 to 47.3 degrees of global shear was reached. In the positive shear direction there was an increase in the number of yellow and orange high shear angle spots that start from the edge of the pre-form and migrate inwards as shear angle increases to 53 degrees. This has been quantified in the error bars in Figure 3-12 which show the standard deviation across the sample over 4 repeats. Investigation into the fibre angle deviation is further analysed in later sections. The high shear angle regions have been attributed to areas of stitch breakage that appear during positive shearing but not during negative shearing. It was notable from the contour plots that the breakage tended to start near the clamped edge of the sample and move inwards as shear angle increased (Figure 3-11 53 degrees). This indicated that stitch failure was not purely random and was affected by the boundary conditions on the fabric.

The 0 degree shear angle data in the contour plots from Figure 3-10 and Figure 3-11 showed large regions of poor data (that appear black on the contour plot). These regions disappeared as shearing increased and was due to the difference in initial surface topology of the fabric. At 0 shear the fibres lie close to one another and the edge detection algorithm used by the optical scanner cannot accurately distinguish between individual yarns. This caused the software to identify the stitch as a primary yarn direction which was filtered out in the custom Matlab code. The use of edge lighting enabled the contrast of the yarns to be improved to remove this error.

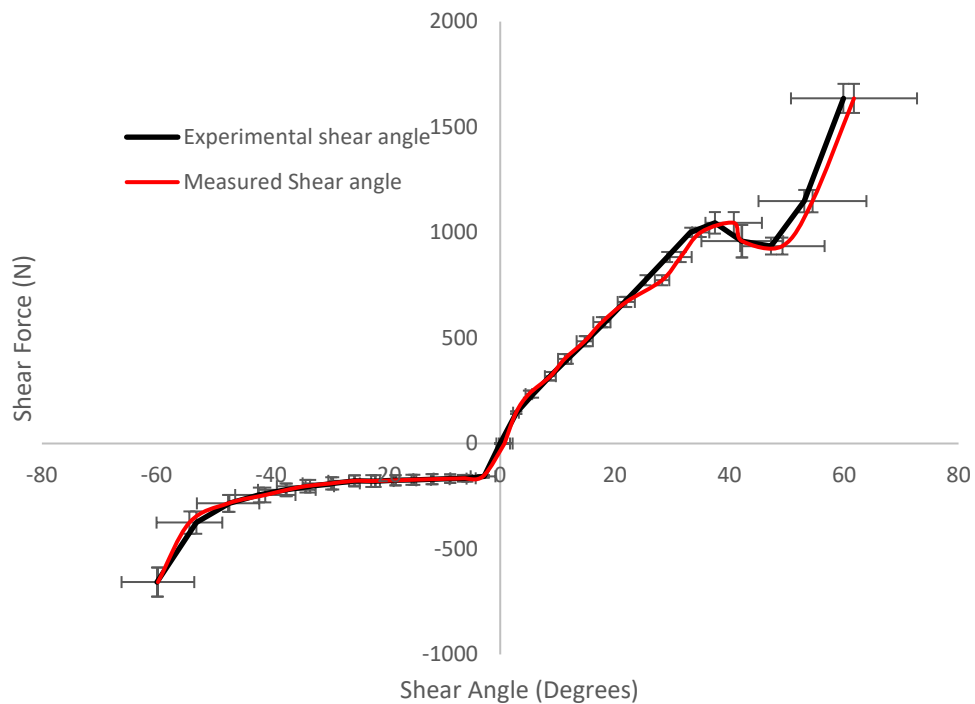


Figure 3-12 Shear force versus shear angle curve for a picture frame test of NCF FCIM379. The experimental shear angle was calculated from the crosshead displacement and the measured shear angle was taken from optical measurements of the fabric. Error in the y-axis shows the shear force variation over multiple samples. Error in the x-axis shows standard deviation in the fibre angle in the measured results.

Between shear angle values of -60 and 30 degrees there was a difference of 0.5 degrees between calculated and measured values, which is similar to the level of agreement observed for the woven fabric. After 30 degrees the difference increased to 3 degrees. The increase in discrepancy at 30 degrees may be attributed to early onset of stitch breakage that can be seen by the drop in shear force over the range

of 38 to 44 degrees and the increase in standard deviation (shown by the wide error bars). The crosshead displacement was an accurate measure of shear angle up until stitch breakage occurred in the fabric. After stitch breakage the crosshead displacement could be used as an input. However, the increase in fibre misalignment will cause a large amount of localised error in the values.

3.3.2.2 NCF bias extension shear analysis

The scanning methodology has been applied to the bias extension test in a similar manner as for the picture frame test and the homogeneity of samples and the accuracy of crosshead displacement calculated shear angle was assessed. The results are presented for both positive and negative shearing with the stitches aligned parallel (positive) and perpendicular (negative) to the displacement direction in Figure 3-13 and Figure 3-14 respectively. The sample was measured on a single side with the identical clamping condition on both sets of yarns used to assume symmetrical conditions. The undeformed sample was 350mm long and 115mm wide, with 250mm of length exposed after clamping.

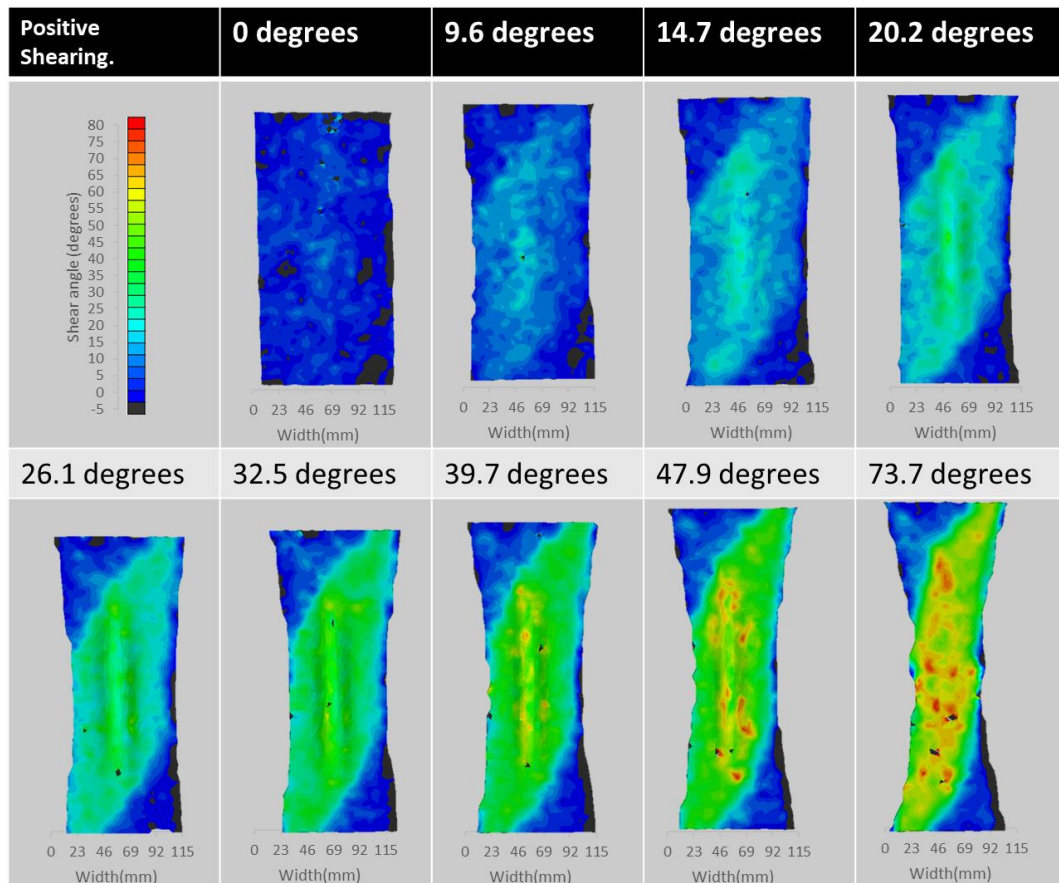


Figure 3-13 Full field shear angle distribution of the NCF FCIM379 at 9 discrete points in the bias extension test. Shear is in the positive direction where the stitching is parallel to the crosshead displacement.

Observations from the positive shear contour showed a homogenous pure shear region that is consistent with the literature for NCFs. Between 39.7 degrees and 47.9 degrees there was the appearance of high shear spots in local regions. This matched the stitch breakage point in the theoretical shear function and was also observed during the picture frame test. In these local regions there was evidence of broken stitches and fibre misalignment around each broken stitch. The stitch breakage increased further at 73.7 degrees. Between 14.7 degrees and 20.2 degrees the preform began to experience out of plane buckling which increased in severity as the shear angle increased. This agrees with previous literature [80] showing a similar buckling point with wrinkling starting around 8 degrees and becoming visible at 20 degrees. The wrinkle amplitude was also comparable to the literature with a peak amplitude of 3-3.5mm.

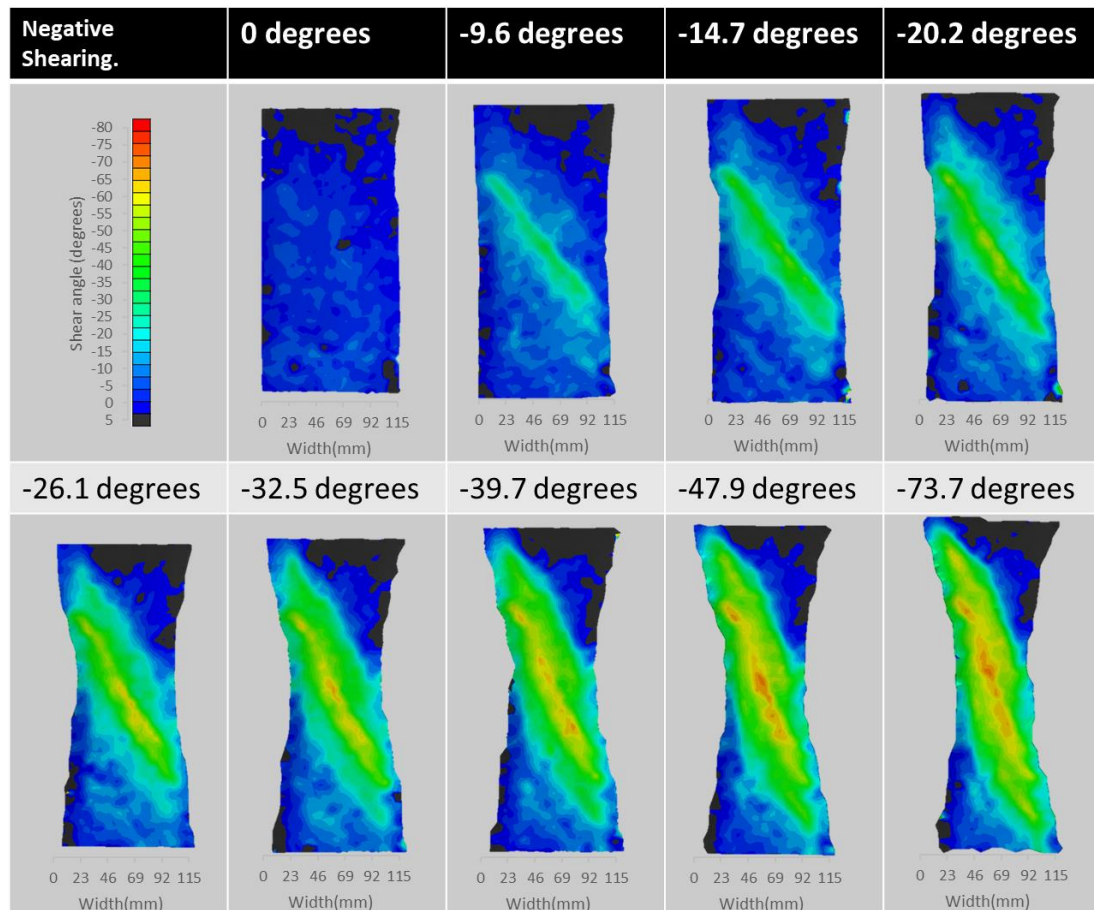


Figure 3-14 Full field shear angle distribution of the NCF FCIM379 at 9 discrete points in the bias extension test. Shear is in the negative direction and as such the stitching is perpendicular to the crosshead displacement.

In the negative shear direction (Figure 3-14) there was no sign of out of plane buckling. However, the distribution of shear across the pure shear region was far less consistent than in the positive direction. The shear peaked in yarns crossing the entire length of the pure shear region with a 5-10 degree drop in the rest of the region. This was caused by immediate slippage of the yarns negating the pin jointed assumption used to calculate a pure shear zone in the sample. This caused the sample to become skewed as can be seen by the non-uniform edge profile between -26.1 and -73 degrees. There was no evidence of localised high shear points at shear angles between -39.7 degrees and -47.9 degrees and no evidence of broken stitches on the sample.

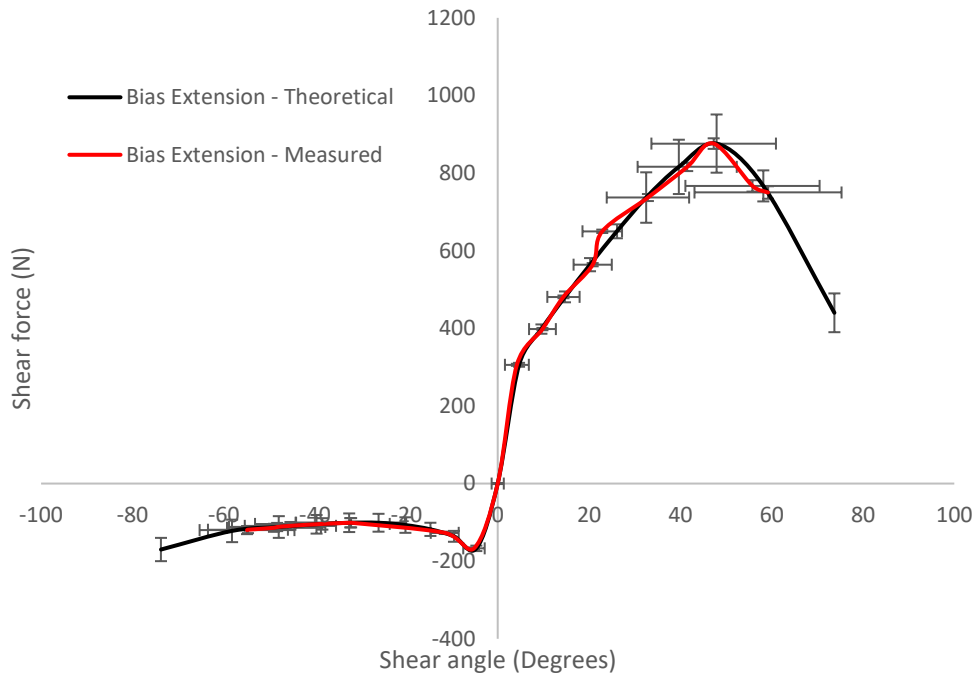


Figure 3-15 Shear force versus shear angle curve for a picture frame test of the NCF FCIM379. The experimental shear angle is calculated from the crosshead displacement and the measured shear angle is taken from optical measurements of the fabric. Error in the y-axis shows the shear force variation over 3 samples. Error in the x-axis shows deviation in the fibre angle in the measured results.

Plotting the measured shear angle against values calculated from the crosshead displacement showed a similar level of agreement between the two data sets as the data produced from the picture frame test. There is a peak difference between the measured and theoretical values of 3 degrees, which appears around the stitch breakage range. A similar deviation between the measured and theoretical shear values was observed past the stitch breakage point as shown from the rapid increase in the shear angle error. Slippage is evident from the drop in shear force at 42 degrees without the characteristic rise as locking occurs. There is evidence of local non-uniformity occurring early on in the test at 6-8 degrees causing a reduction in shear modulus of 52%. On the contour plot, this was the region where out of plane buckling was first seen. In the negative region Figure 3-14 showed slippage occurring between 0 and -10 degrees. This appears in Figure 3-15 as a reduction in absolute shear force

from -191N to -180N followed by a negligible shear modulus for the remainder of the test.

The local inconsistencies found in the full-field shear map (Figure 3-14 -39.7 degrees) during the bias extension test indicates that the test is not accurately capturing the shear stiffness of the fabric in either the positive or negative shear direction. A normalisation of the two tests has been conducted using the methodology of I.Taha [81]. Separate testing has been employed for both positive and negative shearing directions. The normalization process has been conducted separately for each direction, followed by the amalgamation of the results in a single plot for ease of interpretation. When compared to the picture frame test in Figure 3-16 there is a 100% modulus difference between -50 and 0 degrees, 30% difference between 0 and 40 degrees and a difference in stitch breakage point of 9 degrees. Fabric tested via the bias extension test never experienced fibre locking due to the slippage that occurred in the pure shear zone. The bias extension test was found to be unsuitable for collecting shear modulus input data for a pillar stitched NCF.

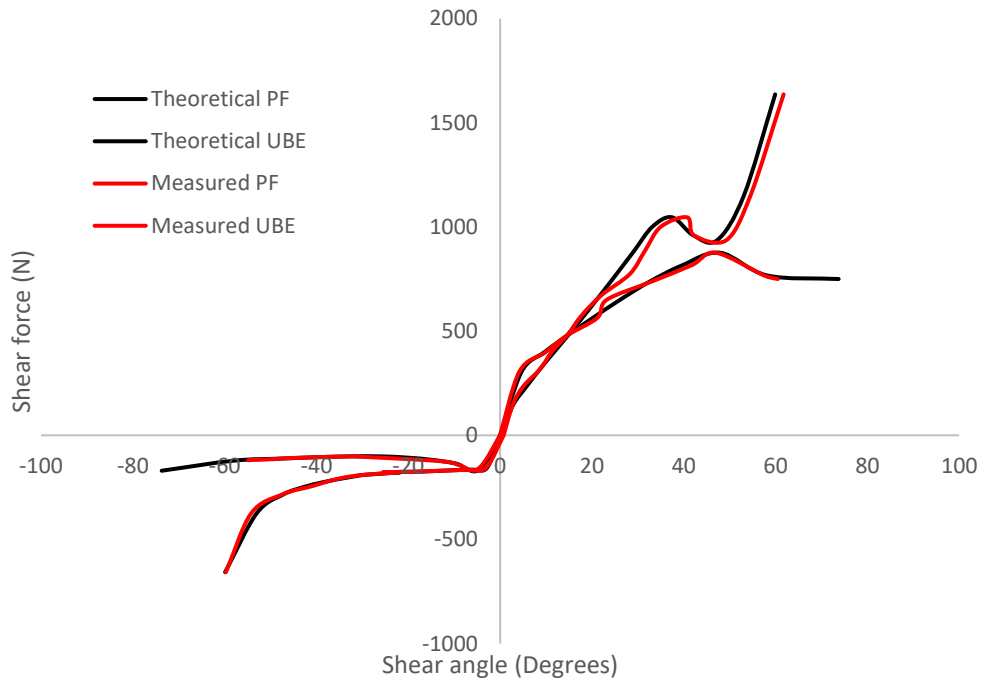
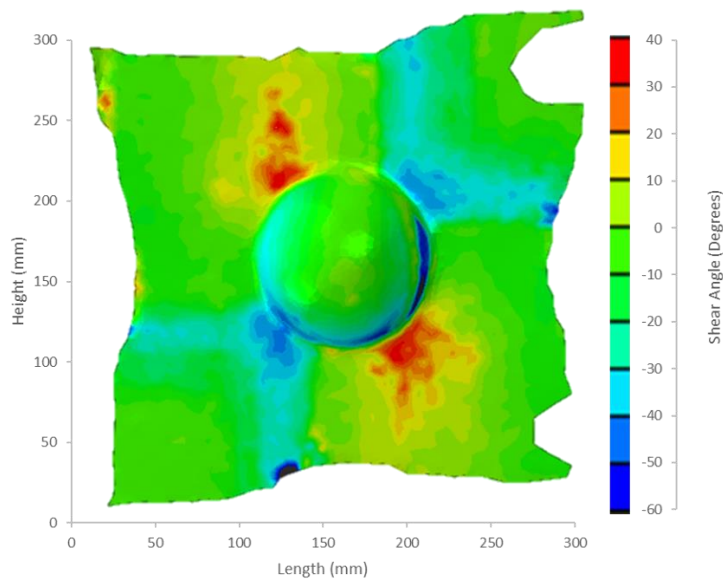
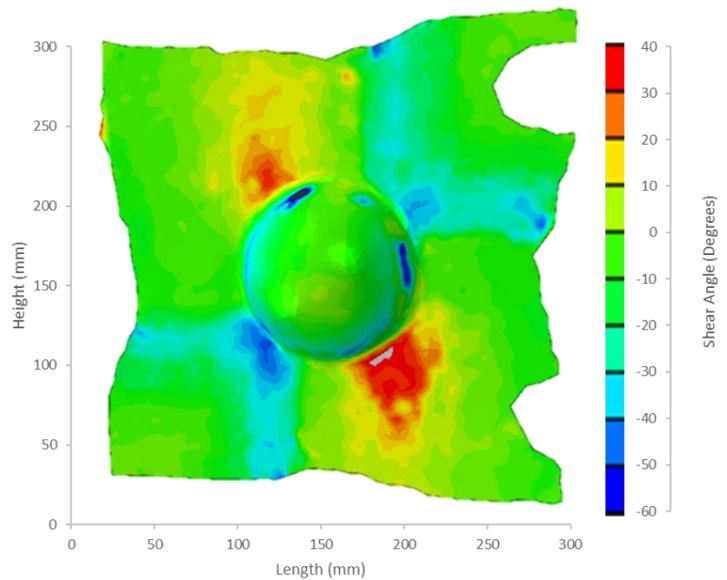


Figure 3-16 Normalised and compared shear force shear angle plots for FCIM379 NCF using the picture frame and bias extension test.

3.3.2.3 NCF 3D forming analysis

To measure the consistency of scanned 3D NCF components, a series of scans were taken from the same hemisphere form and variations between the scans have been measured. New point data, a new mesh and new set of images have been generated for each repeat as shown in Figure 3-17. Two paths were taken through the regions of peak shear angle and compared across the three scans to quantify the differences in Figure 3-18 Figure 3-19 and Figure 3-20. The mesh from each scan differs slightly as new mesh data was collected for each repeat. This extends to the regions that have been removed where the specimen has been clamped (done to stop mesh data from the clamp interfering with the shear angle calculation code.)



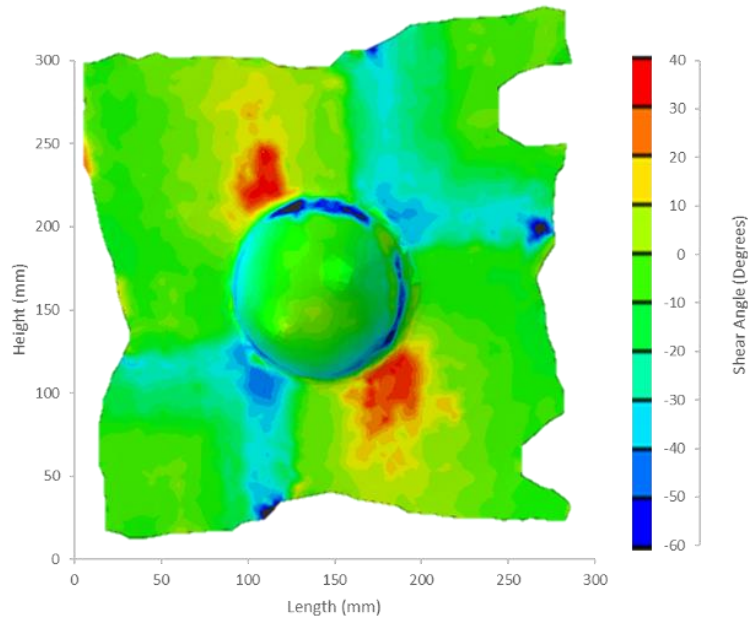


Figure 3-17 Three independent scans of a single formed NCF hemisphere using the optical scanning methodology showing shear angle contour plots.

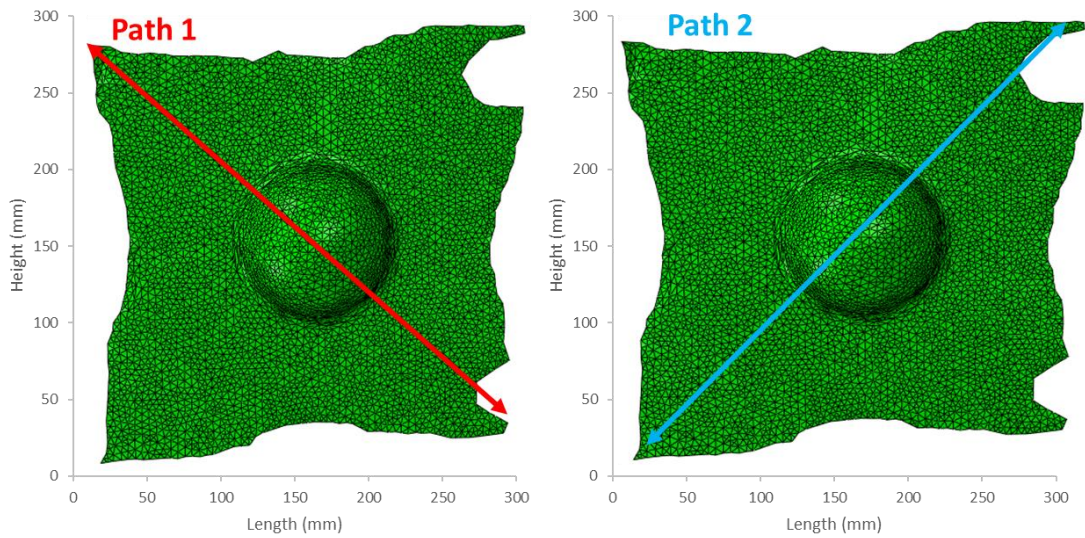


Figure 3-18 Definitions of the 2D paths taken over the formed hemisphere for comparison of shear angle data between the 3 hemisphere scans. Each path extends through the opposing regions of maximum and minimum shear angle.

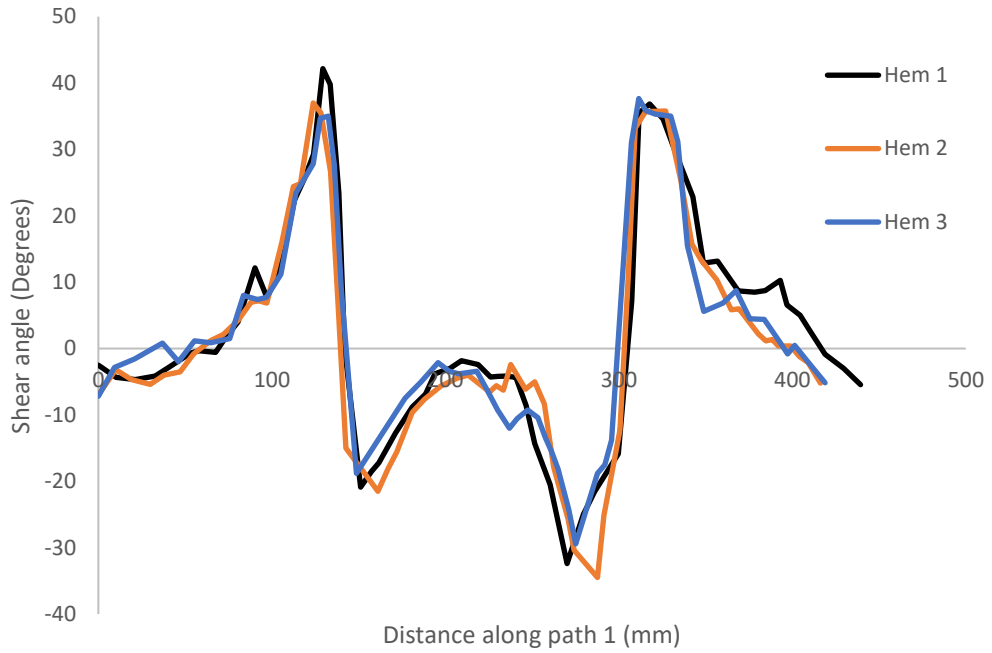


Figure 3-19 Shear angle distribution over path 1 for three scans of a single hemisphere using the optical scanning methodology.

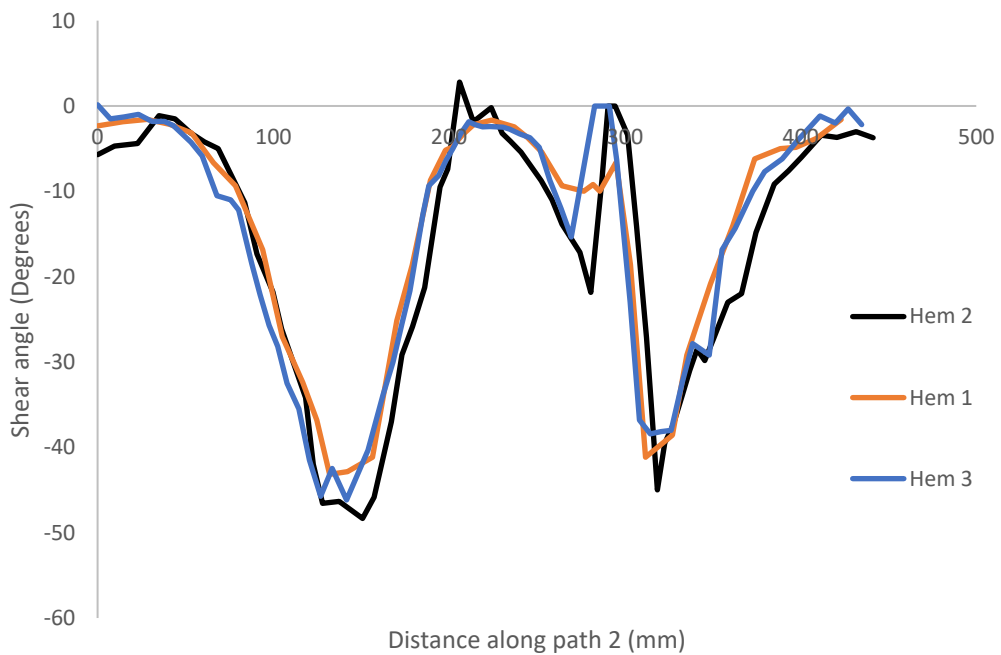


Figure 3-20 Figure 18 Shear angle distribution over path 1 for three scans of a single hemisphere using the optical scanning methodology.

The contour plots in Figure 3-17 qualitatively show the similarities between the scans. The location and magnitude of the high shear angle regions on each scan span the same 60mm regions on opposing sides of the hemisphere and the minimum shear extends from edge to edge on each scan. The position of the maximum and minimum shear angle element were within a 10mm range across the 3 scans. There were regions of poor data that differ from scan to scan where the edge detection algorithm misinterpreted the fibre angle. These appear as very low shear angle regions. This data loss does not affect regions where there is genuine shearing, due to the change in fabric surface quality discussed above. Across the two paths, the difference in shear angle between the three scans peaked at 7 degrees and averaged 3 degrees (shown in Figure 3-19 and Figure 3-20). On each path the maximum difference between scans occurred at 280mm which coincides with the lower edge of the dome feature. These are areas of poor data as can be seen in the contour plots in Figure 3-17. Removal of the 250-300mm region in each path lowers the average difference between scans to 2 degrees.

3.3.3 Tensile properties of sheared fabrics

Fibre misalignment can negatively affect the elastic properties of a component. Undesired and inconsistent fibre direction will lead to poor part performance or premature failure. Measurement of the fibre alignment during in-plane testing can be used to improve prediction accuracy for the tensile modulus of formed components. This can be incorporated into material characterisation for simulations to improve the accuracy of structural modelling. The scanning methodology will be used to identify the level of misalignment found in formed structures and calculate the influence on mechanical performance that is caused by the change in directional consistency and change in fibre volume fraction.

3.3.3.1 *Local fibre misalignment*

Local fibre misalignment across a test sample can generate a wide range of shear angle values following fabric draping. This has been quantified by investigating the standard deviation of the local fibre angles, which has been plotted as error bars in the graphs above (Figure 3-12, Figure 3-15). The misalignment in the fibre angle is

dependent on the amount of induced shear and differs between woven fabrics and NCFs, as seen in Figure 3-21 and Figure 3-22.

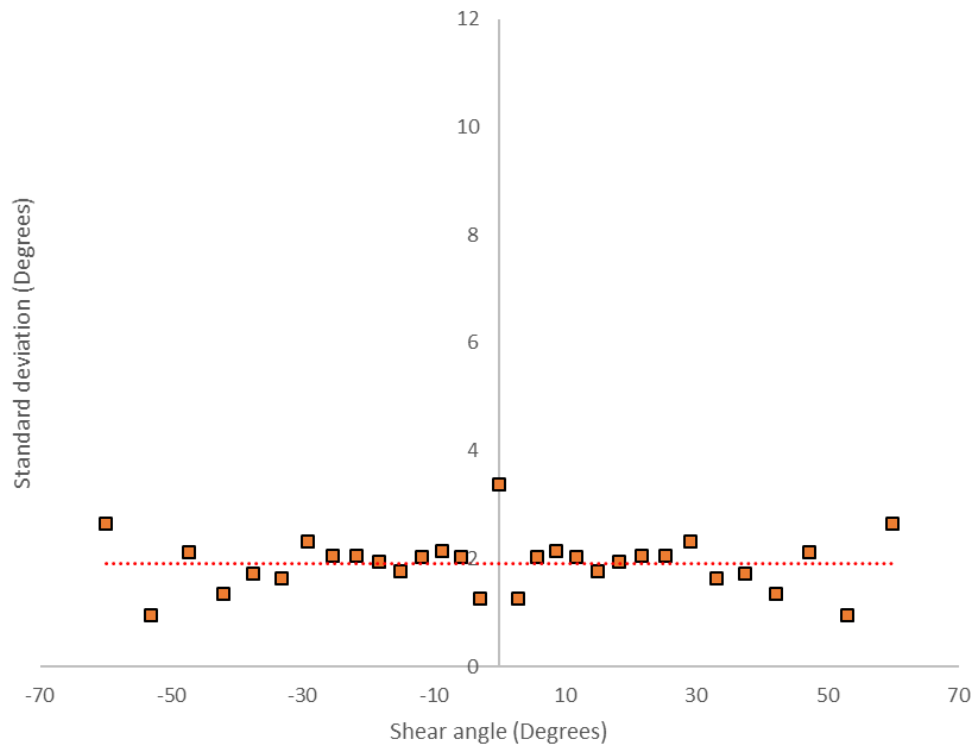


Figure 3-21 Fibre angle deviation for a woven fabric from -60 to 60 degrees of shear

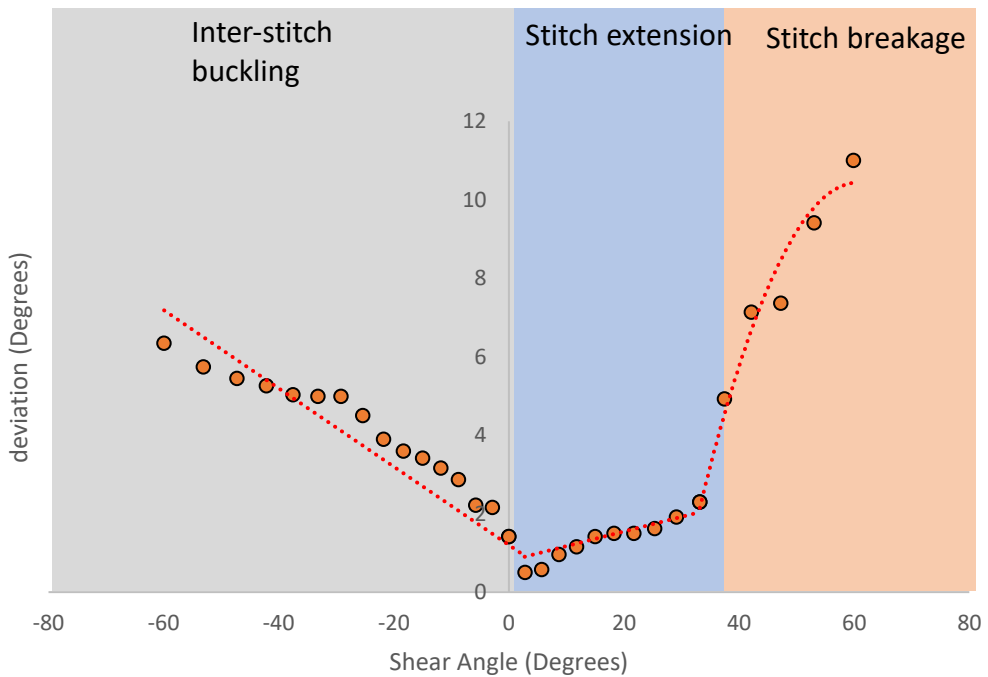


Figure 3-22 Fibre angle deviation for an NCF from -60 to 60 degrees of shear

The woven fabric had a consistently low deviation peaking at 3.3 degrees at zero shear angle with an average deviation from -60° to 60° of 1.9° . The peak deviation at 0° was likely due to misalignment caused by handling of the samples before testing. The NCF sample showed a broader range of deviation values over the measured shear angles. The variation can be split into 3 sections, depending on the cause of the fibre misalignment, as shown in Figure 3-22. From 0° to -60° of shear there was a steady increase in the deviation from 0.4 degrees to 6 degrees. From 0° to 35° there was a small change and the standard deviation increased to 2° . A shear angle of 37° marks the stitch breakage point in the fabric. Beyond this point there was a large increase in the standard deviation up to 11° , as local perturbations form around the broken stitches. The increase in fibre misalignment in the negative shear region was caused by yarn buckling, which occurs in-between the stitches as they are compressed. This phenomenon does not occur in the positive direction and is not apparent in the woven fabric. This buckling defect is further analysed in following chapters.

The coefficient of variation as a function of shear angle has been plotted in Figure 3-23 and shows that at high absolute shear angle values, the deviation is 10-15% of the shear angle. In the negative region this ratio increased up to 40%, before dropping suddenly to a value of 12% as the fabric enters positive shearing. Figure 3-23 shows how shearing in the positive direction leads to a lower level of fibre misalignment up until the stitch breakage point.

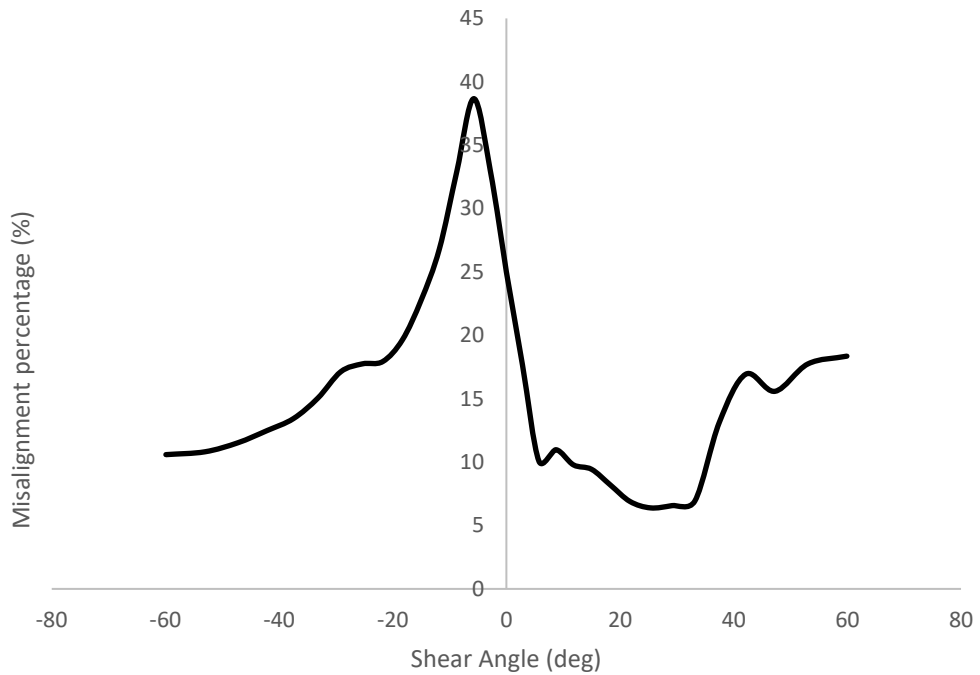


Figure 3-23 fibre misalignment as a percentage of the applied shear angle.

3.3.3.2 Local fibre misalignment on tensile modulus

The impact of absolute fibre misalignment on the tensile modulus of the fabric [82, 83] is shown in the literature and in Figure 3-24. This agrees with studies showing a similar impact of in-plane waviness on tensile modulus [84]. Fibre misalignment has been calculated from the standard deviation data provided by the optical scanning methodology. Values have been taken between -90° and 0° and between 0° and 90° in two separate sets of tests and smoother over the singularity point at 0. Values are calculated in the range of 90° and -90° with the any and any periodically similar angles between -180° and 180° being recalculated into the correct range. Values outside of the -180° to 180° range have their initial period set to 0 so they fall into range.

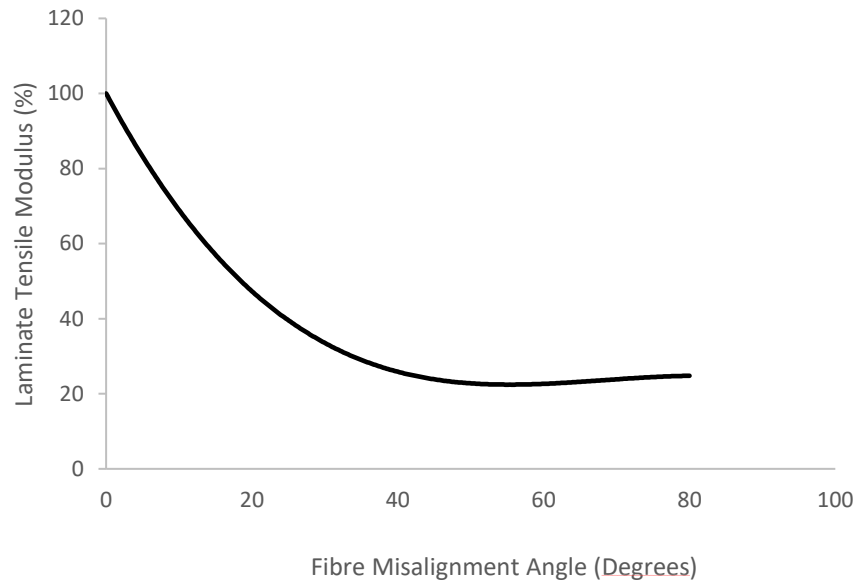


Figure 3-24 Function showing the change in relative tensile stiffness as fibre deviation increases [82, 83].

The reduction in tensile stiffness from the literature is shown as a percentage reduction from the measured modulus, and is for unidirectional fibres (Figure 3-24). It has been captured in Equation 3-4 as a third order polynomial where δ is the fibre misalignment.

$$f_t(\delta) = -3 \times 10^{-4} \delta^3 + 5.51 \times 10^{-2} \delta^2 - 3.61 \delta + 100 \quad \text{Equation 3-4}$$

Equation 3-4 was used to calculate the change in tensile modulus according to the fibre misalignment levels presented in Figure 3-25

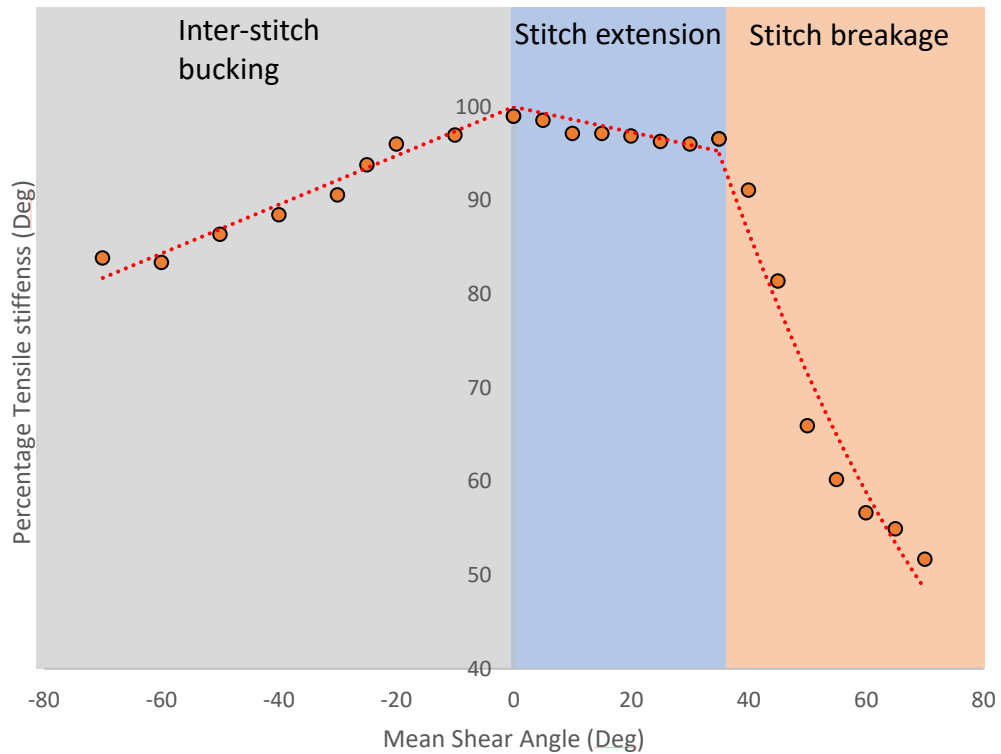


Figure 3-25 Change in in-plane tensile stiffness due to variable fibre misalignment as shear angle increases, as calculated from Equation 3-4 and points from Figure 3-24

The tensile modulus was at a maximum at 0 degrees and dropped by 5% between 0 and 39 degrees of shear. After stitch breakage the fibre misalignment caused a significant drop in modulus of 30% over 30 degrees. In the negative region there is a gradual reduction in tensile modulus which matches the gradual increase in fibre misalignment caused by inter stitch yarn buckling. This theoretical modulus reduction is linear and drops by 15% over 60 degrees. This analysis assumes a constant fibre volume fraction and does not incorporate the effect that shearing has on the thickening of fabric plies.

3.3.3.3 Effect of local volume fraction on tensile modulus

The theoretical maximum fibre volume fraction of a biaxial fabric changes as the amount of shearing increases. This is due to the compaction that occurs in the yarns to accommodate the difference in area between the un-sheared area A_0 and the sheared area A as the yarn number remains constant. At low shear angles this compaction is accommodated by the space between the yarns, increasing the fibre

volume fraction without changing the cross sectional shape of the yarn or the ply thickness. At higher levels of shear the locking angle is reached and yarn compaction occurs. The increase in global fibre volume fraction is then due to the change in cross sectional area of the yarn as it becomes more circular. The theoretical fibre volume fraction is well documented in the Channis equations for both woven fabrics and NCFs and is directly related to the difference in area due to the applied shear [85, 86]. This can be plotted for a sample in simple shear as the area varies alongside the change in shear angle. The function is given in Equation 3-5.

$$\varphi_s(\alpha) = \frac{n_L}{\rho_f \cdot t} \cdot m_{A_0} \cdot \frac{A_0}{A_0 \sin(90^\circ - \alpha)} \quad \text{Equation 3-5}$$

where $\varphi_s(\alpha)$ is the change in fibre volume fraction due to shear angle, ρ_f is the density of the fabric, t is the thickness, and A_0 and m_{A_0} are the area and areal mass respectively in Equation 3-5. The fibre volume fraction directly affects the laminate stiffness according to the Channis equations, so the change in tensile modulus due to the change in fibre volume fraction caused by fabric shearing is given in Figure 3-26.

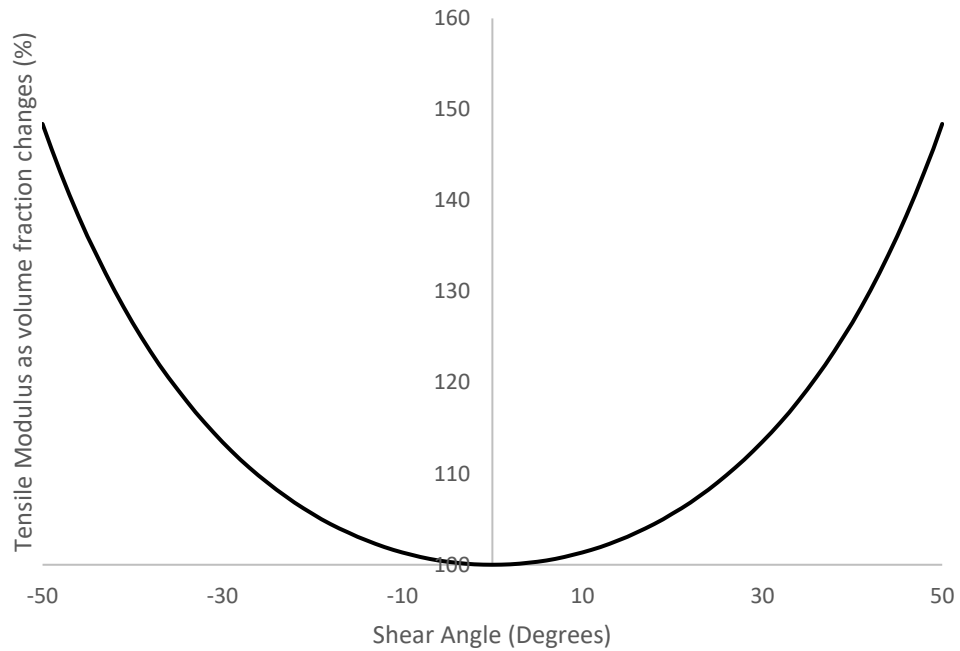


Figure 3-26 Theoretical change in volume fraction as shear angle changes from - 50 degrees to 50 degrees.

3.3.3.4 Combined impact on tensile modulus

As the fibre misalignment and fibre volume fraction are both functions of the shear angle, the influence of both factors was combined into one piecewise equation that measures the overall change in tensile modulus across a range of shear angles. This was plotted as a percentage change in tensile modulus (Figure 3-27). A function has been generated to predict the change in tensile modulus over the range of shear angles typically found in matched tool and diaphragm forming (Equation 3-6).

$$\begin{aligned}
 & F_{(\%)}^{Modulus} && \text{Equation} \\
 & = \begin{cases} 0.0328\alpha^2 + 0.876\alpha + 100, & \alpha < 0; \\ 7X10^{-4}\alpha^3 + 2.47X10^{-2}\alpha^2 - 0.446\alpha + 100, & 0 \leq \alpha < 37; \\ 6.25E - 2\alpha^2 - 4.68\alpha + 200 & 37 \leq \alpha; \end{cases} && \mathbf{3-6}
 \end{aligned}$$

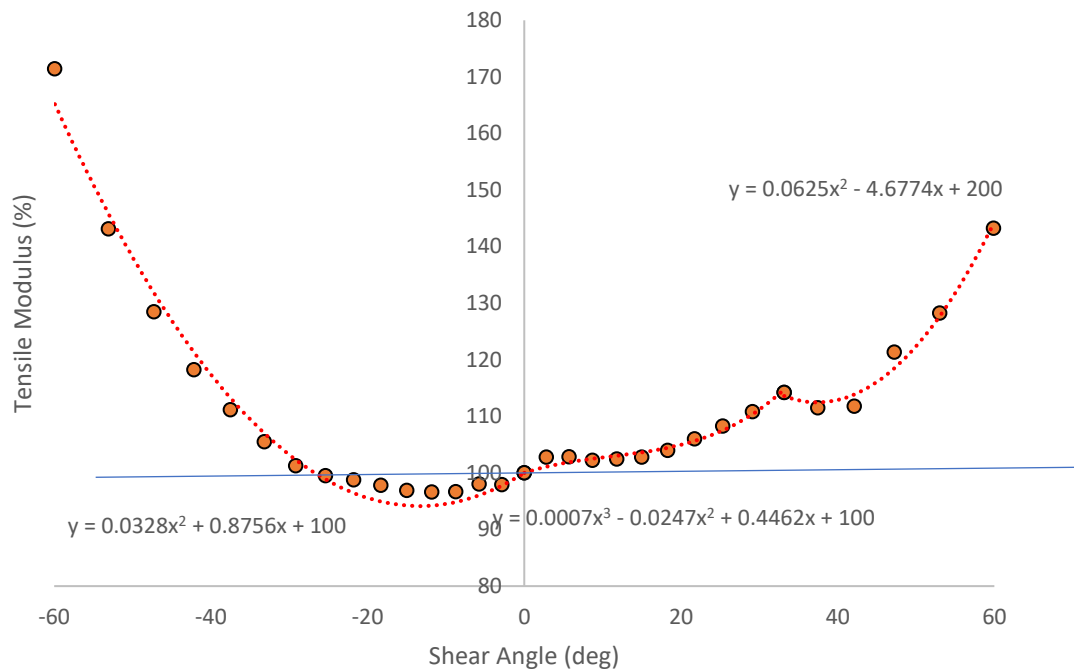


Figure 3-27 Combined effect of volume fraction and fibre misalignment on the tensile modulus as shear angle ranges from -60° to 60° .

Between 0 degrees and -28 degrees of shear there is a reduction in the tensile modulus of the ply due to shearing, with the minimum occurring at -15 degrees of shear (96% stiffness). This is the only region with reduced ply tensile modulus due to the poor fibre misalignment, with all other shear angles experiencing an increase in tensile modulus due to the increase in fibre volume fraction. The function from Equation 3-6 has an R^2 value of 0.988. There is a steady increase in stiffness of 11% between 0 and 38 degrees that is captured by the function with an R^2 value of 0.97. At the stitch breakage point there is a drop in tensile modulus from 112% to 108% between 38 degrees and 41 degrees of shear, however this increases to a new maximum after a shear angle of 46 degrees. The negative region does not show the characteristic drop caused by stitch failure and has a smooth monotonic increase in stiffness up to 170% at -60 degrees of shear. Both of these regions are captured by Equation 3-6 with R^2 values of 0.988 and 0.981 respectively. This high conformity between the experimental and fitted function enables it to be used as input data for simulations, providing the shear angle information is also known. This is critical for

accurately capturing the elastic properties of a formed components that has experienced high levels of shearing during processing.

3.3.3.5 Combined validation

To validate the change in ply tensile modulus that is predicted in Figure 3-27, a series of tensile tests have been conducted on sheared fabrics starting form a 0/90 ply of NCF. The tensile modulus of a single ply in a sheared laminate has been extracted and compared to the expected values given by Equation 3-6. Samples have been tested at shear angles of -30, -15, 0, 15 and 30 degrees using laminate designs presented in Table 3-2. Comparisons between predicted moduli values and values tested experimentally can be found in Figure 3-28.

Table 3-2 Laminates used in tensile coupon testing and associated shear angle.

<i>Sample</i>	<i>Laminate</i>	<i>Shear angle</i>
A	0/60, -60/0	-30
B	0/75, -75/0	-15
C	0/90, -90/0	0
D	0/105, -105/0	15
E	0/120, -120/0	30

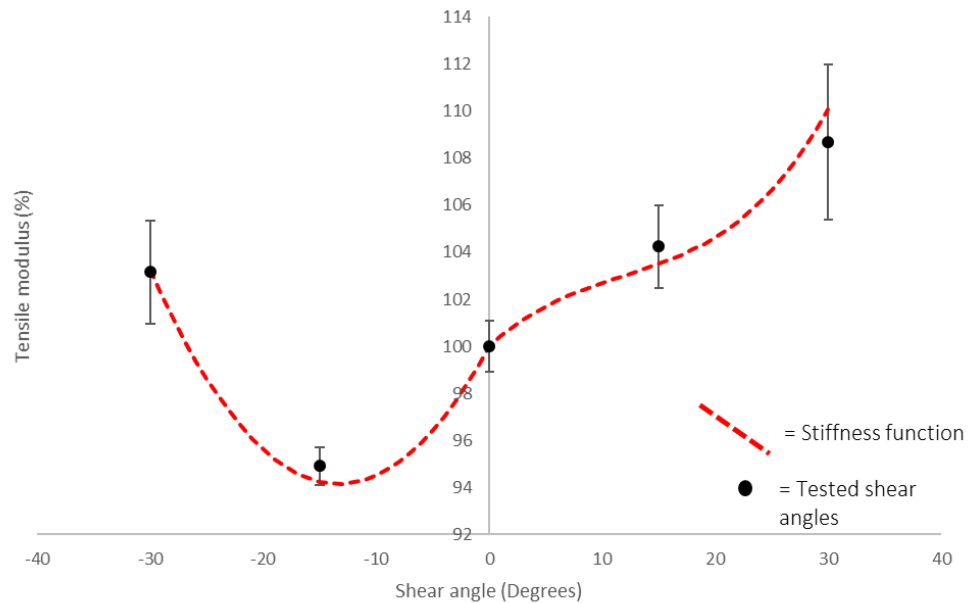


Figure 3-28 Percentage change in tensile modulus due to fibre misalignment. Comparison between predicted values and experimental values from tensile testing

The results gathered from experimental tensile testing agree well with the predicted change in modulus, with an R^2 value of 0.989. The predicted modulus values fall within the experimental error bars for each sample. It can be concluded that Equation 3-6 is an accurate representation of the change in tensile stiffness that occurs due to fibre misalignment cause by fabric shearing.

3.4 Chapter summary

It has been shown that optical scanning using the Apodius vision sensor and custom interpretation code can be used to accurately measure the fibre angles and corresponding shear angles for woven fabrics within 0.5 degrees of the theoretical values.

It has been shown that the theoretical calculation of shear angle from the bias extension test for a woven fabric is incorrect at high values of shear, agreeing with the literature. This discrepancy was worse for the NCFs tested, which experienced large amounts of out of plane deformation at shear angles above 15 degrees. Yarn slippage also occurred, as evidenced by the final ply boundary at shear angles below -15 degrees and above 30 degrees.

The theoretical shear angle calculations for NCFs in the picture frame test were accurate to within ± 1 degree compared to the full-field measured shear angles from the Apodius system, including up to and around the stitch breakage point (within ± 3 degrees of the stitch breakage point).

A 3D punch formed woven hemisphere was optically scanned and local fibre angles were compared to the fibre angles measured using edge detection methods at 12 discrete points. Values from the scan matched the measured values with ± 3 degrees. This validated the accuracy of the optical scanning method and interpretation code against current methods.

It was shown that consistent shear angle distribution results can be attained using the optical scanning methodology for a formed component, with multiple scans showing an average variability of ± 3 degrees.

Shearing was found to cause fibre misalignment that was measured and plotted with a consistent non-linear distribution. It was predicted that the shear induced fibre misalignment and change in volume fraction would affect the tensile stiffness of each ply. With misalignment reducing the modulus and change in volume fraction cancelling this out at higher shear angles.

Tensile testing was conducted on samples that had been sheared to known values. A reduction in tensile modulus was found between 0 and -30 degrees with all other shear angle values showing increases in the tensile modulus due to increased fibre volume fraction. The results agreed with the predictions for modulus gathered from fibre misalignment measurements.

4 Non-linear shear behaviour & inter-stitch defects in non-crimp fabrics

4.1 Introduction

4.1.1 Objectives:

- To explore the link between non-linear shear behavior of non-crimp fabric plies at the onset of shearing and the development of inter-stitch yarn buckling. An analytical model of the initial non-linear shear behavior will be developed, which will be used to predict the likelihood of inter-stitch yarn buckling.
- To understand how inter-stitch yarn buckling generates a difference in fibre misalignment between positive and negative shear directions.
- To propose methodologies for inter-stitch yarn buckling reduction strategies.

4.1.2 2D to 3D fabric forming

Direct 2D to 3D fabric forming processes are a favourable option for high rate automated manufacture of continuous fibre composites. Creating a 2D ply stack is much quicker than depositing material directly onto a 3D mould surface and does not require skilled laminators. Biaxial non-crimp fabrics (NCFs) are increasingly popular for their superior in-plane mechanical properties compared to woven fabrics, however NCFs are more difficult to form due to a more complex in-plane shear modulus. A detailed understanding of this behaviour is necessary to avoid defects during forming and to facilitate accurate process modelling.

4.1.3 Initial non-linear shear region

Biaxial NCFs have a non-linear shear modulus that is dependent on the shear angle of the fabric. The modulus for a typical biaxial NCF can be split into 6 regions according to the average shape and magnitude of the shear function, as shown in Figure 4-1. These changes in curve shape are driven by a change in the dominant deformation mode experienced by the fabric. The majority of the curve is shear dominated, however stitch breakage occurs in the positive shear direction above a specific value (dependent on stitch tension) which dominates the adjacent region. This is then overcome by fibre locking as the shear angle reaches extreme values.

There is an initial non-linear region before the shear dominated region that is visibly distinct, but does not have an associated dominant deformation mode. This is highlighted in pink in Figure 4-1.

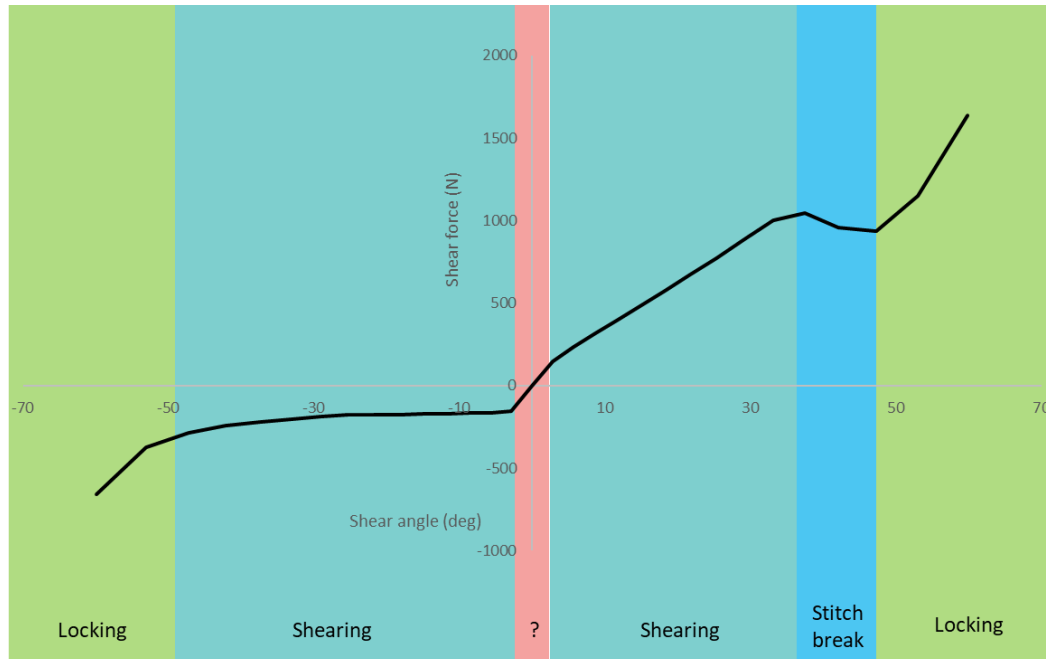


Figure 4-1 NCF shear force versus shear angle curve, with associated dominant deformation modes highlighted.

The presence of an initial non-linear shear region ($0^\circ - 1^\circ$) has been documented for woven fabrics. The cause is due to inter-yarn frictional interactions at each crimp location, which inhibits the full inter-yarn slippage needed for shearing deformation and leads to yarn bending [13]. This region also appears in NCF shear testing [20, 27] and it is proposed that its appearance is due to a similar effect. A significant difference between crimped and non-crimp fabrics is in the calculation of the contact area and normal force at the differently structured yarn crossover points. Yarn slippage is not a function of the contact area for an NCF, as the normal pressure is provided by the stitch rather than a varying crimp geometry (Figure 4-2). If yarn bending is the cause of the initial non-linear shear region then understanding the transition from yarn bending to slippage is important for creating accurate NCF

material models and for a better understanding of meso-scale forming defects that are sensitive to the inter-yarn frictional interactions. This study looks at modelling the yarn and stitch properties to enable accurate prediction of defects based on the magnitude of the initial non-linear shear region.

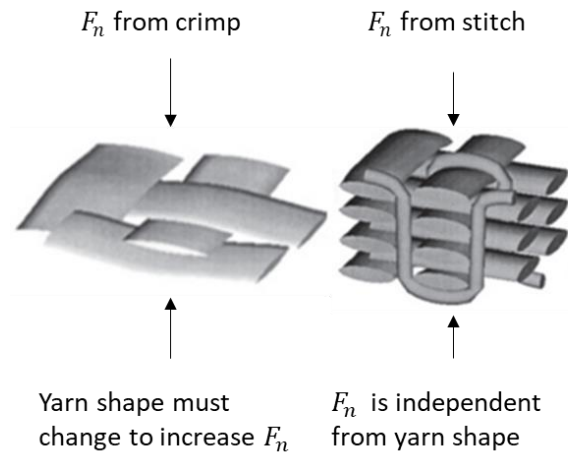


Figure 4-2 Woven and NCF fabric structure diagram [87].

4.1.4 Inter-stitch buckling defect

Inter-stitch yarn buckling appears as an out of plane fibre defect, where the yarn buckles between two stitches. These occurrences can be flattened during forming to have the appearance of in-plane fibre waviness at the mesoscale. Whilst this phenomenon does not lead to more severe out-of-plane wrinkles, this waviness can compromise the in-plane mechanical properties and therefore should be avoided. It is proposed that this waviness is the result of initial frictional interactions between the yarn and the stitch, which can prevent slippage and cause yarn buckling, leading to the initial non-linear region in the shear curve.

4.1.4.1 Fibre misalignment generated by yarn buckling

Small fibre misalignments reduce the post-formed mechanical properties of the component. As an example, a 1° fibre misalignment leads to a 3% relative reduction in the compressive strength [88, 89]. Inter-stitch yarn buckling occurs on formed components wherever there is a compression of the inter-stitch distance. These conditions arise when NCFs experience shear in the negative direction which is determined by the compression (negative) or extension (positive) of the stitch,

(Figure 4-3). Compression of the inter-stitch distance requires the yarn to slide in relation to the stitch, otherwise a compressive force is generated along the yarn. When the yarn is subjected to a large normal force (F_n) it is unable to slide due to the frictional force, f (Equation 4-1) and must deform via buckling to accommodate the strain.

$$f = F_n \mu \quad \text{Equation 4-1}$$

As shown in Figure 4-2, a high local F_n is generated due to high stitch tension. The friction on the primary yarn at the stitch crossover point is too large to allow slippage under the stitch before yarn buckling occurs. This can be seen in the negatively sheared regions of the press formed hemispheres in Figure 4-3.

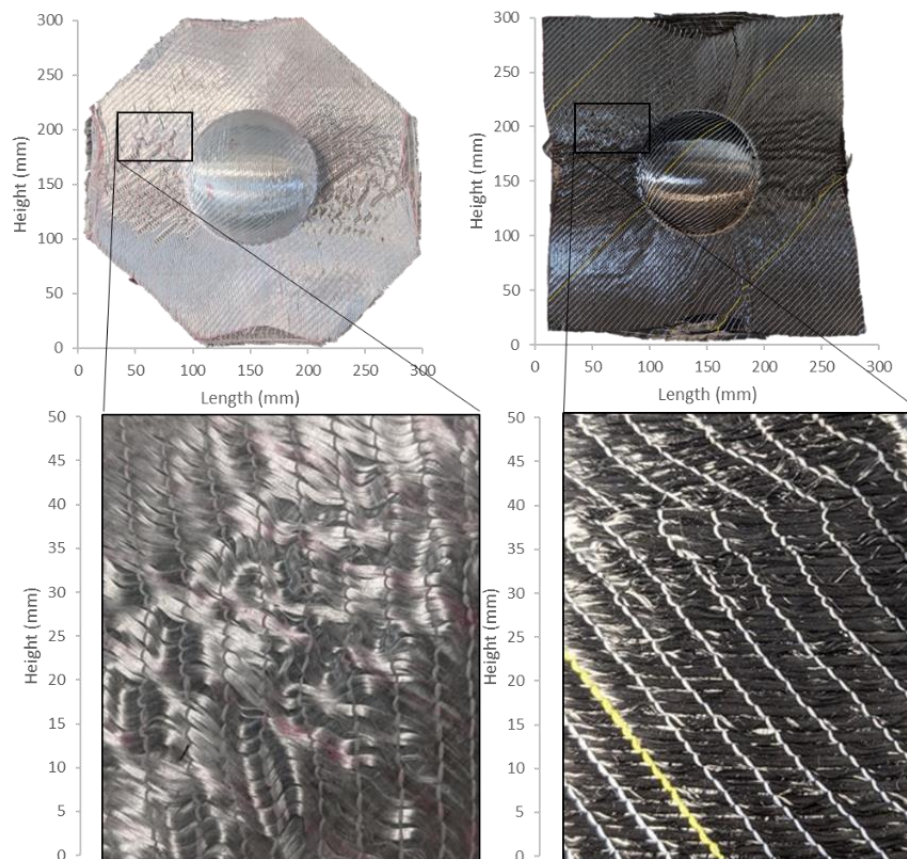


Figure 4-3 Inter-stitch buckling on GFRP and CRFP press formed hemispheres in regions where the inter-stitch distance is being compressed.

4.1.5 Current work

The current investigation determines the cause of the initial non-linear shear modulus region in NCFs and creates an analytical model to predict the size and shape of the region using the yarn bending stiffness and stitch tension parameters. It links the inter-stitch yarn buckling defect to the frictional interaction properties that define the initial non-linear shear region and extends the analytical model to predict the appearance of the defect. The fibre misalignment caused by the inter-stitch yarn buckling defect is quantified and two methods for defect reduction are proposed and investigated. These include selective stitch removal and local lubrication.

4.2 Methodology

4.2.1 Initial non-linear shear behaviour modelling

4.2.1.1 *Rigid intersection deformation mode*

An analytical model describing the deformation of NCFs in the initial non-linear shear region has been created. At the onset of shearing (below $0.2^\circ - 1^\circ$ of applied shear) there is a minimum force required to fully overcome the frictional resistance and initiate slippage of the yarns. The fabric acts as an elastic trellis network, with each stitch point providing a rigid intersection point before any slippage occurs [13]. The strain in the fabric is accommodated by elastic bending of each yarn and rigid rotation at each joint. A unit cell consists of two yarns and a single stitch, as shown in Figure 4-4, with bending moments at the free ends removed due to symmetry, leaving just the shear force acting on the cell. Further assumptions are that each yarn bends as a beam and that the normal force generated by the stitch is independent of the shear angle at low values of θ (shear angle).

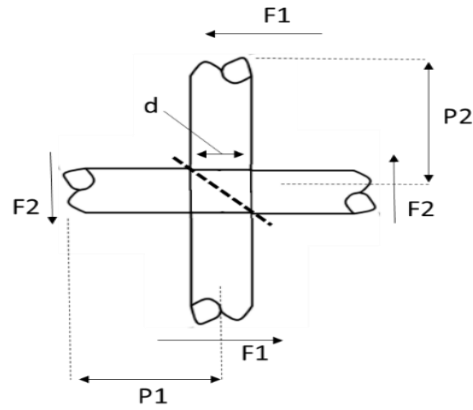


Figure 4-4 Diagram of the stitch at a yarn on yarn crossover point.

The shear force required to achieve a prescribed shear angle is the sum of the forces generated via bending of the two yarn sections (Equation 4-2).

$$\theta = \frac{F_{12}}{12BL} [\text{yarn spacing}] \quad \text{Equation 4-2}$$

$$\theta = \frac{F_{12}}{12BL} \left[\frac{P_1}{P_2} (l_2 - d)^3 + \frac{P_2}{P_1} (l_1 - d)^3 \right] \quad \text{Equation 4-3}$$

where θ is the total shear angle; F_{12} is the total applied shear force; B is the bending stiffness of the yarn; L is the sample width; P_1/P_2 is the yarn spacing; l_1 and l_2 are the yarn lengths.

The lack of crimp means that the contact length d in an NCF is uncoupled from the contact pressure. The contact length is therefore equal to the yarn width and is found from the material properties. The assumptions used in this model simplify the geometry of the yarn and stitch and align with similar analytical models that have been created for woven fabrics [13]:

- Yarns are assumed to be homogenous cylindrical bodies.
- Stitches are assumed to be homogenous cylindrical bodies.

4.2.1.2 *Stitch tension*

Stitch tension was used to calculate the normal force applied at the yarn crossover point, by equating the direct strain in the stitch to the compressive strain in the yarns, as shown in Figure 4-5.

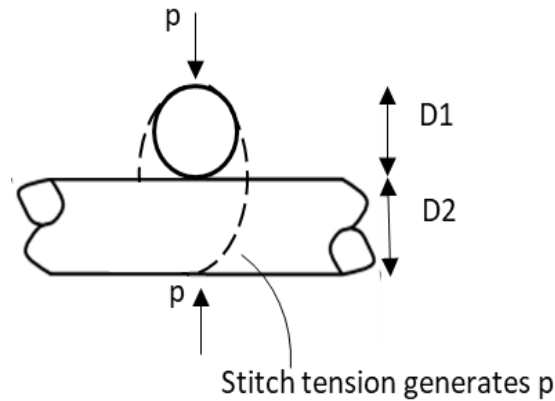


Figure 4-5 Cross section showing a stitch wrapped around two yarns. Yarns compress via rearrangement of the filaments within them.

The compressive strain of two cylinders at inclined angles was determined from the ratio of the two diameters. This was calculated for multiple angled cylinders stacked on top of each other to describe the two yarns and the looped stitch as individual bodies.

$$A + B = \frac{1}{D_1} + \frac{1}{D_2} \quad \text{Equation 4-4}$$

$$(A - B)^2 = \left(\frac{1}{D_1}\right)^2 + \left(\frac{1}{D_2}\right)^2 + \frac{2 \cos 2\theta}{D_1 D_2} \quad \text{Equation 4-5}$$

where the ratio A/B is the ratio of yarn diameters. D is the cylinder diameter and θ is the angle of the crossed stitch. The ratio of stiffness Q is taken from the material properties of the two bodies, for example the compressive modulus E and the Poisson's ratio ν of the yarn.

$$Q = \frac{3}{4} \left[\frac{(1 - \nu_1^2)}{\pi E} + \frac{(1 - \nu_2^2)}{\pi E} \right] \quad \text{Equation 4-6}$$

The general cylindrical compaction equation [90] has been used to find the strain in the joint as a function of the normal pressure P provided by the stitch:

$$\alpha = 2K(PQ)^{2/3} \left(\frac{A}{2 \left(-\frac{1}{e} \frac{dE}{de} \right)} \right)^{1/3} \quad \text{Equation 4-7}$$

where α is the strain in the yarn stack and K and $\left(-\frac{1}{e} \frac{dE}{de} \right)$ are constants determined by the ratio of diameters and are values for the complete elliptical integral and quality respectively [90]. The value for A is taken from the ratio of diameters. The compaction of the yarn stack and the reduction in stitch length has been rearranged to find the normal pressure P applied by the stitch in Equation 4-8. The compaction in the yarn stack was then equated to the reduction in radius of the looped stitch as it tightens:

$$P = 4K(Q)^{2/3} \left(\frac{A}{2 \left(-\frac{1}{e} \frac{dE}{de} \right)} \right)^{2/3} + \left(\frac{9}{2} \right)^{1/3} \frac{(1 - \nu_1^2)^{2/3}}{\pi E} \frac{1}{D_1} \quad \text{Equation 4-8}$$

$$\alpha = \frac{T_s}{2\pi E_s} \quad \text{Equation 4-9}$$

where E_s is the tensile modulus of the stitch and T_s is the tension of the stitch gathered from data sheets. The value for the normal force F_n is calculated from the normal pressure, P (from Equation 4-8) and the compressive strain of the yarns, α (Equation 4-9).

$$F_n = \left(\frac{\alpha}{P}\right)^{\frac{3}{2}} \quad \text{Equation 4-10}$$

From the normal force, the frictional force between the yarns is calculated as:

$$f = \mu F_n \quad \text{Equation 4-11}$$

4.2.1.3 Non-linear slippage

As the shear force increases, the fabric transitions from deforming as a rigid net via bending of the yarns, to deforming through yarn rotation. This is similar to deformation mode found in woven fabrics and the same slippage equation is applied [13] with the new definitions for contact area d and normal force F_n . Slippage occurs first at the outer boundary of the contact area and migrates inwards. As the fabric is sheared, a bending moment is created on the yarn at each stitch point, due to the applied load and frictional forces. This is distributed linearly from the end of the slipped region (a) to the edge of the contact region (b) creating the region ($a-b$) [13]. The frictional moment at $a-b$ is equated to the moment that would be seen at point a if there were no resistance, and from that the frictional moment M has been calculated. a is the distance from the slipped boundary to the edge of the contact length d . μ is the coefficient of friction and F_n is the applied normal force from Equation 4-10. The external moment is an average of the two possible values:

$$M = \frac{1}{2}(M_1 + M_2) \quad \text{Equation 4-12}$$

$$= \frac{F_n}{4L} \left\{ P_2 \left[l_1 - d \left(1 - \frac{a}{d} \right) \right] + P_1 \left[l_2 - d \left(1 - \frac{a}{d} \right) \right] \right\}$$

From the bending moments, the shear force and shear angle were calculated as a function of the amount of slippage that occurred at the joint given by the parameter a/d , which takes a value between 0 and 1.

$$\theta = \frac{F_n}{12BL} \left\{ \frac{P_1}{P_2} \left[l_2 - d \left(1 - \frac{a}{d} \right) \right]^3 + \frac{P_2}{P_1} \left[l_1 - d \left(1 - \frac{a}{d} \right) \right]^3 \right\} \quad \text{Equation 4-13}$$

As the shear angle θ increases, a/d increases from 0 to 1. At $a/d = 1$, the deformation of the fabric is entirely due to fibre slippage, enabling the yarns to rotate at the cross-

over points. The shape of the initial non-linear shear region is predicted from the yarn material properties by changing the parameter a/d .

4.2.1.4 Inter-stitch yarn buckling model

The yarn never experiences free slippage under the stitch at high stitch tension values, therefore in compression (negative shear) the yarn acts as a constrained pillar that can be modelled using the Euler buckling formula [91]. The boundaries are fixed at each end by the stitch and the buckling stiffness E_b of the yarn is equivalent to the bending stiffness of a yarn of length L . The critical buckling force F_{cr} has been calculated according to Euler's theory of column buckling.

$$F_{cr} = \frac{\pi^2 E_b I}{L^2} \quad \text{Equation 4-14}$$

Equating the critical buckling load to the frictional resistance enables the transition point from yarn buckling to yarn slippage to be determined. This has been rearranged to indicate the critical stitch tension value in the biaxial NCF, $T_{s-critical}$.

$$\mu \left(\frac{T_s}{P} \right)^{\frac{3}{2}} = \frac{\pi^2 E_b I}{L^2} \quad \text{Equation 4-15}$$

$$T_{s-critical} = \frac{2\pi E_b (F_{cr})^{\frac{2}{3}}}{P} \quad \text{Equation 4-16}$$

4.2.2 Yarn buckling defect measurement

4.2.2.1 Identification of yarn buckling

As observed at high shear angles, inter-stitch yarn buckling is linked to the initial non-linear shear region frictional effects. A stiff initial non-linear shear region creates areas where yarns are unable to slip in relation to the stitch during shearing and inter-stitch buckling occurs. A modified picture frame test methodology has been used to identify slippage of the yarns in relation to the stitch. A picture frame sample was coated in dry chalk powder to avoid any reflections and then installed into the frame. A video gauge with a 1080p telocentric lens was positioned perpendicular to the sample and set to take images every 1 second. The test was set to extend to 75mm at 1mm/minute, giving a final shear angle of 60 degrees. 450 images were taken over the 7.5 minute time period, giving an image every 0.13 degrees. As the yarns slide,

uncoated segments of the yarn were revealed which were previously covered by the stitch. By measuring the distance between the uncoated bands on the yarn and the stitch lines, the yarn slippage was calculated. This was conducted in 3 regions through the middle of the picture frame test for 3 repeats from which the mean fibre angle standard deviation was taken.



Figure 4-6 Yarn slippage video gauge measurement (Keyence CV-X Series) setup for in-plane shear testing

4.2.2.2 In-plane testing

In-plane shear testing was used to measure the level of fibre misalignment at different values of shear angle. Due to the pure shear state of the test any deviation measured is a measurement of effect of the inter-yarn buckling defect on the fibre misalignment. These results were then used as a baseline and compared to similar tests carried out with resin lubricated and stitch removed samples.

The picture frame test was used for all in-plane fabric shear testing rather than the bias extension test, as the picture frame gives more accurate full field shear angle data. The methodology used is found in Appendix (D). Four dry NCF fabrics were experimentally tested with two pillar stitched materials (FCIM359 and FCIM 789 in

Table 4-1) being used for modelling purposes alongside a tricot and half pillar stitched fabric of similar areal weight.

Table 4-1 Properties for initial non-linear shear region model: FCIM359, FCIM789. Collected from data sheets and supplier exchange.

NAME	STITCH TENSION (CN)	STITCH SPACING (MM)	YARN SPACING (MM)	YARN WIDTH (MM)	YARN LENGTH (MM)
FCIM359	8.5	1.7	1.7	1.7	5.5
FCIM739	10.0	1.62	1.62	1.62	5.0

Full field shear angle distribution data was collected from picture frame tests using the optical scanning methodology from Appendix A laser line scanner was used to collect topology data with a resolution of >1mm per point, followed by a series of high resolution low reflectivity images. A texture based segmentation algorithm was used to measure the greyscale in each image with the texture energy measured via Laws filter masks [92]. The discontinuity was measured against the surrounding region and a threshold was set to binarise the image before the fibre orientation was calculated from the edge vectors. Any measurable deviation across the fabric from the initial state was determined to be fibre misalignment, as the centre of the sample was in a state of pure shear within the picture frame.

4.2.2.3 Hemisphere forming

Hemisphere punch forming was used to highlight the fibre misalignment caused by inter-stitch buckling on a formed component. It was also used to demonstrate the effectiveness of resin lubrication and localised stitch removal as defect reduction strategies. The tool consisted of a 50mm radius hemisphere punch that pressed into a cavity with a 5mm edge fillet. A 300mm by 300mm square blank was placed over the cavity and constrained by a blank holder that provided 0.15bar bar of initial pressure. The tool and blank holder surfaces were tool steel and the relative coefficient of friction between the tool and part was 0.23 [14]. For NCF testing 2 layers of biaxial NCF were placed on-top of one other with aligned fibre direction.

4.2.3 Defect reduction strategies

A number of yarn buckling defect reduction strategies are outlined and fall into two categories. Strategies based around localised stitch removal and those based around yarn lubrication.

4.2.3.1 Resin lubrication

The objective of resin lubrication was to reduce the frictional coefficient between yarns to reduce the frictional resistance to rotation and slippage as explained in Equation 4-11. Lubrication was applied by applying 20g/sqm of epoxy binder to the surface of the fabric before deformation. The sample was then heated to 120°C which melted the binder and coated the yarns in the liquefied resin. This methodology was chosen over application of a resin lubricant so that during forming the amount of lubricant between the ply and the tool surface was minimised. In this way, the impact of resin lubrication on defect generation can be attributed to the reduction in inter-yarn friction coefficient and not to the reduce ply-tool frictional coefficient. The binder was then also free to stabilise the fabric without interference from excess uncured resin. The resin component introduced into the preform may impact infusion or curing. This could be mitigated through tight control of the binder application and further study into optimising binder levels to generate the required lubrication but minimise unwanted pre-infusion. An alternative for reducing the resin component is the use of localised spreading of the resin powder in regions where yarn buckling is expected (similar to the localised stitch removal).

4.2.3.2 Stitch removal

The objective of stitch removal was to reduce the number of stitch-yarn interactions and increase the length of the inter-stitch yarn sections. This reduces the overall number of stitch points which the yarn has to slip at, reducing the force needed. Local-stitch removal was conducted by using a soldering iron to melt the polymer stitch around the perimeter of the desired region. The entire stitch was then removed within the region by pulling on the free end and unravelling the stitch. This caused very little degradation of the yarns and allowed for large sections of stitch to be removed quickly.

4.3 Results

4.3.1 Yarn slippage during shearing

The movement of the yarns was measured to show the appearance of slippage between the yarns and the stitches as the fabric shears. The objective was to measure the yarn slippage at each stitch point and show movement as a proportion of the yarn length. Figure 4-7 shows the level of slippage at 4 different shear angles for the FCIM739 fabric. The slippage length has been measured by photographing shared samples and using computer measurement as per the methodology. The results are shown in Table 4-2.

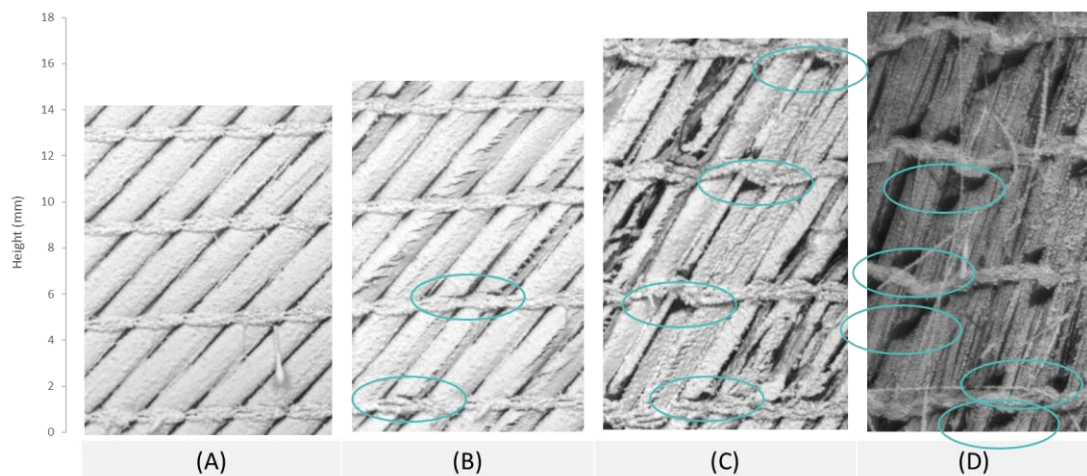


Figure 4-7 Yarn slippage in relation to the stitches at different shear angles. (A) 0 degrees, (B) 8 degrees, (C)29 degrees, (D) 53 degrees

Table 4-2 Mean yarn slippage calculated at increasing levels of shear for the angles shown in for Figure 4-7. (A) 0 degrees, (B) 8 degrees, (C)29 degrees, (D) 53 degrees

Sample	A	B	C	D
Shear angle (degrees)	0	8	29	53
Average slippage length (mm)	0	0.05	0.7	1.5
Number of stitch points with yarn slippage	0	2	10	15

The number of yarn slippage is clear from Figure 4-7 by the appearance of dark uncoated regions that gradually increase in size from Figure 4-7 (B) to Figure 4-7(D). It relates to the movement of yarns in relation to the stitch that are not just pin jointed rotation. Slippage appears to occur along the length of ~50% of yarns in Figure 4-7(C), with a randomised distribution of slipped and un-slipped yarns. The observed slippage increases to 75% of the yarns measured by Figure 4-7(D). Table 4-2 shows the number of stitch points with slipped yarns and the length of slippage at increasing levels of shear. There is a 40% increase in the number of stitch points with slipped yarns between 8 and 29 degrees and a further 25% increase in the following 20 degrees of shearing. The length of the slipped yarn also increases linearly as shear angle increases. The slippage exceeds 25% of the inter-stitch yarn length at shear values above 50 degrees.

4.3.2 Verification of initial non-linear shear behaviour

4.3.2.1 *Varied stitch architecture response*

Four individual NCFs have been sheared from -1 degree to 1 degree and the response has been compared in Figure 4-8. The objective was to identify the appearance of an initial non-linear shear region in NCFs with different stitch architectures. The two fabrics from Table 4-1 have been tested alongside a half pillar and tricot stitched fabric of similar areal weight.

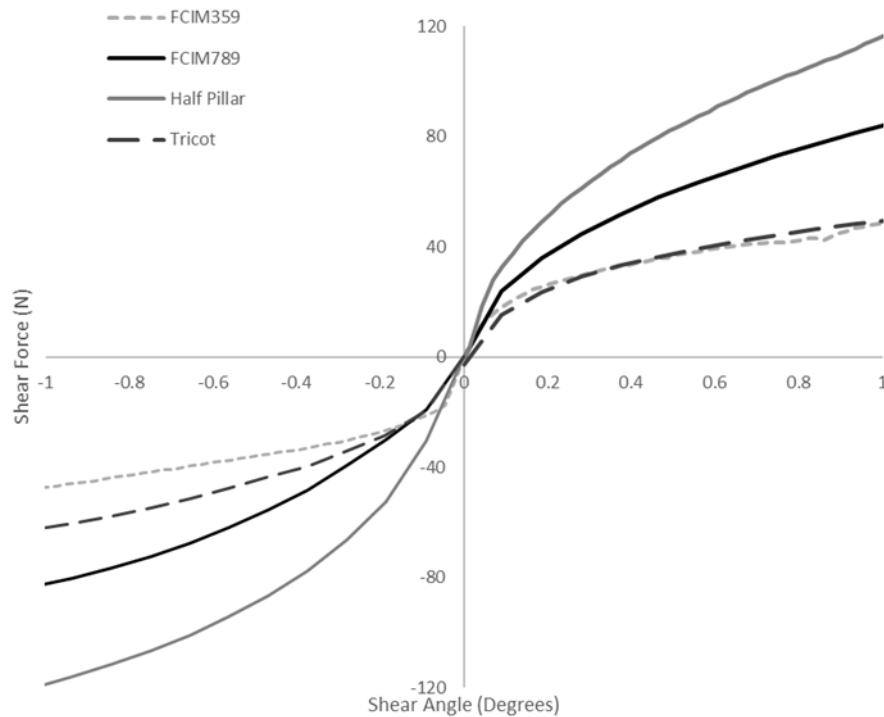


Figure 4-8 Initial non-linear shear region for different NCFs with varied stitch architecture. (3 repeats conducted on each sample, with error removed for clarity)

Each fabric shows a distinct initial non-linear shear region between -1 degree and 1 degree. The gradient of the curve is highest through the origin and degrees as the amount of positive or negative shear increases. The phenomenon is similar to that observed for woven fabrics, which is reportedly due to the frictional interactions at the fibre crossovers [13]. This suggests that similar static frictional effects are also present in NCFs despite a lack of crimp, which are caused due to the normal forces generated on the yarns rather than the yarn geometry.

Each of the different stitch architectures produces an initial non-linear shear region. The positive and negative regions of each fabric are symmetrical about the origin, indicating that the deformation mode generating the initial non-linear shear region is the same for both shear directions. The magnitude of the non-linear shear region varies for the different stitch architectures. If static frictional effects are responsible then this will be driven by the difference in normal force used to contain the yarns in each of the architectures. The relationship between stitch tension and the magnitude

of the initial nonlinear shear region is further investigate during the modelling of the phenomenon.

4.3.2.2 *Varied initial shear angle response*

The initial results point yarnards the initial non-linear shear region being driven by static friction effects. If this is the case then the region will occur irrespective of the fabric's initial shear angle. However, since the stitch tension is integral to the normal force applied to the yarns, the relative orientation of the primary yarns will affect the magnitude of the stitch tension as the stitch extension changes during shearing. This should produce an increasingly large initial non-linear shear region as initial shear angle increases.

The shear response of FCIM789 has been measured using the picture frame methodology. To observe the initial non-linear shear region the frame was stopped and restarted periodically at increasing shear angles. This is a controlled method to represent a static, initially sheared fabric being sheared further. The test was conducted on 5 samples with the average force/shear angle results given in Figure 4-9. The force response and shear angles have been normalised by removing the initial shear angle value from the data for each test. This allows for comparison between the shape and size of the initial non-linear shear regions for fabrics sheared from different points of initial shear. It can be seen in Figure 4-9 that the amplitude of the initial non-linear shear region increases as the initial shear angle increases. The amplitude after 1 degree of shearing increases linearly by 1.5% for every degree of initial shear angle. This is explained by the tightening of the stitch at higher shear angles, causing the normal force experienced on the yarns to increase, thus increasing the inter yarn frictional resistance [93].

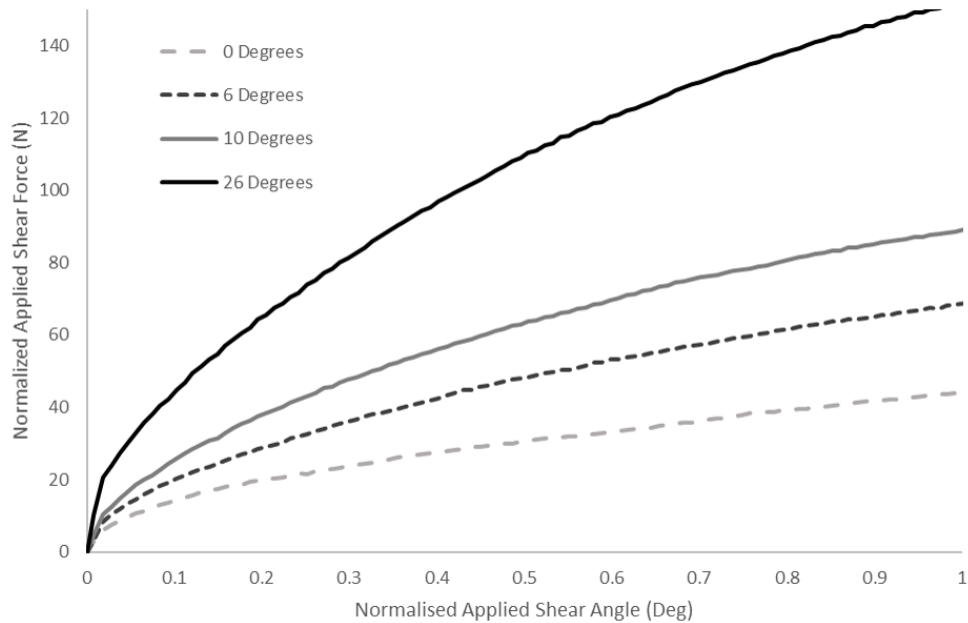


Figure 4-9 Comparison of the normalised shear for shear angle response for the initial non-linear shear region of FCIM789 at 0,6,10 and 20 degrees of applied initial shear angle.

The tests conducted show a distinct initial non-linear shear region found in NCFs below 1 degree of shearing. 1 degree was chosen to ensure that the entire non-linear shear zone was captured for all samples. The increasing size of the region at increasing initial shear angle supports the theory that the region is driven by static frictional effects. The data presented in Figure 4-9 shows that forming a fabric previously sheared to 10 degrees will require 100% more force than an un-sheared fabric for the first 1 degree. At 26 degrees of initial shear the fabric requires 350% more force to reach 1 degree. This increase forming force requirement is present at all levels of shear due to the static frictional effect, not just at high levels of shear due as has previously been stated in the literature (due to the locking angle being reached [94]). During forming this effect could be relevant if multiple forming operations are occurring on a component, as secondary and tertiary forming operations will require more force than the initial operation, which could cause bridging or wrinkling defects.

4.3.3 Initial non-linear shear region model

The Initial non-linear shear region model was created to meet two aims. The first was to further solidify that the non-linear shear region in being caused by static frictional

effects by predicting the shape without using shear test data. The second was to predict the appearance of the inter-stitch buckling defect based off of the static frictional properties of the fabric.

4.3.3.1 Model validation

The analytical model used to determine the initial non-linear shear properties of each fabric has been validated against experimental picture frame data for the pillar stitched materials in Figure 4-10. The materials tested are FCIM359 and FCIM789 (Table 4-1). 5 repeats conducted on each sample, with error removed for clarity. Results in Figure 4-10 extend over the range of a/d , which covers the extent of the initial non-linear region for these materials (0.2°). After this point, full slippage occurs between the yarns and shear becomes the dominant deformation mode. The model predicts an initial non-linear shear region of 0.19 degrees for FCIM359 and 0.2 for FCIM789 which is within 5% of the region end observed from experimental testing. The analytical model gives rotationally symmetrical results about the origin which aligns with the symmetrical profile of the shear curve at very low shear angles. The model predicts the initial non-linear shear region very closely for both materials when compared to picture frame experiments. FCIM359 material (a) has an R^2 value of 0.985 and a maximum deviation of 5N. FCIM789 material (b) has an R^2 value of 0.989 and a maximum deviation of 3N.

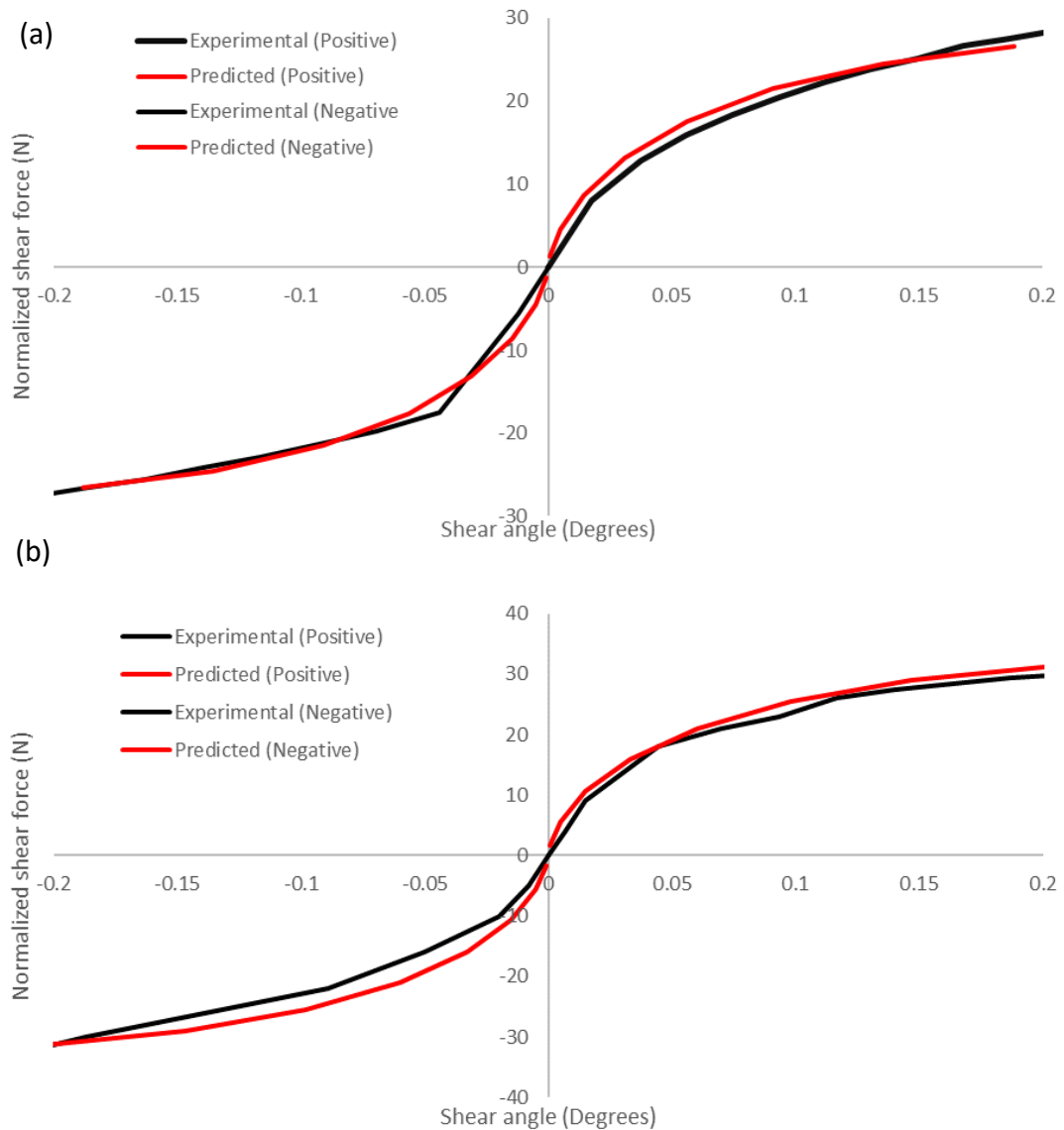


Figure 4-10 Comparison of predicted results from the analytical initial non-linear shear region model (described by Equation 4-17) and experimental values from low shear picture frame testing for: FCIM359 (a) FCIM789 (b).

4.3.4 Defect reduction strategies from the initial non-linear shear region model

The sensitivity of select variables has been measured for the initial non-linear shear model. This was conducted by varying the values by $\pm 25\%$ around a baseline (Set for FCIM359) and measuring the amplitude and shape change in the region. The aim was to identify variables around which buckling defect reduction strategies could be targeted.

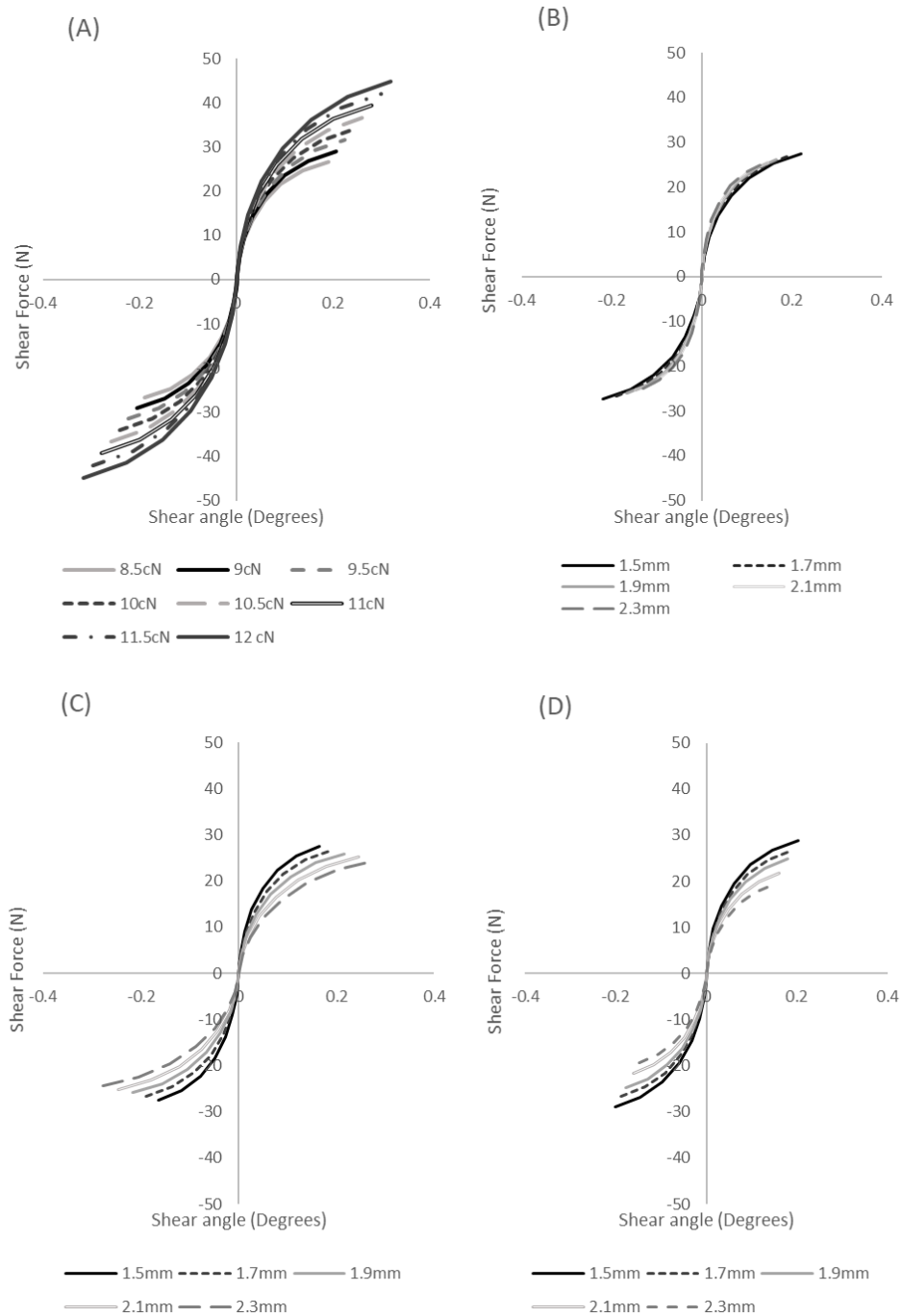


Figure 4-11 Output from Initial non-linear shear region model based on static friction effects. A sensitivity study. Each graph plots a/d from 0 to 0.9, with a unique variable. (A): Stitch tension. (B): Yarn spacing. (C): Yarn length. (D): yarn width.

The most sensitive variable was the stitch tension. Increasing this value by from 8.5cN to 12.5cN (40% increase), increased the amplitude of the initial non-linear shear zone

by 80%. This is due to the stitch tension determining the inter yarn normal force which directly impacts the static frictional effects. This variable is controllable by directly reducing the stitch tension during manufacture of the fabric. An indirect method of controlling the static frictional forces to the after fabric manufacture is to reduce the coefficient of friction between the yarns via lubrication. Alterations to the yarn width and yarn length impacted the amplitude of the region too. An increase to yarn length of 50%, reduced the force requirement by 25% and an increase in yarn width of 50% increased the force requirement by 60%. The yarn width is not controllable after the fabric is manufactured. However the effective yarn length can be changed by using stitch removal to elongate the distance between stitched points. Lubrication and stitch removal are good candidates for inter-stitch buckling defect reduction strategies, based on the results of the model.

4.3.5 Inter-stitch buckling model

The properties from Table 4-1 have been used to calculate the critical buckling force for FCIM789. The frictional resistance and critical buckling force have been plotted over a $\pm 5\text{cN}$ range around the mean stitch tension value to account for variability (Figure 4-12). At the mean stitch tension for FCIM789 of 8.5 cN, assuming an inter-yarn frictional coefficient of 0.28 [95], the critical buckling force is 19.58 cN and the frictional resistance at the stitch point is 38.2 cN. The force needed to buckle the yarn is therefore lower than the frictional force so the fabric is likely to experience yarn buckling.

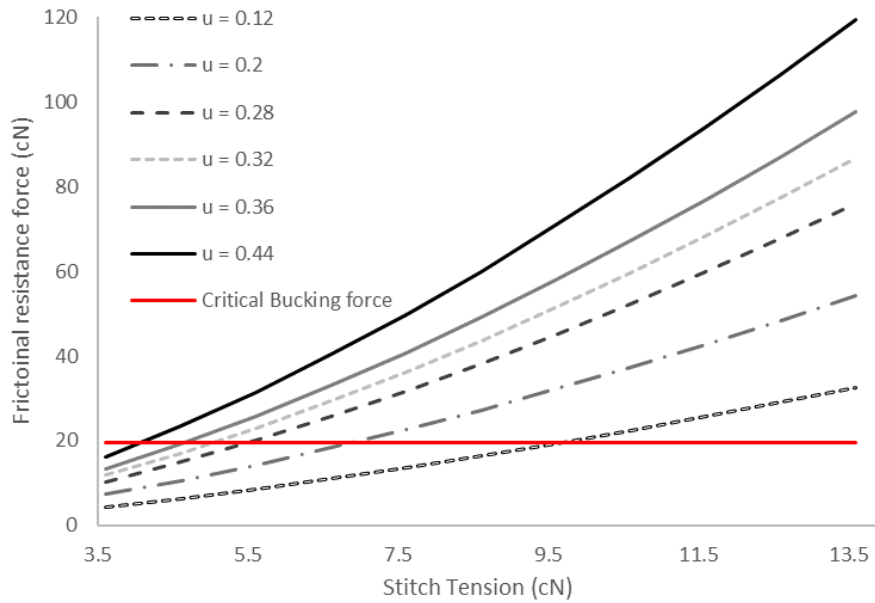


Figure 4-12 Output from theoretical model. Change in resistance force as stitch tension is increased at varied friction coefficient levels.

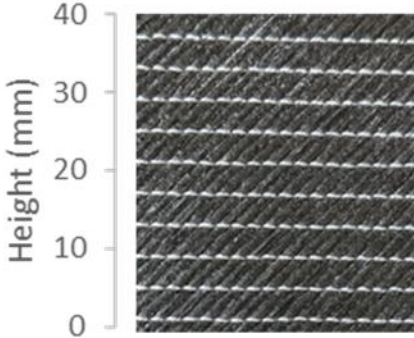
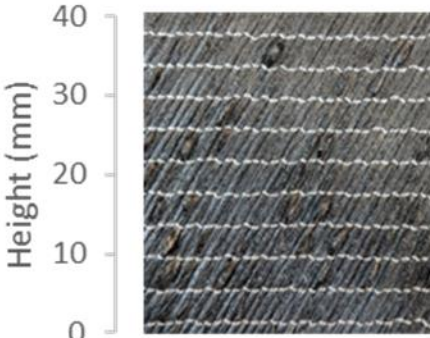
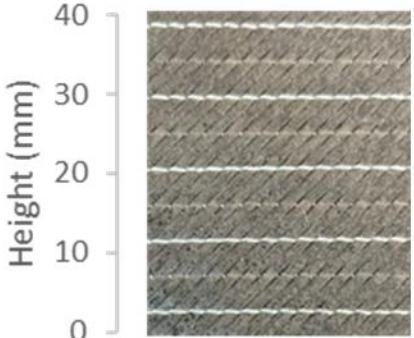
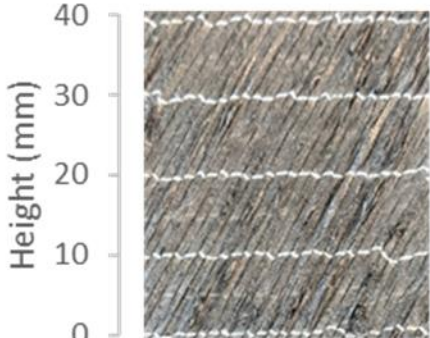
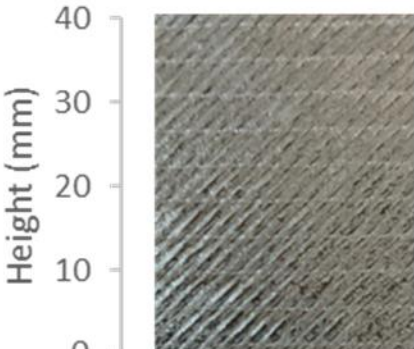
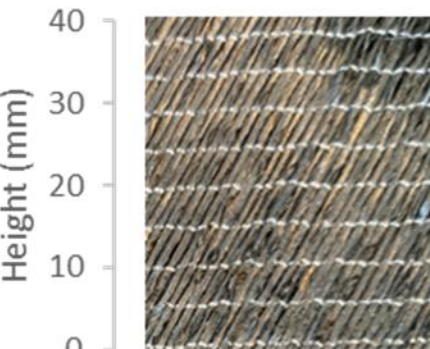
Lubrication was proposed as a method for removing the buckling defect. The literature shows a significant drop in coefficient of friction from 0.25 - 0.48 to 0.1 - 0.28 for lubricated yarns [96]. The current analytical model assumes a value of 0.28 for the frictional coefficient μ , however a range of coefficients have been modelled in Figure 4-12. to show the impact of μ on slippage behaviour. Theoretical predictions show that varying the frictional coefficient is a viable method for reducing the frictional resistance below the critical buckling force. At a mean stitch tension of 8.5cN (for FCIM789) a coefficient of 0.16 would be needed to bring the frictional resistance force below the critical buckling point. This would prevent fibre buckling and improve the quality of the preform during a forming operation.

4.3.6 Inter-stitch yarn buckling defect reduction

Two defect reduction strategies have been proposed to combat the inter-stitch buckling defect. Stitch removal reduced the number of stitch-yarn interactions (results from the yarn slippage test). Yarn lubrication reduces the static frictional effect (results from inter-stitch buckling model).

4.3.6.1 In-plane testing

Table 4-3 : Comparison of inter-stitch buckling on FCIM789 at 0° and 30° of shearing in a picture frame: (Top row) baseline sample with evident yarn buckling, (Middle row) Every 2nd stitch removed (Bottom row) Resin lubricated.

	$\theta = 0^\circ$	$\theta = 30^\circ$
Baseline Sample	<p>Standard deviation = 0.2°</p> 	<p>Standard deviation = 3°</p> 
Every 2nd stitch removed	<p>Standard deviation = 0.2°</p> 	<p>Standard deviation = 0.55°</p> 
Resin lubricated	<p>Standard deviation = 0.2°</p> 	<p>Standard deviation = 0.48°</p> 

Inter-stitch yarn buckling occurs when the critical buckling point is exceeded by a yarn that is constrained at each end by two rows of contracting stitches. The buckling has been measured in terms of fibre misalignment, using optical scanning methodology on a set of in-plane shear tests. The standard deviation in fibre angle was used as the measure for fibre misalignment. The mean was calculated over an area of 30mm x 40mm as shown in Table 4-3. The 6 images show the visual state of a single sample before and after shearing is applied.

A larger number of buckled yarns and a larger buckling amplitude, results in a larger level of fibre misalignment and higher standard deviation. Table 4-3 shows the fibre misalignment captured in the fabric in an un-sheared state and at -30 degrees of shear. The baseline sample has a standard deviation of 0.2° which rises by 2.8° at 30° of shear. This is due to the appearance of 11 inter-stitch (out of plane) yarn buckling defects (over 1mm) and 7 in-plane yarn buckling defects, which involves 14% of the inter-stitch yarn points in the area of interest. The sample with localised stitch removal eliminated all of the out-of-plane defects, but in-plane defects affected 4.5% of the measured inter-stitch yarn points. The resin lubricated sample showed no indication of noticeable in-plane or out-of-plane inter-stitch yarn buckling defects. However, the optical scanning method did highlight a slight increase in the standard deviation of the samples, indicating that a small amount of misalignment was still occurring.

4.3.6.1.1 Localised stitch removal

The objective of localised stitch removal was to remove the number of yarn-stitch interaction points and reduce the overall amount of frictional resistance in the fabric. Methods for changing the influence of stitches on existing fabrics have been tested in the literature [14] showing the effect of selective stitch removal on the shear characteristic of the fabric. The optical scanning methodology was used to measure samples that were sheared to 30° with measurements taken every 5° . Two different stitch removal patterns were tested: one with every 2nd stitch row removed and one with every 3rd stitch removed. This has been compared to a baseline sample in

Figure 4-13. Removing every 2nd stitch or every 3rd stitch provides an 80% and 83% reduction in the standard deviation for a shear angle of 30°. The reduced number of crossover points for samples where the stitches have been removed gives 1/2 or 1/3 of the potential slippage points about which buckling may occur. The enlarged length in between stitches increases the radius of the bent yarn, further reducing the misaligned component of the yarn. Localised stitch removal is an effective defect reduction method for inter-stitch yarn buckling during in-plane testing with the reduction in misalignment highlighted in

Figure 4-13.

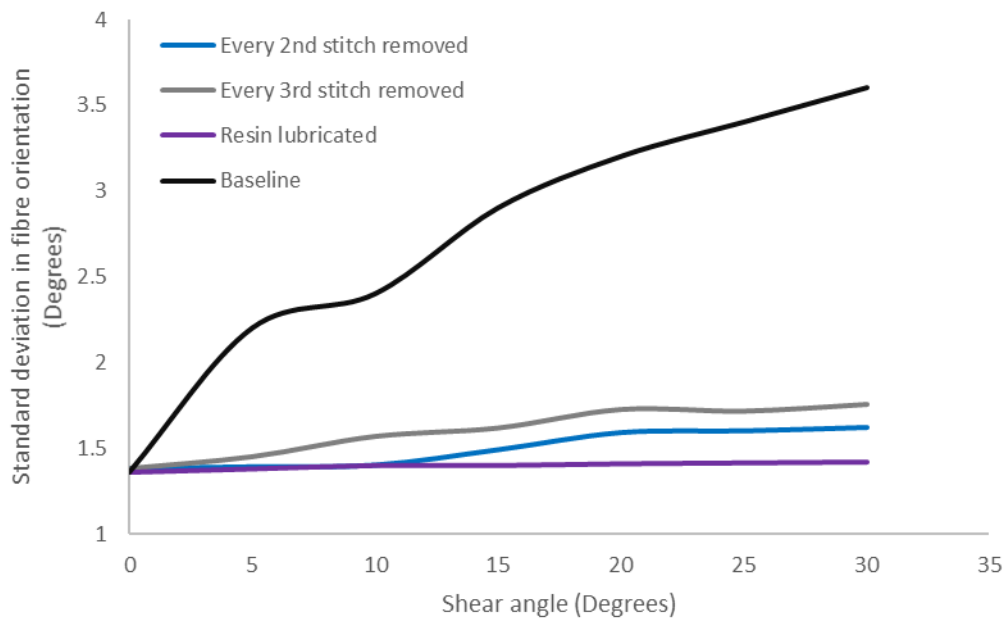


Figure 4-13 Comparison of shear angle standard deviation at increasing levels of shear angle.

4.3.6.1.2 3.5 Resin lubrication

The application of resin lubrication aimed to reduce the inter-yarn frictional coefficient, in order to reduce the frictional force below the critical buckling force, as shown for the theoretical model in Figure 4-12. The effect of lubrication on the shear modulus (gradient of the curve) is shown in Figure 4-14 with 3 repeated picture frame tests generating the data. The initial non-linear region of the dry fabric extends to 0.2 degrees at a shear force of 15N, at which point the stiffness then stabilised to a gradient that continued through the shear deformation dominated region. The

lubricated fabric show a 50% reduction in the size of the initial non-linear region, extending to a shear angle of 0.1 degrees and a maximum shear force of 5N. The reduction in the magnitude of the initial region demonstrates that the modulus of the fabric is responsive to changes in frictional effects as predicted by the buckling model. Resin lubrication is also an effective defect reduction method for inter-stitch yarn buckling during in-plane testing.

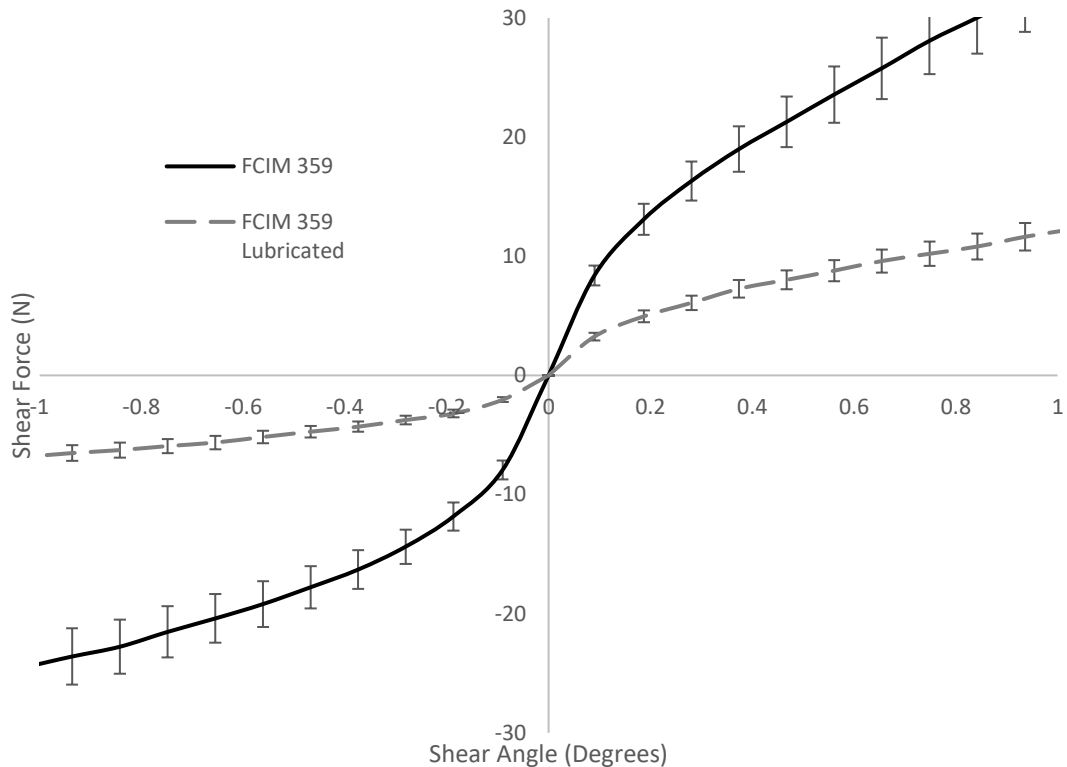


Figure 4-14 comparison of the shear response of lubricated and unlubricated NCF FCIM359 up to 1 degree of shearing.

Lubrication provides a similar level of defect reduction to stitch removal as shown in Figure 4-13. The standard deviation remains constant up to 30° in the lubricated sample and does not follow the characteristic increase at 20° that is found in the baseline sample. This aligns with visual observations of the sample shown in Table 4-3 indicating that the buckling defect that is present in the dry sample has been greatly reduced at 30 degrees, with stitch removal and entirely removed in the lubricated sample. Further assessment of both defect reduction methodologies has been continued on formed components.

4.3.6.2 Formed hemisphere

Hemispheres have been punch-formed out of FCIM789 NCF plies. The resin lubrication and localised stitch removal defect reduction strategies have been compared to a baseline hemisphere to measure the effect of the two strategies on a formed component.

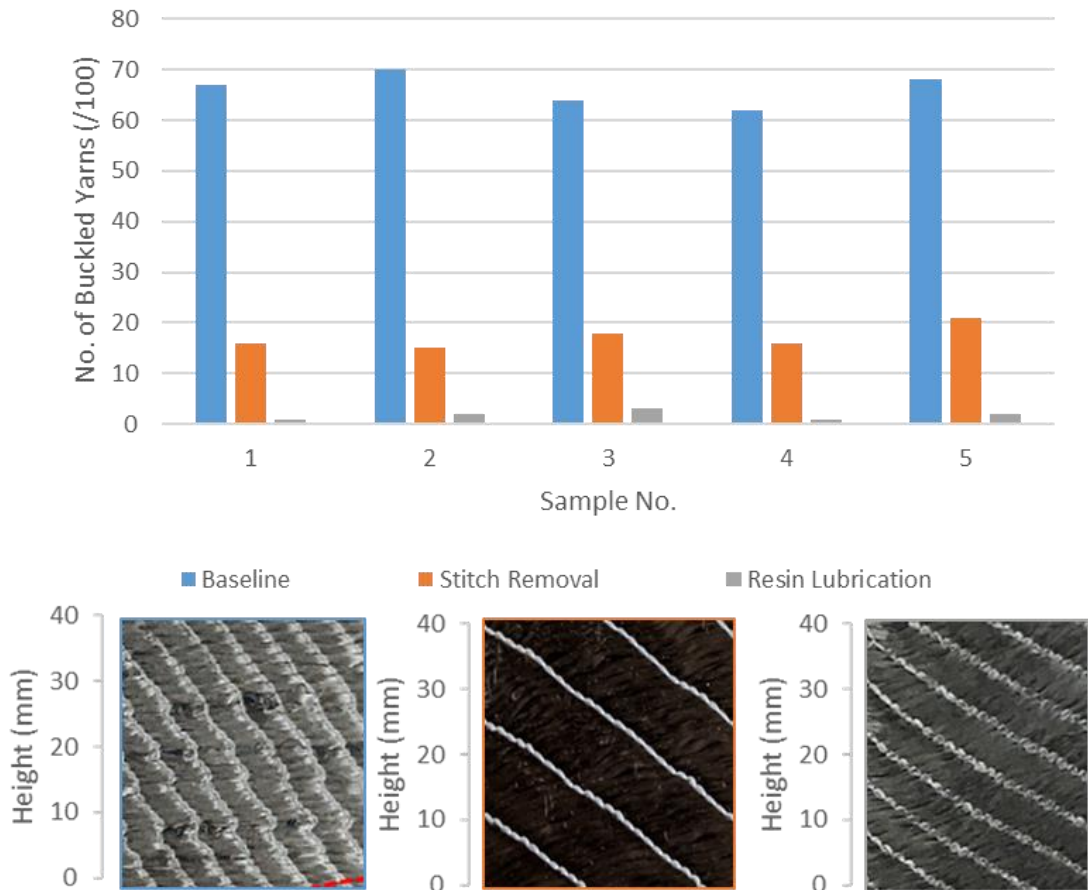


Figure 4-15 Comparison of the number of buckled yarns in the upper left quadrant of a hemisphere measured using the optical measurement methodology. A baseline result has been compared a resin lubricated sample and a sample with stitches removed. A 40mm section from the upper quadrant has been presented to visualise the defects in each hemisphere. Full images found in: Figure 4-16, Figure 4-18 and Figure 4-19

The region containing the highest number of buckling defects was typically the upper right or lower left quadrants (Figure 4-16), which have been used to analyse the success of the defect removal strategies (Figure 4-15). This has been defined from the centre of the hemisphere as the first 100 yarns in the flat region surrounding the

dome after it is symmetrically split into quarters. Comparisons have been drawn between the defects seen in that region for the different strategies. The number of fibres that have buckled out of plane has been used to measure severity of the effect. This was chosen as fibre angle standard deviation can only be used on samples that are entirely in a pure shear state. This is due to other deviation in the fibre path, (such as bending over 3D geometries) being indistinguishable when calculating the deviation.

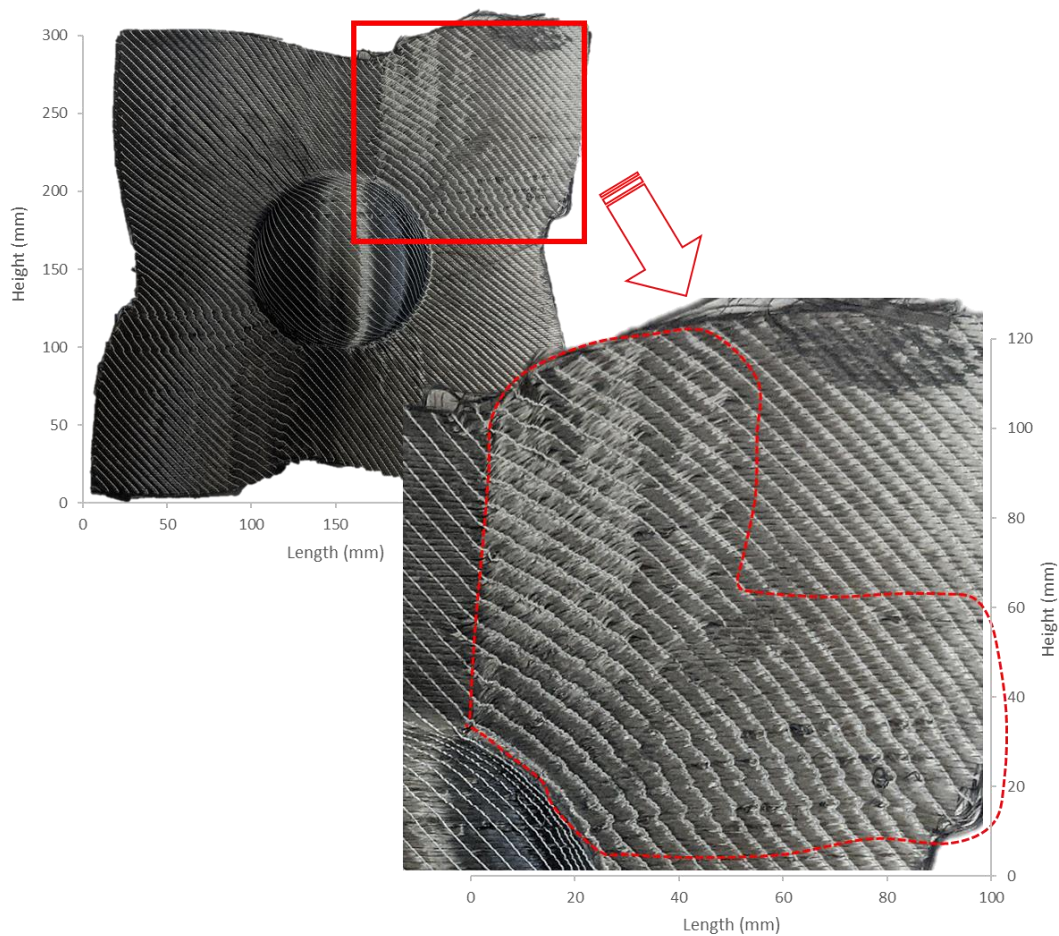


Figure 4-16 Baseline punch formed hemisphere, observations of inter-stitch buckling defect

The selected defect region coincides with a region of high negative shear, as seen in Figure 4-16, highlighting contracted stitches and yarn reorientation (away from the initial yarn direction indicated by the XY axis). The measured region contains 100 yarns and 30 stitch paths running at 45° to the primary yarns. Within the measured

region 67 inter-stitch sections of the yarn experienced buckling defects larger than 1mm in amplitude as measured using the optical imaging methodology.

4.3.6.2.1 Stitch removal

To identify appropriate stitch removal regions, the baseline hemisphere was scanned using the optical scanning methodology and areas that experienced yarn buckling were highlighted. The size and position of the defect pattern was measured and the areas containing the defect zones were transferred onto a flat blank as shown in Figure 4-17. A one in every two ($1/2$) localised stitch removal pattern was chosen over a one in every three ($1/3$) as in-plane testing showed that it was marginally better in terms of reducing fibre misalignment ($1/2$ generated a 0.1° reduction compared to $1/3$) Figure 4-17.

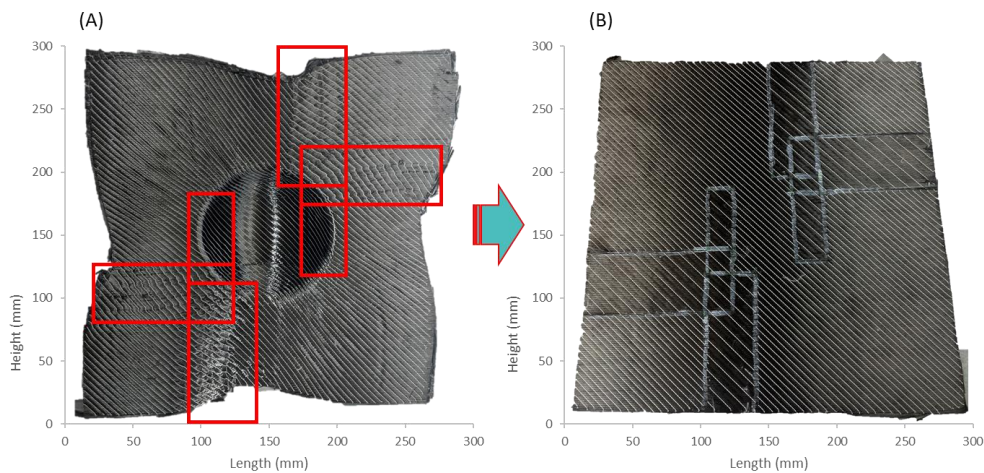


Figure 4-17 Location of stitch removal areas on punch formed hemisphere (A) defect locations on formed hemisphere. (B) Stitch removal on flat blank

Measurements were taken from the flat region surrounding the hemisphere shown in Figure 4-18 that matches the defect region shown in Figure 4-16 on the baseline hemisphere. There was a 74% reduction in the number of yarn buckling defects in the hemisphere when the stitch removal defect reduction strategy was applied. The defect reduction level was equivalent to that found during the in-plane testing in Table 4-3. The improved quality to the preform validates the effectiveness of stitch removal for eliminating inter-stitch yarn buckling from formed components, with the

broader effects discussed. Selectively removing stitches changes the boundary conditions applied to the primary yarns around that local region. This is one of the effects predicted by the inter-stitch buckling model. The number of stitch yarn interactions is a sensitive variable and a reduction in that number, generates a reduction in the size of the initial non-linear shear region (Loose stitches present the possibility of foreign object debris (FOD) during resin infusion, as a small section of stitches may be swept out of the fibres under high pressure. Localised stitch removal is a slow process, however there is the possibility of automation during kit cutting procedures with the use of a specialised gantry head or arm.

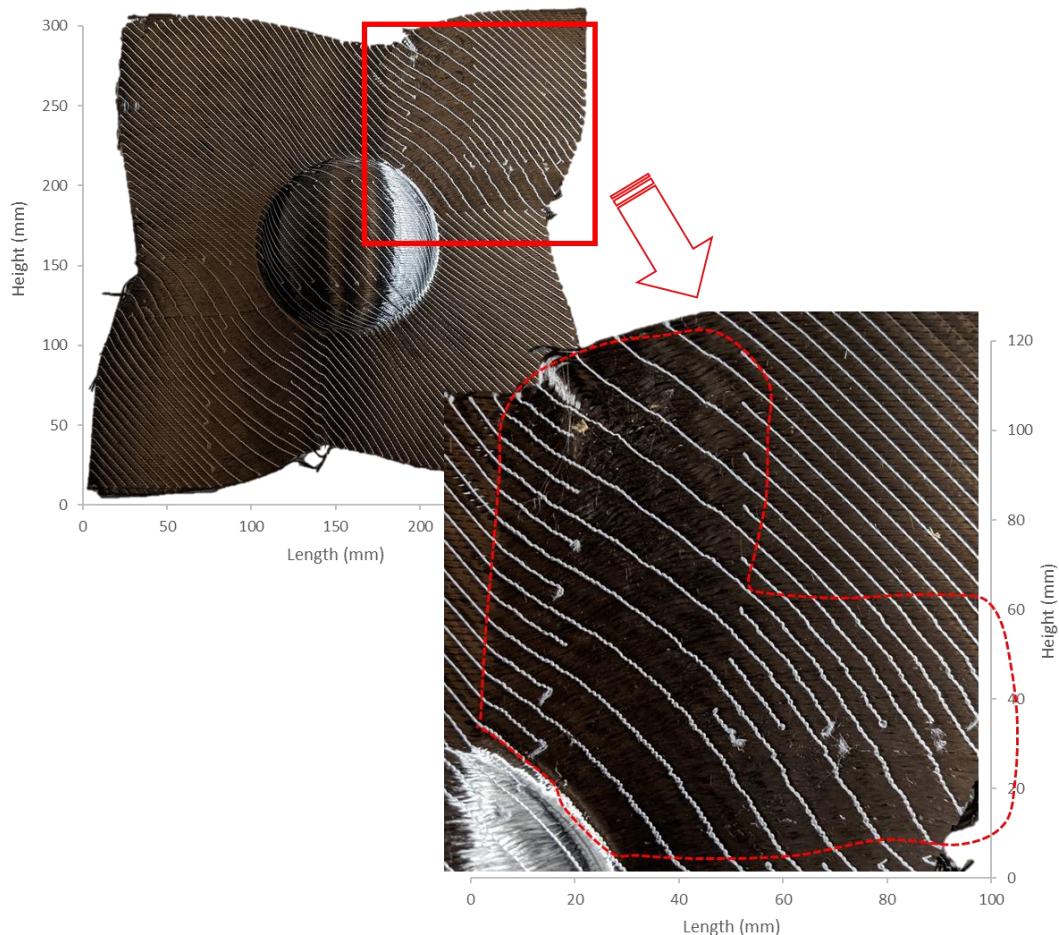


Figure 4-18 Punch formed hemisphere with stitch removal defect reduction strategy. Observations of inter-stitch buckling defect

4.3.6.2.2 Resin lubrication

Resin lubrication was applied as per the resin lubrication methodology. The powder binder on the surface of the plies was heated over the entire surface of the hemisphere to help lubricate the yarns.. Observations of yarn buckling defects on the lubricated hemisphere show similar reduction to those observed during in-plane testing. There was a 97% reduction in the number of out-of-plane defects over 1mm as shown in Figure 4-19 and Figure 4-15. The defect reduction method is highly successful with results on the formed hemisphere aligning with the negligible 0.28° rise in misalignment measured at 30 degrees during in-plane testing (Figure 4-19).

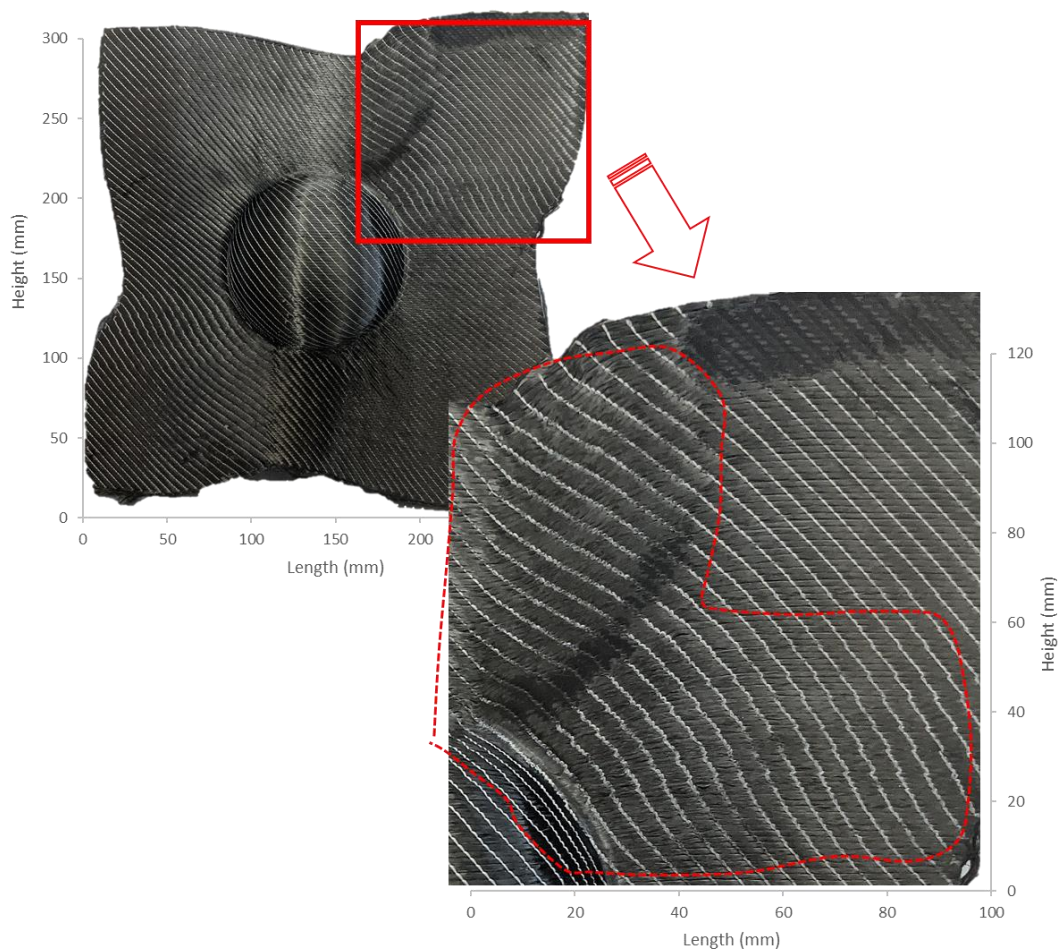


Figure 4-19 Punch formed hemisphere resin lubrication defect reduction strategy. Observations of inter-stitch buckling defect

Both defect reduction strategies are plausible methodologies for significantly reducing or removing inter-stitch yarn buckling defects in formed components. The

application of one over another is dependent on the impact of lubrication on the resin system being implemented (part dependent) and the time allocation for stitch removal (process dependent). Also in consideration is the method of application for both strategies. In a hand layup environment it is a quick task to coat the pre-form in binder powder (or spray with liquid resin) taking only 10-30 seconds. This can be achieved without significantly increasing laminating time, as even on a 1:8:1 layup (industry standard tooling layup, where a sandwich of lightweight plies is placed over heavier fabric bulking plies) the task would add 5 minute to the overall laminating time which could be up to 10 or more hours long. Applying stitch removal by hand would be a more laborious process, as individual rows of stitches would need identifying and removing. This was conducted one stitch row at a time in this study, but could be scaled up through the use of a heated jig. If the process were automated then stitch removal becomes simple as an operator or a robot arm could perform the stitch melting using a custom jig that could process all the stitches simultaneously.

4.4 Chapter summary

There is a deformation mode that occurs in NCFs at very low shear angles (0° - 1°) where frictional interactions between the yarns prevents slippage at the stitch points. This causes a non-linear shear region at low shear angles observed for many NCF shear force/angle graphs. The mechanisms driving the initial non-linear shear region has been linked to inter-stitch buckling defects that occur at higher shear angles.

The initial non-linear shear region has been identified in multiple NCFs and found to be independent of the initial relative yarn orientations. An analytical model to identify the responsible deformation mode was adapted from woven fabrics. The model assumed a frictional interaction between the primary yarns and the stitch, which is overcome within the initial non-linear shear region as the yarns eventually slide. This has been compared against picture frame data for two pillar stitched fabrics with R^2 values above 0.98 between modelled and experiment shear test data, thus validating the modelling approach.

The model was used to identify the link between the initial non-linear shear region and inter-stitch buckling that occurs at higher absolute shear angles. It was found that at high levels of stitch tension, the yarn is liable to buckle under compressive stress instead of slipping at each stitch point. The frictional resistance inhibiting slippage is the same as that found in the initial non-linear shear region and is dependent on the stitch tension. It was also shown that reduction in the frictional coefficient could remove the buckling defect.

The optical scanning methodology was used to quantify the level of fibre misalignment caused by inter-stitch yarn buckling as a standard deviation. A series of in-plane shear tests were carried out showing a 15x increase in fibre misalignment as the absolute value of negative shear angle increased from 0 to 30 degrees. This caused large out of plane buckles that were visible on the surface of the sample and measurable by the 3D scanning system used. These defects are severe enough to cause stress concentration points in a formed component, potentially leading to premature failure.

Two defect reduction strategies were used on the in-plane tests: local stitch removal and resin lubrication. Each strategy was developed for the output of the theoretical model and reduced the number of stitch-yarn interactions and the friction coefficient respectively. The testing showed a large reduction in fibre misalignment of 1.8° (51% reduction in fibre misalignment) for localised stitch removal and 2° (57% reduction in fibre misalignment) for resin lubrication. During inspection of the two samples, the out of plane defects had been reduced to a negligible number. This study highlighted the success of small process alterations to the 2D-3D forming process specifically designed combat inter-stitch buckling defects.

A set of hemispheres were press formed and the section of the geometry most affected by inter-stitch buckling defect was highlighted so the defect reduction strategies mentioned above could be applied. The results showed that localised stitch removal reduced the number of out-of-plane buckling defects by 74%, whilst resin lubrication removed 97% of the buckling defect. On visual inspection of the samples, the quality of the preform dramatically improves using both strategies matching the results from the in-plane shear variant of the test (discussed above). Application of

the methods was discussed emphasizing how resin lubrication is a quick process alteration that would have little effect on laminating time in a hand layup environment. However, incorporating extra resin components may impact the cure if done incorrectly and may have structural implications when applied to aerospace and automotive parts. This is because non co-curable resins (if different resins are used for lubrication and cure), or residual resins (if similar resins are used for lubrication and cure), could cause an imbalance during the infusion process and hinder curing. On the other hand, stitch removal is labour intensive to perform by hand, but with a large enough capital outlay an automated jig could be developed and implemented during the kit cutting operation.

5 Modelling the multi-cycle shear behaviour of biaxial non-crimp fabrics

Abstract

5.1 Introduction

5.1.1 Objectives:

- Explore the effect of multiple shear cycles on the shear modulus of biaxial non-crimp fabrics (NCFs).
- Generate a finite element (FE) material model that encompasses the multi-cycle shear properties of a biaxial NCF and accurately captures the shear angle distribution during a multi-stage forming process.
- Propose and simulate a modified forming process that utilises multiple shear cycles to improve formability.

5.1.2 Non-crimp fabrics

Biaxial non-crimp fabrics can be formed in a similar manner to woven fabrics with the additional benefit of improved mechanical properties due to the lack of crimp [97]. NCFs use a stitch to create the normal force that constrains the yarns rather than relying on inter-yarn friction. In a similar manner to a woven crimp, the friction between yarns resists the relative motion and presents itself as a shear resistance at fabric level [14]. The deformation type allows biaxial NCFs to be modelled with the same methods used for woven fabrics and characterised with methods such as the picture frame and bias extension test.

5.1.3 2D-3D Forming

5.1.3.1 *Multiple shear cycles in forming*

2D-3D forming of biaxial fabrics over complex double curvature geometries requires the fabric to drape via inter-yarn shearing, to achieve proper conformity to the tool. Typically, non-crimp fabrics (NCFs) have a higher shear modulus than woven fabrics as the stitch provides additional resistance and as such they are more difficult to form [14]. Industrial pull has led to more complex forming processes that involve fabrics undergoing multiple shear cycles [98-101]. However, the impact of this on the drape properties is not fully understood and can not currently be accurately modelled.

5.1.3.2 *Diaphragm forming*

This is increasingly apparent in forming processes with lower forming forces such as diaphragm forming. Diaphragm forming is a method for low cost automated 2D-3D fabric forming as it removes the requirements for match tooling or a press. It relies on a hydrostatic vacuum force to draw a dry fabric stack over the tool, which is then stabilised with a binder to create a preform which can be used with liquid moulding techniques [43, 102]. The lower forming forces involved in the process make it a good candidate for drape improvement studies as poor conformity and wrinkling defects are common. The double diaphragm setup uses the multi-axial in-plane friction generated between the diaphragms to control tension in the fabric [103]. However, the lack of a matched tool or blank holder opens the process up to out-of-plane wrinkling defects and thickness variation. The quality of the formed component is heavily geometry dependant as the fabric must be able to drape over a tool without generating regions of high tension [37, 46]. Diaphragm forming presents an innovative technique for the high-rate production of composite components, especially those with flatter profiles and components that have been optimised for the manufacturing process. This method not only facilitates the potential for automation in composite manufacturing but also opens avenues increased efficiency in composite component production by drastically reducing laminating time. In the case of a male section of the tool, the lower diaphragm will contact the tool at the highest points and generate tension in the fabric between those points [54]. For female sections, the flat expanses on the tool face will generate large frictional forces that lock the fabric in place which also generates tension in the fabric. Excessive tension between these regions causes poor tool conformity called fabric bridging where the vacuum compaction force is unable to overcome the frictional forces and the fabric is prevented from fully conforming to the tool [104]. A low shear modulus fabric requires lower forming forces to achieve full conformity and is less likely to experience this type of defect so NCFs typically experience a higher number of bridging defects. In the case of diaphragm pre-forming, the issues mentioned are non-critical as a subsequent forming force will be applied and remove many of the stated potential defects.

5.1.4 Finite element forming models

Finite element (FE) modelling methodologies for forming of NCFs commonly use a macroscopic scale approach, as the dynamic motion of fabric draping generates a large computational load that is unsuitable for smaller scale models [14]. Current models use a continuum membrane approach to characterise the non-linear in-plane shear resistance of the fabric. Further derivations of this approach use shell elements to incorporate non-linear bending stiffness [30] and give an improved map of the wrinkling generated. This approach is less computationally efficient and currently unsuitable for processes with an extended time scale such as multi-stage forming operations. For this reason the membrane approach has been used in this study and characterisation has been focused on the fabric shear properties.

5.1.5 Current work

The current study looked to use in-plane testing to generate shear modulus input data for non-crimp fabrics undergoing multiple shear cycles and use comparative testing to understand the meso-scale material interactions. A new comprehensive multi-cycle material model was generated in Abaqus/Fortran using the input data gathered that captured the correct shear angle distribution during diaphragm forming simulations. To do this a novel multi-stage forming process was proposed that highlights the use of multi-cycle modelling in complex forming processes.

5.2 Experimental Methodology



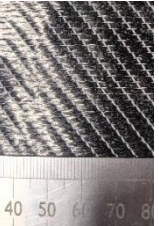
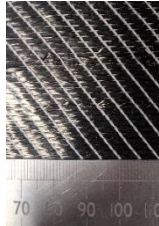
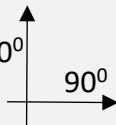
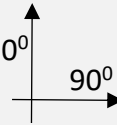
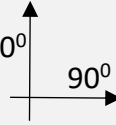
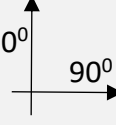
5.2.1 Materials

5.2.1.1 *Non-crimp fabrics*

An NCF is a multiscale material with interactions at the fibre, yarn and fabric level. It is expected that there will be some permanent deformation of the fabric when it is severely deformed and returned to its base state during shearing, as yarns and stitches are rearranged within the fabric and fibres are deformed within the yarns. This has been observed at extreme deformation such as stitch breakage in the positive shear direction for biaxial NCFs [105]. However, permanent deformation begins before this critical failure point.

To identify the extent of permanent deformation during multiple cycles of shear, a selection of NCFs with differing stitch architectures have been tested under multi-cyclic shear conditions. The materials chosen were a pillar stitched material, pillar stitched material with epoxy binder powder, a half-pillar stitched fabric and a tricot stitched fabric. Images and information for the fabrics chosen are given in Table 5-1. Differing stitch architectures produced different shear force responses so a range of cyclic response patterns could be assessed and compared between materials.

Table 5-1 List of materials with different stitch architectures considered during multi-cycle picture frame shear testing.

Code	D	C	B	A
Name	Tricot	Half- Pillar	FCIM789	FCIM359
Stitch type	Tricot	Half-Pillar	Pillar	Pillar
image				
Fibre Direction				
Data	-45/+45	-45/+45	-45/+45	-45/+45
	600g	600g	600g	600g
	24K	24k	24k	24k
	6gsm binder	6gsm binder	6gsm binder	No binder

5.2.1.2 Diaphragm material

Double diaphragm forming was used as the forming methodology to observe and model the effect of multi-cycle shearing. The diaphragms used were made from

StretchLon HT-350 [106] with a thickness of 0.05mm. This is a high strain thermoplastic bagging film usable up to 187°C and is compatible with epoxy resin systems. This was chosen over silicone reusable diaphragms as a significant amount of epoxy binder was used to set the geometry part for scanning and there was a high risk of damaging a silicone diaphragm during demoulding.

5.2.2 Multi-cycle in-plane shear testing methodology

5.2.2.1 Multi-cycle shear test comparison of the bias extension and picture frame test

The bias extension and picture frame test are both used to characterise the shear response of woven fabrics in the literature [21, 22, 97]. However, speculation exists around the validity of both tests when being used on NCFs. The bias extension test has free edges which causes slippage in the NCF where it is under constrained (Figure 5-1) and consequently invalidates the central pure shear zone needed for accurate testing of the fabric [6, 20]. The difference between the tests was further explored and highlighted in Chapter 3 and Appendix (C) .



Figure 5-1 Comparison of the sample shape during the bias extension test of FCIM789 before cycle 1(a) and during cycle 1(b).

It was necessary for the sample to be returned to an un-sheared state after the first cycle even after permanent deformation occurred, so that a second cycle could be implemented. This was not possible with the bias extension test as the permanent

deformation during the test causes elongation of the sample and creates slack at the beginning of the second cycle (Figure 5-1 (a), Figure 5-1 (b)). The bias extension test was inadequate for cyclic testing so a multi-cycle shear testing methodology has been created around the picture frame test.

5.2.2.2 *Multi cycle picture frame methodology.*

A methodology was created that shears a fabric to known value before returning it to an un-sheared state and re-loading it in a second cycle. This was conducted in an Instron tensile testing machine using a 5kN load cell and measured shear angle from the head displacement.

- Cycle 1: Figure 5-2 (1,2)
 - Sheared in the positive/negative direction to a known shear angle (A) by extending the picture frame rig by a set displacement (F1). Noting the force requirement.
 - Returned to a state of 0 mm of extension and 0 theoretical shear angle whilst noting the force requirement.
- Cycle 2: Figure 5-2 (1,2) (3,4)
 - Sheared in the positive/negative direction to full extension of 70 (B) degrees by extending the picture frame rig by a set displacement of 75mm (F2). Noting the force requirement.
 - Returned to a state of 0 mm of extension and 0 theoretical shear angle whilst noting the force requirement.

This test was repeated with a 3rd cycle which was placed in between the first two cycles and was a copy of cycle 1. The test enabled the second cycle shear response of a material to be tested after being pre-conditioned to a variety of shear angles in the first cycle.

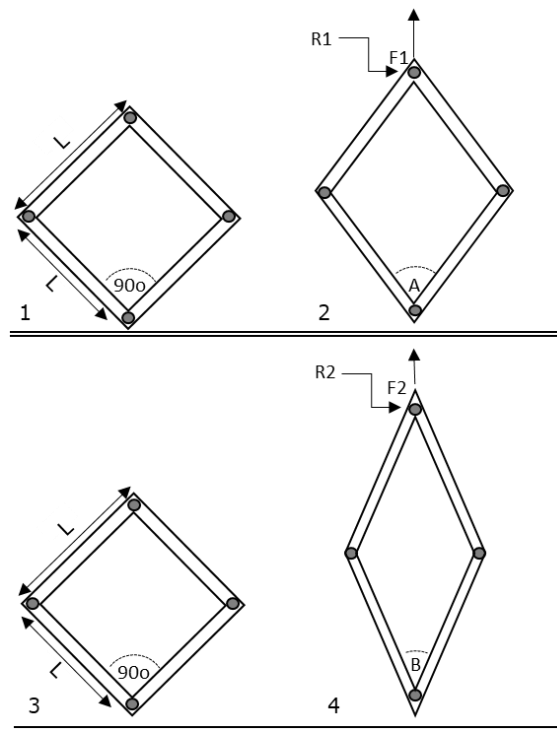


Figure 5-2 Four extension stages for multi cyclic picture frame test

5.2.2.3 Yarn and stitch measurement methodology

The cross sectional area and shape of the stitch and yarns were measured during picture frame testing to identify meso-scale changes to the fabric architecture during shearing. Samples for the stitch deformation measurement were created by freezing the strain in the fabric through the use of epoxy binder. 20gsm of dry powder binder was placed on the sample before testing. After the desired strain was reached, the sample was heated to 120°C and allowed to cool to 30°C before the frame was removed from the Instron testing rig and the sample was removed from the frame. Once the sample was stabilised it was vacuum infused with Prime 20 epoxy resin to a fibre volume fraction of approximately 50%. Samples were then cut into 15mm x 15mm squares for potting. The samples for measuring fibre area were stabilised and infused in the same way, but potted so the edge profile was perpendicular to the visible surface from which measurements were taken from.

5.2.3 Multi-stage double diaphragm forming

A variation on double diaphragm forming has been created that involved multiple forming stages. The process was used to highlight multi-cyclic shear properties in complex forming scenarios. The process is non-optimised, but highlights the potential benefits of multi stage processes that mimic those found in the metal forming industry. The process and sample setup was similar to a standard single-stage double diaphragm forming and is shown in Figure 5-3:

Stage 1: A flat, dry fabric laminate was sandwiched in between two StretchLon diaphragms with a vacuum drawn between the layers. The diaphragm-ply stack was lowered and then vacuum formed over the stage 1 mould tool. The forming pressure was removed and the frame was raised.

Objective: The blank was formed over a tool which has been designed to induce high levels of localised shearing in regions that are difficult to form. No stabilising agents were used, however permanent deformation occurs to the fabric as it shears to conform to the stage 1 mould tool.

Stage 2: The stage 1 mould tool was removed and replaced with the stage 2 mould tool. The frame was lowered over the stage 2 mould tool and the diaphragm-ply stack was formed over the stage 2 tool. Heating was applied to stabilise the pre-form before the vacuum pressure was removed and the component extracted.

Objective: The blank was formed over the desired mould tool shape. Regions that were locally sheared in stage 1 have different a modulus which helps to improve conformity in stage 2.

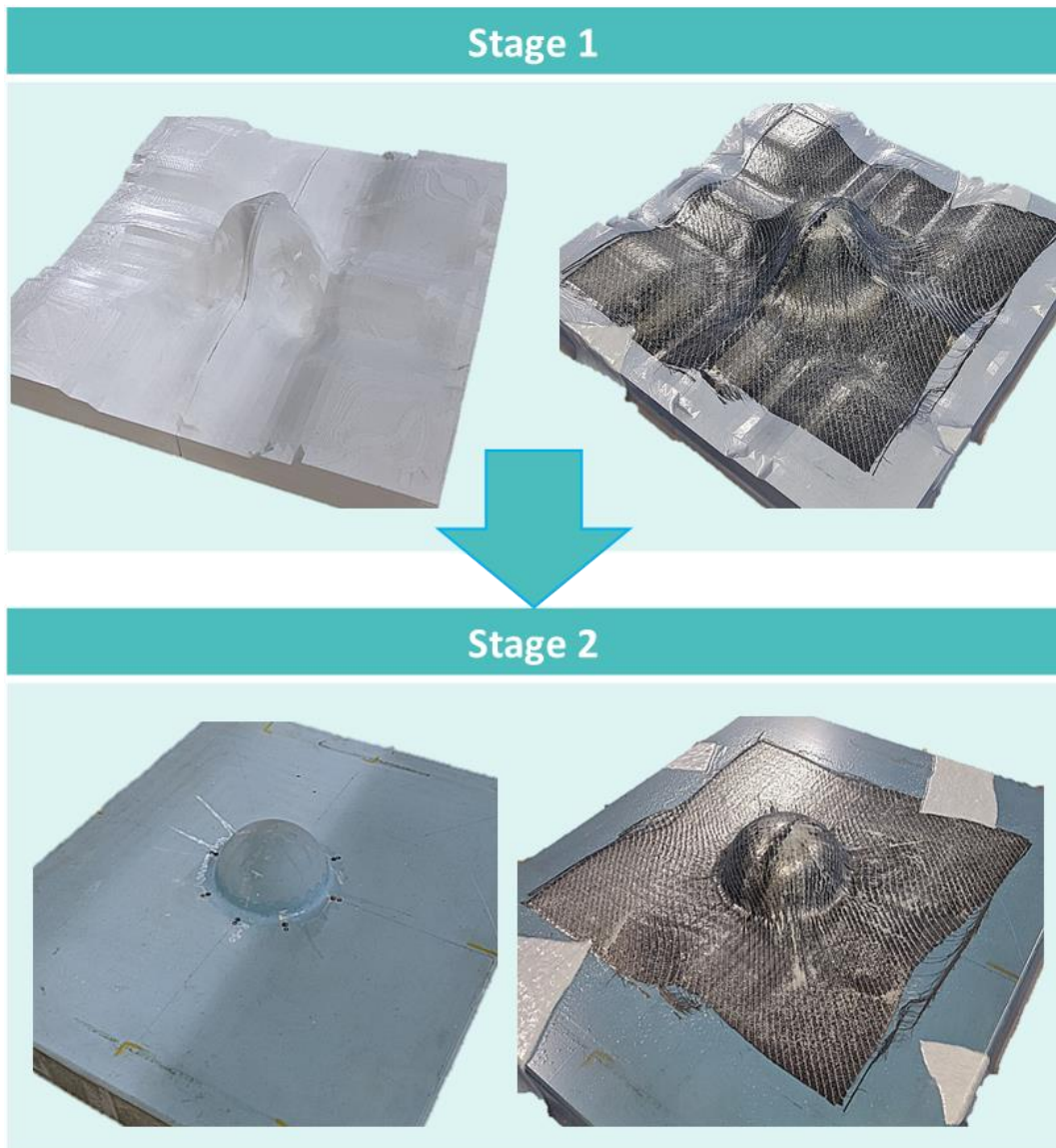


Figure 5-3 Multi-stage diaphragm forming. Example form for stage 1 and stage 2 with a hemisphere mould tool (mould tool on the left and moulded component on the right)

5.2.3.1 Stage 1 “localised high shear” mould tool

To maximise the pre-conditioning of the fabric during the first cycle of the forming process, a form was created that aimed to induce a high level of shearing in localised regions. This was then replaced with the desired final shape form for stage 2. The stage 1 mould tool differed based on the stage 2 final mould tool shape and was created from a geometry transformation of the desired final mould tool. The local regions were identified as areas where shearing already occurred in the fabric and there was also the appearance of bridging defects or poor conformity.

5.2.3.2 Stage 1 mould tool transformation

A bridged piece of fabric has been simplified and modelled in a similar way to a supported 2D beam. The boundary conditions were produced where the ends of the fabric become trapped due to high frictional forces between the tool face and the fabric. The forming force was uniformly distributed from the diaphragm bag pressure.

$$\frac{5wl^4}{384EI} = \delta \quad \text{Equation 5-1}$$

W = Load, l = Length of bridged region, E = Young's Modulus, I = Second moment of area, δ = Deflection

The fabric is assumed to be inextensible in the principal directions. However, it is likely that bridging occurs in regions where the fabric is at some form of bias angle. This is due to there only being a 4/360 chance that the tool geometry (causing bridging) perfectly matches the fibre directions. This means that shear occurs as the fabric becomes trapped allowing for some deformation.

$$\frac{\sin 2\theta 5wl^4}{384GI} = \delta \quad \text{Equation 5-2}$$

G = Shear Modulus, θ = Bias Angle,

The level of strain needed to reach the desired maximum depth (and therefore conformity to the tool) was calculated.

$$2\left(\sqrt{\delta^2 + \left(\frac{l}{2}\right)^2} - \frac{l}{2}\right) = \varepsilon_f \quad \text{Equation 5-3}$$

ε_f = Depth of midpoint of the sample, l = length of bridged region

Equating both equations show how the strain in the fabric is affected by the length of the bridged region and the shear stiffness of the fabric

$$2\left(\sqrt{\left(\frac{\sin 2\theta 5wl^4}{384GI}\right)^2 + \left(\frac{l}{2}\right)^2} - \frac{l}{2}\right) = \varepsilon_f \quad \text{Equation 5-4}$$

Increasing bridged length 'l' increases the strain seen in the fabric, as does decreasing shear stiffness 'G'. For a geometry transformation to the tool 'l' must be increased in areas that experience shearing.

In 3D space, to achieve an increase in length in the bridged regions a nodal transformation was applied to the desired final form geometry. The normal 'N' to the mesh surface. This normal was used as the direction for the transformation vector **Equation 5-5**.

$$\begin{aligned}
 i &= (i_1, i_2, i_3) \quad j = (j_1, j_2, j_3) \quad k = (k_1, k_2, k_3) & \text{Equation 5-5} \\
 A &= (A_x \mathbf{i} + A_y \mathbf{j} + A_z \mathbf{k}) = (j_1 - i_1, j_2 - i_2, j_3 - i_3) \\
 B &= (B_x \mathbf{i} + B_y \mathbf{j} + B_z \mathbf{k}) = (k_1 - j_1, k_2 - j_2, k_3 - j_3)
 \end{aligned}$$

This was multiplied by the shear angle *SA* found for each node from an initial forming simulation, so the transformation only affects regions undergoing shear that will benefit from being transformed.

$$\mathbf{N} = \mathbf{A} \times \mathbf{B} = \begin{bmatrix} \mathbf{i} & \mathbf{j} & \mathbf{k} \\ A_x & A_y & A_z \\ B_x & B_y & B_z \end{bmatrix} \quad \text{Equation 5-6}$$

$$|\mathbf{SA}| \cdot \mathbf{N} = |\mathbf{SA}| \cdot \begin{bmatrix} \mathbf{i} & \mathbf{j} & \mathbf{k} \\ A_x & A_y & A_z \\ B_x & B_y & B_z \end{bmatrix} \quad \text{Equation 5-7}$$

Finally this was multiplied by a scaling factor $|\mathbf{P}|$ that controls the magnitude of the transformation on the geometry and can be used to alter and control the level of pre-shear seen in the first forming stage (**Equation 5-8**).

$$\mathbf{Transformation T} = |\mathbf{P}| \cdot |\mathbf{SA}| \cdot \mathbf{N} \quad \text{Equation 5-8}$$

Figure 5-4 shows a 2D diagram of the stage 1 mould tool transformation for a dome. In the original geometry Figure 5-4 (a) the fabric tries to conform to the tool through shear. However, it bridges over the L1 region as the forming force is not high enough to overcome the frictional resistance. With the transformed geometry Figure 5-4 (b), the length of the bridged region has been increased and forming over the transformed geometry will produce a greater forming force over the bridged region and generate greater shear strain in the fabric. The depth of the region has also been increased, so forming over the transformed region will allow for an increased displacement of the fabric before contacting the tool.

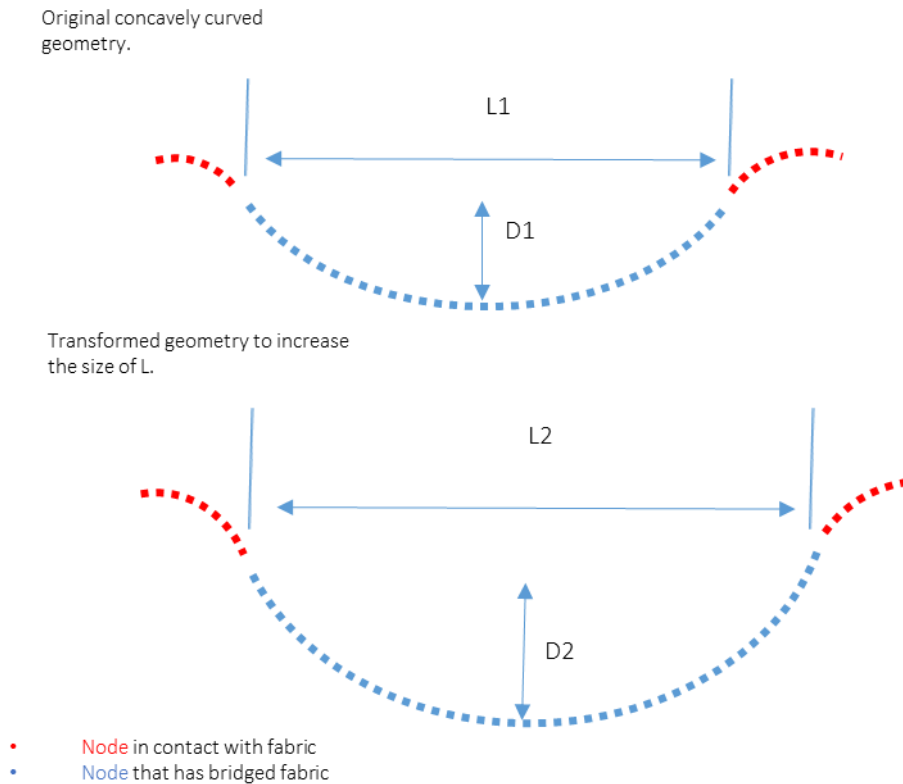


Figure 5-4 2D representation of the geometry transportation applied to the tool surface to generate increased localized shearing. (a) is the original geometry section and (b) is the transformed section.

5.2.3.3 Stage 1 mould tool application to a hemisphere

The stage 1 mould tool transformation from Figure 5-4 has been applied to the hemisphere form. Equation 5-8 has been applied to each node of the hemisphere form with the required shear angle data being gathered from a single cycle FE forming simulation using a non-cyclic NCF material model. Multiple values for the scaling factor $|P|$ have been tested in Figure 5-5 to show the level of transformation that the geometry can accommodate before the removal of material causes degradation of the mould shape. Figure 5-5 shows the transformation of the geometry as the scaling factor was increased from 0 to 0.01. To give the greatest impact on subsequent stages, the highest scaling factor was applied. This was limited by the maximum amount of material that could be removed from high shear regions before holes appeared in the tool (tool degradation). For the hemisphere geometry, this value was $|P| = 0.01$.

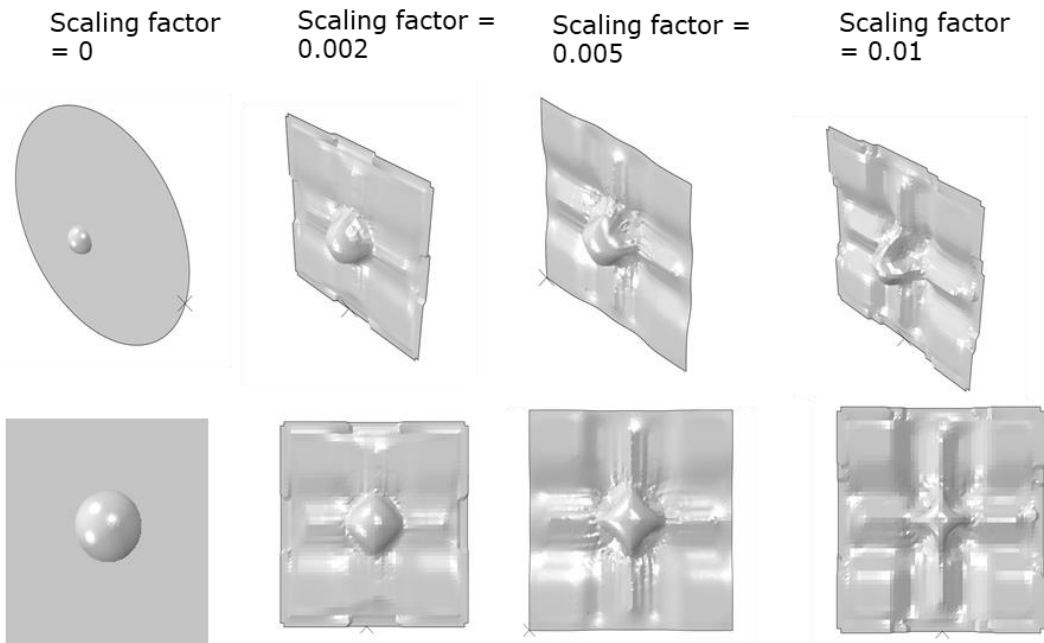


Figure 5-5 Transformed hemisphere for first cycle fabric pre-conditioning. Scale values set to 0, 0.002, 0.005 and 0.01.

5.2.4 Multi-cycle stitch extension methodology

5.2.4.1 First-cycle stitch extension methodology

The objective of measuring the stitch extension was to see how much of the non-linear shear curve is due to the elastic properties of the stitch during its extension and how much is due to changing frictional interactions between the yarns as they shear. The test isolates a single line of stitching with the corresponding yarn bundles and measures the tensile force and extension as shown in Figure 5-6. A 1kN load cell was attached to an Instron 5581 mechanical testing machine. A pair of flat rubber faced aluminium clamps were mounted to the load cell and the base of the testing rig. Each clamp was 50mm deep and a threaded bolt at each end of the clamp was used to apply pressure. The rig was set to produce a 50mm extension at 5mm/min giving a 10 minute test time. The pre-loading and post-loading states of the sample are shown in (A) and (B) respectively in Figure 5-6. A sample consisted of a single stitch cut from the pillar stitch fabric (B). The stitch material remains in its stitched state with 5mm of fabric protruding from each edge of each stitch. The overall sample size was 120mm by 10mm. The jaws were moved to be 50mm apart from each other and the sample was mounted and clamped with 35mm of the sample secured by each clamp and the sample taut between the jaws. During the testing the

sample was extended and the force required to extend the stitch and the displacement of the testing head were measured by monitoring the head displacement. The displacement was validated by comparison of video measurements of the stitch extension against the head displacement data tracked with the points given in Figure 5-6. To prep a sample a sheet of pillar stitched NCF was laid on a cutting board and a single stitch was located. A sharp rotary cutter was used to slice either side of the stitch, leaving 5mm of fabric protruding from the stitch. The stitch and accompanying fabric were removed and observed for defects. Due to the fragile nature of the sample a variety of defects may occur. Common sample defects were:

- Laddering of the sample during cutting: where the sample stretched during the cutting processes leading to a preconditioned stitch.
- Rotation of the fabric about a stitch: where during handling of the sample, the sample is rotated midway down, giving a twisted stitch.
- Fabric pull out: where during the cut out process the fabric is caught and pulled out of the stitch, leaving a looped stitch with no fabric inside.

Because of the ease with which samples were damaged the samples were prepped in situ at the testing site and measured immediately after cutting. Due to the difficulty in prepping samples the most stable material was chosen for undergoing stitch extension. This was material B, as the pillar stitch constrained the fibres for the largest extension before failing.

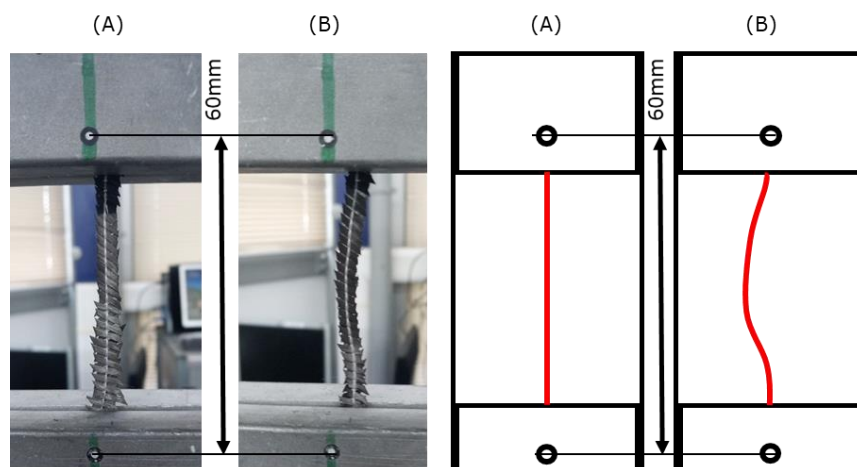


Figure 5-6 Single stitch clamped for stitch extension test. (A) Before testing. (B) After a displacement of 10mm is applied before returning to 0.

5.2.4.2 *Second-cycle stitch extension methodology*

The cyclic stitch extension test was set up in a similar manner to the regular stitch extension test and samples were prepared identically. The load settings were altered to allow the sample to be extended in 3 stages:

- Initial extension to a specified value (5mm/10mm/15mm).
- Returning to a head extension of 0mm
- Re-extension to a maximum value of 20mm, or until the sample failed.

Multiple values for the initial extension were used so that variability in the second cycle force response could be observed. Identifying a similar response pattern between the stitch extension and the shear response of the fabric would give an indication that the deformation to the stitch was a primary cause of the fabric multi-cyclic shear behaviour.

5.2.4.3 *Stitch extension and picture frame shear test normalisation*

To compare picture frame and stitch tension results, the stitch tension must be interpolated over the sample size found in the picture frame. The shear in the picture frame test is homogenous, so although the length of the clamped stitch changes across the picture frame, the strain at each point remains the same. A single stitch strain can be found and used as an approximation for the stitch strain across each stitch in the sample. The strain in one stitch in the picture frame is calculated by dividing the crosshead displacement by the number of stitches. The un-deformed average length of the stitch is 2mm (± 0.15 mm) and the final length of a single stitch is 2.99mm (± 0.15 mm). The strain was confirmed by optical measurements taken from video gauge images of the stitch length over the testing period and confirmed to agree with the value calculated from the crosshead displacement. The load-strain curve known for a single stitch from the stitch extension test was multiplied by the number of stitches in the sample (averaging 1628). The stitch strain was equated to the shear angle in the picture frame test through the crosshead displacement. This allowed for the tensile response of the stitches in the fabric to be plotted alongside the shear response of the fabric.

5.3 Multi-cycle non-orthogonal material model

5.3.1 Homogenisation

Composites are multi-resolution materials defined in multiple geometrical scales, so homogenisation is needed to embody the material in continuous elements which can be used in forming simulations. The properties of uncured fabrics are highly dependent on the fibre direction and reorientation of the local yarn direction gives differing properties across the material. In a biaxial NCF, the pair of fibre directions can shift away from their initial state of orthogonality at each stitch point as the fabric is deformed. To homogenise the fabric, a non-orthogonal coordinate system is used at each integration point so that local fibre angle can be followed. This is essential to tracking the local change in fibre angle over multiple deformation cycles. The method outlined by S.Chen was used as a basis for this material model [14].

5.3.1.1 *Material model implementation*

A VFABRIC user subroutine has been developed to define the material properties for the fabrics in the study over multiple loading and unloading cycles. The VFABRIC routine is designed for materials with two non-orthogonal principal directions. At each explicit time step the old stresses and strains are calculated and transformed into the global coordinate system. A time step is a discrete time increment that the solver progresses by after each set of calculations. Material properties are transformed into the non-orthogonal fibre coordinate system from which the stress increment tensor is superimposed on the initial stress tensor which gives the new stress tensor. This is further processed by Abaqus/Explicit in conjunction with the rest of the model. VFABRIC automatically defines the coordinate systems and transformations which is less computationally expensive than generating non-orthogonal coordinate transformation in the more generalised VUMAT material subroutine as the number of tensor operations in a VFABRIC is lower.

5.3.2 Non-crimp fabric material model

The material modelling approach used was created by M.Khan [107] and applied to NCFs by S.Chen [14] to accommodate asymmetric shearing. In the case of an NCF, the force required to shear the fabric is a combination of the yarn rotation and tension in the stitches. In S.Chen's work a single polynomial is used to describe the

effect of yarn rotation and the modulus generated by the stitch is added afterwards with two piecewise equations. In this study an alternative fitting approach has been used to give greater flexibility. Separate regions in the shear curve can be distinguished by the corresponding deformation modes:

- Frictional effects dominate the initial non-linear shear region [13].
- The low shear forces are overcome and shear drives the deformation.
- The stitches break at which point stitch failure characteristics are dominant.
- Yarns are sheared to the point of locking up on themselves at excessive degrees of shear.

To describe the progression through deformation modes the shear curve has been broken down into 3 polynomials which are joined to give a full description of the material. A single polynomial describes the negative shear region. The initial non-linear shear and shear dominated region up until the stitch breakage point are described by a second polynomial and the stitch breakage and yarn locking are described in the final polynomial. The result is a shear angle dependant piecewise equation incorporating each of the three regions. Equation 5-9 shows the shear force response equation for material B used to generate Figure 5-7 with θ ranging from: -90° to 0°, 0° to 35° and 35° to 90°.

$$Y = 0.0045x10^{-3}\theta^4 + 0.2158x10^{-3}\theta^3 \quad \text{Equation 5-9}$$

$$Y = -0.0053\theta^3 + 0.31\theta^2 - 5.3737\theta + 53.9$$

$$Y = -0.0075\theta^3 - 0.328\theta^2 - 9.84\theta + 422$$

Splitting the shear curve this way allows for independent control over the shape of the positive and negative shear region which is needed to incorporate the effects of cycling the material. This fitting methodology has been validated against S.Chen's NCF model and against experimental forming experiments in Figure 5-7. The segmented polynomial approach has an R² value of 0.98 which is similar to that of the Yarn rotation + stitch force method used by S.Chen.

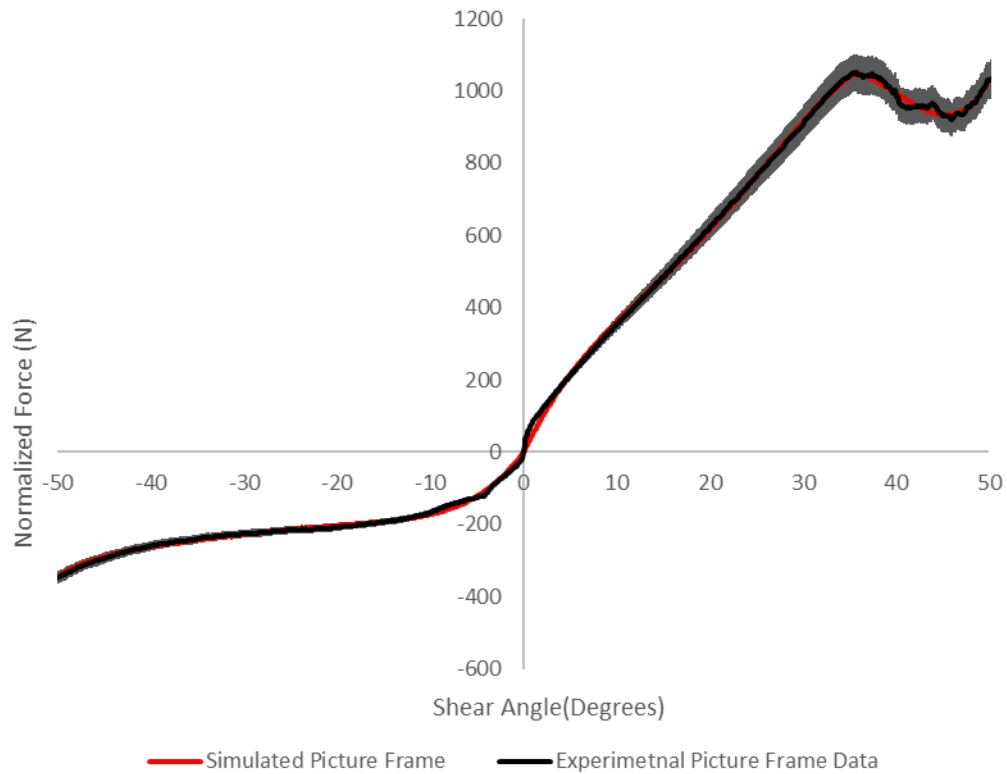


Figure 5-7 Shear force response during picture frame testing for FCIM379. Simulated results gathered using the updated fitting function. (error from 3 experimental repeats signified by shaded region)

5.3.3 Non-linear cycle dependant shear modulus

To incorporate the material response when unloading and re-loading the fabric, a variable was determined alongside the shear angle to indicate past deformation that has occurred in the fabric. Results show that the magnitude of the unloading and re-loading response over the second cycle is dependant on the maximum shear angle (θ_{max}) previously experienced by the fabric. Due to this, a nested function was needed to describe the second cycle response that is dependent on the maximum magnitude of shear seen in the first cycle. Testing the second cycle response at differing values of θ_{max} showed that the unloading part of the second cycle is scale invariant to θ_{max} meaning that the same polynomial could be used at all values of θ by scaling it proportionally to the current value of θ_{max} . A similar case was seen for the re-loading section of cycle 2 where a separate scale invariant function was used to describe the fabric response.

As the unloading and re-loading polynomial scaling is dependant on the shear angle, the functions were inverted, scaled with θ_{max} , and then re-inverted within the material model. This was done using an approximate inversion of high order polynomials [108]. Values for A1, A2, A3 and A4 are the constants in the polynomial after the first inversion which have then been multiplied by a scaling factor that is proportional to θ_{max} . This was then divided by the original maximum shear angle experienced by the fabric θ_{max-o} . The original function for the values seen in Figure 5-8 and Figure 5-9 has used $\theta_{max} = 10$ and as such θ_{max-o} has been set to 10 for Figure 5-8 and Figure 5-9. Values for B1, B2, B3 and B4 correspond to the constants for each order of the new re-inverted polynomial and are found as follows:

$$b_1 = \frac{1}{a_1} \quad \text{Equation 5-10}$$

$$b_2 = \frac{a_2}{a_1^3} \quad \text{Equation 5-11}$$

$$b_3 = \frac{2a_2^2 - a_3a_1}{a_1^5} \quad \text{Equation 5-12}$$

$$b_4 = \frac{1}{a_1^7} (5a_1a_2a_3 - a_1^2a_4 - 5a_2^3) \quad \text{Equation 5-13}$$

This method allowed for any shear force response polynomial to be scaled to the correct value so the unloading and re-loading shear moduli functions could be expressed at all values of θ_{max} up to the stitch breakage point.

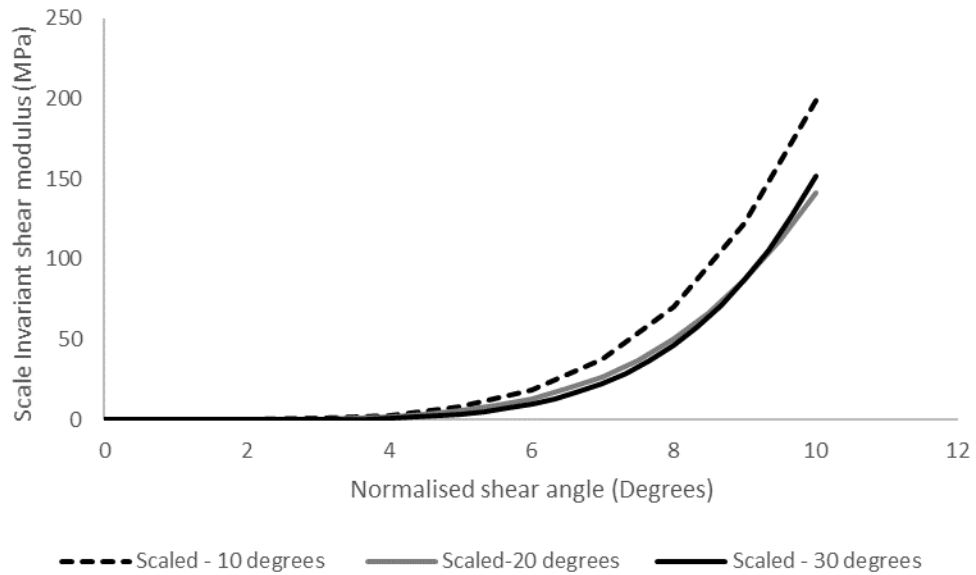


Figure 5-8 Cycle 2 nested, scaled un-loading polynomial for FCIM789. Tested to 10, 20 and 30 degrees of shear in cycle 1.

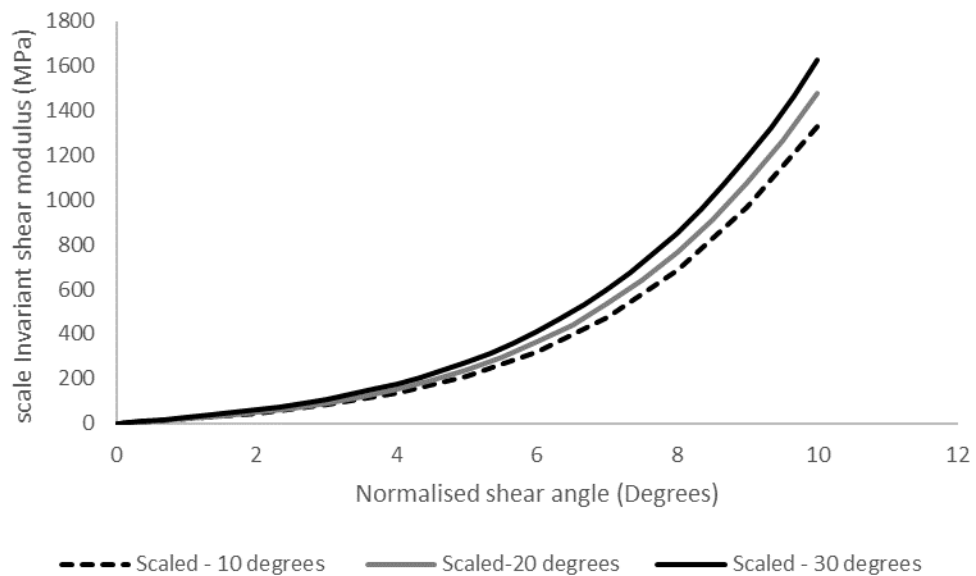


Figure 5-9 Cycle 2 nested, scaled re-loading polynomial for FCIM789. Tested to 10, 20 and 30 degrees of shear in cycle 1.

Figure 5-8 shows the unloading curve for material B from first cycle values of 10, 20 and 30 degrees. The results have been scaled proportionally to $\theta_{max-o} = 10^\circ$, (so the unloading from 20° has been divided by 2 and the unloading from 30° has been divided by 3). Once scaled the results align with each other, showing a steep decline in force from maximum shear to almost 0 at roughly half the applied shear angle and an R^2 value of 0.96. On the re-loading step at the beginning of cycle 2 a similar scale

invariance is seen with Figure 5-9 showing the re-loading force, shear angle graphs from the NCF loaded at 10, 20 and 30 degrees. The shape of each result is identical with a smooth polynomial increase from 0 to maximum applied shear and an r^2 value of 0.97. Shear modulus polynomials for material B for unloading and re-loading have been generated from Figure 5-8 and Figure 5-9 and are given in Equation 5-14 and Equation 5-15 respectively where G is the shear modulus (PA) and θ is the shear angle (degrees).

$$G = 0.0046e^{4.645\theta} \quad \text{Equation 5-14}$$

$$G = 0.0077\theta^4 + 0.064\theta^3 + 0.67\theta^2 + 10\theta - 10 \quad \text{Equation 5-15}$$

A comparison between experimental results and the theoretical multi-cycle shear modulus is shown in Figure 5-10. There is very good conformity between the theoretical function and the experimental data with an R^2 value of 0.97. This conformity remains irrespective of the level of first cycle θ_{max} as the unloading and re-loading functions can be multiplied by the scaling factor in Equation 5-16:

$$S_{10^\circ} = \frac{\theta_{max}}{10} \quad \text{Equation 5-16}$$

Figure 5-10 shows the cyclic response for a fabric that has been sheared to a first cycle θ_{max} of 10 degrees before being re-loaded from 0 degrees to +50 degrees. It has also been sheared in the negative direction to -50 degrees. This is compared to the function given from Equation 5-9, Equation 5-14 and Equation 5-15 with the scaling factor S_{10° set to 1.

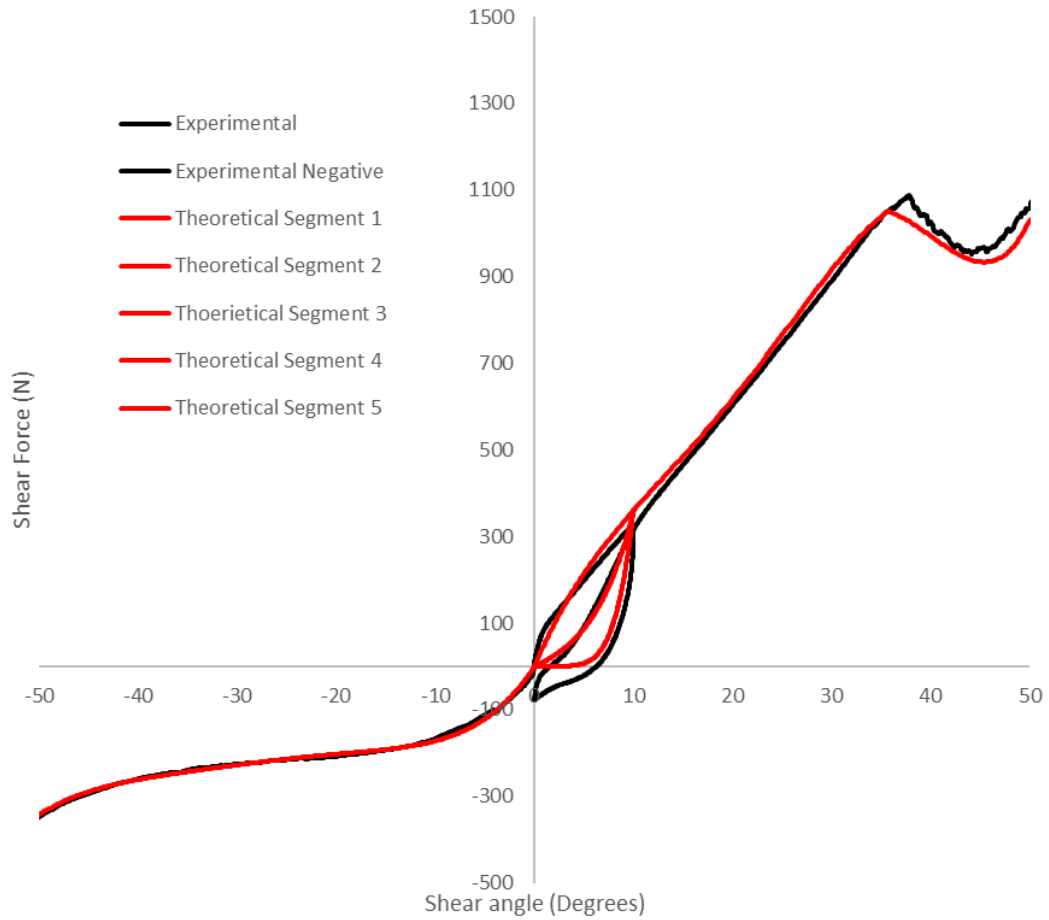


Figure 5-10 Shear force shear angle results for a multi cyclic picture frame test cycled to 10 degrees. Comparison between theoretical values to be used in material modelling with experimental results. (re-loading curve, sits in between the initial loading and unloading polynomials)

5.3.3.1 Multi-cycle polynomial implementation

Implementation of the nested polynomials for the cycled material properties into the VFABRIC required a new state variable for θ_{max} to be created. This was tracked for each node at each time step and fed back into the subroutine. At the beginning of each increment θ_{max} is read from the state variable and used to update the function for G_{12} .

5.3.4 Multi-cycle picture frame model

Numerical tests verify that the constitutive relation used by the VFABRIC is representative of the shear behaviour of a biaxial NCF over multiple shearing cycles. A virtual picture frame simulation was created with dimensions matching the experimental test setup from Appendix (D). A rigid 4 bar linkage was used to replicate

the frame with the fabric constrained so each principal material direction is perpendicular to the adjoined frame edge. 3mm x 3mm membrane (M3D4R) elements were used to represent the fabric with constructed VFABRIC material section applied. The varied displacement was applied using multiple steps:

- 1st cycle loading.
 - Positive frame displacement = A
- 1st cycle unloading.
 - Negative frame displacement = 1st cycle Positive frame displacement
- 2nd cycle loading.
 - Positive frame displacement = B

The variable A has been varied to monitor the success of the nested functions in determining the shear modulus, as variations to A will cause θ_{max} to change over the sample. The variable B was set to generate a shear angle of 60 degrees, as this is a point at which the shear modulus drastically increases due to yarn locking and forming beyond this region is undesirable.

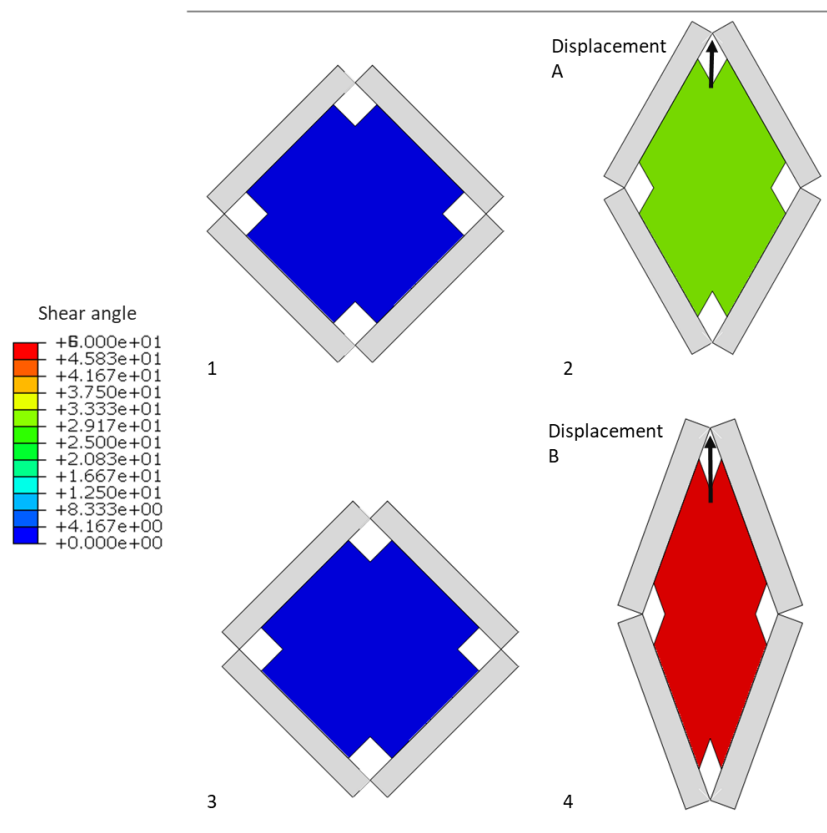


Figure 5-11 Four extension stages for simulated multi cyclic picture frame test

5.3.5 Multi-stage diaphragm forming model

The multi-stage diaphragm forming process has been modelled with the objective of displaying how accurate simulation of the multi-cyclic material properties is essential for accurate modelling of complex forming operations.

5.3.5.1 Diaphragm material model

A Marlow hyperelastic non-linear isotropic model was used to define the behaviour of the StretchLon HT-350 diaphragms. The uniaxial, biaxial and planer tests were conducted on a universal testing machine at a strain rate of 0.03s^{-1} at ambient temperature, following the methodology from Chen [37]. As the diaphragms are thin, the compressibility was not being taken into account and volumetric data was not included, so a standard Poisson ratio of 0.475 was automatically set. Abaqus then interpolated the strain energy potential from the test data.

$$W_u = \int_0^{\lambda T_u^{-1}} T_u(\varepsilon) d\varepsilon \quad \text{Equation 5-17}$$

$$W_b = \int_0^{\lambda T_b^{-1}} T_b(\varepsilon) d\varepsilon \quad \text{Equation 5-18}$$

$$W_p = \int_0^{\lambda T_p^{-1}} T_p(\varepsilon) d\varepsilon \quad \text{Equation 5-19}$$

With the subscripts u , b and p relating the uniaxial, biaxial, and planar data, respectively. The diaphragms were modelled as shells to capture bending stiffness, as the bending stiffness has an impact of wrinkle formation of the composite contained within them.

5.3.5.2 Multi-cycle hemisphere forming model

All modelling has been done in Abaqus/Explicit. The model setup can be seen in Figure 5-12 and Figure 5-13. The fabric plies and diaphragms were modelled as separate entities with unique material properties [14]. The boundary conditions applied approximate those in the lab scale double diaphragm former in The University of Nottingham Composites department. The diaphragms have been constrained at the perimeter to mimic the clamps on the experimental double diaphragm (DD) setup and modelled using 4 mm by 4 mm shell elements. Each fabric ply was modelled using membrane elements (M3D4R) with shell edge length of 3mm.

The tools were modelled as rigid bodies and friction was applied using a penalty contact algorithm with constant coulomb friction coefficients found from S.Chen [37].

A custom Matlab code was used to apply the stage 1 mould tool transformation to the desired hemisphere mould tool to give the form from Figure 5-5. A forming simulation was conducted for a single ply of material B and the output shear angle data was collected per node and transposed onto the mould tool to give coordinate data and shear angle data. This was fed into the transformation for each node to generate the stage 1 mould tool hemisphere points cloud. A simple Poisson screen positioning meshing algorithm [109] was used to generate a surface which could be imported into Abaqus/Cae.

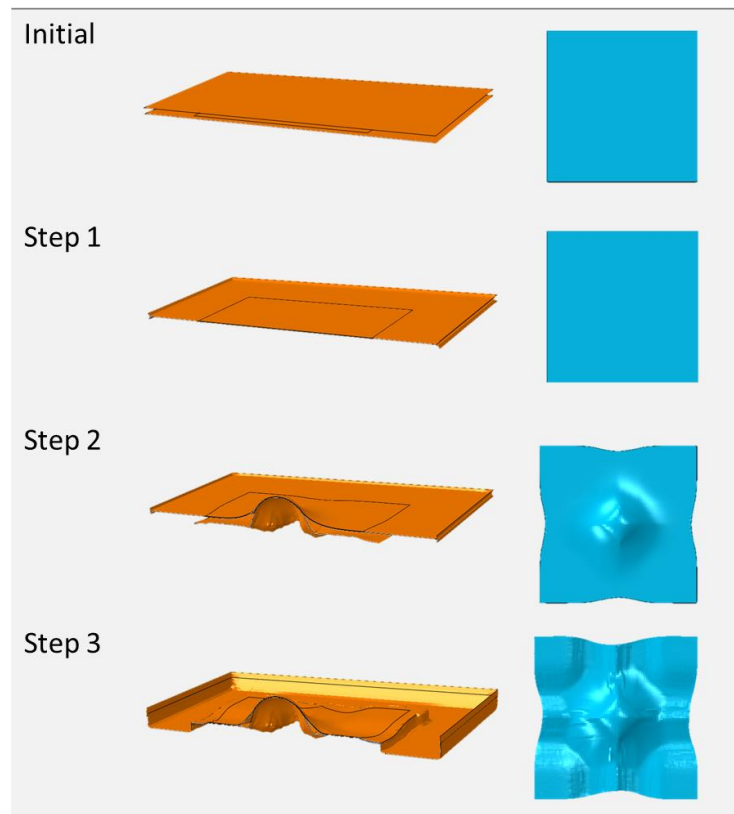


Figure 5-12 Step 0 to 3 for multi-cyclic diaphragm forming process

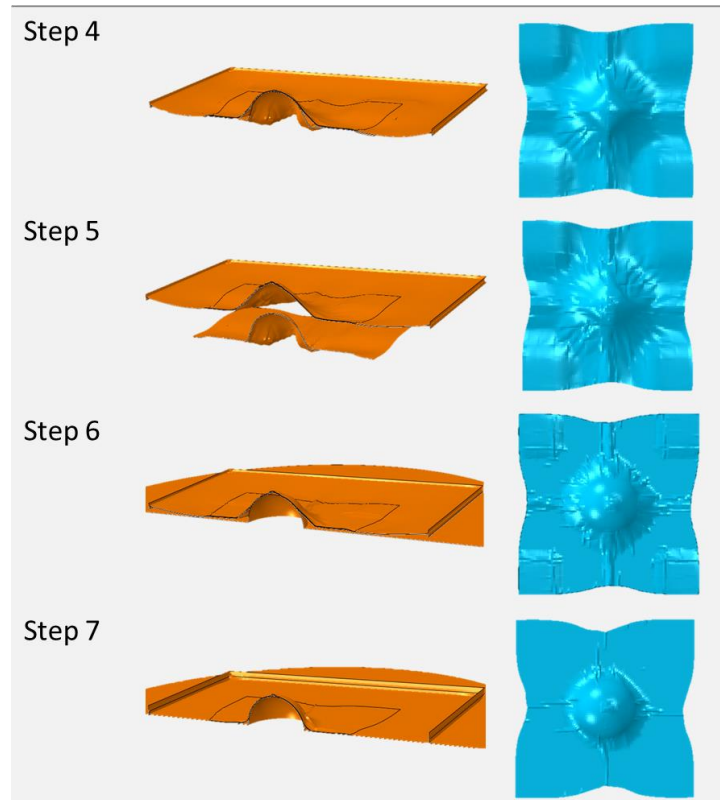


Figure 5-13 Step 4 to 7 for multi-cyclic diaphragm forming process

The simulation is split into the initial step and 6 forming steps.

- The first step - 1 second. Used to apply a 1 bar pressure to the outer surface of each diaphragm compacting the ply centered between them via the contact between the diaphragm and ply layers.
- The second step - 3 seconds. The diaphragm and ply stack descend over the stage 1 mould tool.
- The third step - 3 seconds. A 1bar uniformly distributed load is applied to the surface of the upper diaphragm, approximating the vacuum compaction in Double diaphragm forming. This forms the diaphragm and ply stack over the stage 1 mould tool preconditioning the fabric.
- The fourth step - 1 second. 1bar compaction force is removed. With this the diaphragms are unloaded and elastic effects return the ply to a semi-deformed state.
- The fifth step – 1 second. the frame is raised so the ply diaphragm stack is separated from contact with the tool. This allows for the stage 1 mould tool to be swapped out for the final mould tool.

- The sixth step – 3 seconds. The diaphragm ply stack re-descend over the final mould tool.
- The seventh step – 3 seconds; A 1bar uniformly distributed load is applied to the surface of the upper diaphragm, approximating the applied vacuum compaction over the final tool.

5.4 Experimental results

5.4.1 Multi-cycle picture frame results

The materials from Table 5-1 have been tested according to the multi-cycle picture frame methodology. A range of cycle 1 shear angle values have been tested for each material: -30, -20, -10, 10, 20, 30 and the difference between positive and negative shear has been investigated. The investigation examines the shape of the hysteresis in the shear modulus over multiple cycles and how that shape varies with the initial deformation experienced by the fabric. The reduction in shear force needed to shear the fabric in cycle 2 has been plotted in Figure 5-14. Figure 5-14 shows the reduction in shear force from cycle 1 to cycle 2 of the multi-cycle picture frame test for each of the fabrics given in Table 5-1. All the materials chosen show hysteresis in the shear force after the first deformation cycle. Each of the materials experiences a distinct positive and negative shear direction which impacts the magnitude of the force reduction identified as a larger reduction in the positive direction and smaller in the negative direction. In every material the force reduction seen increases as the magnitude of the first cycle displacement (A) and first cycle θ_{max} increases. The force reduction peaks at 1/3 to 1/2 of the first cycle θ_{max} and then significantly drops as θ further increases. The two pillar stitched fabrics show the lowest force reduction in the positive direction, peaking at 355N and 372N for FCIM359 and FCIM378 respectively. FCIM359 in the negative shear direction has a very low force reduction of only 20N that is independent of θ_{max} . For the tricot stitch and the half pillar stitched fabrics a similar force reduction is seen in the negative and positive direction, with negative shear direction magnitude that is roughly 25% of the positive values. These materials differ from the pillar stitch fabrics because there is a component of the stitch that extends in the negative shear direction as can be seen from the images in Table 5-1. There is still a distinct positive direction which contains the majority of the stitch extension. However, the diagonal stitch pattern in both these materials

provides resistance in the negative direction too. Overall, each material shows a significant and measurable reduction in shear force that is a function of the shear angle experienced in cycle 1. The shape of the shear force reduction is dependant on stitch architecture. The reduction in shear force appears as a hysteresis effect in the shear modulus when compared to the unreformed fabric shear modulus.

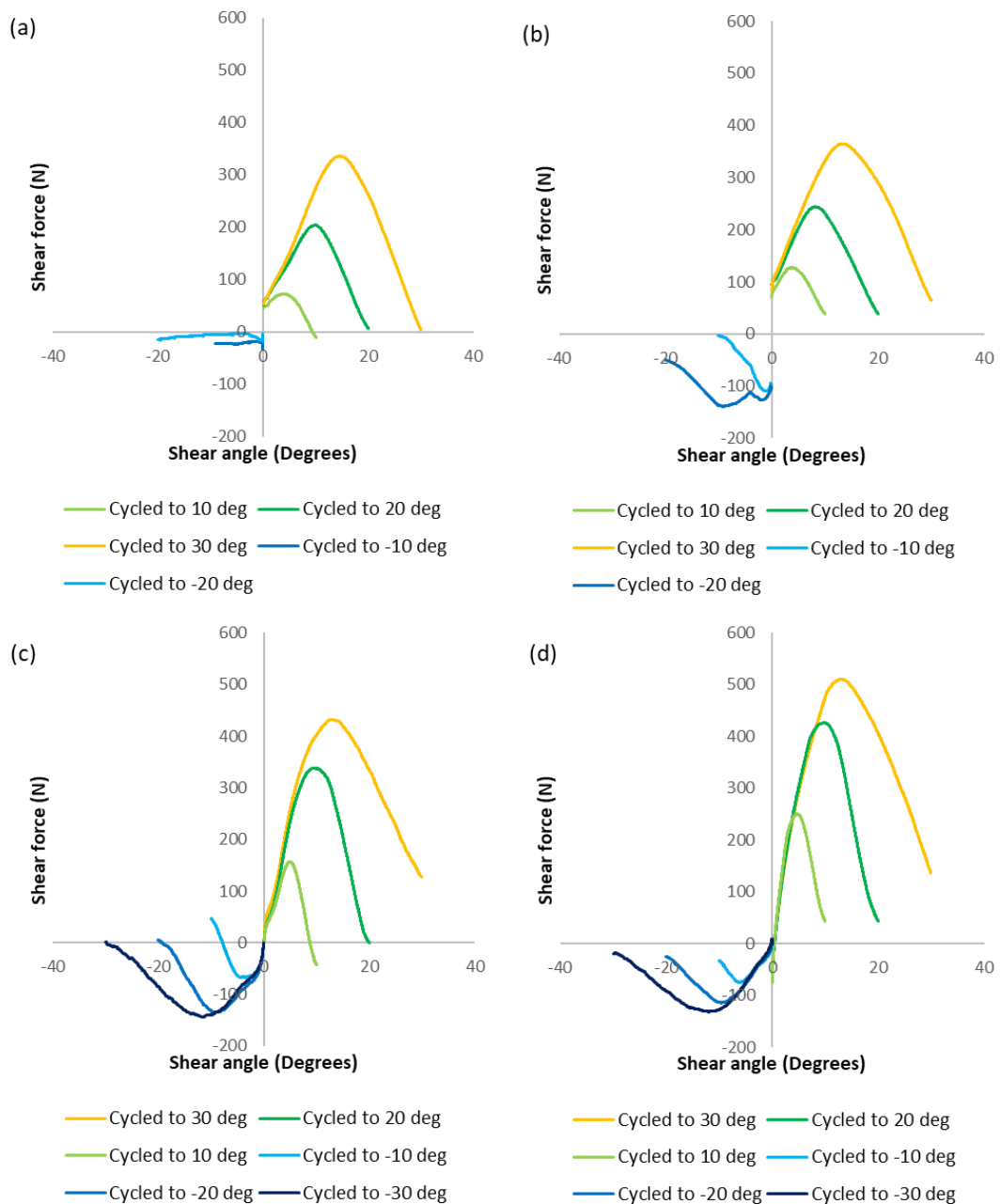


Figure 5-14 Reduction in shear force during second cycle extension in multi-cycle picture frame testing (a) Pillar stitched FCIM359. (b) Pillar stitched FCIM379. (c) Half pillar stitch pattern. (d) Tricot stitch pattern. Each fabric has sheared to the values in the legend before being returned to 0 and re-sheared. Separate tests conducted for positive and negative shear directions.

5.4.2 Multi-cycle stitch and yarn deformation

To study the deformation of the stitch during multiple shear cycles a selection of micrographs have been taken at various points during the multi-cycle picture frame test. Samples were taken before the test, after the maximum extension and after the frame had been returned to 0 extension. This was conducted with a value for A giving a shear angle of 30° . The material chosen was the pillar stitched material B, as the pillar stitch was the simplest stitch architecture from which to measure extension. 3 images have been created capturing the stitch deformation and 3 images capturing the change in yarn cross sectional shape and area in Figure 5-15 and Figure 5-16.

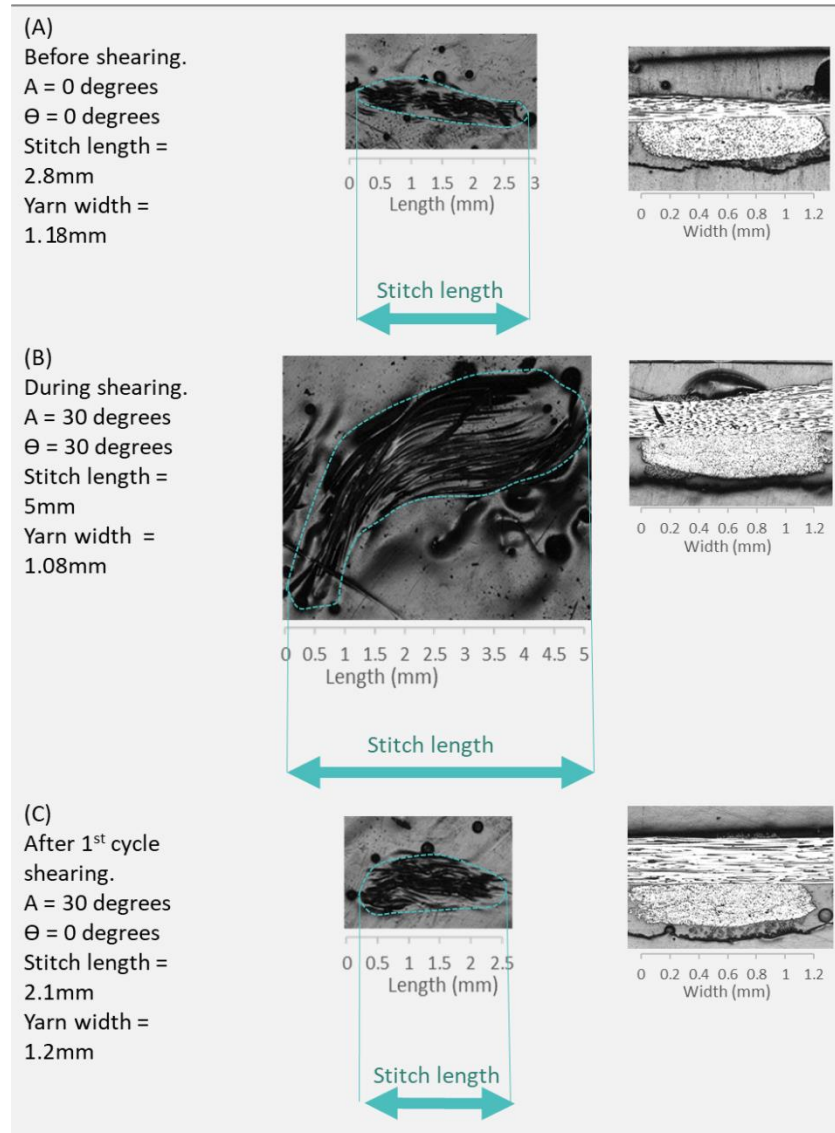


Figure 5-15 Micrographs of a pillar stitch (left) and accompanying yarn (right) NCF in an un-sheared state (A), during 30 degrees of imposed shear angle (B) and after being sheared to 30 degrees and returned to 0 degrees of shear (C).

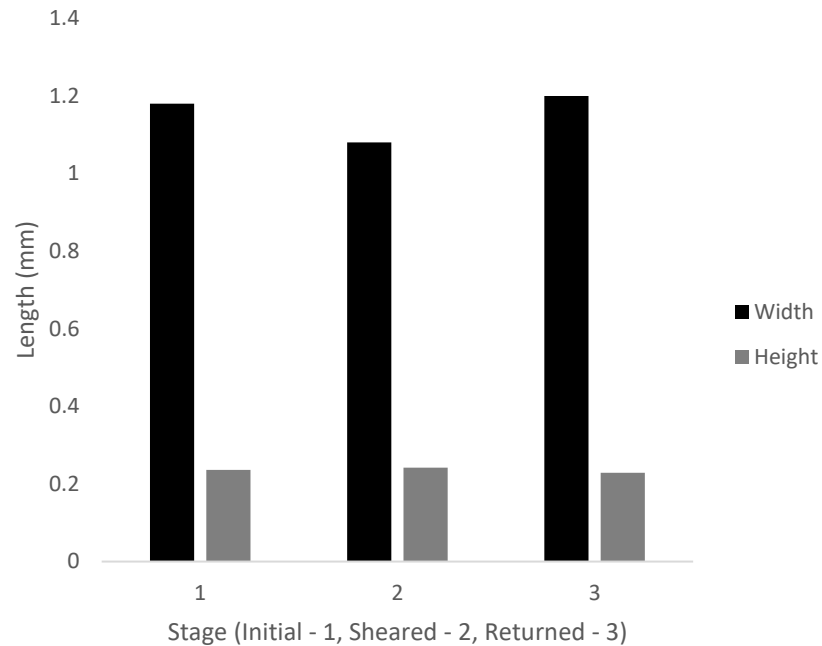


Figure 5-16 Mapping the yarn height and width for a pillar stitched NCF in an un-sheared state (a), during 30 degrees of imposed shear angle (b) and after being sheared to 30 degrees and returned to 0 degree of shear.

Figure 5-15 (A) shows the stitch before shearing. The stitch has a thin profile and a length of 2.8mm. Figure 5-15 (B) shows the elongation of the stitch during shearing to 30 degrees where it has almost doubled in length to 4.8mm. The curving of the stitch in Figure 5-15 (B) is due to the uneven tension in the loop of the pillar architecture. Figure 5-15 (C) shows the stitch when the fabric is returned to 0 degrees and a reduction in the stitch length has occurred from 2.8mm to 2.1mm. There is also an increase in the thickness and a bundling of the fibres that appears as a fuzziness to the stitch when observed with the naked eye. The change in stitch shape indicates a reduction in the amount of tension that is in the stitch post shearing. There is little change to the cross sectional area of the yarn during shearing and post shearing. Figure 5-15 shows the cross section of the yarn before shear (1), at 30 degrees of shearing (2) and after shearing (3). Figure 5-16 plots the width and height of the yarn at each of those stages. There is a 6% reduction in the yarn width at point (2) at maximum shear when compared to point (1) negligible change to the height of the yarn. The lack of deformation in the yarns indicates that the deformation to the stitch is a predominant factor in the shear force reduction seen in Figure 5-14 for the fabric during multiple cycles. When cycling the material a third time there is very little

change in the shear response when compared to the second cycle and results for 3rd cycle testing can be found in Appendix D.

5.4.3 Stitch extension results

5.4.3.1 Single-cycle stitch extension results

The objective of the stitch extension test was to quantify the impact that the stitch extension observed in Figure 5-15 has on the reduction in shear force over multiple cycles. The data was processed to allow a direct comparison to the picture frame shear test. The interpolated stitch extension in Figure 5-17 was shown to mirror the force requirement of the fabric shear response with the exception of the initial non-linear shear region in Figure 5-18. The gradient of the stitch extension results over 10 degrees is 35N/deg compared to 38N/deg for the picture frame test when the initial non-linear region is omitted. The lack of the initial non-linear shear high stiffness region that is seen in the picture frame test is due to the initial non-linear shear region being an artefact from a different deformation mode that is separate from the stitch extension and was explored in chapter 4. The similarity in gradients aligns with S.Chen's findings on the impact that removing the stitch during picture frame testing has on the shear modulus [14].

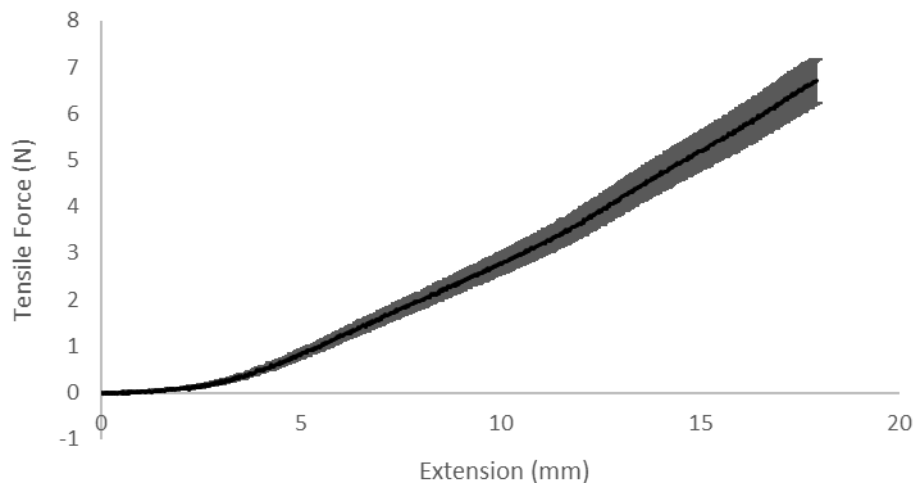


Figure 5-17 Average stitch force, extension results for a single pillar stitch

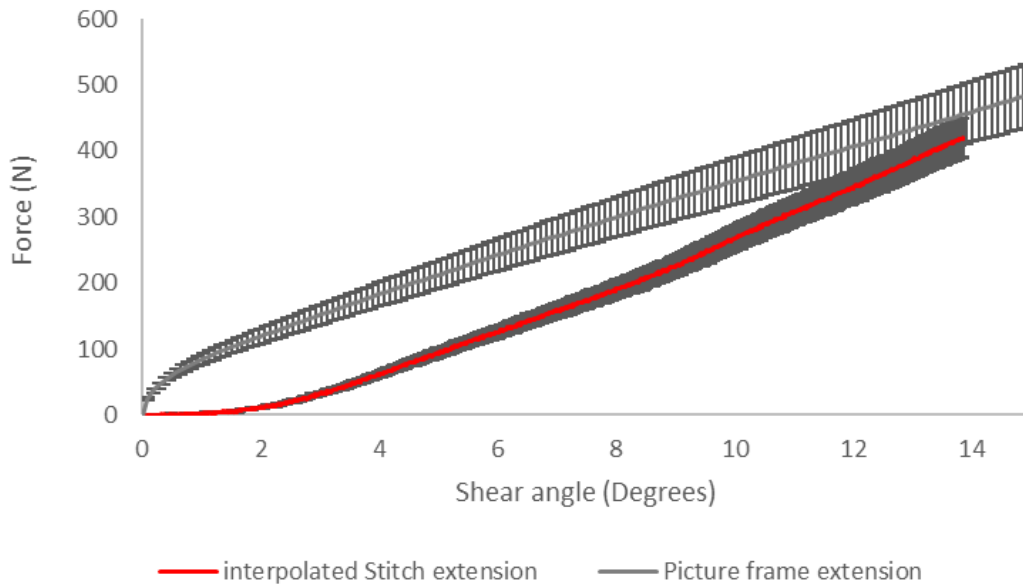


Figure 5-18 Comparison between picture frame shear results and interpolated stitch tension results for fabric (B)

5.4.3.2 Multi-cycle stitch extension results

Results from the multi-cycle stitch extension test showed that there was a significant reduction in the extension force needed to strain the sample in the second cycle compared to the first (Figure 5-19). By altering the initial amount of pre-extension in the first cycle, the second cycle response was altered, with increasing amounts of pre-extension generating greater reduction in the second cycle force requirement (Figure 5-19). This pattern is similar to that of the multi-cycle shear test where increasing amounts of first cycle shearing reduced fabric modulus in the following cycles. The comparison of the second cycle stitch extension to the second cycle of fabric shear shows a similarity in the shape and magnitude of the equivalent responses. An example is given in Figure 5-20 where the first cycle stitch extension of 15mm is compared to a multi-cycle picture frame test with first cycle shear of 5 degrees. In both cases there are two regions, a low stiffness region before 6.5 degrees of shear, followed by an increase in stiffness. Both tests show a similar low stiffness region. However, the stitch extension test produces a slightly higher modulus after the transition point at 6.5 degrees. The observations confirm that the stitch is responsible to the majority of the change in shear response after cycling.

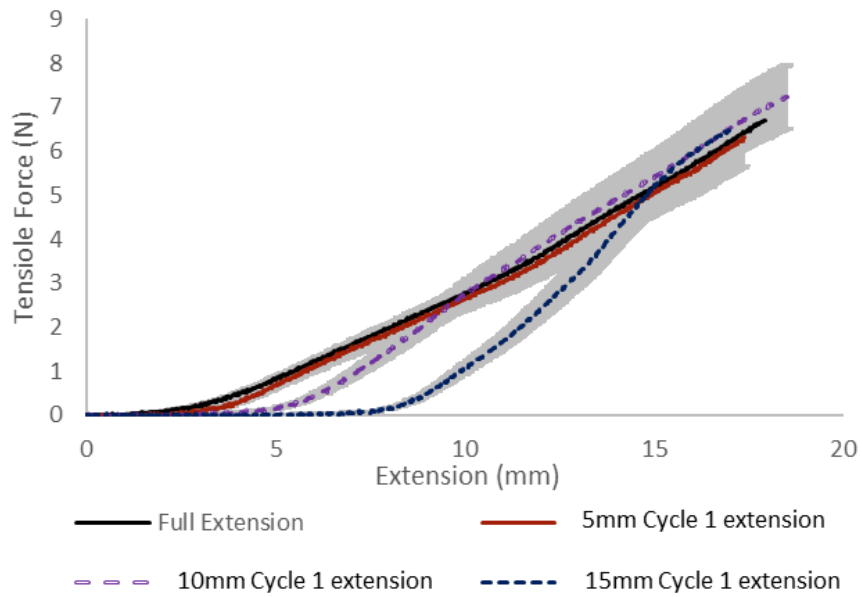


Figure 5-19 Multi-cycle stitch extension test results.

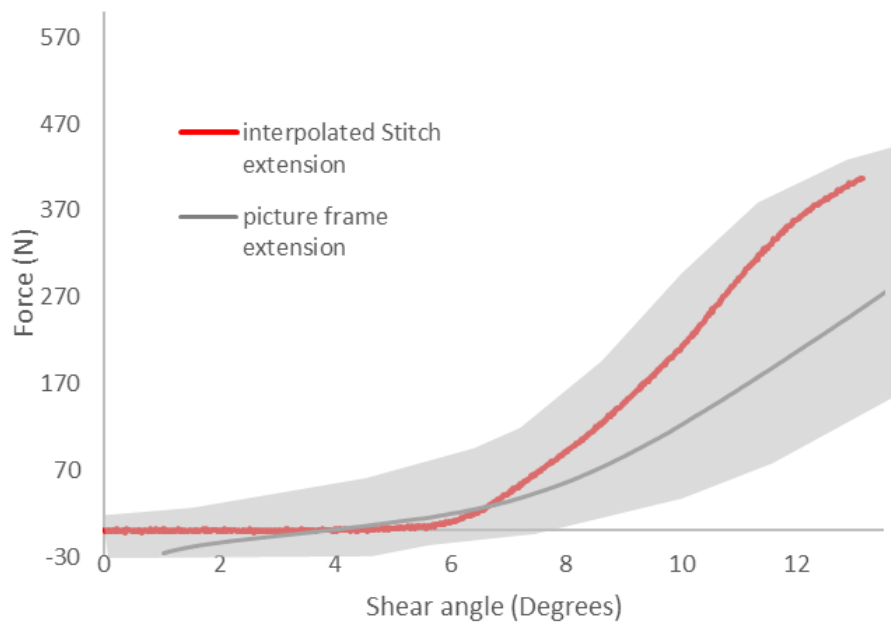


Figure 5-20 Comparison between interpolated stitch tension results and multi-cycle picture frame results for a fabric that has been strained to 15mm (7 degrees) in cycle 1.

5.5 Multi-cycle modelling results

5.5.1 Multi-cycle picture frame simulation results

Force-displacement data from the simulated picture frame test has been compared against experimental multi-cycle picture frame shear data for material B (pillar stitched NCF FCIM789). The material has been cycled so first cycle extension A generated shear angle values for 10, 20 and 30 degrees of shearing.

There is a good agreement between the output of the simulated finite element picture frame and the experimental results for each value of A with an R^2 value of 0.97, 0.95 and 0.98 for 10, 20 and 30 degrees of first cycle shearing between 0 and 50 degrees. The reduced shear force generated by the permanent stitch deformation at the end of the unloading cycle is well captured by the simulation with a peak deviation (over 10, 20 and 30 degrees of first cycle shear) of 5° and an average of 2° . The scale invariant polynomials are successful with R^2 values remaining high between the simulated and experimental results at 10-30 degrees of first cycle shearing. This extends to the re-loading section of the graphs, where the transition point from permanent deformation stitch to un-deformed stitch, is within 2° at all levels of first cycle shearing. The drop in shear force requirement at 0 degrees after the first cycle is well captured with the simulation averaging a $\pm 10\text{N}$ deviation. The stitch breakage point is accurately captured in all tests, falling within the experimental error and deviating from the average stitch breakage point by an average of 3° . The results show a high level of accuracy when modelling the multi-cyclic material behaviour under in-plane conditions. In order to maintain efficiency and avoid a significant increase in computation time per cycle, the experimental values reflecting a dip below 0 force on the returning shear cycle were deliberately excluded from the model. Incorporation of these values necessitated the addition of an additional variable. The observed force change is consistent with the presence of a residual compressive force resulting from the permanent deformation of the stitches during the initial cycle.

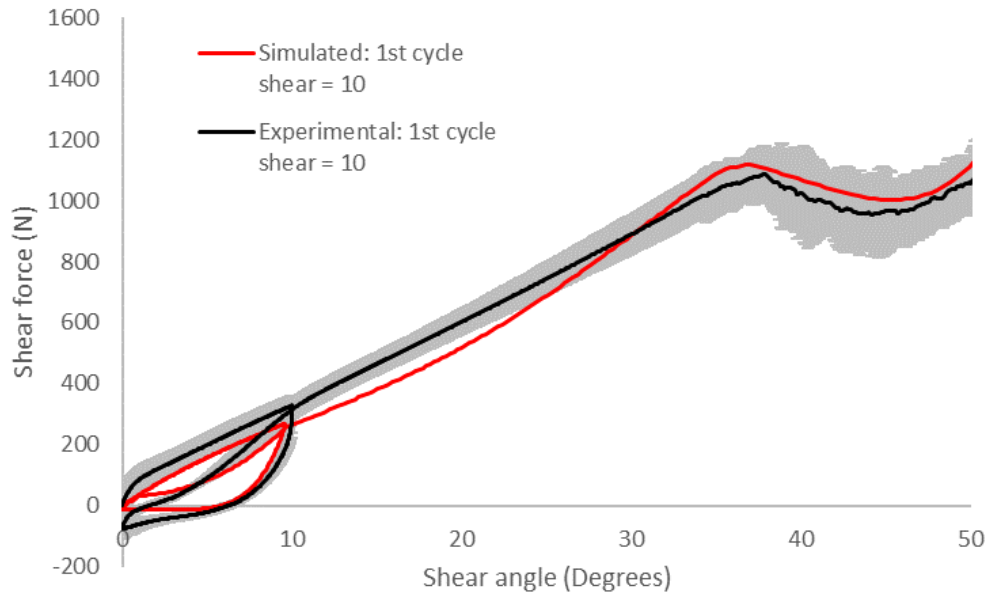


Figure 5-21 Multi-cycle picture frame test comparison between finite element picture frame and experimental test data. First cycle shearing = 10 degrees. Second cycle shearing = 50 degrees.

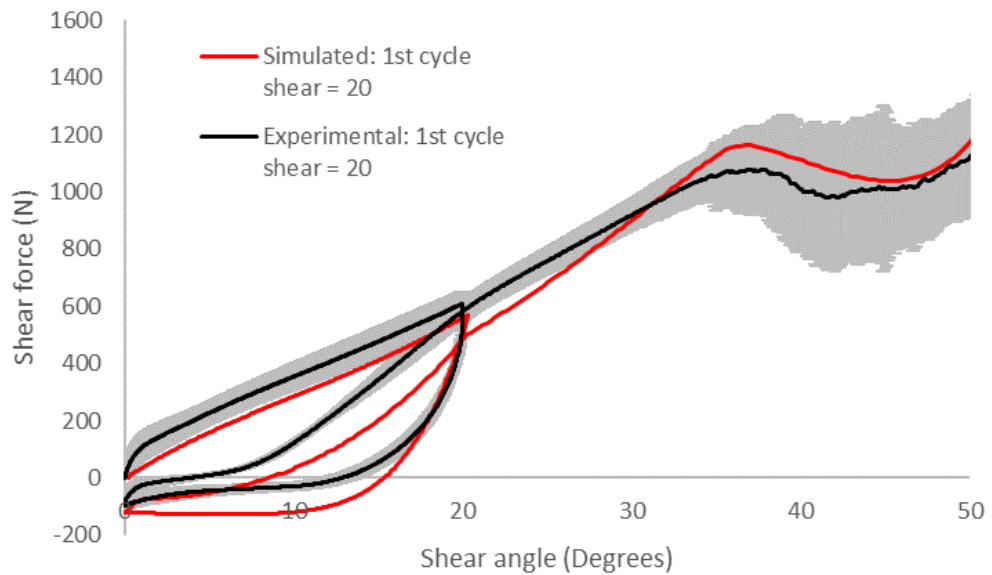


Figure 5-22 Multi-cycle picture frame test comparison between finite element picture frame and experimental test data. First cycle shearing = 20 degrees. Second cycle shearing = 50 degrees.

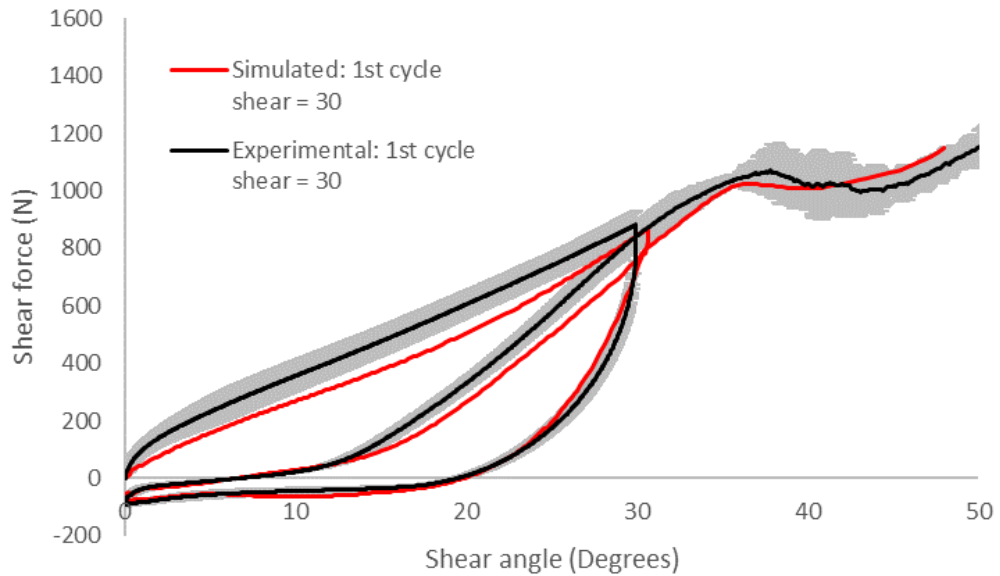


Figure 5-23 Multi-cycle picture frame test comparison between finite element picture frame and experimental test data. First cycle shearing = 30 degrees. Second cycle shearing = 50 degrees.

5.5.2 Multi-cycle diaphragm forming results

The multi-cyclic material model was applied to multi-stage forming simulations to test the practical application of the model. A representative model of the multi-stage double diaphragm forming process was created and assessment criteria were established, shear angle distribution and topology. Simulation results for shear angle distribution and topology were compared to experimentally formed hemispheres. The aim was to explore how use of the multi-cyclic material model improved simulation accuracy under these two criteria. A secondary objective was to see the difference in ply-tool conformity between a single-stage and multi-stage forming process and assess the potential forming benefits of a 2 stage forming process.

5.5.2.1 Multi-cycle material model forming validation

A hemisphere was formed using the multi-cyclic diaphragm forming process. This was scanned using the optical scanning methodology from Appendix (A) and chapter 3 to output the geometry data and the shear angle distribution. The distribution of shearing matched what is expected for a formed NCF hemisphere. There are two opposing and symmetric regions of high negative shearing. At 90 degrees to those regions are 2 roughly equal regions of positive shearing. The positive shear regions

are underrepresented on the contour plot in Figure 5-24, due to the wrinkle formation that has been captured as areas of very high shear angle using the optical scanning method.

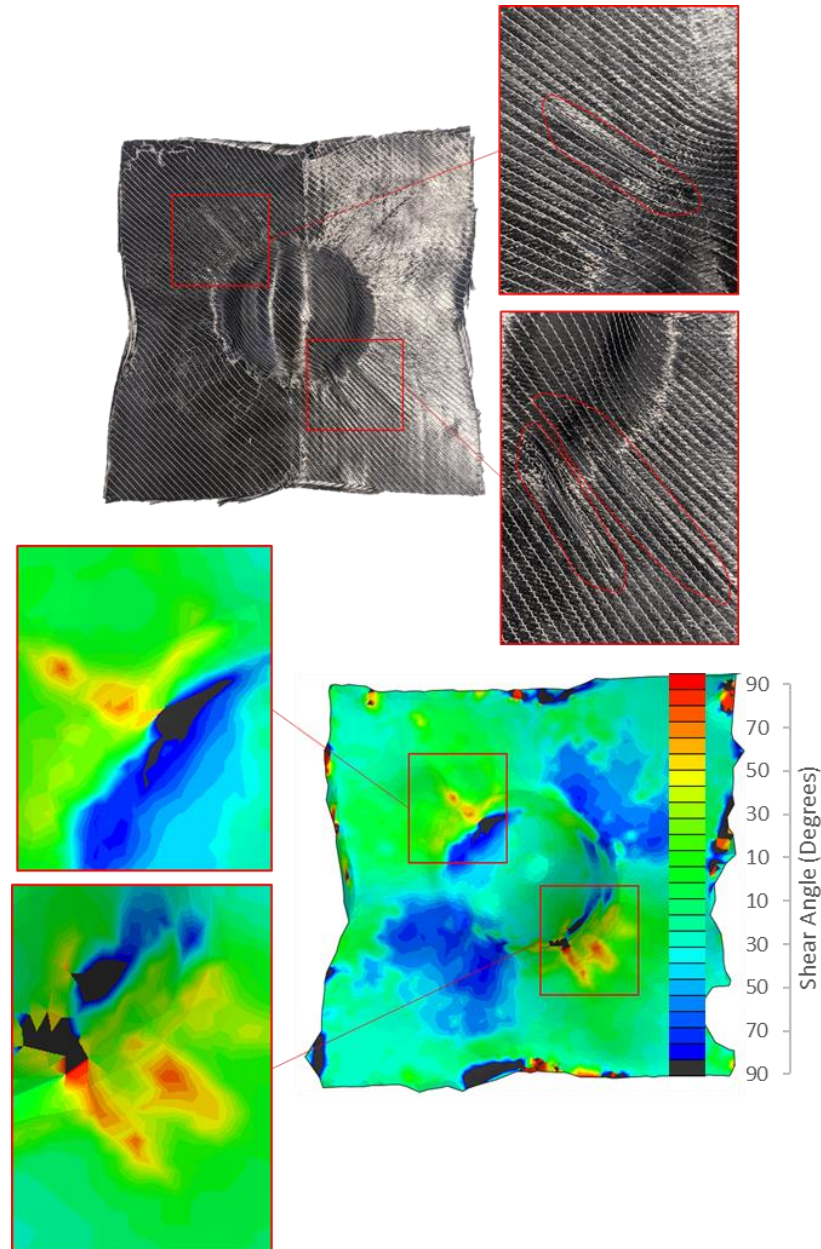


Figure 5-24 *Imaging and optical scanning of a multi-cycle diaphragm formed hemisphere. Wrinkling defects have been identified as regions of high shear angle.*

The optically scanned hemisphere was compared to simulations run under the same conditions outlined in the simulation methodology (Figure 5-25). The simulation was run with an equivalent non-cyclic material model that does not include the unloading and re-loading curves from Equation 5-14 and Equation 5-15. This was

compared to a simulation run with the multi-cyclic material model. There is a significant difference between the simulation that includes the multi-cyclic material model and the one that does not. Twelve elements were evaluated from each of the positive and negative shear regions on the hemisphere and compared between models, showing a 40% increase in the average shear angle using the multi-cyclic model. The non-cyclic material simulation had a peak shear angle that does not exceed 23 degrees compared to 43 degrees for the multi-cycle model. The simulation that includes the multi-cyclic material model has a shear angle distribution that is very close to the experimentally formed hemisphere with a difference in peak shear angle of 4%. Differences between experimental and simulated results occur in the regions where wrinkles were identified. It is a known flaw of the membrane element approach to non-constitutive modelling that the model does not accurately capture this wrinkling behaviour.

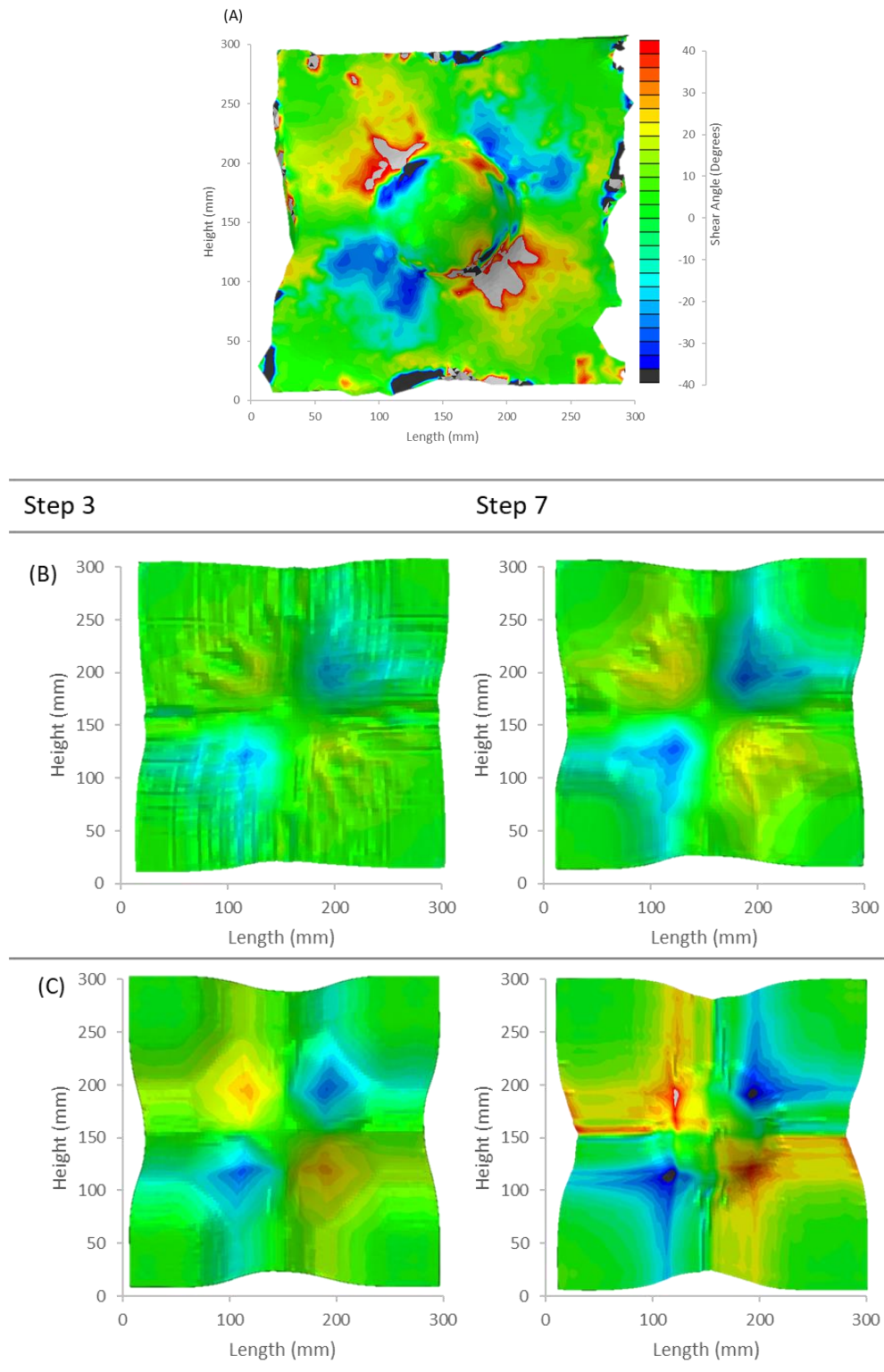


Figure 5-25 Multi-cycle diaphragm formed hemisphere simulation. Comparison of results between experimental testing (A) simulated results with a non-cyclic material mode (B), and simulated results with the multi-cyclic material model (C)

5.5.2.2 Assessment of multi-stage diaphragm forming process

Simulations have been run for a single-stage diaphragm forming process and compared to the multi-stage method. This was repeated experimentally and data was collected using the optical scanning methodology. The shape of the pre-form is compared for both processes in Figure 5-26. The multi-stage diaphragm forming model conforms to the tool visibly to a higher degree than in the single-stage process.

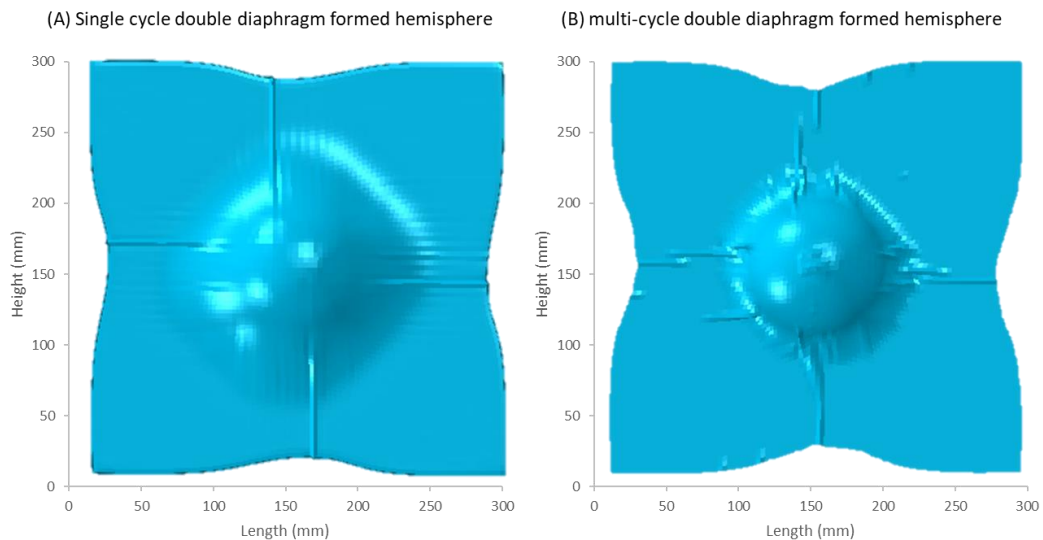


Figure 5-26 (A) Single-stage double diaphragm formed hemisphere simulation using multi-cyclic material model. (B) Multi-stage double diaphragm formed hemisphere simulation using multi-cyclic material model.

To quantify the conformity of the ply, the difference between the ply and tool surface was measured and compared between the single-stage and multi-stage forming processes. This was conducted for both the simulated and experimental results. A point to plane distance algorithm was used in CLOUDCompare to measure the space between the ply and the tool surface. A baseline thickness of 2mm was used to accommodate the material thickness and as such each ply surface measured above 2mm was classed as a defect. Figure 5-27 compares the number of nodes classed as a defect in each of the forming processes. The results cover the output from the simulation and the experimental testing. Results from Figure 5-27 show a reduction in the average defect amplitude of 50% using the 2 stage diaphragm forming methodology. The maximum defect size is reduced by 25% and the average number of nodes with poor conformity (tool ply distance of over 2mm) is reduced by 57%.

Comparison between the simulated hemispheres and experimental testing shows a good agreement with a R^2 value for the single stage method of 0.92, and 0.94 for the multi-stage method. The multi-stage experimental form and the cyclic material model show an average nodal discrepancy of 3 nodes and a peak of 20 nodes for a ~5000 node model. The cyclic material model predicts a slightly lower conformity than is observed in the experiment. This is more apparent at larger defect sizes where the cyclic model predicts the appearance of 300% more defects above 5mm than is captured in the experiment. In the experiment the number of defects is negligible for defects larger than 7mm. The difference between results is likely due to the inability of the membrane modelling approach to accurately capture wrinkling. The high magnitude wrinkles are in local concentrations and make up a small proportion of the nodes in the simulation and as such the cyclic material model can be used to accurately predict the final formed shape for multi-stage forming processes. Future work would look to implement the scale invariant polynomials into a shell based continuum approach material model that includes bending stiffness, so wrinkling can be properly captured.

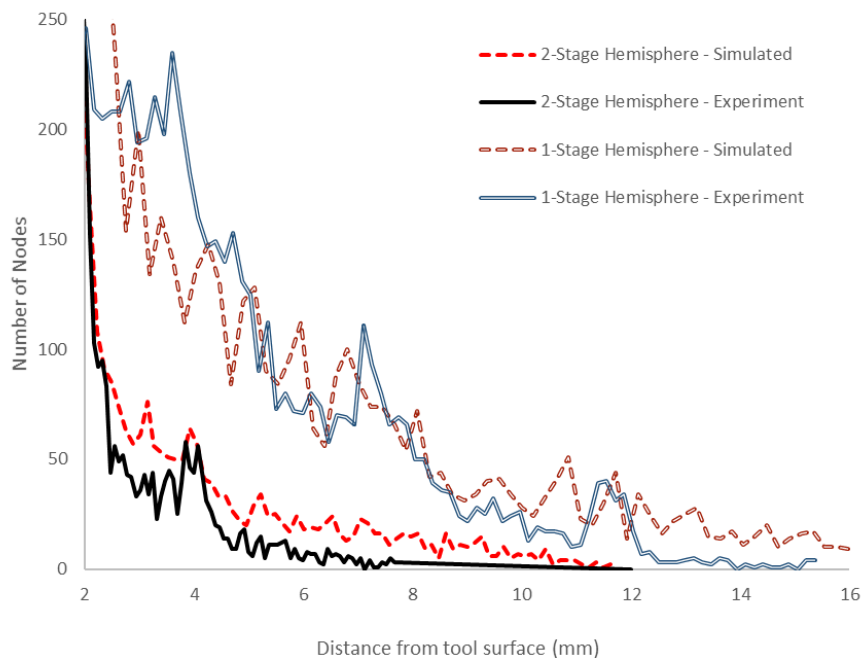


Figure 5-27 Nodal difference between the ply and the tool for a double diaphragm formed hemisphere. Simulated and experimental results for simulated and experimental tests for single and multi-stage diaphragm forming processes.

5.6 Chapter summary

A hysteresis has been identified in the shear force response of biaxial NCF fabrics when they are subjected to multiple load cycles. This is determined to be due to permanent deformation of the stitch during loading. The reduction in the shear force requirement has been found to vary based on the cycle 1 shear angle, and in the majority of cases a significant reduction in shear force is observed.

A multi-cycle finite element material model has been created that accurately captures the hysteresis phenomenon on a simulated picture frame test to within 8% of experimental values.

A multi-stage double diaphragm forming process has been proposed as a method of validating the new material model in a forming scenario and showing the benefits of multiple stage forming processes. The process uses a novel mould tool in stage 1 that is related to the final mould tool (to be used in stage 2) and locally induces regions of high shear with the objective of taking advantage of the multi-cycle hysteresis in the fabric.

The process was successfully modelled with the multi-cycle material model and demonstrated a significant improvement to the accuracy of the shear angle distribution over the simulated hemisphere when compared to current (non-cyclic) membrane modelling techniques. When compared to experimentally formed components the model predicted the formed shape with a deviation of 2mm.

The multi-stage diaphragm forming process using the novel stage 1 mould tool showed an improvement in ply-tool conformity with maximum defect size reduced by 25%. This is successful in generating a better pre-form by conditioning the fabric via multiple forming stages.

6 Maintaining fibre continuity over formed composite components

Abstract

A method has been developed to align the fibres within biaxial non-crimp fabric (NCF) plies along the principal load path of a spar-like geometry, following an automated forming process using local fabric pre-shearing. This generates a 20% improvement in the stiffness of the part over an equivalent standard laminate of the same ply count. A structural finite element (FE) model has been created to show the reduction in peak stress that can be achieved through the use of pre-sheared laminates in comparison to standard laminates for beam-like geometries. To inform the structural FE model, a forming simulation has been generated to model the fibre orientations of pre-sheared fabrics. Together with the orientation data, an experimental study has been conducted to measure the increase in fibre misalignment that occurs as pre-shear angle increases, incorporating the change in fibre volume fraction into the material input data used in the constitutive model. The amount of material needed to create pre-sheared laminates has been compared to standard trimming methods through geometric analysis and the wastage was evaluated showing a 16%-35% reduction in the amount of material needed. Results from mechanical modelling indicate a 23% reduction in the peak stress in the component under tensile loads when using pre-sheared laminates over a similar standard laminate architecture. A 20% reduction in peak stress was observed in bending and 16% in torsion.

6.1 Introduction

6.1.1 Chapter Objectives:

- Develop a methodology to locally control fibre orientations in a 2D blank, to enable fibres to follow key geometric features within the component using pre-sheared fabrics from low cost broad goods.
- Create a finite element model that can accurately predict and plot the fibre orientation of pre-sheared fabrics.
- To model the effect of localised fabric pre-shearing on the structural performance of formed components.

6.1.2 Local fibre alignment

The advantage of fibre reinforced composites is the anisotropy that enables the mechanical properties to be tailored for each individual application. Yet most composites are un-optimised and are therefore over conservative, as they the fibres are not aligned with the principal stresses . The literature shows that a small misalignment in fibre angle from the load path will cause a significant reduction in laminate stiffness (up to 20% per 5 degrees) [110]. To retain a laminate that meets the structural criteria, complex parts have regularly been split into sections that can be designed independently or semi-independently [111, 112]. Variable angle yarn (VAT composites) have proven to be an effective method of sectioning components and locally aligning fibres to the desired structural load path. However sectioned laminates are susceptible to stress concentration points that form at the boundary between the continuous regions [113], therefore modern composite manufacturing methods aim to maximise fibre continuity where possible. Fibre steered laminates were first developed to reduce the sensitivity of the first ply failure response to holes and were used as an alternative to increasing the laminate thickness. Locally tailoring the fibre direction was an achievable and effective method for improving buckling failure characteristics than un-steered fabrics, as the steered fabric showed a 13% reduction in peak stress around the hole [98]. Currently research is being conducted into advancing the control of fibres in automated fibre placement (AFP) to apply fabric steering globally through the use of continuous yarn shearing [114]. By continuously deforming the yarn, the curved yarn path maximises continuity, providing new levels of freedom in the laminate design space. A similar level of laminate design freedom is desired in 2D-3D forming processes without the use of an AFP head.

6.1.3 2D-3D forming

The tailoring of local fibre angles through fabric shearing is simple during hand layup, but much more difficult to implement when the forming process is automated. 2D-3D formed composites aim to maximise mechanical properties. However, as 2D blanks are used rather than a 3D preform there is far less control that can be had over the local fibre angle distribution. The fibre orientation and content (volume

fraction) dominate the maximum mechanical stiffness, but conversely affect the drape characteristics of the un-infused laminate. Significant research has been dedicated to reducing forming induced defects governed by fibre angle and intra-ply shearing [48, 115-117]. Drapability is a term derived from the textiles industry describing a fabric's conformity to moulds. Drape is heavily shear dependent as localised shearing allows for drape (alongside fabric bending stiffness). Controlling drape has been used to improve the quality of preforms. Optimally positioned grippers [48] around the edge of the fabric have previously been used to control fibre tension during forming and control the level of shear generated. This was successfully used to remove wrinkling defects in areas that previously suffered from over shearing. Darts have been implemented to reduce tension in local regions and improve formability (Figure 6-1). The use of darts is only possible in run off areas and fabric that will be trimmed away from the part in a later operation. This is because the darts open up during the forming operation creating a local thickness reduction. There is the possibility of utilising or adapting the current orientation control methodologies designed for defect reduction to improve the stiffness and damage criteria properties. The effectiveness of these strategies can also be quickly tested using current finite element forming models [14].

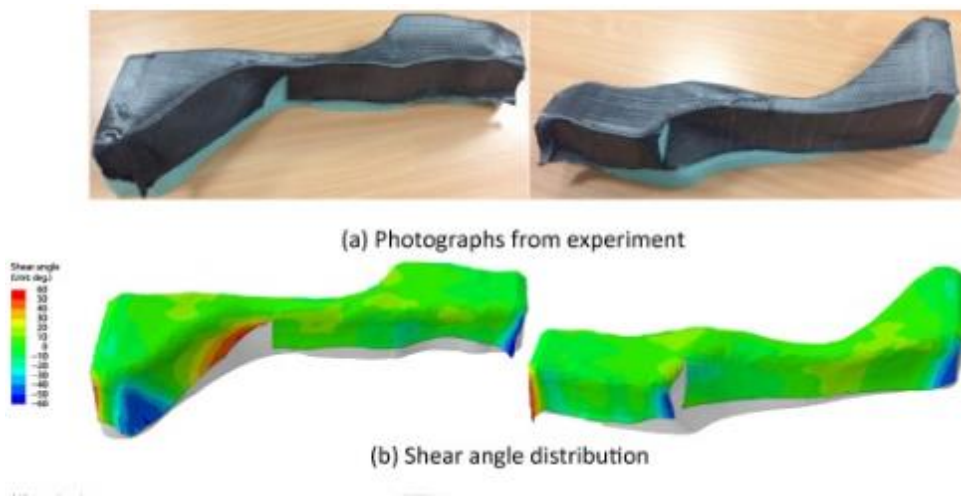


Figure 6-1 Demonstrator sill section Geometry formed with darts to improve formability. Simulation was conducted in Abaqus by S.Chen and compared to experimental images. [37]

6.1.4 Current work

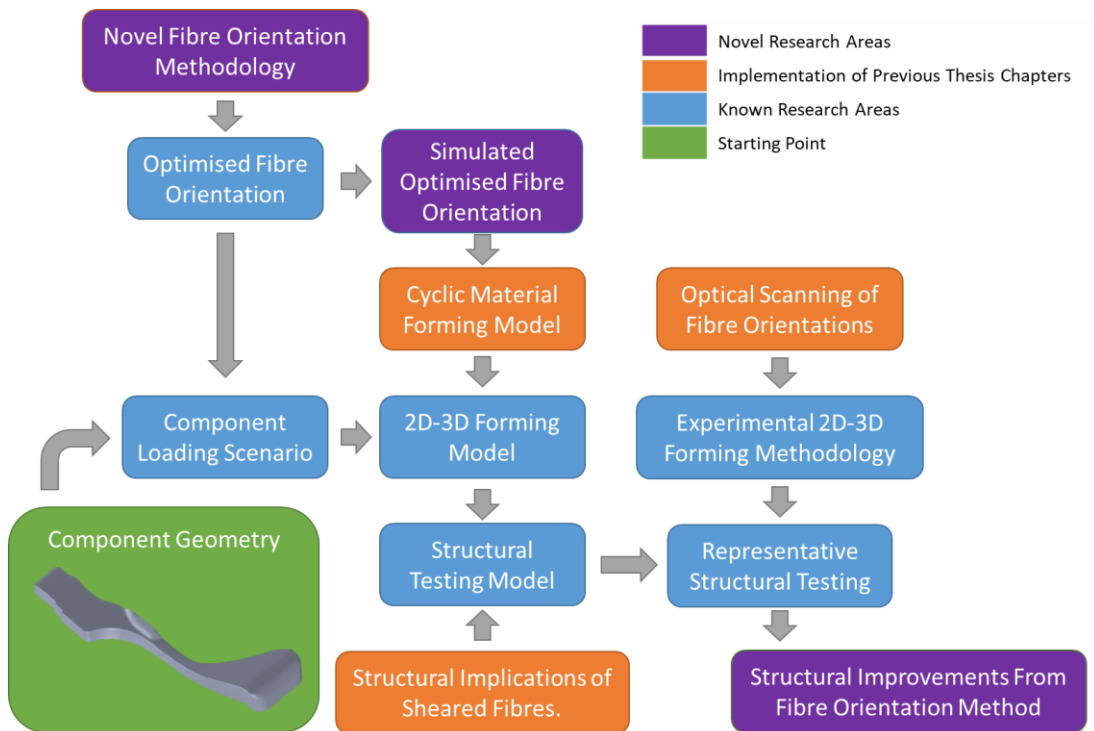


Figure 6-2 Flow chart of chapter research areas and the implementation of previous chapters.

This study looks at developing a novel fibre orientation control methodology to pre-shear the flat blank used in NCF forming. The objective was to improve fibre continuity in local regions along load paths, in order to generate improvements to the stiffness of the final laminate. The multi-cyclic material model was used in forming simulations to generate topology and fibre angle data, which was used to update fibre misalignment figures. This was integrated into a custom material model, which assessed the structural improvements of the moulded composite to be gained from incorporating pre-sheared laminates. The optical scanning methodology was used to measure the pre-shearing generated with the orientation control methodology and validate the successfulness of the method and the validity of the simulation results. A complex structure was then formed to highlight the application of multiple pre-shearing regions.

6.2 Methodology:

6.2.1 Non-uniform shearing across a fabric length

Shearing of fabrics creates non-orthogonal regions where the principal yarn directions are dependent on the amount of strain applied and the initial orientation. This naturally occurs in local regions during forming operations, as the fabric shears to accommodate double curvature surfaces, but it can also be manually applied to the fabric to control fibre direction [54, 118]. Applying uniform shear across a section of fabric causes the yarns to rotate, which is well documented from shear tests such as the bias extension and picture frame test [71]. The local fibre orientation distribution and the blank shape and can be controlled, by selectively shearing regions of a fabric as seen in Figure 6-3. This has the effect of bending the fibres in between sheared and un-sheared region, which maintains fibre continuity across the blank. Figure 6-3 shows that a complex blank shape can be generated from a simple initial blank. This also opens up the opportunity of reducing wastage during kit cutting by reducing the trimming needed to create complex blanks. The 100mm x 300mm rectangular blank in Figure 6-3 (b) can easily be tessellated with little wastage compared to the more complex 200mm x 300mm L-beam blank from Figure 6-3 (a) where there will be a compromise on utilisation and fibre orientation.

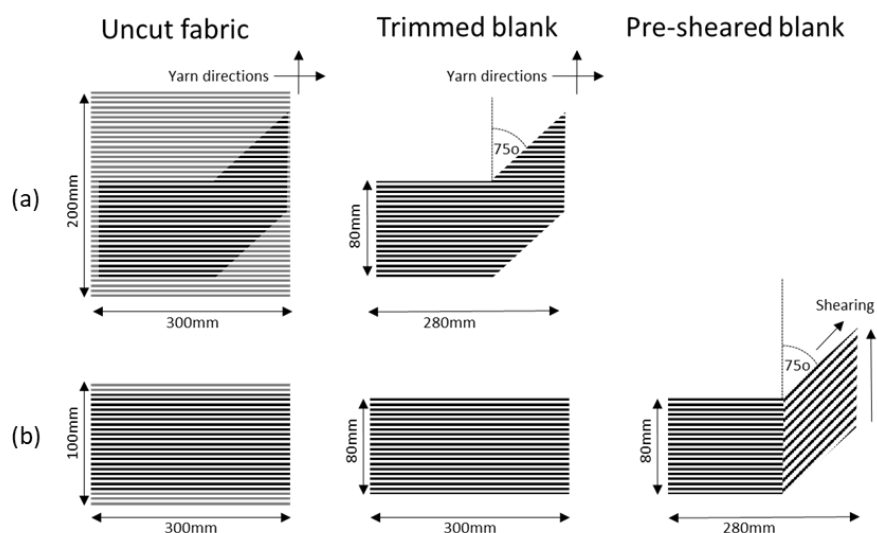


Figure 6-3 Comparison of (a) a standard trimming process and (b) a pre-shearing process for an L-beam geometry. A variable fibre orientation is not possible through standard trimming methods.

6.2.1.1 Measuring wastage

A standard kit cut area was measured by taking the smallest rectangular piece of fabric that would accommodate the entire blank. This assumed that tessellation of multiple preforms is not possible, (due to small batch numbers, complex geometries and the necessity to use specific fibre orientations).

The kit designed for pre-shearing was calculated by locating the areas to be pre-sheared on the blank, then the blank was created by taking a rectangular section and shearing it at the required points. All of the sheared preforms required additional width in the areas that were to be sheared to account for the angular translation, in order to maintain a constant section width. An additional 10mm of fabric was also needed on either edge of the pre-sheared regions to enable the clamps to grip and manoeuvre the fabric. The area for both blanks was calculated with the inclusions stated above. The difference between the two areas gives an indication for the improvement in material usage that could be gained through pre-shearing.

6.2.1.2 Localised shear frame

The picture frame test shears the fabric sample uniformly over the entire blank area, as it is constrained within the frame. By changing the shape of the frame, shearing can be applied to control the local fibre direction. This enables the ply shape from Figure 6-3 to be created as-well as other more complex sheared blank shapes with multiple locally sheared regions.

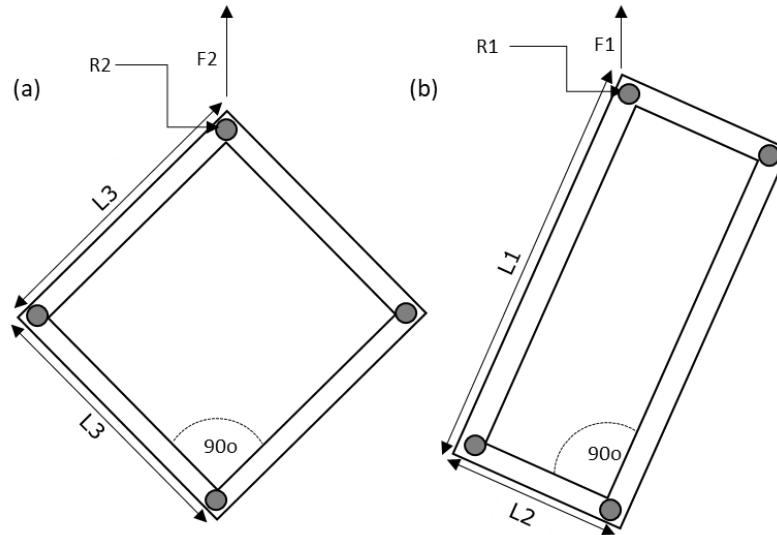


Figure 6-4 (a) Picture frame shear rig with equal side length and (b) localised shear frame with non-equal side length

Similar to the picture frame test, the shear angle of the material in the localised shear frame can be directly related to the crosshead displacement, however the frame lengths are un-equal due to the difference between L_1 and L_2 [21] shown in Figure 6-4. A square frame with an equal edge length, L_3 , is compared to an equivalent rectangular frame with edge lengths L_1 and L_2 and is described by Equation 6-1 . With the square frames $2L_3$ replaced with $L_1 + L_2$

$$\theta = \frac{\pi}{2} - 2\arccos \left[\frac{1}{\sqrt{2}} + \frac{d_{pf}}{L_1 + L_2} \right] \quad \text{Equation 6-1}$$

The force required to shear a rectangular area to a set angle is the same as a similarly sized square section. Equation 6-2 and Equation 6-3 describe two shear frames with different shapes: a rectangle of side lengths L_1 and L_2 , and a square frame of side length L_3 . Forces F_1 and F_2 act on points R_1 and R_2 respectively.

As an energy equation, the work done to extend the frame is W_1 and W_2 , and the corresponding displacements are Δ_1 and Δ_2 [119]

$$W_1 = \int F_1 d\Delta = \bar{F}_1 \Delta_{R_1} \quad \text{Equation 6-2}$$

$$W_2 = \int F_2 d\Delta = \bar{F}_2 \Delta_{R_2} \quad \text{Equation 6-3}$$

The work done is converted to strain energy in the form of a shear deformation to the composite with more yarns in a larger area resulting in the need for a higher load. The work done per unit area is the same in both frames, so by normalising for area, a comparison of the work done in a rectangular frame has been compared to that of a square one.

$$\frac{W_1}{W_2} = \frac{\bar{F}_1 \Delta_{R_1}}{\bar{F}_2 \Delta_{R_2}} = \frac{A_{L12}}{A_{L3}} = \frac{L1 \cdot L2}{L3^2} \quad \text{Equation 6-4}$$

Equation 6-4 calculates the shear angle of non-square samples with a force requirement similar to that of an equal square area. By clamping sections of a fabric with correctly shaped frames, local shearing can be applied along a length. This can be seen in Figure 6-5, where a series of linked clamps have been used to shear small regions along the fabric. The final preformed shape can be controlled by changing the target angle of each clamp, following the same principle described above for shearing non-square sections. The top and bottom edge of the sample are traditionally clamped for each small section. The vertical edges of the sample are unclamped and are constrained by the un-sheared material neighbouring the clamped region. The vertical yarns in the neighbouring regions are also clamped to prevent unwanted shearing at the boundary. This removes the need for clamps to be placed across the sample length at each point where transitions in shear angle occur. Multiple small clamped regions can be sheared simultaneously to locally shear larger sections of the fabric, as shown in Figure 6-5.

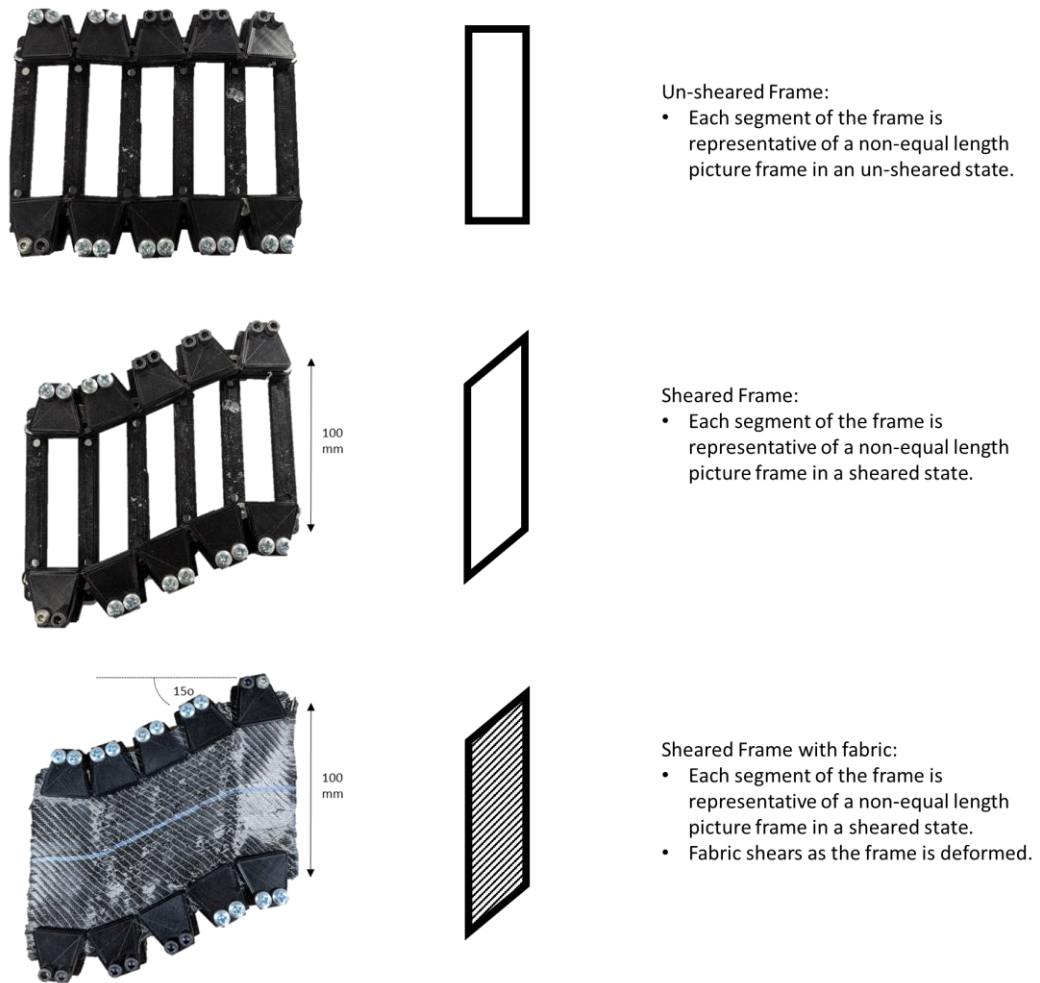


Figure 6-5 Development of multi point pre-shearing rig showing the application of 15 degrees of shearing to the middle of a beam like sample.

6.2.2 Diaphragm forming pre-sheared fabrics

Diaphragm forming requires the ply stack to be suspended between two polymer diaphragms which are vacuum formed over a mould tool. To form a pre-sheared blank via diaphragm forming it was first stabilised with binder to maintain the applied shear angle. The blank was then placed between the diaphragms along with the rest of the ply stack and the inter-diaphragm vacuum was applied to compress the plies. This was heated to above 75°C to allow the binder in the pre-sheared ply to melt, enabling the ply to be vacuum formed along with the rest of the ply-stack, as shown in Figure 6-6.

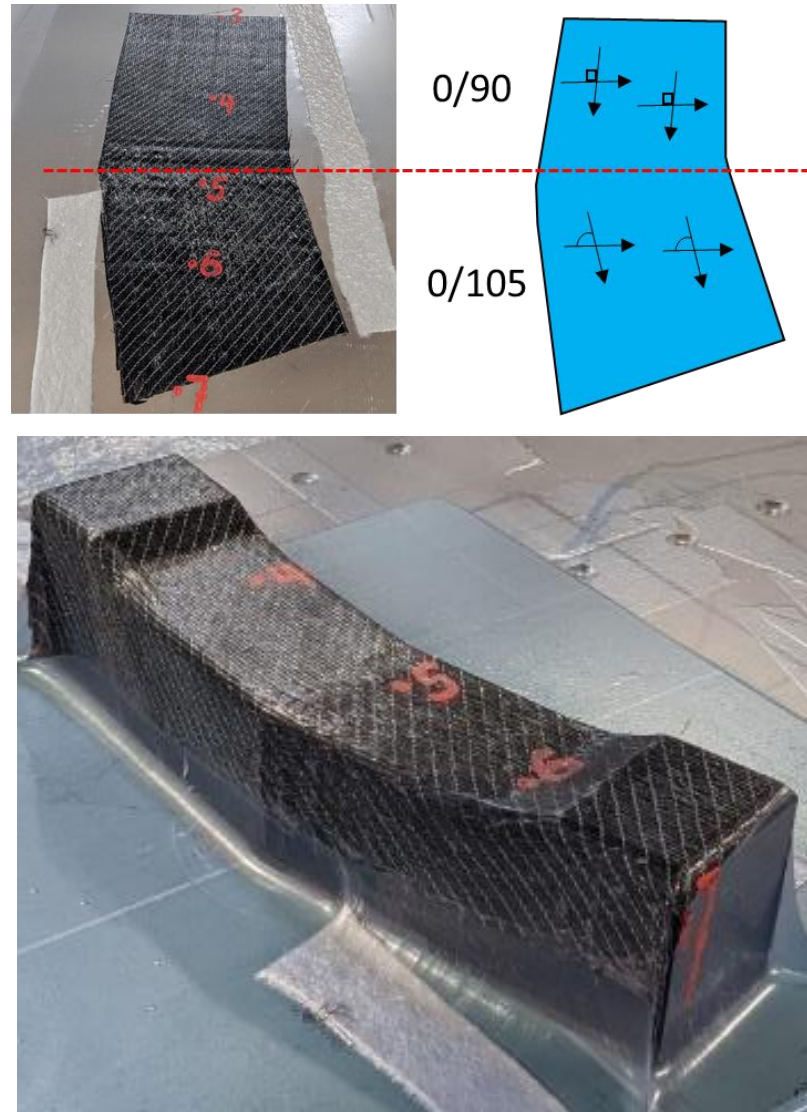


Figure 6-6 double diaphragm vacuum forming of pre-sheared ply.

6.2.3 Finite element forming model

A finite element simulation has been employed to enable the testing of different loading scenarios and laminate options in a compressed timeframe, without the need for multiple custom experimental test rigs. The modelling has been conducted in 2 parts. A forming simulation provided the shear angle data, volume fraction information and misalignment data, which is then superimposed onto an idealised mesh of the component from which mechanical testing was performed. The forming simulation was conducted in Abaqus/Explicit and the mechanical simulation by Abaqus/Standard, with the mesh data transfer and analysis being run in Matlab. The

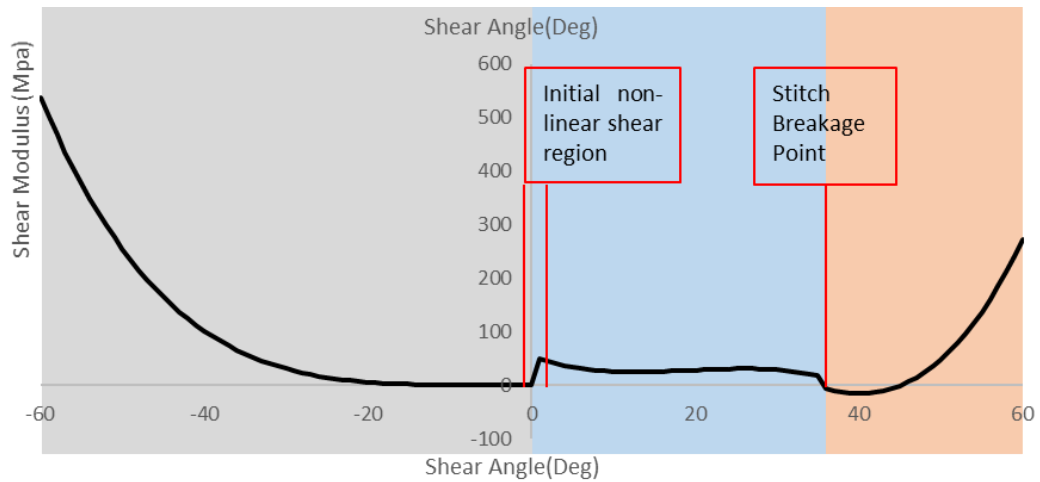


Figure 6-8 Shear modulus- shear angle plots for NCF fabric over shear angle ranges of -60 degrees to 60 degrees. Highlights the changing stitch deformation modes.

6.2.3.2 Pre-shearing implementation

To apply pre-shearing, a localised orientation was introduced onto Arm 1 of the L-beam model. A rectangular local orthogonal coordinate system was created for each principal fibre direction. These were defined by a point on the X' -axis and a second point in the X' - Y' plane of the material. The local direction for each principal fibre direction was defined as shown by Figure 6-9. These were implemented in the orientation parameter within Abaqus, which provided control over the section assignment and relative orientation of each coordinate system. Forming simulation were run for biaxial ($45^\circ, -45^\circ$) and ($0^\circ, 90^\circ$) plies, and pre-sheared ($0^\circ, 90^\circ$) – ($-15^\circ, 90^\circ$) plies shown in Figure 6-10.

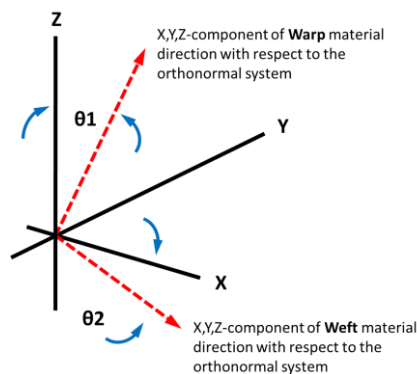


Figure 6-9 Components of local warp and weft material direction in respect to the global material orientation

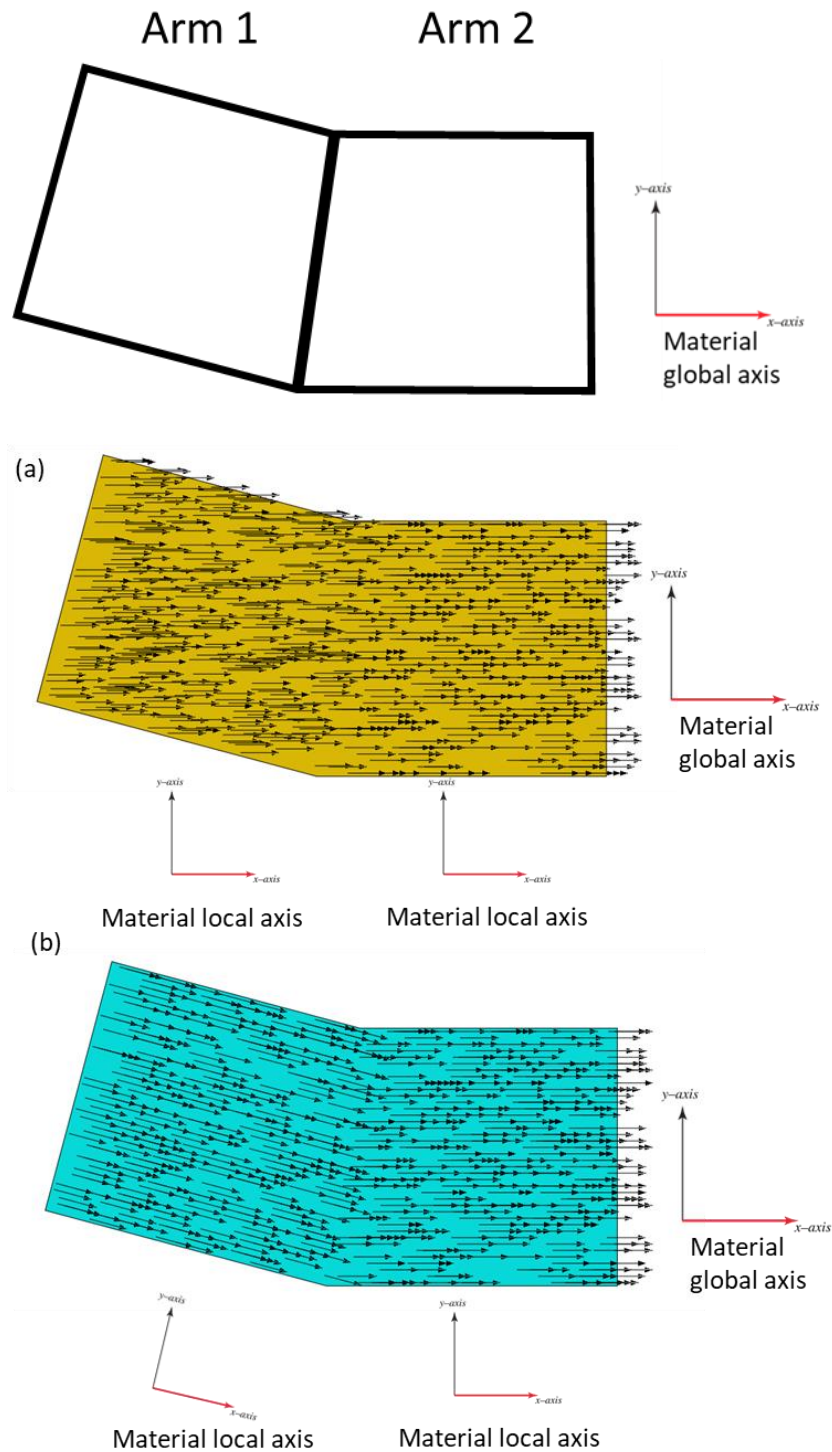


Figure 6-10 Standard L-beam blank (a) L-beam blank with locally re-orientated material direction on arm 1 to -15 degrees (b).

6.2.3.3 3D Forming simulation

The forming model is a representation of the diaphragm forming process described in Section 4.2.2. The two diaphragms, the ply and the tooling were modelled as

individual parts, with the tooling defined as a rigid body similar to the simulation setup used in the previous chapter. Each ply was cut into an L-shape with Arm 1 at a 15° offset from Arm 2, as seen in Figure 6-10 (b). The width of each leg was 100mm and the ply was discretised into 1mm x 1mm square membrane elements. Interactions between all bodies were modelled by a set of penalty contact algorithms at each surface to surface interface. These use a constant Coulomb friction coefficient of 0.67 between the tooling and the diaphragms and 0.52 between the diaphragms and the fabric according to ASTM D1894 ISO08295 and similarly to the literature [37]. A 9.81m/s^2 acceleration was added to the upper diaphragm to incorporate gravity via the gravitational force module in Abaqus. The diaphragm edge nodes were held with a rigid constraint and a uniformly distributed load was applied in Step 1 (Figure 6-11) to the upper face of the upper diaphragm and the lower face of the lower diaphragm. This generated a through-thickness clamping force on the ply as the diaphragms were loaded in-plane. The tool was displaced over a 3 second time period in Step 2 (Figure 6-11) to simulate the picture frame descending over the tool. The load on the upper diaphragm was then increase by a factor of 2 in Step 3 (Figure 6-11), representing the 1 bar pressure difference during the vacuum draw-in step of the process. This load forms the fabric/diaphragm arrangement over the tool surface.

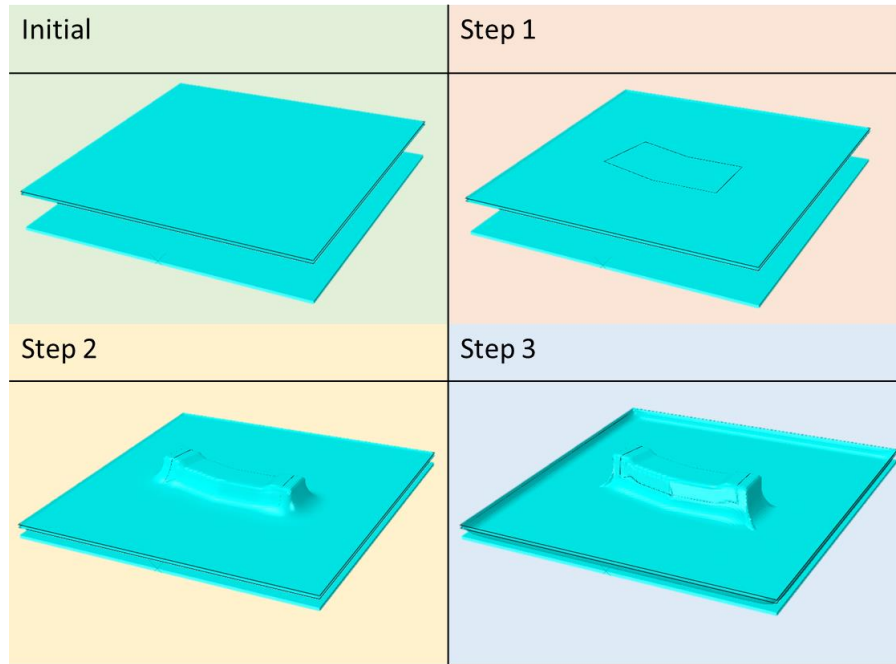


Figure 6-11 Diaphragm forming model operations: steps 1 through 3

6.2.3.4 Diaphragm material model

A Marlow hyperplastic non-linear isotropic model was used to define the behaviour of the StretchLon HT-350 diaphragms. The Marlow model assumes that the strain energy potential is independent of the second derivative and is defined by inputting test data. The uniaxial, biaxial and planer tests were conducted on an Instron 5581 testing machine at a strain rate of 0.03s^{-1} at ambient temperature, following the methodology from Chen [37]. As the diaphragms are thin, the compressibility was not being taken into account and volumetric data was not included, so a default Poisson's ratio for elastic materials of 0.475 was automatically set in Abaqus. Abaqus then interpolated the strain energy potential from the test data.

$$W_b = \int_0^{\lambda T_b^{-1}} T_b(\varepsilon) d\varepsilon \quad \text{Equation 6-5}$$

$$W_p = \int_0^{\lambda T_p^{-1}} T_p(\varepsilon) d\varepsilon \quad \text{Equation 6-6}$$

$$W_u = \int_0^{\lambda T_u^{-1}} T_u(\varepsilon) d\varepsilon \quad \text{Equation 6-7}$$

where subscripts u , b and p relate to the uniaxial, biaxial and planar data, respectively.

6.2.4 Finite element mechanical model

6.2.4.1 *Mesh interpolation from forming model to component mechanical model.*

The forming simulation was used to provide shear angle input data for mechanical stiffness modelling. The shear angle nodal data was transferred onto a trimmed geometry for stiffness modelling shown in Figure 6-12, using a custom-built Matlab script shown. Transferring the data across to an idealised model is representative of a real fabric trimming process and removed unwanted regions that can lead to stress concentrations in the simulation. The integration points and vector components alongside the shear angle data from the forming model were imported into Matlab along with an ideal mesh of the component. The square Euclidean distance between the forming model and component model was calculated with the component model as the slave. Element pairs were created by assessing the closest master mesh node to slave mesh node and pairing it before deleting any repeat points. The mesh size was matched between both models to minimise repeat points and loss of data. The vector component data for the two principal directions in each biaxial ply was applied to two individual uniaxial plies in the component model. The local orthogonal coordinate system for each principal direction on each uniaxial ply was established and the material orientation at each point on the trimmed mesh was then calculated.

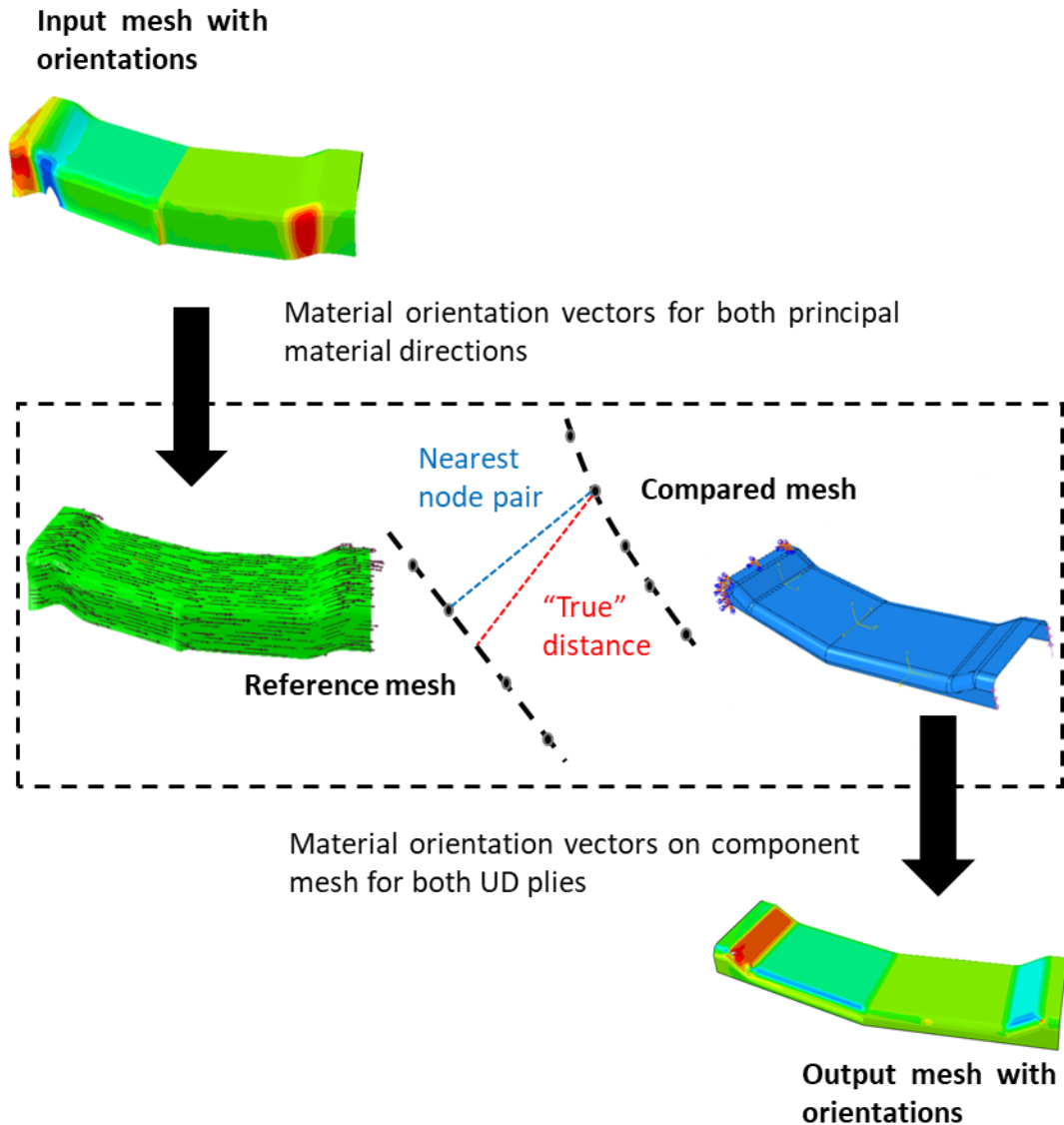


Figure 6-12 Mesh interpolation methodology used to output orientation data from the forming model to the component mechanical model.

6.2.4.2 Mechanical model setup

The purpose of the mechanical modelling was to compare the response of the pre-sheared laminate with the standard laminate under different loading conditions, using Abaqus/Standard. The L-Beam was modelled using a conventional shell element, discretised into 1mm x 1mm elements. The output mesh was used in 3 different simulations for loading via: 3-point bending, tension and torsion along the length axis of the component. This is shown in Figure 6-13. This was done through the application of appropriate ENCASTRE displacement boundary conditions

($U_1=U_2=U_3=UR_1=UR_2=UR_3=0$) and a shell edge load of 100N at each respective loading point given in Figure 6-13.

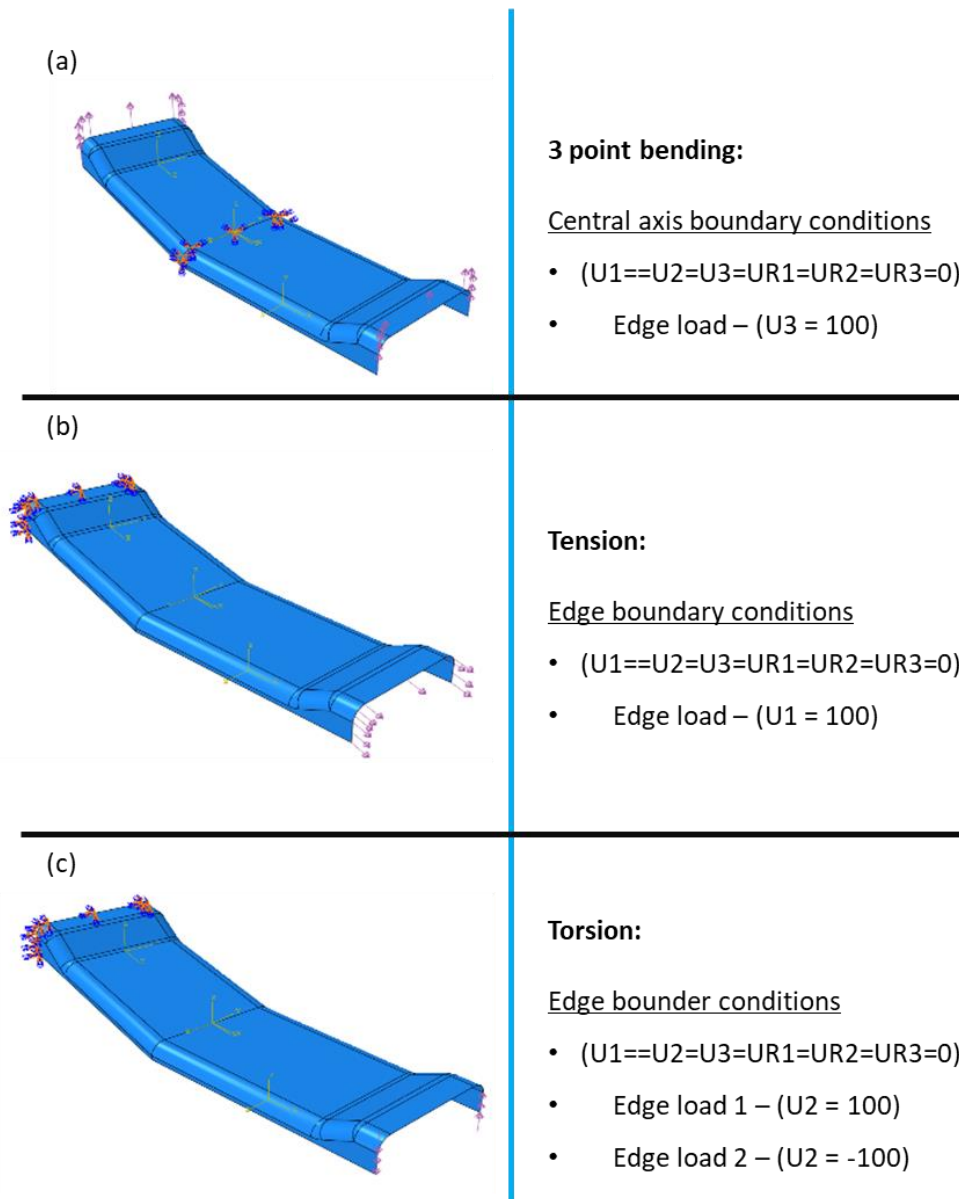


Figure 6-13 Diagrams of the loading conditions used in the component mechanical model for: 3 point bending (a), tension (b) and torsional loading (c).

The composite was made from a continuum shell composite laminate which defines a single element through the thickness for multiple plies. The material behaviour was calculated from 3 integration points defined for each ply. The shell for the pre-sheared laminate is defined by Table 6-1.

Table 6-1 Ply information for example laminate stack used in the component mechanical model.

Ply number	Material	Thickness	Orientation	Integration points
1	FCIM789-Infused	0.5mm	Formed -45° distribution	3
2	FCIM789-Infused	0.5mm	Formed +45° distribution	3
(3,5,7,9,11)	FCIM789-Infused	0.5mm	Formed -15° distribution	3
(4,6,8,10,12)	FCIM789-Infused	0.5mm	Formed 90° distribution	3

Each biaxial ply was modelled as 2 separate UD fibre layers with their own principal material directions and associated local orientation data. The orientation data from each node in each ply was taken from the interpolated paired mesh from the relevant forming model. Orientation data was taken from forming simulations run for a [45°/-45°] ply [0°/90°] ply and a [0°/90°]/[-15°/90°] pre-sheared ply.

The mechanical properties per uniaxial layer are shown in Table 6-2. Post processing of the model was conducted within Abaqus/CAE utilising the visualization module. Stresses were output at each integration point to avoid extrapolation error, which is known to overestimate nodal stress values in Abaqus. The peak stress was measured from the Von Mises stress and converted into a percentage stiffness improvement in comparison to the standard [0°/90°] laminate in the L-beam stress analysis.

Table 6-2 Elastic and failure properties used in component mechanical model. (L = longitudinal) (Tr = transverse).

Density (Kg/m ³)	E1(Pa)	E2(Pa)	E3(Pa)	Nu12	Nu13	Nu23	G12(Pa)
1100	138E9	45E8	45E8	0.28	0.28	0.4	52E8

G13 (Pa)	G23 (Pa)	Tensile strength (L) (Pa)	Compressive strength (L) (Pa)
52E8	14.5E8	3.71E8	3.92E8

Tensile strength (Tr) (Pa)	Compressive strength (Tr) (Pa)	Shear strength (L) (Pa)	Shear strength (Tr) (Pa)
9.5E6	2.08E7	1E8	1E8

There are 3 different laminate layups that were tested: A standard 24 ply laminate at $[(0,90)_4,(45,-45),(0,90)]_s$ with the ± 45 bias ply incorporated for improved torsional stiffness. A pre-sheared 24 ply laminate, where the material forming over Arm 1 of the L-beam is pre-sheared to $(-15, 90)$. This laminate has the same ply architecture as the previous laminate $[(-15,90)_4 ,(45,-45),(-15,90)]_s$, with the difference being the pre-shearing over half of the fabric as shown in the forming models from Figure 6-10. The peak stress contours have been shown in Figure 6-18, Figure 6-19 and Figure 6-20. The final laminate tested is a 20 ply laminate that has the same architecture as the previous pre-sheared laminate, however two of the $(-15, 90)$ plies have been removed to create a low mass laminate. This laminate has been tested to see if the stiffness improvements can be translated into alternative benefits such as light weighting.

6.2.4.3 *Fibre misalignment and volume fraction*

Pre-shearing the fabric causes fibre misalignment that results in a change in the in-plane modulus of the final laminate (outlined in Chapter 3). The misalignment and change in fibre volume fraction were incorporated into the mechanical model to accurately simulate the properties of a formed component. The combined volume fraction and fibre misalignment for FCIM789 found in chapter 3 has been incorporated as a field variable using the USDFLD user subroutine. The routine gives element by element control over material properties by individually editing the values in Table 6-2. Element shear angle values were known from the forming model and as such the fibre misalignment and volume fraction function for FCIM739 was applied to each element. The percentage change in tensile stiffness was used to modify values for E1, from which the laminate modulus was updated through the composite manager in Abaqus.

6.2.5 Experimental forming of L-Beam

To validate the shear angle results generated by the forming simulation, a representative experimental test was conducted to apply pre-shearing to a component. The component geometry chosen, matched that one that had been modelled so a comparison could be drawn. The shear angle values were measured and compared to the model at specific points to measure the simulation accuracy. Tool design was conducted on the L-beam geometry and it was rapid prototyped in PLA. A selection of non-pre-sheared and pre-sheared samples were cut and formed using the double diaphragm forming process. Each sample was pre coated with epoxy binder before the forming process. For the baseline sample, a (0,90) ply of FCIM789 was cut to match the 15 degree kink in the L-beam as given in Figure 6-7, matching the preform shape used during the modelling. For the pre-sheared sample, a straight (0,90) ply was cut and the pre-shearing methodology was used to shear half the blank to -15 degrees (-15,90). The negative shear direction was chosen as it has lower spring back and it was expected that there would be observable fibre misalignment which could be measured with the optical scanning methodology. Each sample was formed at 100°C and the mean fibre angle and corresponding standard deviation were measured in 3 discrete regions over the top surface of the sample in Table 6-6.

The sample was measured in the middle of the un-sheared face (Arm 2), just after the transition point, and on the centre of the sheared face of the L-Beam (Arm 1) as shown by Points 1, 2 and 3 respectively in the diagram (.

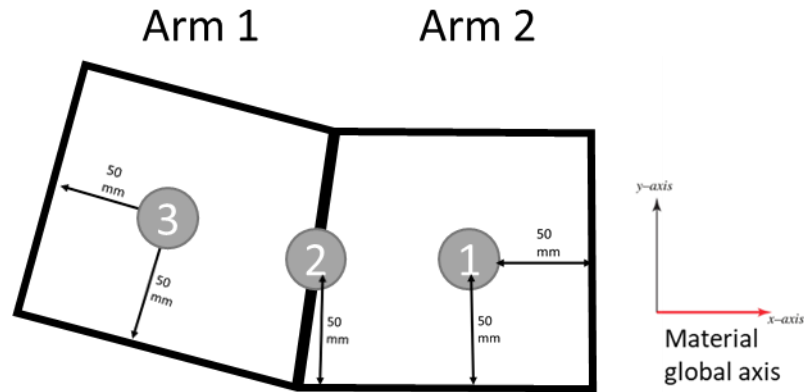


Figure 6-14 Diagram of optical measurement position on the L-Beam. Positions 1, 2 and 3 are located across the centre of the beam at 175mm, 120mm and 75mm in from the left edge of arm 1.

6.2.6 Experimental forming – Sill section

The desired pre-shearing in each region was -23 degrees to align both of the pre-sheared regions to the edge of the geometry. A pre-shear of -25 degrees was applied to account for the expected spring back.

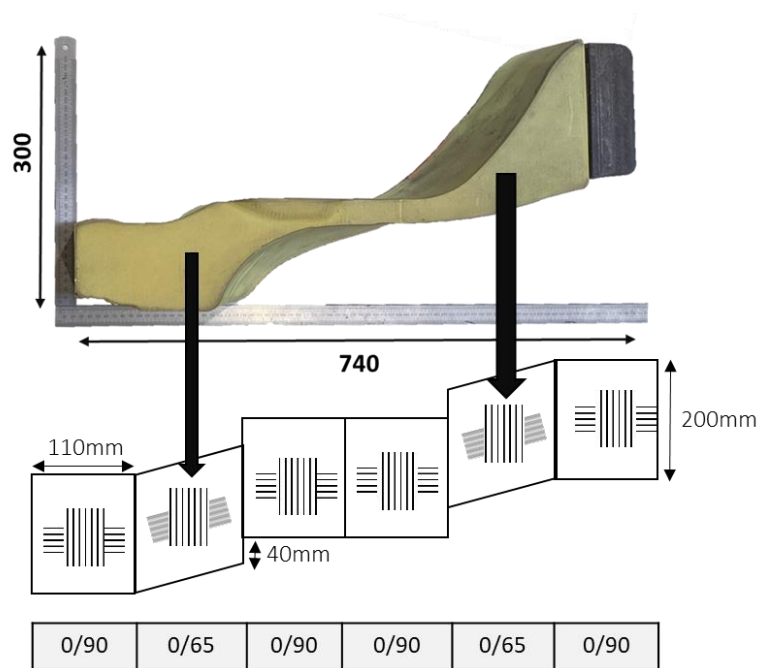


Figure 6-15 Pre-sheared ply arrangement for the demonstrator sill section

The demonstrator sill section consists of 6 sections of 110mm long that cover the entire length of the sill. The 2nd and 5th section were pre-sheared to -25 degrees to give a final orientation of 0/65. The laminate was sheared in 110mm by 200mm regions to fit within the pre-shearing frame and then trimmed to give the blank shown in Figure 6-15.

6.3 Results:

6.3.1 Simulating pre-sheared fabric forming

An assessment of the applied pre-shearing has been conducted by monitoring the homogeneity of the fibre orientations over the top face of the L-Beam before and after forming. Regions that may be subjected to defects due to over-shearing have been identified by comparing shear angle to the stitch breakage point of the material. The effectiveness of pre-shearing over the geometry has been assessed by measuring the proportion of the top face fibres after forming that conform to the -15 degree pre-shear angle that was originally set before forming. The plots in Figure 6-16 and Figure 6-17 show all angles below 0 degrees as only negative values are relevant to assessing the successfulness of the negative pre-shearing. Positive values are homogenised into a single grey colour in the contour plot to allow for better visualisation of the negative shear angle distribution.

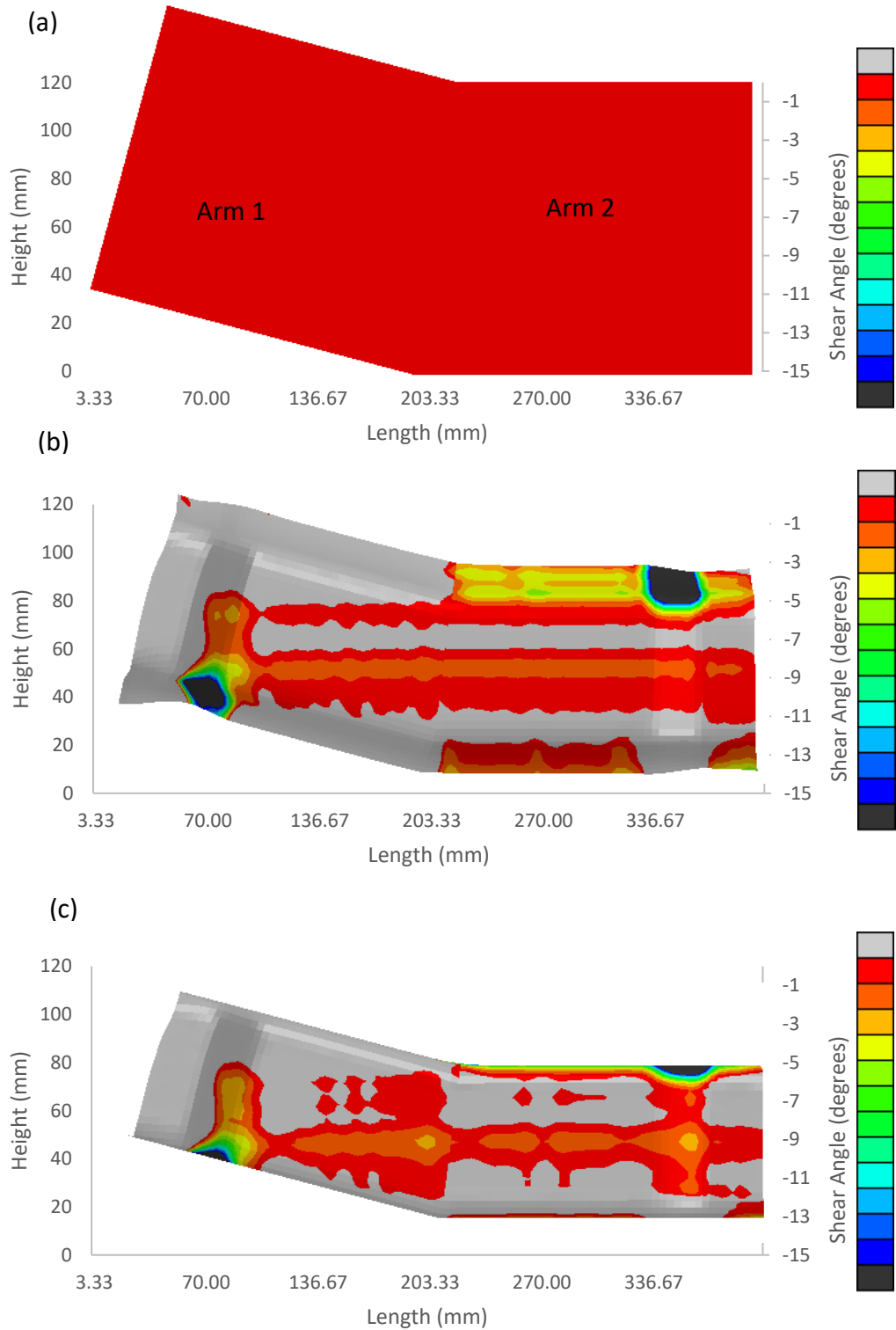


Figure 6-16 shear angle contour plot between 0° and -15° for: (a) before forming, (b) after the DDF frame has descended and (c) after full vacuum compaction for a standard $(0^\circ, 90^\circ)$ ply.

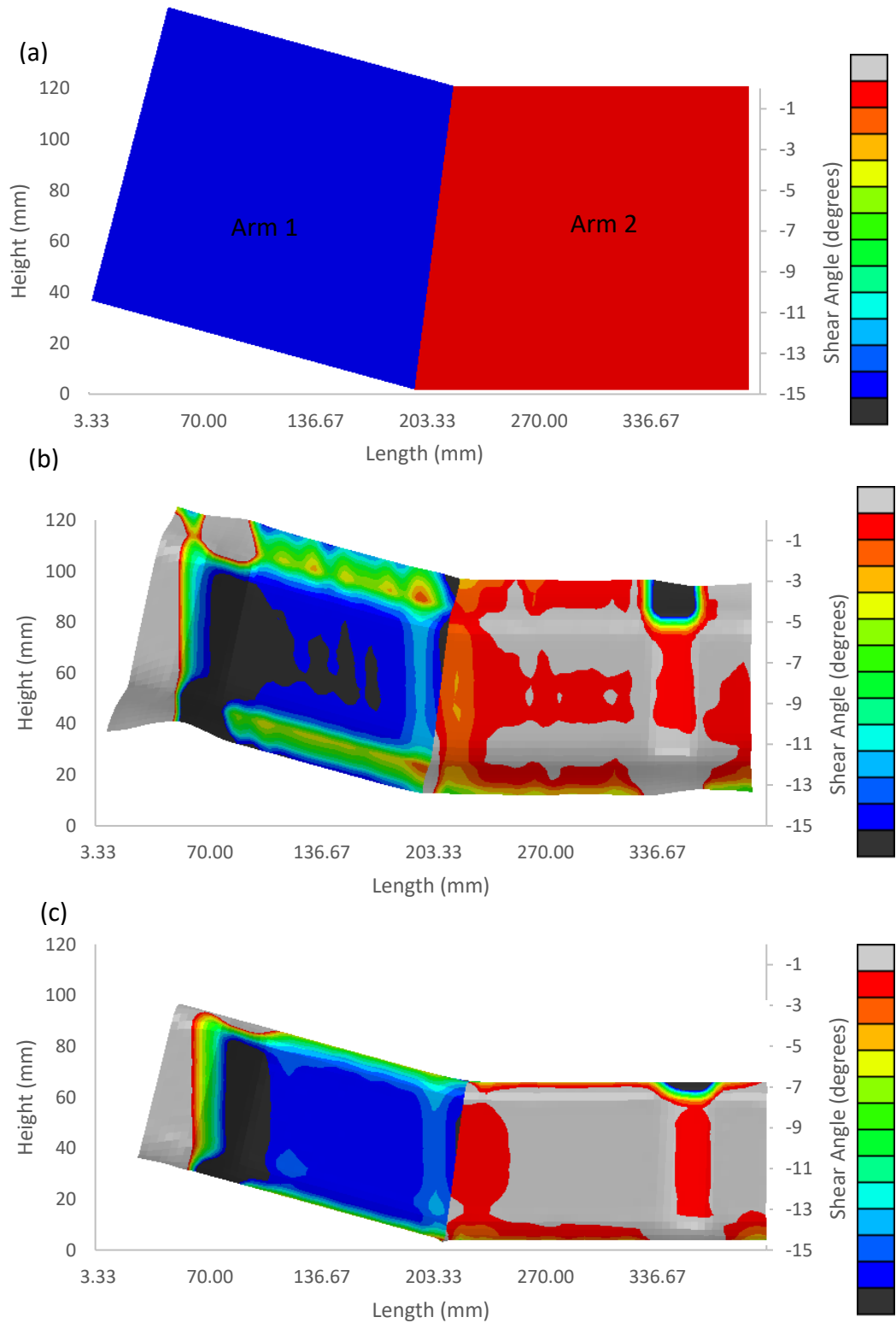


Figure 6-17 (a),(b),(c) shear angle contour plot between 0° and -15° (a) before forming (b) after the frame descending step (c) after full vacuum compaction for a pre-sheared ($-15^\circ, 90^\circ$) ply.

Figure 6-16 and Figure 6-17 show the shear angle distribution for a standard ply ($0^\circ, 90^\circ$) and a pre-sheared ply, starting at ($0^\circ, 90^\circ$) and sheared to ($-15^\circ, 90^\circ$) for producing the L-beam. The contour plot extends from 0 to -15 degrees to allow for easy visualisation of the relevant shear angle information. It shows the shear angle distribution at 3 points during the forming process: Step 1, before forming but after the pre shearing step; Step 2 after the frame drop step but before the vacuum compaction is applied; and Step 3 after the full vacuum is drawn between the blank and the tool surface.

The distribution of shear angles at the end of the forming step between the standard (Figure 6-16) and pre-sheared (Figure 6-17) blank differs due to the initial fabric pre-shearing. The standard blank has a continuous shear angle before forming. After Step 2 there is a relatively uniform shear angle distribution across the top of the preform, with magnitude of shear not exceeding -3° with standard deviation across the top surface of Arm 1 of 1.9 degrees with no concentration points. The sides of the preform show significant shearing of below -15 degrees in the upper right of Arm 2 and lower left of Arm 1. This is found in both of the formed plots as the shearing is required for the fabric to conform to the L-beam tool and increases to -18 degrees after vacuum compaction. After vacuum compaction in step 3 the majority of the surface remains within 1 and -5 degrees with a standard deviation in arm 2 of 2.3 degrees and 2.4 degree in arm 1. The pre-sheared L-beam has a distinct transition at the midpoint where the shear angle changes for 0 to -15 degrees which remains throughout the forming process (Figure 6-17 b). The shear angle distribution over Arm 1 remains between -13 degrees and -17 degrees with an average over that top face of 14.4 degrees and a standard deviation of 1.9 degrees meaning that the fibre angle remains continuous across the face of the part as desired. The deviation across arm 2 is similar to the standard preform at 2.5 degrees. Shearing during the forming process causes a peak of -28 degrees over the bottom left quadrant of arm 1 which is 10 degrees higher than for the standard preform. The homogenous application of pre shearing using custom orientation control in Abaqus has been successful as deviation across the pre-sheared region is within 0.1 degrees of the standard preform.

6.3.2 Stress analysis of L-Beam

A selection of 20 and 24 ply laminates outlined in Table 6-3 were constructed and modelled using the mechanical modelling described in the methodology. The aim of the investigation was to assess the stiffness gains that could be achieved with a suitably pre-sheared laminate. The adapted VFABRIC material model includes the variable tensile modulus function due to fibre misalignment and variable fibre volume fraction as well as the local orientation data for each ply from the respective forming simulation.

Table 6-3 Results from component mechanical model showing the peak stress for various laminate layups under different loading conditions.

Laminate type	Load	Ply number	Pre-sheared/Standard	Layup	Peak Mises Stress (Mpa)	Peak Stress location
Symmetric (1 ply in bias direction)	3 point bending	24	Standard	[(0,90),(0,90),(0,90),(0,90),(45,-45),(0,90)]s	2.4	Centre, Underside
Symmetric (1 ply in bias direction)	3 point bending	24	Pre-sheared	[(0/-15,90),(0/-15,90),(0/-15,90),(0/-15,90),(45,-45),(0/-15,90)]s	1.85	Centre, Underside
Symmetric (1 ply in bias direction)	3 point bending	20	Pre-sheared	[(0,90),(0,90),(0,90),(45,-45),(0,90)]s	2.57	Centre, Underside
Symmetric (1 ply in bias direction)	Axial tension (Local Direction 1)	24	Standard	[(0,90),(0,90),(0,90),(0,90),(45,-45),(0,90)]s	89.7	Lower Arm 1, Upper side
Symmetric (1 ply in bias direction)	Axial tension (Local Direction 1)	24	Pre-sheared	[(0/-15,90),(0/-15,90),(0/-15,90),(0/-15,90),(45,-45),(0/-15,90)]s	68.7	Lower Arm 1, Upperside
Symmetric (1 ply in bias direction)	Axial tension (Local Direction 1)	20	Pre-sheared	[(0,90),(0,90),(0,90),(45,-45),(0,90)]s	87.02	Lower Arm 1, Upper side

Chapter 6 - Maintaining fibre continuity over formed composite components using biaxial non-crimp-fabrics

Symmetric (1 ply in bias direction)	Torsion (about longitudinal Axis)	24	Standard	[(0,90),(0,90),(0,90),(0,90),(45,-45),(0,90)]s	0.237	Lower Arm 1, Underside
Symmetric (1 ply in bias direction)	Torsion (about longitudinal Axis)	24	Pre-sheared	[(0/-15,90),(0/-15,90),(0/-15,90),(0/-15,90),(45,-45),(0/-15,90)]s	0.199	Lower Arm 1, Underside
Symmetric (1 ply in bias direction)	Torsion (about longitudinal Axis)	20	Pre-sheared	[(0,90),(0,90),(0,90),(45,-45),(0,90)]s	0.267	Lower Arm 1, Underside

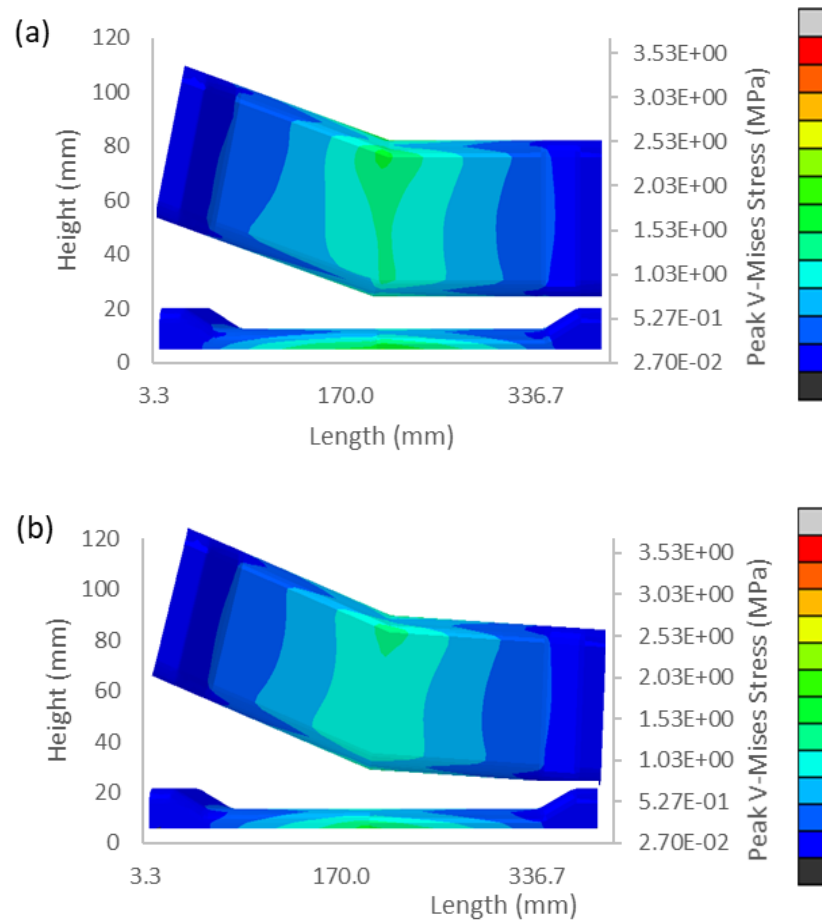


Figure 6-18 Stress distribution for (a) a pre-sheared and (b) standard laminates under bending.

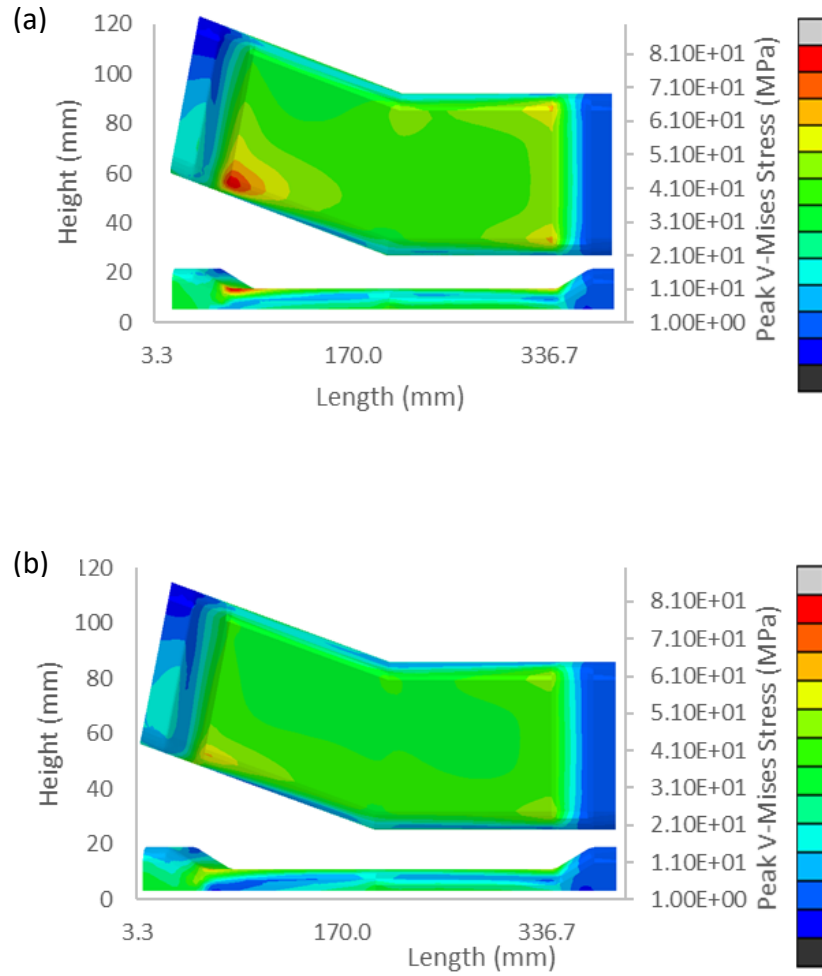
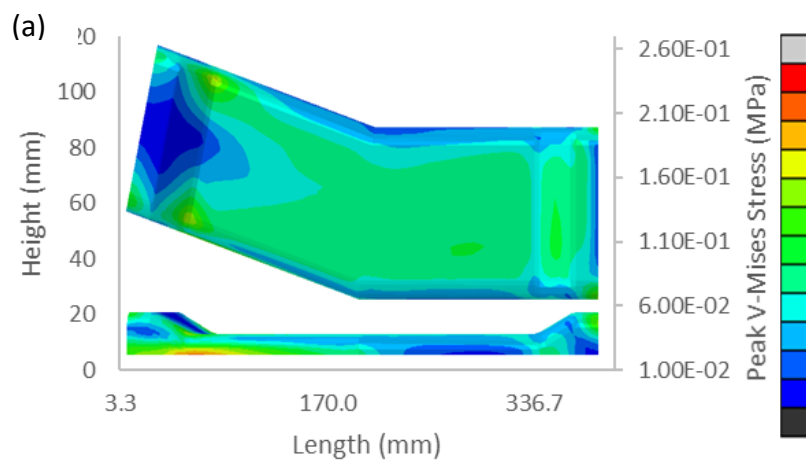


Figure 6-19 Difference in peak stress location between a pre-sheared (a) and standard (b) laminates under: Tensile load.



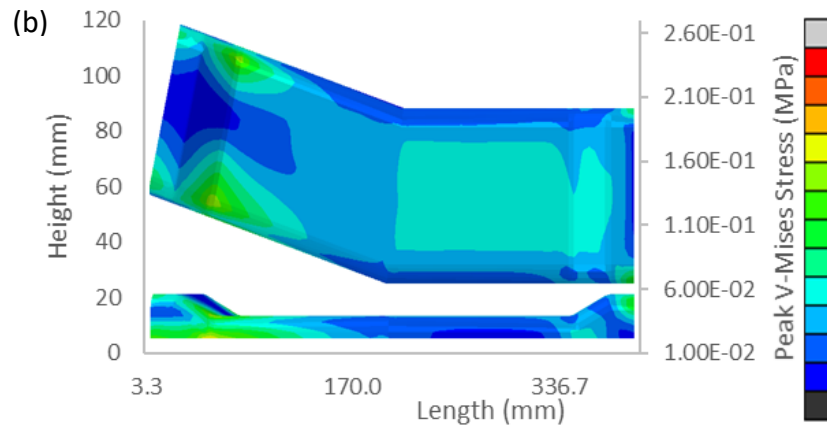


Figure 6-20 Difference in peak stress location between a pre-sheared (a) and standard (b) laminates under: Torsional load.

The peak stresses in Table 6-4 show that the 24 ply pre-sheared laminate has a higher peak stress than the 24 ply standard laminate under every loading condition presented. Peak stress was used as an indicator for the change in mechanical properties over the laminate. This was followed by Table 6-5 showing the deflection magnitude of the samples to indicate the stiffness changes. The percentage increase in peak stress from pre shearing shown in Table 6-4 is over 15% across all loading conditions. The largest increase is under tensile load at 23.4%. In the case of the 20 ply pre-sheared laminate the peak stresses seen were comparable to that of the standard 24 ply layup. The 20 ply pre-sheared laminate's peak stress was 6.7% lower than the 24 ply standard laminate in bending, 3% higher in tension and 11% lower in torsion. These stress differences values are not significantly larger, but these preforms produce a 17% weight reduction from the removal of 4 plies from the laminate. The distribution of stress is plotted in Figure 6-18, Figure 6-19 and Figure 6-20. The contour plots show the same trend across all load cases, with the peak stress location remaining the same, but at a higher magnitude. The alignment of the fibres with the principal stress direction through the use of pre-shearing gives an average increase in peak stress across tested loading conditions of 21% and an average decrease in deflection of 15%. Simulating the application of pre-shearing as a process alteration to matched tool and diaphragm forming has shown large improvements to the components mechanical properties, without increasing the mass.

Table 6-4 Percentage change in peak stress seen by using pre-sheared laminated over comparable standard laminate layups.

Loading type	Standard laminate peak stress (MPa).	Pre-sheared laminate peak stress (MPa).	Percentage increase in peak stress from pre-shearing (%).
Bending	2.4	1.85	22.9
Tensile	89.7	68.7	23.4
Torsional	0.237	0.199	16.0

Table 6-5 Percentage change in sample deflection by using pre-sheared laminated over comparable standard laminate layups.

Loading type	Standard laminate deflection (mm).	Pre-sheared laminate deflection (mm).	Percentage change in deflection from pre-shearing (%).
Bending	4.86	4.25	12.3
Tensile	4.86	4.2	13.5
Torsional	1.29	1.02	20.9

6.3.3 Experimental forming of L-Beam

Table 6-6 shows the results of the shear angle and fibre angle analysis performed using the optical scanning methodology. With Figure 6-21, Figure 6-22 and Figure 6-23 showing the 3 different visualisation stages of the optical scanning process (Image, fibre angle plot and shear angle plot).

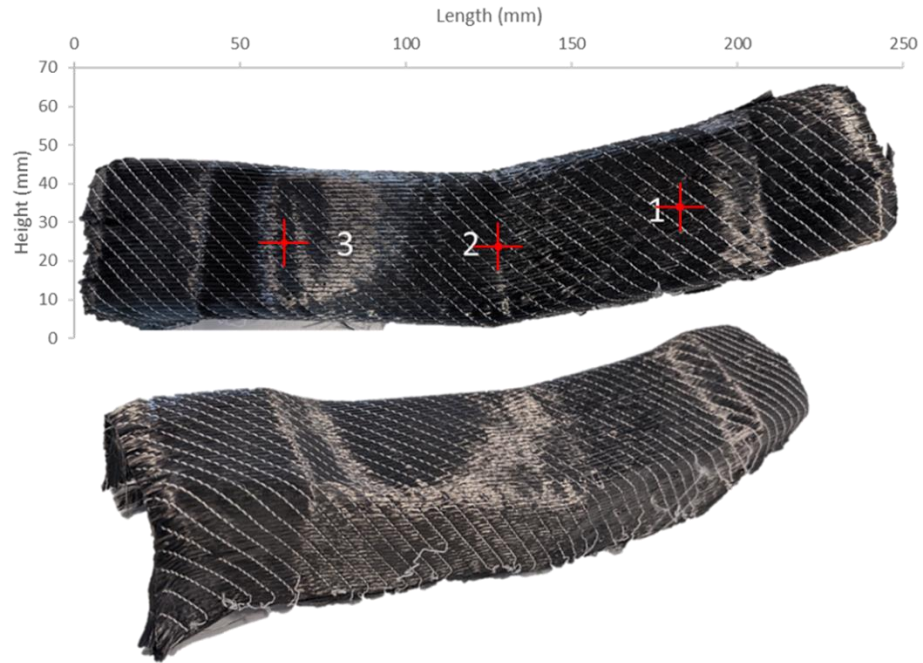


Figure 6-21 Optical imaging of the double diaphragm formed L-beam with a pre-sheared -15/90 ply. Positions 1, 2 and 3 are located across the centre of the beam at 175mm, 120mm and 75mm in from the left edge of arm 1.

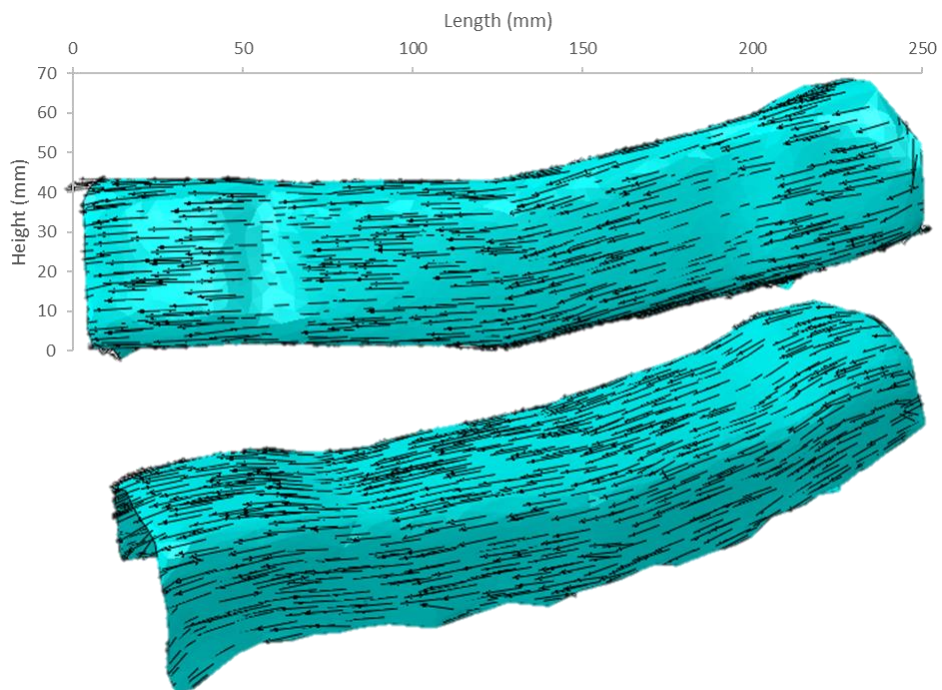


Figure 6-22 Optical scanning of the double diaphragm formed L-beam with a pre-sheared -15/90 ply. Scan Highlighting fibre direction

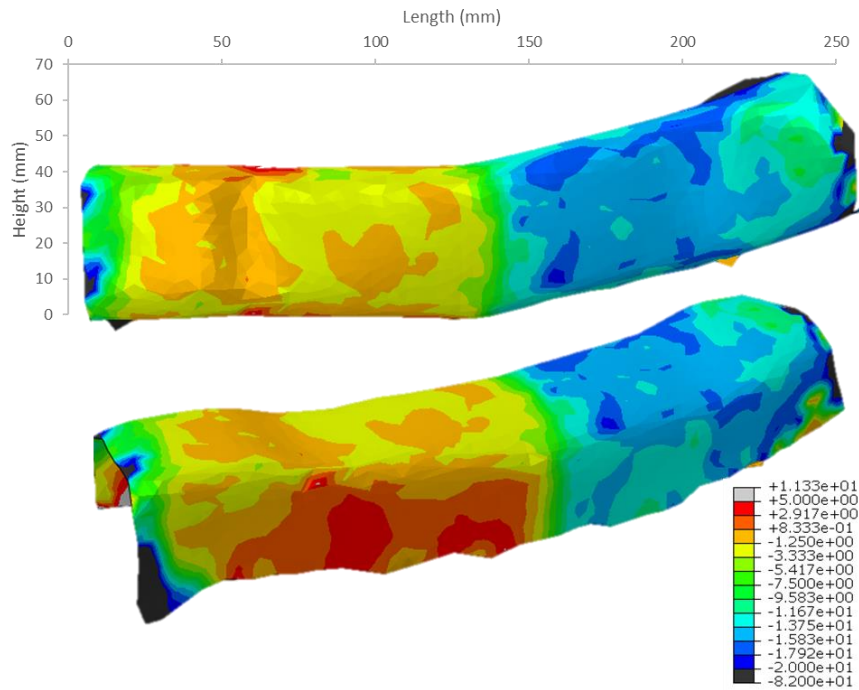


Figure 6-23 Optical scanning of the DDF L-beam with a pre-sheared -15/90 ply. Contour plot showing shear angle in degrees.

Table 6-6 Mean fibre angle and standard deviation data from Apodius analysis of L-beam at 3 points: arm 2 (1) post arm 12 transition (2) and arm 2 (3).

<i>Point</i>	<i>Mean fibre angle</i>	<i>Mean simulated Fibre angle</i>	<i>Mean Standard deviation</i>
1	0.2	0	0.5
2	13.9	14.6	2.5
3	14.5	14.9	3.1

The results from the optical scanning methodology show that the desired -15 degrees of pre shearing has been applied to the fabric to within 3.1 degrees. The fibres take a distinct change in direction that is in full effect after point 2. This has been successful in applying the desired fibre reorientation to the sample. The pre-shear applied using the shear frame was 15.5 degrees and the fabric experienced some spring back of 1 degrees to 14.5 degrees. This equates to 6.5% spring back which

aligns with the estimates given in Appendix (E). Drawing a comparison between the experimental results and the simulated L-beam showed that the model predicted valid shear angle values. A 0.9 degree difference between the simulated and experimental shear angle was observed on the top face of Arm 1 and a 0.2 degree difference in shear angle was observed on the top face of Arm 2. The variation between simulated and experimental results is smaller than the standard deviation of the fibre distribution which is 2.5° - 3.1° . The strong agreement between the forming model and the experimental fibre angle validated the forming model for 2D-3D forming of pre-sheared fabrics.

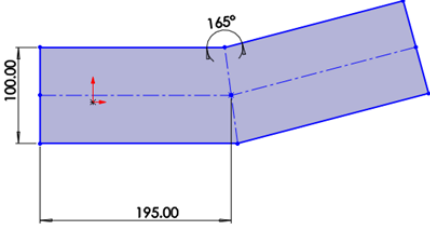
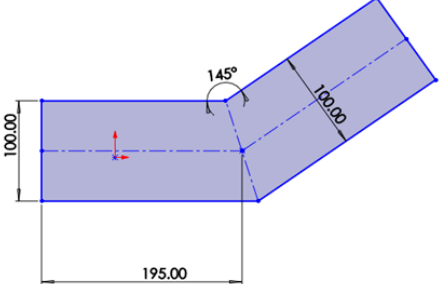
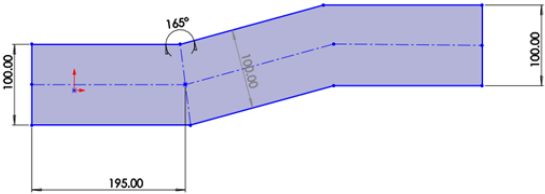
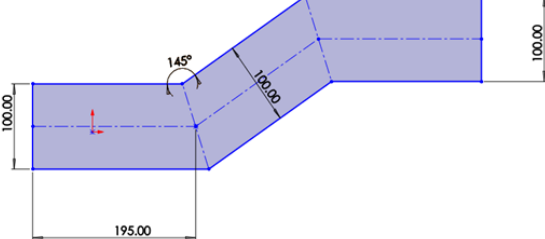
Fibre misalignment caused by inter-stitch buckling was observed as a “waviness” to the surface of the fabric and can be distinguished in Figure 6-21, Figure 6-27 and Figure 6-28. The sheared section showed a distinct surface malformation which was not present in the un-sheared section. This was quantified as a fibre angle standard deviation of 3.1 degrees matching the misalignment values predicted from picture frame testing in from Chapter 4. Overall the implementation of pre-shearing on a small scale component was successful. The experimental shear angle distribution results match those seen in the forming simulation and as such the methods devised in the methodology for applying pre-shearing to the fabric were effective.

6.3.4 Wastage reduction, L-beam

A secondary benefit of ply pre-shearing is the simplification of kit cutting which reduces wastage for regions of trimmed fabric. Pre shearing allows for preforms to be sheared into the desired shape, giving greater kit tessellation and a higher percentage usage from the fabric roll. This is especially noticeable if tessellation of complex preforms is not possible due to small batch numbers or large component sizes. Figure 6-3 shows a rectangular preform sheared into shape as an alternative to cutting out an irregular blank. To measure wastage reduction, a selection of simple preforms have been created in Table 6-7, that can be produced through a standard kit cutting method, or by a cutting operation followed by pre-shearing operation. The majority of pressed and vacuum formed components are computer numerically control (CNC) machined after curing. Because of this trimming operation, a near net shape is not required for the blank, and a simplistic approximation can be made that

ignores frayed edges and regions clamped during the pre-shearing process. This approximation has been applied to pre sheared and non-pre sheared preforms.

Table 6-7 Comparison of area of fabric needed to create 4 beam like preforms using standard trimming methodologies and pre shearing methodologies.

Name	Standard Trim area	Pre-sheared trimmed area	Percentage area reduction from pre-shearing	Image
L Beam 165	58.9E3 mm ²	49.8E3 mm ²	15.5%	
L Beam 145	77.7E3 mm ²	50.9E3 mm ²	34.5%	
N Beam 165	85.1E3 mm ²	71.5E3 mm ²	16%	
N Beam 145	108.9E3 mm ²	80.8E3 mm ²	25.7%	

The percentage reduction in column 4 of Table 6-7 is calculated as the difference between the standard trimmed area and the pre-sheared trimmed area. In each case there is a noticeable reduction in the theoretical wastage for the pre-sheared preform with a 15.5%-34.5% reduction in material usage. The same preform has been chosen with two different pre-shearing angles, 165 ° and 145 ° (15° and 25° of pre-shear respectively.) Two geometry types (L-beam and Z-beam configurations) have been chosen to look at the impact of the pre-shearing angle on the material usage.

In both beam configurations the larger shear angle provides a larger reduction in the wastage, with a further 19% reduction in wastage between the L-beam 165 and the L-beam 145 and 9.7% reduction between the N-beams. Pre-shearing can significantly reduce wastage for appropriate geometries. The benefits in wastage reduction are supplementary to the desired mechanical property improvements.

The wastage reduction figures calculated here are best case scenario figures. It is assumed that 0 tessellation of plies is possible within the kit. This is the case in one-off and small batch scenarios, and where single kits must be cut in a batch to allow operators to correctly compile the individual pieces without mistakes. Simplification of the preform geometry improves tessellation and will increase material utilisation.

6.3.5 Stress analysis of demonstrator sill section

The pre-shearing methodology was applied to a more complex component that is representative of beam-like structures used in the automotive industry. The aim was to see if the pre-shearing methodology could be successfully transferred onto a complex part. The objective was to measure the application of multiple regions of pre-shearing for maintaining fibre continuity along a complex section.

Two representative laminates were applied to a simulated double of the Sill demonstrator component. A standard quasi isotropic laminate consisting of $(0^\circ / 90^\circ), (45^\circ / -45^\circ)^s$ plies and a pre-sheared laminate consisting of $(0/90), (45/-45)^s$ plies and $(-23^\circ / 90^\circ), (45^\circ / -45^\circ)^s$ plies in the regions to the pre-sheared. (The pre shear angle of -23 degrees matches the geometry change in the beam allowing for fibre continuity). The two laminates were tested under 3 different loading conditions shown in Figure 6-25 to assess the effect of the pre-sheared laminate on the mechanical properties of the component under a variety of different loading conditions.

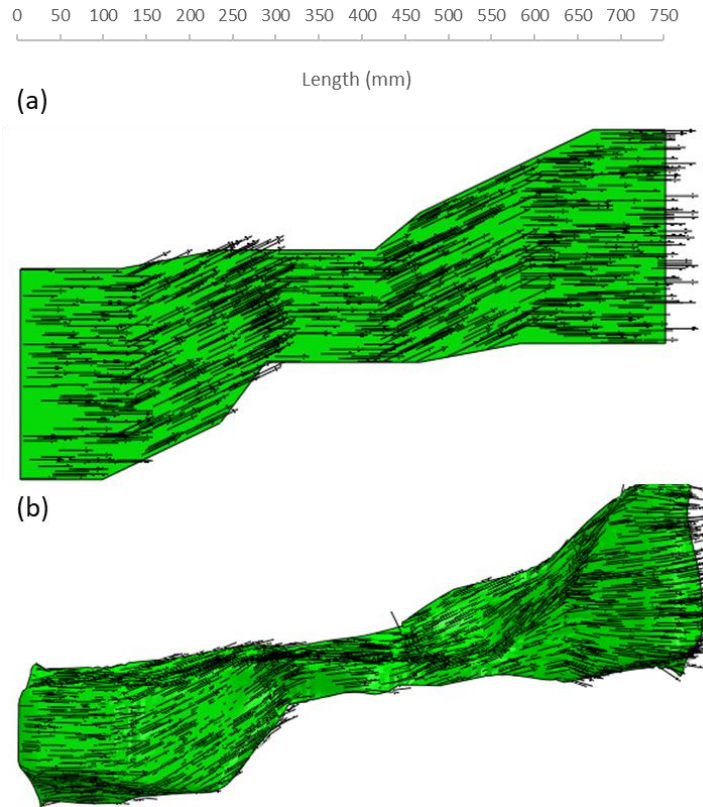


Figure 6-24 Demonstrator sill section pre-sheared blank (a) and pre-sheared forming model (b)

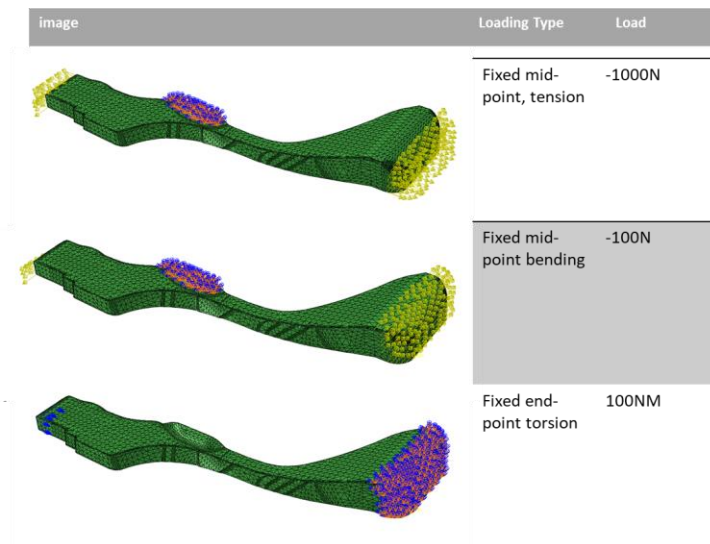


Figure 6-25 Loading conditions applied to the demonstrator sill, structural testing FEA model.

Chapter 6 - Maintaining fibre continuity over formed composite components using biaxial non-crimp-fabrics

The material model used was the same combined model used during the L-beam simulations. The fibre angle plot in Figure 6-24 shows good conformity of the pre-sheared fibre angle to the tool geometry, with the fibre angle in Sections 2 and 5 remaining within 3 degree of the target -23 degree angle on the top surface after forming. An 8 ply laminate (4 biaxial plies) has been applied for the structural testing. This is less than half the thickness of the L-beam component as, the Sill demonstrator is representative of a lightweight bodywork component with a lower ply count.

Table 6-8 Results from the demonstrator sill structural model showing the peak stress for various laminate layups under different loading conditions.

Laminate type	Load	Ply number	Pre-sheared/Standard	Layup	Peak Stress (Mpa)	Peak Stress location
Symmetric (1 ply in bias direction)	Fixed mid-point tension	8	Standard	[(0,90), 45,-45]s	4.05	Centre, top edge
Symmetric (1 ply in bias direction)	Fixed mid-point tension	8	Pre-sheared	[(0/-23, 90),(45,-45]s	3.85	Centre, top edge
Symmetric (1 ply in bias direction)	Torsion	8	Standard	[(0,90), 45,-45]s	4.1	Top face
Symmetric (1 ply in bias direction)	Torsion	8	Pre-sheared	[(0/-23,90),(45,-45]s	3.65	Top face
Symmetric (1 ply in bias direction)	Fixed mid-point bending	8	Standard	[(0,90), 45,-45]s	2.57	Centre, top edge
Symmetric (1 ply in bias direction)	Fixed mid-point bending	8	Pre-sheared	[(0/-23,90),(45,-45]s	2.56	Centre, top edge

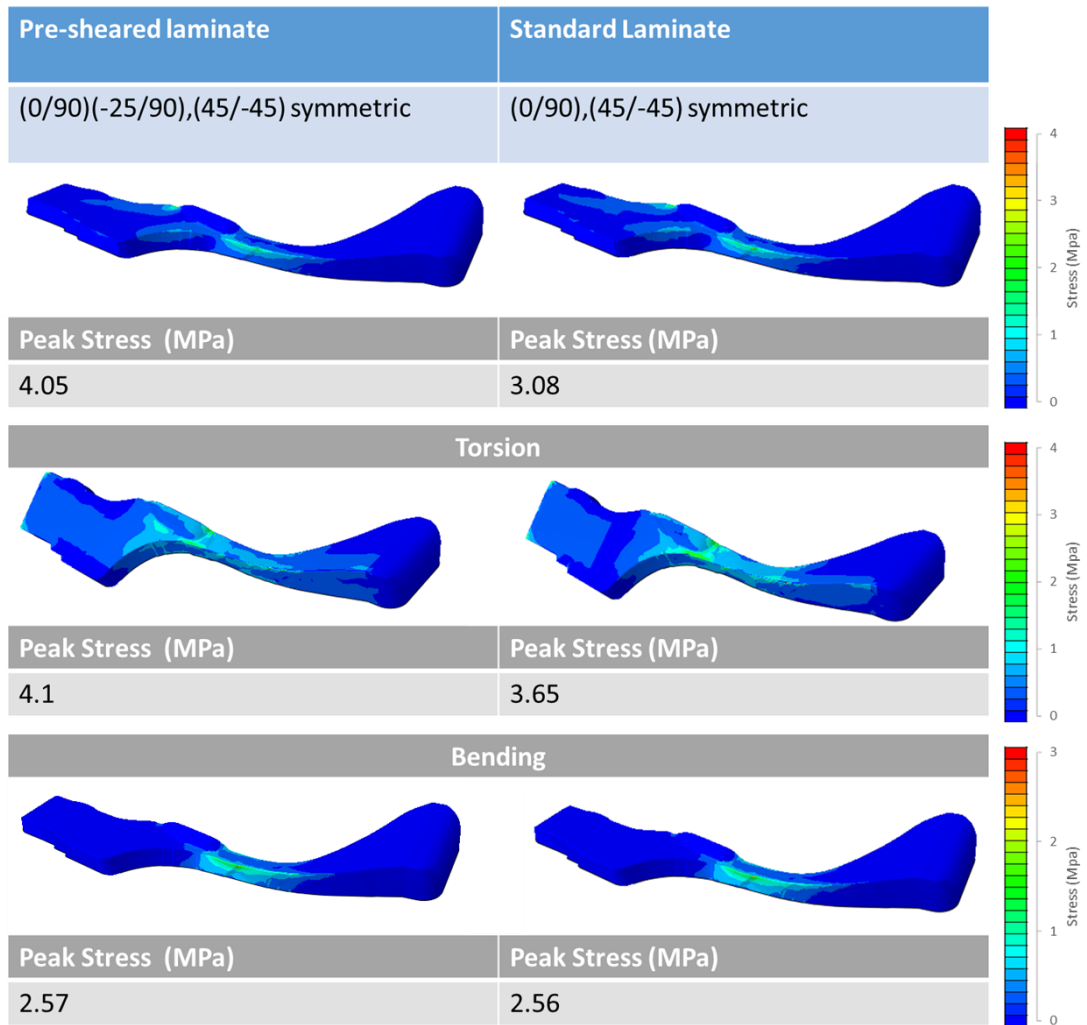


Figure 6-26 Peak stress contour plots under the 3 loading conditions for a standard and a pre-sheared laminate.

The two laminates were directly compared under the same loading conditions and the pre-sheared laminate showed a reduced peak stress under all tested loads. There was a 4.9% increase in the peak tensile stress, an 11% increase in the peak torsional stress and 0.4% increase in the peak bending stress as shown in Figure 6-25. The pre-sheared laminate has been successful in increasing peak stress on the more complicated geometry indicating an increase in the mechanical stiffness. This is corroborated with a reduction in the part deflection of:

- 7% in tension
- 5% in torsion
- 9% in bending

6.3.6 Experimental forming – Sill section

The sill section was formed as per the double diaphragm forming methodology. Figure 6-27 shows the preform after the pre-shearing operation and Figure 6-28 shows the preform after the forming operation.

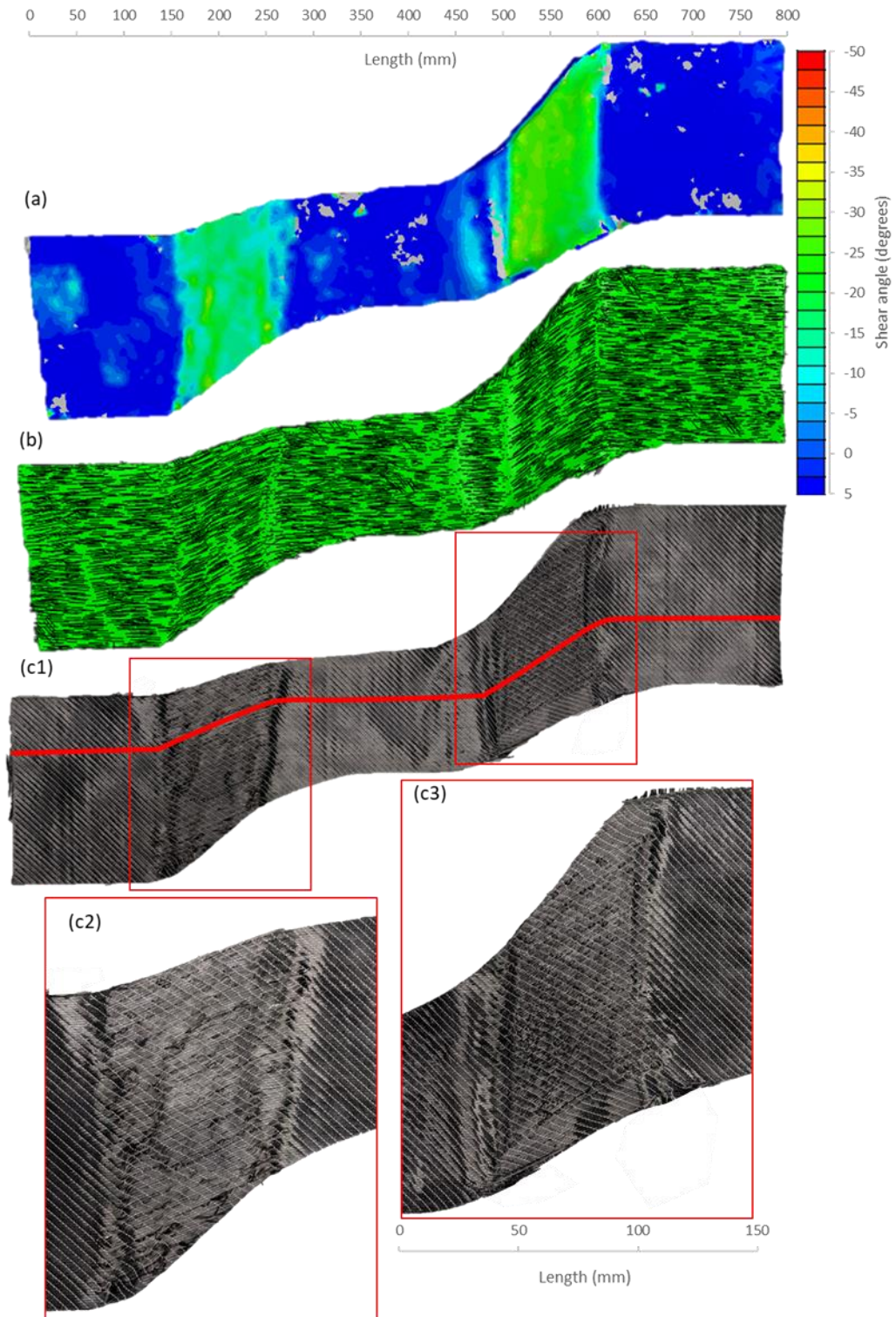


Figure 6-27 Pre-sheared blank for demonstrator sill section. (a) Optically scanned to show shear angle. (b) Optically scanned using Apodius system to show fibre direction. (c1) imaged with pre-sheared regions highlighted. (c2/c3) pre-sheared regions

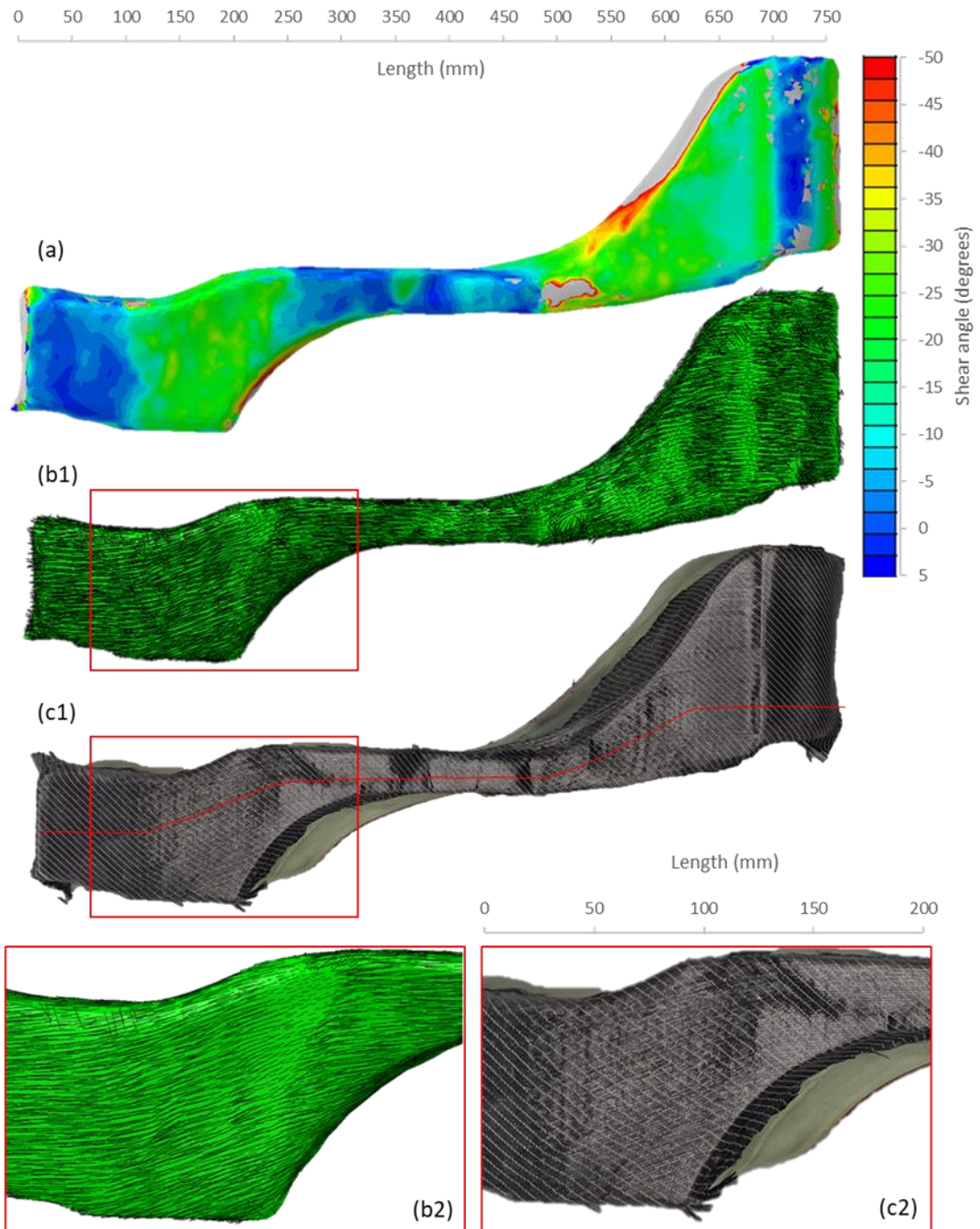


Figure 6-28 Formed demonstrator sill section. (a) Optically scanned showing shear angle in degrees. (b1) optically scanned showing fibre angle distribution. (c1) imaged. (b2) close up of pre-sheared region 1 showing fibre angle distribution. (c2) close up of pre-sheared region.

The pre-sheared blank shows a successful level of shearing to -25 degrees in both the specified regions. There is homogenous shear that ranges from -20 to -27 degrees over the two regions shown in Figure 6-27(a). The continuous fibre continuity is shown in Figure 6-27 (b) and further highlighted in Figure 6-27 (c1/2/3) showing successful application of the pre-shearing methodology for its intended purpose. The pre-shearing caused the expected level of fibre misalignment with standard deviation values of 3.7 degrees over each local region. The results from the scanned pre-sheared blank validate the use of the pre-shearing methodology on a geometry that mimics industrial components. The pre shearing successfully reached the desired 23° which was targeted for the initial pre-shearing value. The reduction in initial blank size for the Sill geometry generated a 31% improvement to material utilisation. Result during manufacturing of the Sill blank show that pre-shearing could be simply incorporated into a 2D hand layup process. Operators could be given plies that have been pre sheared, or the pre shearing could be applied during the lamination step by hand or assisted by a pre-shearing jig. The later method is similar to what cruelty occurs in hand layup when plies are sheared to conform to 3D preform shapes. The optical methodology was successful in capturing the fibre angle and shear angle values as shown by the detailed output from Figure 6-27. An in-process version of this method could be setup alongside manufacturing and used as a Go/no-go check to see if the fibre angle is within tolerance for each ply. Similar systems such as the Lap-Laser and Aligned-Vision currently use laser projection to aid in ply layup and could be extended to incorporate this fibre angle checking feature.

The post forming fibre angle distribution is captured in Figure 6-28 and showed success in maintaining fibre continuity with continuous fibres spanning the length of the form. Figure 6-28 (a) shows that the pre-sheared regions have maintained a level of shear that is homogenous between the values of -18 and -27 degrees in the left pre-sheared region with a mean of -23.5 degrees and between -17 and -26 degrees in the right pre-sheared region with a mean of -23.2 degrees. These results are promising as they align to the initial goal of achieving -23 degrees of shear in both pre-sheared regions to match the edge geometry of the tool and create fibre

continuity. According to the model the improvement to fibre continuity on this single ply will give up to an 11% improvement in mechanical stiffness (this differs based on the loading case). Adverse effects of the pre-shearing can be seen in Figure 6-27 and Figure 6-28 in the optical images. In the pre-sheared areas there is evidence of increased fibre waviness. This fibre waviness is more pronounced directly after the pre-shearing process and reduced after the forming operation. This is captured by a reduction in the shear angle standard deviation in the pre sheared regions from 3.7 degrees to 2.4 degrees (1.3 degree reduction). This can be attributed to the stresses during the forming process straightening out loose yarns that were under constrained during the pre-shearing operation. The fibre waviness is incorporated into the stress analysis model via the equations outlined in chapter 3. The increase to manufacturing time can be minimal if pre-shearing is incorporated as an operation during hand lamination. For automated and large scale operation the pre-shearing process can be performed simultaneously with other actions, removing it from the critical path.

6.4 Chapter summary

It has been shown that plies running longitudinally along a formed component can be pre-sheared before the forming operation to locally align fibres in the desired orientation. This can be conducted using a modified picture frame shearing jig at multiple sections along the length of a preform, as long as the entirety of the transverse region is subjected to shear. Alternatively this can be applied by hand during a hand lamination operation and measured with optical projection methods. The pre-shearing can be stabilised through the use of epoxy binder allowing for the decoupling of the pre shearing and forming operation.

The pre-shearing process generated a reduction in the wastage from trimming fabrics. The overall fabric area needed for beam like geometries was calculated for standard and pre-sheared preforms. For the simple preform shapes tested there was a reduction in material needed of 15.5%-34.5%. This is highly geometry dependent with the pre-shear angle and length being dependent factors. However the simplest low shear angle geometry tested showed a reduction of 15.5% with more complex geometries only showing greater reduction in the material needed. The Sill

demonstrator showed a reduction of 31% due to its multiple pre sheared zones and elongated length.

A non-orthogonal biaxial NCF material was successfully modelled in a forming simulation using Abaqus/explicit. The results were validated experimentally with comparison of shear angles in the pre-sheared and non-pre-sheared regions of the component, which showed a good prediction and an average discrepancy between modelled and experimental results of 0.9°. The forming model combined: a multi-shear cycle forming model from chapter 4 and novel non-orthogonal biaxial ply forming model.

A structural simulation was created for the L-beam to model the difference in stresses seen using pre-sheared and non-pre-sheared laminates. The simulation used the fibre orientations for the forming model in conjunction with the cyclic forming material model from Chapter 4. This was imported into a stress analysis model that incorporated variable fibre volume fraction and fibre misalignment due to shearing to alter mechanical properties. The results for the L- beam show that a pre-sheared laminate has a lower peak stress under all the tested load cases: 22.9% increase under bending loads. 23.4% increase under tensile loads and 16% increase under torsional loads. This was matched by a reduction in deflection of 13 % under bending loads.12% under tensile loads and 20.5% under torsional loads. The improvement to mechanical stiffness was shown to be transferable to component weight reduction of 17%.

A demonstrator Sill section was successfully formed with two pre-sheared regions of -23.5 degrees highlighting the viability of the method on complex industrial geometries. (The objective was to reach -23 degrees to generate fibre continuity across the component). The demonstrator Sill was modelled and showed up to an 11% improvement in mechanical properties based on peak stress magnitude (varied based on the loading condition). Secondly, there was a 31% improvement to material utilisation from shearing a reduced size initial blank. Overall the process was successful in achieving its goals of generating fibre continuity in 2D preforms and multiple routs for incorporating pre-shearing into industrial processes have been discussed.

7 Conclusions

The studies conducted in the previous chapters have been individually assessed against the objectives stated in the Introduction, followed by a discussion on the application of pre-shearing as a fibre alignment technique. The novelty of the research and the significance has been stated alongside what has been learnt and what can be achieved with the new knowledge.

7.1 Fibre angle measurement

Accurate fibre orientation information is critical for evaluating the structural properties of formed components. This includes the influence of fibre misalignment that occurs during forming processes as fabrics are made to shear in-plane. A novel methodology was successfully created around the Apodius Vision Sensor that outputs fibre angle and fibre misalignment information from the surface of formed components. This has been formatted to enable direct and easy comparison of inspected parts to simulated counterparts, with a view to allowing industry to utilise the increasing number of forming models on the market. From this research criteria has been also be developed for assessing fibre alignment in formed parts, which can be implemented at the inspection stage to give feedback for whether parts are likely to perform as predicted.

- I. Fibre angle measurements have been recorded during in-plane testing of NCFs and the shear angle distribution has been compared between bias extension and picture frame tests. The results showed inconsistencies in the assumptions of the bias extension test when applied to NCFs, as full-field testing highlighted the lack of distinct shear deformation zones due to out of plane buckling and stitch breakage. Results indicated that bias extension tests should not be used for pillar stitched NCFs beyond 10 degrees of shear. The use of the crosshead displacement to calculate the average shear angle during the picture frame shear test was validated for NCFs. Full-field data produced a homogenous shear angle distribution until the stitch breakage point was reached. Beyond the initial breakage point the average shear angle maintained agreement with the crosshead displacement and an increase in the distribution range captured the stitch breakage. Further shear testing on NCFs should use the picture frame test over the bias extension test and can be satisfied by measuring crosshead displacement to capture shear angle up to the stitch breakage point and beyond if necessary.

- II. There is a measureable level of fibre misalignment that occurs during NCF shearing (misalignment from the desired shear angle). This is asymmetric about the positive and negative shear directions (similar to the shear force/angle distribution) and has been quantified by calculating the standard deviation of the in-plane fibre angle during shear testing. The effect of fibre misalignment and varied fibre volume fraction on the in-plane stiffness of the ply was calculated and a non-linear function was created to express the change in tensile stiffness as the fibre angle changes. This function should be calculated for each material before applying it to any structural component that has been modelled and experienced shearing during manufacture. Shear angles that cause increased stiffness are of low importance. However, angles that cause a reduction in stiffness should be measured and avoided in critical structures. This occurs at -15 degrees (negative shear) which is a common level of shear experienced for formed components and produces a 6% reduction in stiffness.
- III. The fibre angle distribution was measured for a selection of 3D formed components including: punch formed hemispheres, double diaphragm formed hemispheres, multi-cycle double diaphragm formed hemispheres and double diaphragm formed complex beam and sill geometries. The measurements were compared to current algorithmic based measurement methods and showed a deviation between the methods of 1.7 degrees. The level of accuracy between the novel visualisation method and current techniques is higher than many aerospace drawing specifications of ± 3 degrees. The novel method is quick and enables the transfer of fibre angles on physically inspected parts to online data that can be compared to reference models. The mechanical performance of a component can therefore potentially be determined from a visual test. Many interior aerospace parts are 3 to 4 plies thick, with the outer plies aligned in the loading direction. In these cases this method would be very useful as the majority of the required information is available from the surface plies.

7.2 Initial non-linear shear region and inter-stitch yarn buckling.

The occurrence of inter-stitch yarn buckling was found during shear testing and was a large contribution to the fibre misalignment seen in the negative shear direction (measured during the work in Chapter 3). This defect was linked to a yarn bending deformation mode that had not been previously attributed to NCF shearing. Chapter 4 went on to highlight the appearance of this deformation mode at the onset of shearing and link the size of the initial non-linear shear zone with prevalence of inter-stitch yarn buckling. This research can be implemented to gauge the likelihood of fibre misalignment (due to yarn buckling) from an in-plane shear test. This helps test the suitability of materials for high shear applications, without the need to do 3D forming testing, saving on setup cost and time during process prove out. Defect

reduction strategies were tested to give a range of process alteration options that can be used to improve the quality of a preform without needing to change material or tool geometry.

- I. It was found that at the onset of shearing, the shear stiffness is dominated by the inter-yarn frictional interactions at the yarn crossovers. The transition from frictional to slippage based deformation was analytically predicted in two pillar-stitched NCFs with an R^2 value of 0.98. The sensitivity of fabric properties on the initial non-linear shear curve was analysed showing that stitch tension has the greatest effect on the amplitude of the initial non-linear shear zone. Later results showed a positive relationship between a high amplitude initial-shear zone and inter-stitch buckling, so this research can be used to inform users of the disadvantages of NCFs with high stitch tension.
- II. The analytical model used to predict the initial non-linear shear zone was extended to predict the maximum stitch tension that could be applied to a yarn before slippage is reduced to a detrimental effect. A reduction in yarn slippage was found to cause inter-stitch buckling defects when the force required for yarn slippage was exceeded by the critical buckling point of the yarn. This was predicted by the analytical model and was observed during physical shear testing. The likelihood of buckling was found to be reduced by controlling the inter-yarn frictional interaction through stitch removal and lubrication.
- III. Local stitch removal and resin lubrication were tested as buckling defect reduction strategies. Both methods successfully removed the buckling defect during in-plane samples and punch formed hemispheres. Stitch removal was chosen as it scales easily and does not introduce foreign object debris (FOD) into the composite. It could be implemented into current manufacturing processes at the laminating stage, using hand held soldering irons, or heated jigs to melt the required stitches. Similarly a heated end effector could be placed on a robot arm to automate the process. Optimisation of the stitch removal process would need to be conducted to keep laminating time to a minimum. Lubrication has the drawback of introducing another material into the composite which may affect the cure cycle. However, it proved to be effective at completely removing the inter-stitch buckling defect. Further research could be conducted into the removal of lubrication after shearing for 2D-3D manufacturing. Initial thoughts are to create a resin lubricant that co-cures with the infusion resin, or a water based lubricant that could be evaporated after the preforming stage.

7.3 Modelling of consecutive forming processes.

Multi-stage consecutive forming processes, such as multi-punch forming or the forming of pre-sheared fabrics, cannot be simulated with current finite element material models. The research conducted here captures the non-linear behaviour of NCF fabrics that have undergone multiple previous shear cycles. This was used to

generate a novel material model that accurately captures the shear angle distribution during multi stage forming processes. The application of this model is in testing manufacturing possibilities that are too high risk to optimise with a physical test. The simulation can also be used to inform the formability of geometries that require multiple punches to create adequate compaction, which will be adopted for complex preformed components.

- I. The effect of multiple shear cycles was measured on a selection of NCFs with different stitch architectures and in all cases a significant drop in shear stiffness (a shear force reduction of 20x from the initial cycle) was generated after the first cycle. This has not previously been noted in NCFs and differs from woven fabrics which have a steady cyclic shear response. The same shear force drop was found in 4 fabrics with different stitch architectures (Pillar, Bound Pillar, Half Pillar and Tricot) showing that this is a characteristic that is common to NCFs. The change in non-linear modulus was found to be caused by permanent deformation to the stitch as it was stretched during shearing. Micrographs show permanent elongation to the stitch structure after 30 degrees of shearing. This highlights the necessity for good material control during processing so that unwanted shearing does not occur, as the change to material properties is permanent.
- II. A set of functions were generated which predict the non-linear shear modulus for a pillar stitched NCF during multiple shear cycles. These were implemented into a macro-scale elastic material model which was successfully used to simulate the shear angle distribution for a 3D formed hemisphere that had undergone multiple forming cycles. The model was validated and it was found that there was a peak deviation of 2° between the simulation data and the experimental in-plane shear testing. This model can be implemented during current drape analyses when creating ply kits for 2D and 3D preforms, to ensure the kit will conform to the required geometry with the desired fibre angles.
- III. A representative multi-stage forming process was developed to validate the material model and explore forming benefits to be gained from the local changes in shear stiffness generated from the multi-stage process. The process outlined how an initial stage can be used to generate local regions of very high shear in the fabric, creating a pre-sheared state mimicking that found during hand layup. The process was successful in validating the multi-cycle material model and increasing the tool-ply conformity for a double diaphragm formed hemisphere by 57%. Further developments would be necessary to prove out the process, as there are limitations on the complexity of the final formed shape. The process improves conformity in areas where double curvature causes bridging or wrinkling, so it is only applicable in specific use-cases where the geometry meets those criteria. A development would be required to use this process to form around complex metallic inserts, as they tend to create geometries that are protruding cylinders, cuboids and domes.

7.4 Fibre alignment control during forming processes.

Fibre angle control is difficult in automated forming processes as the transition of the fabric from 2D to 3D causes movement of the yarns away from the desired orientations. By utilising the forming model created in the previous chapter, alongside the material understanding from the research presented earlier, a consecutive forming process has been developed that controls fibre alignment in a 2D to 3D forming operation through pre-sheared fabric forming. The use case for pre-sheared fabric forming is to imitate the continuous yarn orientations that can be generated from manual shearing during hand layup to give improved component mechanical properties. A representative pre-shearing rig was created to demonstrate how controlled pre-shearing could be implemented into current 2D pre-forms in a laboratory setting. The 200mm test frame used to produce pre-sheared preforms was then scaled up to 600mm, with no foreseen reasons why it could not be scaled further. The studies conducted showed a reduction in peak stress of 16% - 23% for pre-sheared laminates over typical quasi-isotropic laminates during stiffness modelling, accompanied by a 15% material utilisation improvement for some plies. The stiffness improvements have been directly translated into component weight savings (by removing unnecessary plies) which is critical in aerospace, automotive and sporting industries. A reduction in ply count creates a component cost reduction as material usage is reduced (further dropped by the improvements to material utilisation that can be generated) as well as a reduction in labour for laminating those plies.

- I. A methodology has been created to locally pre-shear blanks used in automated 2D-3D forming processes with the intention of aligning the fibre angle to the principal loading direction of the component. A continuous yarn spans the length of the blank with locally sheared regions bending the yarns to align to the component. A simple and complex geometry component have been successfully formed using the pre-shearing methodology with local fibre angles matching the principal load directions of the component. The beam geometry chosen relates to the automotive industry (pillars and sills) and the aerospace industry (ribs and spars). Specifically in the automotive space, there are key economical and weight saving objectives as electrified vehicles enter the market. The method presented

here was designed to be a tool that can be utilised improve mass manufactured composite parts to meet those objectives.

- II. A finite element model has been created to simulate the application of localised shearing to a blank before the subsequent forming operation. The model utilised novel the multi-cycle material model created previously in this research and accurately captured shear angle data when compared to experimental trials. The shear angle data was used in conjunction with the novel fibre misalignment functions (also generated previously in the research) as inputs to a structural analysis model. This structural model is a step beyond previous formed NCF component models, as it captures two new elements:
 - a. The change in structural material properties from the fibre waviness generated during forming.
 - b. The corrected final formed fibre orientations and material state after complex (multi stage) forming.

Meeting the weight saving objective: During stiffness testing, the model indicated an increase in peak stress of 16% - 23% for pre-sheared laminates over typical quasi-isotropic laminates and an average 15% reduction in deflection. Translating these stiffness improvements into weight savings through ply removal demonstrated a 17% weight reduction that could be achieved at a small stiffness penalty (averaging 5% over deflection test modes).

Meeting the economic objective: Pre-shearing enabled a 15% improvement in material utilisation in this test, due to the improvements to nesting that are achieved with rectangular preforms. This can be added to the material utilisation improvements from ply removal to give a 32% reduction in material usage. This number is geometry dependent, but representative of what can be achieved with an ideal geometry.

7.5 Discussion of pre shearing in 2D-3D composite forming.

Pre-shearing an NCF has been shown to dramatically influence the formability of the fabric, potentially generate defects and impact the infused structural properties. However, the methodology has proven successful in granting a new level of control over fibre alignment in a highly automated process with desirable structural improvements to infused components. The change in fabric properties has been shown to be predictable, and strategies have been implemented to remove any minor defects generated. This enables multiple shear cycles to be used on NCFs without detrimental effects to the fabric, allowing for local fibre angle control. This control opens up manufacturing possibilities that give definitive benefits to the mechanical structure of formed components. The understanding gained from the

studies conducted here could be applied in an industrial setting to generate a novel pre-conditioning process for fabric blanks for traditional 2D-3D forming methods. This has been proven at a small scale and can be implemented by hand laminators, or scaled up to accompany the industry desire to automate the forming process. The benefits are an improvement in the mechanical properties for a formed components due to fibre orientation control, translating into a reduction in the required ply count and consequently the associated component mass, material costs and labour costs.

8 Appendix A

8.1 Apodius scanning methodology.

8.1.1 Laser scanning

The laser line scanner equipped to the Apodius system has a resolution of >1mm per point. Scanning is conducted by manoeuvring the scan head around the component within the fully extended range of the Absolute arm. The base of the arm is the fixed datum in relation to the component and can be mounted on a desk or tripod configuration. Live scanning data is fed back to a virtual environment in the software to give updates on missed points and scan quality. The scanned points were processed in Polyworks meshing software and the custom Apodius 3D software. Polyworks allows for very high resolution points clouds to be generated and converted into detailed meshes for tool/part comparisons. The Apodius 3D software allows for the combination of the laser line points cloud and optical data from the Vision sensor.

8.1.2 Optical imaging

The Vision sensor generates a high resolution, low reflectivity image with high contrast, which can be used for fibre angle analysis. The images are acquired in a similar manner to the topology data, however discrete images are taken with the sensor and then stitched together to create a surface model. This occurs in real time in the virtual environment allowing for a high level of control over missed regions. To acquire the local fibre direction in a designated material a reference must be given to the software and a single or multiple fibre directions must be defined. An assumption is made that all fibres within a yarn align with the primary yarn direction. This can be generated by feeding an example image to the software or by altering the noise threshold, peak border, peak width and peak margin. From this a range of expected fibre angles is generated based off of the dominant yarn direction in the sample. This lets the stitch be identified and removed from fibre angle calculations.

A texture based segmentation algorithm is used to measure the greyscale in each image [120]. A texture energy image is created by measuring and combining the occurrence of lines, points and edges via Laws filter masks [92]. This energy is coded

using 256 grey values and averaging the absolute pixel values over 7 x 7 windows. A high energy value is an image with lots of points, small corners and edges. The discontinuity is measured against the surrounding region and a threshold is set to binarise the image. This threshold value has a large influence on the final image with a small value leading to a large number of small regions, and a large value creating fewer larger regions. From this the desired region can be selected and coloured as in Figure 8-1. **Error! Reference source not found.** The fibre orientation can be calculated from the edge vector in the digital model.

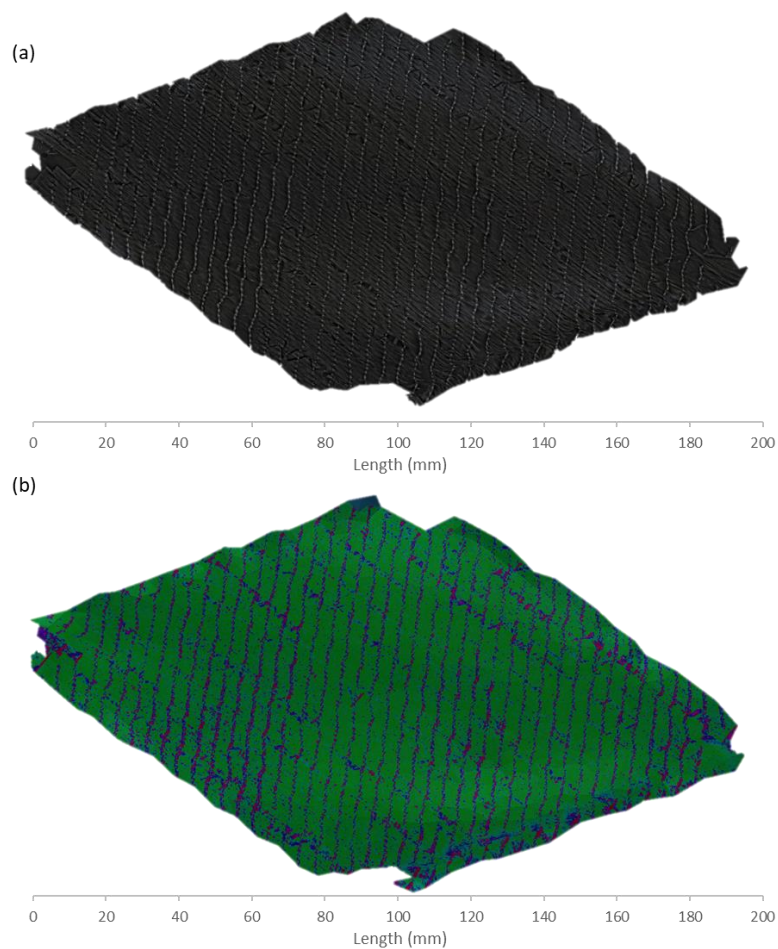


Figure 8-1 Raw data from the Apodius scanning system. (a) Is the low reflectivity image mapped onto the 3D mesh generated from the laser scanner. (b) Is a fine detail map of the principal direction in the sample as determined by the system.

The data collected with the optical scanning methodology generates a 3D mesh of the sample allowing for out of plane defect to be distinguished from in-plane defects as shown by the highlighted (blue) regions.

9 Appendix B

9.1 Shear angle calculation and export to Abaqus, Matlab code

Note, xml2struct and find_perp

Wouter Falkena

(2022). xml2struct (<https://www.mathworks.com/matlabcentral/fileexchange/28518-xml2struct>), MATLAB Central File Exchange. Retrieved June 16, 2022.

Christoffer Stausland (2022). Finds a perpendicular vector (<https://www.mathworks.com/matlabcentral/fileexchange/32811-finds-a-perpendicular-vector>), MATLAB Central File Exchange. Retrieved June 16, 2022.

9.1.1 Single sided scanning

```
% _____  
% _____  
%Apodius 2 Abaqus V1.1.1  
% _____  
% _____  
%Matlab code utilising xml1strut to create an output node+element  
list from which  
%data can be imported into Abaqus or points comparison software.  
%Input - Apodius scanned mesh with orientaito information in a  
[.xml]  
%format, provided by the didgimat export.  
clear  
% _____  
% _____  
%Input didgimat file in .xml format  
  
%Input 2 Directional XML  
Input = 'BIAS_NEG_50MM.xml';  
  
% _____  
% _____  
  
%input original stitch direction  
BaseOri = [450.195E-03, -2.210083, -228.74411]  
  
% _____  
% _____  
% _____  
  
%Restructure and output Mesh, element and Orientation Values  
  
% _____  
% _____
```

```

%
-----

    struct = xml2struct(Input) ;
%Structuring XML
    structS = xml2struct(InputS) ;

MeshSize = size(struct.root.Mesh.Nodes.Node) ;
smesh = MeshSize(1,2) ;
for k = 1:smesh
%outputting Node data (ID,XYZ)
    NID = str2num(struct.root.Mesh.Nodes.Node{1,k}.Attributes.ID) ;
    X = str2num(struct.root.Mesh.Nodes.Node{1,k}.Attributes.X) ;
    Y = str2num(struct.root.Mesh.Nodes.Node{1,k}.Attributes.Y) ;
    Z = str2num(struct.root.Mesh.Nodes.Node{1,k}.Attributes.Z) ;
    Mesh(k,1) = NID ;
%"Mesh" is the nodal output
    Mesh(k,2) = X ;
    Mesh(k,3) = Y ;
    Mesh(k,4) = Z ;
end

ElementSize =
str2num(struct.root.Mesh.Elements.Attributes.nElements) ;
emesh = ElementSize ;
for e = 1:emesh
%Outputting element data (ID(Node 1 Node 2 Node 3)
    EID =
str2num(struct.root.Mesh.Elements.Element{1,e}.Attributes.ID) ;
    Nodes =
str2num(struct.root.Mesh.Elements.Element{1,e}.NodesID.Text) ;
    NODE1 = Nodes(1,1) ;
    NODE2 = Nodes(1,2) ;
    NODE3 = Nodes(1,3) ;
    Element(e,1) = EID ;
%"Element" is the element output
    Element(e,2) = NODE1 ;
    Element(e,3) = NODE2 ;
    Element(e,4) = NODE3 ;

end

OriSize = size(struct.root.DataSet.Element) ;
omesh = OriSize(1,2) ;
for o = 1:omesh
%Outputting Orientation data (ID,vector 1,2,3, perpendicular vector
1,2,3)
    OID = str2num(struct.root.DataSet.Element{1,o}.Attributes.ID) ;
    Orientation =
str2num(struct.root.DataSet.Element{1,o}.Layer.Data.Text) ;
    Ori1 = Orientation(1,1) ;
    Ori2 = Orientation(1,2) ;
    Ori3 = Orientation(1,3) ;
    fPerp = find_perp([Ori1,Ori2,Ori3]) ;
    Orient(o,1) = OID ;
%Orient is teh elemetn output
    Orient(o,2) = Ori1 ;
    Orient(o,3) = Ori2 ;
    Orient(o,4) = Ori3 ;
    Orient(o,5) = fPerp(1,1) ;

```

```

        Orient(o,6) = fPerp(1,2) ;
        Orient(o,7) = fPerp(1,3) ;
        Orient(o,8) = 3E+9 ;
%younghs modulus
        Orient(o,9) = 0.2 ;
%poisson ratio

end

        cn1 = 0 ;
%setting values for Loops
        cn2 = 0 ;
        cn3 = 0 ;
        cori1 = 0 ;
        cori2 = 0 ;
        cori3 = 0 ;
        cp1x = 0 ;
        cp1y = 0 ;
        cp1z = 0;
        cp2x = 0 ;
        cp2y = 0 ;
        cp2z = 0;
        cp3x = 0 ;
        cp3y = 0 ;
        cp3z = 0;
for c = 1:omesh
%compiling all data into elemetn ID with orentaitons and nodal
positions
        for cb = 1:emesh
                if Orient(c,1) == Element(cb,1)
%(Ellement ID,Point1 XYZ,Point2 XYZ,Point3 XYZ,Orientation vector
XYZ)

                        cn1 = Element(cb,2) ;
                        cn2 = Element(cb,3) ;
                        cn3 = Element(cb,4) ;
                        cori1 = Orient(c,2) ;
                        cori2 = Orient(c,3) ;
                        cori3 = Orient(c,4) ;

                end
                ELOR(c,1) = Orient(c,1) ;
                ELOR(c,2) = cn1 ;
                ELOR(c,3) = cn2 ;
                ELOR(c,4) = cn3 ;
                ELOR(c,5) = cori1 ;
                ELOR(c,6) = cori2 ;
                ELOR(c,7) = cori3 ;
        end
for cc = 1:smesh
        if Mesh(cc,1) == ELOR(c,2)
                cp1x = Mesh(cc,2) ;
                cp1y = Mesh(cc,3) ;
                cp1z = Mesh(cc,4) ;

        end
        if Mesh(cc,1) == ELOR(c,3)
                cp2x = Mesh(cc,2) ;
                cp2y = Mesh(cc,3) ;
                cp2z = Mesh(cc,4) ;

        end
        if Mesh(cc,1) == ELOR(c,4)
                cp3x = Mesh(cc,2) ;
                cp3y = Mesh(cc,3) ;

```

```

        cp3z = Mesh(cc,4) ;
    end
    All_DATA(c,1) = Orient(c,1) ;
%All Data is output
    All_DATA(c,2) = cp1x ;
    All_DATA(c,3) = cp1y ;
    All_DATA(c,4) = cp1z ;
    All_DATA(c,5) = cp2x ;
    All_DATA(c,6) = cp2y ;
    All_DATA(c,7) = cp2z ;
    All_DATA(c,8) = cp3x ;
    All_DATA(c,9) = cp3y ;
    All_DATA(c,10) = cp3z ;
    All_DATA(c,11) = ELOR(c,5) ;
    All_DATA(c,12) = ELOR(c,6) ;
    All_DATA(c,13) = ELOR(c,7) ;
end
end

%
%
%

%Finding shear angle
OSA1 = 0 ;
OSA2 = 0 ;
OSA3 = 0 ;
OSA4 = 0 ;
OSA5 = 0 ;
OSA6 = 0 ;
OSA7 = 0 ;
OSA8 = 0 ;
OSA9 = 0 ;

for sa = 1:omesh
    OSA1 = Orient(sa,1) ; %element number
    OSA2 = Orient(sa,2) ;
    OSA3 = Orient(sa,3) ;
    OSA4 = Orient(sa,4) ;
    OSA8 = 3E+9 ;
    OSA9 = 0.2 ;

    FibreA = [OSA2,OSA3,OSA4] ; %fibre angle
    Dot = dot(FibreA,BaseOri) ;
    Dotabs =
sqrt(FibreA(1,1)^2+FibreA(1,2)^2+FibreA(1,3)^2)*(sqrt(BaseOri(1,1)^2
+BaseOri(1,2)^2+BaseOri(1,3)^2)) ; %vector calculation
    OriDifAngle = acos(Dot/Dotabs) ;
    ShearAngle(sa,1) = OSA1 ;
    SATEST = round((-((180/pi)*((OriDifAngle)-(pi/4))+(0))*2));
%shear angle calculation
    ShearAngle(sa,2) = SATEST ;
    ShearAngle(sa,3) = sa ;
    ShearAngle(sa,4) = OSA8 ;
    ShearAngle(sa,5) = OSA9 ;
    m1 = "          matrix(" ;

```

```

    m1s = string(m1) ;
    Substring(sa,1) = [m1s] ;
    m2 = ",1) =" ;
    m2s = string(m2) ;
    Substring(sa,2) = [m2s] ;
    m3 = ",2) =" ;
    m3s = string(m3) ;
    Substring(sa,3) = [m3s] ;

end
Superstring =
[Substring(:,1),ShearAngle(:,3),Substring(:,2),ShearAngle(:,2),Subst
ring(:,3)] ;

%
%
%
%Writing Abaqus Input file for comparison analysis
%
%

fileID = fopen('A2A.inp','w');
fprintf(fileID, '%s\r\n', "**Heading");
fprintf(fileID, '%s\r\n', "*** Job name: Job-1 Model name: A2A");
fprintf(fileID, '%s\r\n', "File generated by Apodius 2 Abaqus
v1.1.1");
fprintf(fileID, '%s\r\n', "**Preprint, echo=NO, model=NO, history=NO,
contact=NO");
fprintf(fileID, '%s\r\n', "**Node");
fprintf(fileID, '%4d,%4d,%4d,%4d\r\n',
[Mesh(:,1),Mesh(:,2),Mesh(:,3),Mesh(:,4)].');
fprintf(fileID, '%s\r\n', "**Element, Type=S3R");
fprintf(fileID, '%4d,%4d,%4d,%4d\r\n',
[Element(:,1),Element(:,2),Element(:,3),Element(:,4)].');
fprintf(fileID, '%s\r\n', "*****");
fprintf(fileID, '%s\r\n', "*** ORIENTATIONS ***");
fprintf(fileID, '%s\r\n', "*****");
fprintf(fileID, '%s\r\n', "*** Orientation vectors");
fprintf(fileID, '%s\r\n', "*** 1st vector represents the fibre
direction");
fprintf(fileID, '%s\r\n', "*** 2nd vector is an arbitrary vector
perpendicular to the first");
fprintf(fileID, '%s\r\n', "**Distribution Table,
Name=A2AOrientationVectors");
fprintf(fileID, '%s\r\n', "COORD3D,COORD3D");
fprintf(fileID, '%s\r\n', "**Distribution, Location=Element,
Table=A2AOrientationVectors, Name=A2AOrientationVectors,
Input=A2AOrientationVectors.ori");
fprintf(fileID, '%s\r\n', "**Orientation, Name=A2AOrientations,
Definition=coordinates");
fprintf(fileID, '%s\r\n', "A2AOrientationVectors");
fprintf(fileID, '%s\r\n', "1, 0");
fprintf(fileID, '%s\r\n', "**Orientation, name=Ori-PART-
1_A2AORIENTATIONVECTORS, system=RECTANGULAR");

```

```

fprintf(fileID, '%s\r\n', "PART-1_A2AORIENTATIONVECTORS");
fprintf(fileID, '%s\r\n', "3, 0.");
fprintf(fileID, '%s\r\n', "*** Section: Section-1-ALLELEMENTS");
fprintf(fileID, '%s\r\n', "*Shell Section, elset=ALLELEMENTS,
material=MAT1, orientation=Ori-PART-1_A2AORIENTATIONVECTORS");
fprintf(fileID, '%s\r\n', "1., 5");
fprintf(fileID, '%s\r\n', "*****");
fprintf(fileID, '%s\r\n', "*** ELEMENT SETS ***");
fprintf(fileID, '%s\r\n', "*****");
fprintf(fileID, '%s\r\n', "*** A2A generates a number of element
sets:");
fprintf(fileID, '%s\r\n', "*** All - Contains all elements");
fprintf(fileID, '%s\r\n', "*ElSet, ElSet=AllElements, Generate");
fprintf(fileID, '%4s,%4d,%4s\r\n', "1", emesh.', "1");
fprintf(fileID, '%s\r\n', "*****");
fprintf(fileID, '%s\r\n', "*** NODE SETS ***");
fprintf(fileID, '%s\r\n', "*****");
fprintf(fileID, '%s\r\n', "*** A2A generates a number of node sets:");
fprintf(fileID, '%s\r\n', "*** AllNodes - Node set containing all
elements");
fprintf(fileID, '%s\r\n', "*NSet, NSet=AllNodes, Generate");
fprintf(fileID, '%4s,%4d,%4s\r\n', "1", smesh.', "1");
fprintf(fileID, '%s\r\n', "*Nset, nset=Set-2, Generate");
fprintf(fileID, '%4s,%4d,%4s\r\n', "1", smesh.', "1");
fprintf(fileID, '%s\r\n', "*****");
fprintf(fileID, '%s\r\n', "*** MATERIALS ***");
fprintf(fileID, '%s\r\n', "*****");
fprintf(fileID, '%s\r\n', "*Material, Name=Mat1");
fprintf(fileID, '%s\r\n', "*Depvar");
fprintf(fileID, '%s\r\n', "      2,");
fprintf(fileID, '%s\r\n', "*Elastic, dependencies = 1");
fprintf(fileID, '%4d,%4d,%4d.,%4d.\r\n', [ShearAngle(:,4), ShearAngle(:,5), ShearAngle(:,2), ShearAngle(:,1)].');
fprintf(fileID, '%s\r\n', "*Expansion");
fprintf(fileID, '%s\r\n', "6.5e-06");
fprintf(fileID, '%s\r\n', "*User Defined Field");
fprintf(fileID, '%s\r\n', "*Shell Section, ElSet=AllElements,
Material=Mat1, Thickness = 0.5, Orientation=A2AOrientations");
fprintf(fileID, '%s\r\n', "1.0,");
fprintf(fileID, '%s\r\n', "***");
fprintf(fileID, '%s\r\n', "***BOUNDARY CONDITIONS");
fprintf(fileID, '%s\r\n', "***");
fprintf(fileID, '%s\r\n', "*** Name: BC-1 Type:
Symmetry/Antisymmetry/Encastre");
fprintf(fileID, '%s\r\n', "*Boundary");
fprintf(fileID, '%s\r\n', "Set-2, ENCASTRE");
fprintf(fileID, '%s\r\n', "*** -----
-----");
fprintf(fileID, '%s\r\n', "***");
fprintf(fileID, '%s\r\n', "***STEP: Step-1");
fprintf(fileID, '%s\r\n', "***");
fprintf(fileID, '%s\r\n', "*Step, name=Step-1, nlgeom=NO");
fprintf(fileID, '%s\r\n', "*Static");
fprintf(fileID, '%s\r\n', "1., 1., 1e-05, 1.");
fprintf(fileID, '%s\r\n', "***");
fprintf(fileID, '%s\r\n', "***OUTPUT REQUESTS");
fprintf(fileID, '%s\r\n', "***");
fprintf(fileID, '%s\r\n', "*Restart, write, frequency=0");
fprintf(fileID, '%s\r\n', "***");
fprintf(fileID, '%s\r\n', "***FIELD OUTPUT: F-Output-1");
fprintf(fileID, '%s\r\n', "***");

```

```

fprintf(fileID, '%s\r\n', "*Output, field");
fprintf(fileID, '%s\r\n', "*Node Output");
fprintf(fileID, '%s\r\n', "CF, RF, U");
fprintf(fileID, '%s\r\n', "*Element Output, directions=YES");
fprintf(fileID, '%s\r\n', "FV, LE, PE, PEEQ, PEMAG, S, SDV, TEMP");
fprintf(fileID, '%s\r\n', "*Contact Output");
fprintf(fileID, '%s\r\n', "CDISP, CSTRESS");
fprintf(fileID, '%s\r\n', "***");
fprintf(fileID, '%s\r\n', "***HISTORY OUTPUT: H-Output-1");
fprintf(fileID, '%s\r\n', "***");
fprintf(fileID, '%s\r\n', "*Output, history, variable=PRESELECT");
fprintf(fileID, '%s\r\n', "*End Step");
fclose(fileID);

```

%

%Writing .ori file for lookup table of orientations

%

```

fileID = fopen('A2AOrientationVectors.ori', 'w');
fprintf(fileID, '%s\r\n', "*****");
fprintf(fileID, '%s\r\n', "*** ORIENTATIONS ***");
fprintf(fileID, '%s\r\n', "*****");
fprintf(fileID, '%s\r\n', "*** Orientation vectors");
fprintf(fileID, '%s\r\n', "*** 1st vector represents the fibre
direction");
fprintf(fileID, '%s\r\n', "*** 2nd vector is an arbitrary vector
perpendicular to the first");
fprintf(fileID, '%s\r\n', ", 1.0, 0.0, 0.0, 0.0, 1.0, 0.0");
fprintf(fileID, '%4d,%4d,%4d,%4d,%4d,%4d,%4d\r\n',
[Orient(:,1),Orient(:,2),Orient(:,3),Orient(:,4),Orient(:,5),Orient(
(:,6),Orient(:,7)].');
fclose(fileID);

```

%

%Writing .f Subroutine for USDFLD

%

```

fileID = fopen('A2AFieldVariables.f', 'w');
fprintf(fileID, '%s\r\n', '!DEC$ ATTRIBUTES ALIAS:"usdfld":USDFLD');
fprintf(fileID, '%s\r\n', "      SUBROUTINE
USDFLD(FIELD, STATEV, PNEWDT, DIRECT, T, CELENT, ");
fprintf(fileID, '%s\r\n', "      1
TIME, DTIME, CMNAME, ORNAME, NFIELD, NSTATV, NOEL, NPT, LAYER, ");
fprintf(fileID, '%s\r\n', "      2
KSPT, KSTEP, KINC, NDI, NSHR, COORD, JMAC, JMATYP, MATLAYO, LACCFLA ");
fprintf(fileID, '%s\r\n', "C");
fprintf(fileID, '%s\r\n', "      INCLUDE 'ABA_PARAM.INC'");
fprintf(fileID, '%s\r\n', "C");
fprintf(fileID, '%s\r\n', "      CHARACTER*80 CMNAME,ORNAME");
fprintf(fileID, '%s\r\n', "      CHARACTER*3  FLGRAY(15)");
fprintf(fileID, '%s\r\n', "      DIMENSION
FIELD(NFIELD), STATEV(NSTATV), DIRECT(3,3), ");
fprintf(fileID, '%s\r\n', "      1 T(3,3), TIME(2)");
fprintf(fileID, '%s\r\n', "      DIMENSION
ARRAY(15), JARRAY(15), JMAC(*), JMATYP(*), COORD(*), ");
fprintf(fileID, '%s\r\n', "      1 matrix(9534,2)");

```

```

fprintf(fileID, '%s\r\n', '!DEC$ ATTRIBUTES
ALIAS:"getpartinfo":GETPARTINFO');
fprintf(fileID, '%s\r\n', "          FIELD(1) = NOEL");
fprintf(fileID, '%s\r\n', "          STATEV(1) = FIELD(1)");
fprintf(fileID, '%4s %4s %4s
%4s\r\n', [Superstring(:,1), ShearAngle(:,3), Substring(:,2), ShearAngle
(:,1)].');
fprintf(fileID, '%4s %4s %4s
%4s\r\n', [Superstring(:,1), ShearAngle(:,3), Substring(:,3), ShearAngle
(:,2)].');
fprintf(fileID, '%s\r\n', "          DO i =1,9534");
fprintf(fileID, '%s\r\n', "          IF (matrix(i,1) == FIELD(1))
then");
fprintf(fileID, '%s\r\n', "          STATEV(2) = matrix(i,2)");
fprintf(fileID, '%s\r\n', "          endif");
fprintf(fileID, '%s\r\n', "          enddo");
fprintf(fileID, '%s\r\n', "          RETURN");
fprintf(fileID, '%s\r\n', "          END SUBROUTINE");
fclose(fileID);

```

9.2 Doubled sided scanning

```

% _____
% _____
%Apodius 2 Abaqus V1.1.1
% _____
% _____
%Matlab code utilising xmlstrut to create an output node+element
list from which
%data can be imported into Abaqus or points comparison software.
%Input - 2 Apodius scanned mesh with orientaito information in a
[.xml]
%meshed must be aligned
%format, provided by the didgimat export.
clear
%
% _____
%
% _____
%Input didgimat file in .xml format

%Input 2 Aligned Top and Bottom Face XML
Input_Top = 'HF23_front_1.xml';

Input_Bottom = 'HF23_back_1.xml';

%
% _____
%
% _____
%Input Stitch vector -
Stitch_Vector2 = [2.70789e+01, 1.74919e+01, -3.78699e+01] ;
Stitch_Vector = [2.93997e+01, 2.57290e+01, -4.29761e+01] ;

%
% _____
%
% _____

```



```

%Restructure and output Mesh, element and Orientation Values

%
%
%

    struct = xml2struct(Input_Top) ;
%Structuring XML
    structS = xml2struct(Input_Bottom) ;

MeshSize = size(struct.root.Mesh.Nodes.Node) ;
smesh = MeshSize(1,2) ;
for k = 1:smesh
%outputting Node data (ID,XYZ)
    NID = str2num(struct.root.Mesh.Nodes.Node{1,k}.Attributes.ID) ;
    X = str2num(struct.root.Mesh.Nodes.Node{1,k}.Attributes.X) ;
    Y = str2num(struct.root.Mesh.Nodes.Node{1,k}.Attributes.Y) ;
    Z = str2num(struct.root.Mesh.Nodes.Node{1,k}.Attributes.Z) ;
    Mesh(k,1) = NID ;
%"Mesh" is the nodal output
    Mesh(k,2) = X ;
    Mesh(k,3) = Y ;
    Mesh(k,4) = Z ;
end

ElementSize =
str2num(struct.root.Mesh.Elements.Attributes.nElements) ;
emesh = ElementSize ;
for e = 1:emesh
%Outputting element data (ID(Node 1 Node 2 Node 3)
    EID =
str2num(struct.root.Mesh.Elements.Element{1,e}.Attributes.ID) ;
    Nodes =
str2num(struct.root.Mesh.Elements.Element{1,e}.NodesID.Text) ;
    NODE1 = Nodes(1,1) ;
    NODE2 = Nodes(1,2) ;
    NODE3 = Nodes(1,3) ;
    Element(e,1) = EID ;
%"Element" is the element output
    Element(e,2) = NODE1 ;
    Element(e,3) = NODE2 ;
    Element(e,4) = NODE3 ;
    for enodes = 1:smesh
        if NODE1 == Mesh(enodes,1)
            N1X = Mesh(enodes,2) ;
% find intergration points in elements
            N1Y = Mesh(enodes,3) ;
            N1Z = Mesh(enodes,4) ;
        end
        if NODE2 == Mesh(enodes,1)
            N2X = Mesh(enodes,2) ;
            N2Y = Mesh(enodes,3) ;
            N2Z = Mesh(enodes,4) ;
        end
        if NODE3 == Mesh(enodes,1)
            N3X = Mesh(enodes,2) ;
            N3Y = Mesh(enodes,3) ;

```

```

        N3Z = Mesh(enodes,4) ;
    end
    end
    NXCentre = mean([N1X,N2X,N3X]) ;
    NYCentre = mean([N1Y,N2Y,N3Y]) ;
    NZCentre = mean([N1Z,N2Z,N3Z]) ;
    Integration(e,1) = EID ;
    Integration(e,2) = NXCentre ;
    Integration(e,3) = NYCentre ;
    Integration(e,4) = NZCentre ;

end

OriSize = size(struct.root.DataSet.Element) ;
omesh = OriSize(1,2) ;
for o = 1:omesh
    %Outputting Orientation data (ID,vector 1,2,3, perpendicular vector
    1,2,3)
    OID = str2num(struct.root.DataSet.Element{1,o}.Attributes.ID) ;
    Orientation =
str2num(struct.root.DataSet.Element{1,o}.Layer.Data.Text) ;
    Ori1 = Orientation(1,1) ;
    Ori2 = Orientation(1,2) ;
    Ori3 = Orientation(1,3) ;
    fPerp = find_perp([Ori1,Ori2,Ori3]) ;
    Orient(o,1) = OID ;
    %Orient is teh elemetn output
    Orient(o,2) = Ori1 ;
    Orient(o,3) = Ori2 ;
    Orient(o,4) = Ori3 ;
    Orient(o,5) = fPerp(1,1) ;
    Orient(o,6) = fPerp(1,2) ;
    Orient(o,7) = fPerp(1,3) ;
    Orient(o,8) = 3E+9 ;
    %younghs modulus
    Orient(o,9) = 0.2 ;
    %poisson ratio
    for ino = 1:emesh
        if Orient(o,1) == Integration(ino,1)
            Orient(o,10) = Integration(ino,2) ;
            Orient(o,11) = Integration(ino,3) ;
            Orient(o,12) = Integration(ino,4) ;
        end
    end
end

end

%
%
%

%Unpacking Bottom face XML orientatoinis
MeshSizeBF = size(structS.root.Mesh.Nodes.Node) ;
smeshBF = MeshSizeBF(1,2) ;
for kBF = 1:smeshBF
    %outputting Node data (ID,XYZ)
    NIDBF =
str2num(structS.root.Mesh.Nodes.Node{1,kBF}.Attributes.ID) ;

```

```

    XBF = str2num(structS.root.Mesh.Nodes.Node{1,kBF}.Attributes.X)
;
    YBF = str2num(structS.root.Mesh.Nodes.Node{1,kBF}.Attributes.Y)
;
    ZBF = str2num(structS.root.Mesh.Nodes.Node{1,kBF}.Attributes.Z)
;
    MeshBF(kBF,1) = NIDBF ;
%"Mesh" is the nodal output
    MeshBF(kBF,2) = XBF ;
    MeshBF(kBF,3) = YBF ;
    MeshBF(kBF,4) = ZBF ;
end

ElementSizeBF =
str2num(structS.root.Mesh.Elements.Attributes.nElements) ;
emeshBF = ElementSizeBF ;
for eBF = 1:emeshBF
%"Outputting element data (ID(Node 1 Node 2 Node 3))
    EIDBF =
str2num(structS.root.Mesh.Elements.Element{1,eBF}.Attributes.ID) ;
    NodesBF =
str2num(structS.root.Mesh.Elements.Element{1,eBF}.NodesID.Text) ;
    NODE1BF = NodesBF(1,1) ;
    NODE2BF = NodesBF(1,2) ;
    NODE3BF = NodesBF(1,3) ;
    ElementBF(eBF,1) = EIDBF ;
%"Element" is the element output
    ElementBF(eBF,2) = NODE1BF ;
    ElementBF(eBF,3) = NODE2BF ;
    ElementBF(eBF,4) = NODE3BF ;
    for enodesBF = 1:smeshBF
        if NODE1BF == MeshBF(enodesBF,1)
            N1XBF = MeshBF(enodesBF,2) ;
            N1YBF = MeshBF(enodesBF,3) ;
            N1ZBF = MeshBF(enodesBF,4) ;
        end
        if NODE2BF == MeshBF(enodesBF,1)
            N2XBF = MeshBF(enodesBF,2) ;
% find intergration points in elements
            N2YBF = MeshBF(enodesBF,3) ;
            N2ZBF = MeshBF(enodesBF,4) ;
        end
        if NODE3BF == MeshBF(enodesBF,1)
            N3XBF = MeshBF(enodesBF,2) ;
            N3YBF = MeshBF(enodesBF,3) ;
            N3ZBF = MeshBF(enodesBF,4) ;
        end
    end
    NXCentreBF = mean([N1XBF,N2XBF,N3XBF]) ;
    NYCentreBF = mean([N1YBF,N2YBF,N3YBF]) ;
    NZCentreBF = mean([N1ZBF,N2ZBF,N3ZBF]) ;
    IntegrationBF(eBF,1) = EIDBF ;
    IntegrationBF(eBF,2) = NXCentreBF ;
    IntegrationBF(eBF,3) = NYCentreBF ;
    IntegrationBF(eBF,4) = NZCentreBF ;
end

OriSizeBF = size(structS.root.DataSet.Element) ;
omeshBF = OriSizeBF(1,2) ;

```

```

for oBF = 1:omeshBF
%Outputting Orientation data (ID,vector 1,2,3, perpendicular vector
1,2,3)
    OIDBF =
str2num(structS.root.DataSet.Element{1,oBF}.Attributes.ID) ;
    OrientationBF =
str2num(structS.root.DataSet.Element{1,oBF}.Layer.Data.Text) ;
    Ori1BF = OrientationBF(1,1) ;
    Ori2BF = OrientationBF(1,2) ;
    Ori3BF = OrientationBF(1,3) ;
    fPerpBF = find_perp([Ori1BF,Ori2BF,Ori3BF]) ;
    OrientBF(oBF,1) = OIDBF ;
%Orient is the element output
    OrientBF(oBF,2) = Ori1BF ;
    OrientBF(oBF,3) = Ori2BF ;
    OrientBF(oBF,4) = Ori3BF ;
    OrientBF(oBF,5) = fPerpBF(1,1) ;
    OrientBF(oBF,6) = fPerpBF(1,2) ;
    OrientBF(oBF,7) = fPerpBF(1,3) ;
    OrientBF(oBF,8) = 3E+9 ;
%younghs modulus
    OrientBF(oBF,9) = 0.2 ;
%poisson ratio
    for inoBF = 1:emeshBF
        if OrientBF(oBF,1) == IntegrationBF(inoBF,1)
            OrientBF(oBF,10) = IntegrationBF(inoBF,2) ;
            OrientBF(oBF,11) = IntegrationBF(inoBF,3) ;
            OrientBF(oBF,12) = IntegrationBF(inoBF,4) ;
        end
    end
end
end

%Finding shear angle
OSA1 = 0 ;
OSA2 = 0 ;
OSA3 = 0 ;
OSA4 = 0 ;
OSA5 = 0 ;
OSA6 = 0 ;
OSA7 = 0 ;
OSA8 = 0 ;
OSA9 = 0 ;

for sa = 1:omesh
    OSA1 = Orient(sa,1) ; %element number
    OSA2 = Orient(sa,2) ;
    OSA3 = Orient(sa,3) ;
    OSA4 = Orient(sa,4) ;
    OSA5 = Orient(sa,5) ;
    OSA6 = Orient(sa,6) ;
    OSA7 = Orient(sa,7) ;
    OSA8 = 3E+9 ;
    OSA9 = 0.2 ;
    FibreA = [OSA2,OSA3,OSA4] ;
    PlaneA = [OSA4,OSA5,OSA6] ;
    Planernorm = cross(FibreA,PlaneA) ; %reorientating stitch vector
    PlanernormStitch = cross(FibreA,Stitch_Vector) ;
    Scew = vrrotvec(PlanernormStitch,Planernorm) ;
    Rotvec = [Scew(1,1),Scew(1,2),Scew(1,3)] ;
    Rortheta = [Scew(1,4)] ;
    BaseOri = rodrigues_rot(Stitch_Vector,Rotvec,Rortheta) ;
end
end

```

```

    Dot = dot(FibreA,BaseOri) ;
    Dotabs =
sqrt(FibreA(1,1)^2+FibreA(1,2)^2+FibreA(1,3)^2)*(sqrt(BaseOri(1,1)^2
+BaseOri(1,2)^2+BaseOri(1,3)^2)) ;
    OriDifAngle = acos(Dot/Dotabs) ;
    ShearAngle(sa,1) = OSA1 ;
    SATEST = round((((180/pi)*(OriDifAngle))-135));
    ShearAngle(sa,2) = SATEST ;
    if ShearAngle(sa,2) >= 60
        ShearAngle(sa,2) =0 ;
    end
    if ShearAngle(sa,2) <= -60
        ShearAngle(sa,2) =0 ;
    end
    ShearAngle(sa,3) = sa ;
    ShearAngle(sa,4) = OSA8 ;
    ShearAngle(sa,5) = OSA9 ;
    m1 = "          matrix(" ;
    m1s = string(m1) ;
    Substring(sa,1) = [m1s] ;
    m2 = ",1)   =" ;
    m2s = string(m2) ;
    Substring(sa,2) = [m2s] ;
    m3 = ",2)   =" ;
    m3s = string(m3) ;
    Substring(sa,3) = [m3s] ;

```

```
end
```

```
%Finding shear angle bottom face
```

```

OSA1BF = 0 ;
OSA2BF = 0 ;
OSA3BF = 0 ;
OSA4BF = 0 ;
OSA5BF = 0 ;
OSA6BF = 0 ;
OSA7BF = 0 ;
OSA8BF = 0 ;
OSA9BF = 0 ;

```

```
for saBF = 1:omeshBF
```

```

    OSA1BF = OrientBF(saBF,1) ; %element number
    OSA2BF = OrientBF(saBF,2) ;
    OSA3BF = OrientBF(saBF,3) ;
    OSA4BF = OrientBF(saBF,4) ;
    OSA5BF = OrientBF(saBF,5) ;
    OSA6BF = OrientBF(saBF,6) ;
    OSA7BF = OrientBF(saBF,7) ;
    OSA8BF = 3E+9 ;
    OSA9BF = 0.2 ;

```

```
FibreABF = [OSA2BF,OSA3BF,OSA4BF] ;
```

```
PlaneABF = [OSA4BF,OSA5BF,OSA6BF] ;
```

```
PlanernormBF = cross(FibreABF,PlaneABF) ; %reorientating stitch
```

```
vector
```

```
PlanernormStitchBF = cross(FibreABF,Stitch_Vector2) ;
```

```
ScewBF = vrrotvec(PlanernormStitchBF,PlanernormBF) ;
```

```
RotvecBF = [ScewBF(1,1),ScewBF(1,2),ScewBF(1,3)] ;
```

```
RorthetaBF = [ScewBF(1,4)] ;
```

```
BaseOriBF = rodrigues_rot(Stitch_Vector2,RotvecBF,RorthetaBF) ;
```

```
DotBF = dot(FibreABF,BaseOriBF) ;
```

```

    DotabsBF =
sqrt(FibreABF(1,1)^2+FibreABF(1,2)^2+FibreABF(1,3)^2)*(sqrt(BaseOriB
F(1,1)^2+BaseOriBF(1,2)^2+BaseOriBF(1,3)^2)) ;
    OriDifAngleBF = acos(DotBF/DotabsBF) ;
    ShearAngleBF(saBF,1) = OSA1BF ;
    SATESTBF = round(-(((180/pi)*(OriDifAngleBF)))-45)) ;
    ShearAngleBF(saBF,2) = SATESTBF ;
    if ShearAngleBF(saBF,2) >= 60
        ShearAngleBF(saBF,2) =0 ;
    end
    if ShearAngleBF(saBF,2) <= -60
        ShearAngleBF(saBF,2) =0 ;
    end
    ShearAngleBF(saBF,3) = saBF ;
    ShearAngleBF(saBF,4) = OSA8BF ;
    ShearAngleBF(saBF,5) = OSA9BF ;
    m1 = "          matrix(" ;
    m1s = string(m1) ;
    SubstringBF(saBF,1) = [m1s] ;
    m2 = ",1)    =" ;
    m2s = string(m2) ;
    SubstringBF(saBF,2) = [m2s] ;
    m3 = ",2)    =" ;
    m3s = string(m3) ;
    SubstringBF(saBF,3) = [m3s] ;

end

%
%
%Linking elements
for TF = 1:omesh
    Top_Face(TF,1) = ShearAngle(TF,1) ;
    Top_Face(TF,2) = Orient(TF,10) ;
    Top_Face(TF,3) = Orient(TF,11) ;
    Top_Face(TF,4) = Orient(TF,12) ;
    Top_Face(TF,5) = ShearAngle(TF,2) ;
    TFNODE(TF,1) = Orient(TF,10) ;
    TFNODE(TF,2) = Orient(TF,11) ;
    TFNODE(TF,3) = Orient(TF,12) ;
end

for BF = 1:omeshBF
    Bottom_Face(BF,1) = ShearAngleBF(BF,1) ;
    Bottom_Face(BF,2) = OrientBF(BF,10) ;
    Bottom_Face(BF,3) = OrientBF(BF,11) ;
    Bottom_Face(BF,4) = OrientBF(BF,12) ;
    Bottom_Face(BF,5) = ShearAngleBF(BF,2) ;
    BFNODE(BF,1) = OrientBF(BF,10) ;
    BFNODE(BF,2) = OrientBF(BF,11) ;
    BFNODE(BF,3) = OrientBF(BF,12) ;
end

for link = 1:omesh
    neigh = TFNODE(link,:) ;
    [LNum,dist] = dsearchn(neigh,BFNODE) ;
    [MinVal,MinIndex] = min(dist);
    LinkMesh(link,1) = Top_Face(link,1) ;
end

```

```

LinkMesh(link,2) = Top_Face(link,2) ;
LinkMesh(link,3) = Top_Face(link,3) ;
LinkMesh(link,4) = Top_Face(link,4) ;
LinkMesh(link,5) = Top_Face(link,5) ;
LinkMesh(link,6) = Bottom_Face(MinIndex,5) ;
Combined_Shear_Angle(link,1) = LinkMesh(link,1) ;
Combined_Shear_Angle(link,2) = LinkMesh(link,5)+LinkMesh(link,6)
;
end

%
%
%
%Writing Abaqus Input file for comparison analysis
%
%

fileID = fopen('A2A.inp','w');
fprintf(fileID, '%s\r\n', "**Heading");
fprintf(fileID, '%s\r\n', "*** Job name: Job-1 Model name: A2A");
fprintf(fileID, '%s\r\n', "File generated by Apodius 2 Abaqus
v1.1.1");
fprintf(fileID, '%s\r\n', "**Preprint, echo=NO, model=NO, history=NO,
contact=NO");
fprintf(fileID, '%s\r\n', "**Node");
fprintf(fileID, '%4d,%4d,%4d,%4d\r\n',
[Mesh(:,1),Mesh(:,2),Mesh(:,3),Mesh(:,4)].');
fprintf(fileID, '%s\r\n', "**Element, Type=S3R");
fprintf(fileID, '%4d,%4d,%4d,%4d\r\n',
[Element(:,1),Element(:,2),Element(:,3),Element(:,4)].');
fprintf(fileID, '%s\r\n', "*****");
fprintf(fileID, '%s\r\n', "*** ORIENTATIONS ***");
fprintf(fileID, '%s\r\n', "*****");
fprintf(fileID, '%s\r\n', "*** Orientation vectors");
fprintf(fileID, '%s\r\n', "*** 1st vector represents the fibre
direction");
fprintf(fileID, '%s\r\n', "*** 2nd vector is an arbitrary vector
perpendicular to the first");
fprintf(fileID, '%s\r\n', "**Distribution Table,
Name=A2AOrientationVectors");
fprintf(fileID, '%s\r\n', "COORD3D,COORD3D");
fprintf(fileID, '%s\r\n', "**Distribution, Location=Element,
Table=A2AOrientationVectors, Name=A2AOrientationVectors,
Input=A2AOrientationVectors.ori");
fprintf(fileID, '%s\r\n', "**Orientation, Name=A2AOrientations,
Definition=coordinates");
fprintf(fileID, '%s\r\n', "A2AOrientationVectors");
fprintf(fileID, '%s\r\n', "1, 0");
fprintf(fileID, '%s\r\n', "**Orientation, name=Ori-PART-
1_A2AORIENTATIONVECTORS, system=RECTANGULAR");
fprintf(fileID, '%s\r\n', "PART-1_A2AORIENTATIONVECTORS");
fprintf(fileID, '%s\r\n', "3, 0.");
fprintf(fileID, '%s\r\n', "*** Section: Section-1-ALLELEMENTS");

```

```

fprintf(fileID, '%s\r\n', "**Shell Section, elset=ALLELEMENTS,
material=MAT1, orientation=Ori-PART-1_A2AORIENTATIONVECTORS");
fprintf(fileID, '%s\r\n', "1., 5");
fprintf(fileID, '%s\r\n', "*****");
fprintf(fileID, '%s\r\n', "*** ELEMENT SETS ***");
fprintf(fileID, '%s\r\n', "*****");
fprintf(fileID, '%s\r\n', "*** A2A generates a number of element
sets:");
fprintf(fileID, '%s\r\n', "*** All - Contains all elements");
fprintf(fileID, '%s\r\n', "**ElSet, ElSet=AllElements, Generate");
fprintf(fileID, '%4s,%4d,%4s\r\n', "1", emesh.', "1");
fprintf(fileID, '%s\r\n', "*****");
fprintf(fileID, '%s\r\n', "*** NODE SETS ***");
fprintf(fileID, '%s\r\n', "*****");
fprintf(fileID, '%s\r\n', "*** A2A generates a number of node sets:");
fprintf(fileID, '%s\r\n', "*** AllNodes - Node set containing all
elements");
fprintf(fileID, '%s\r\n', "**NSet, NSet=AllNodes, Generate");
fprintf(fileID, '%4s,%4d,%4s\r\n', "1", smesh.', "1");
fprintf(fileID, '%s\r\n', "**Nset, nset=Set-2, Generate");
fprintf(fileID, '%4s,%4d,%4s\r\n', "1", smesh.', "1");
fprintf(fileID, '%s\r\n', "*****");
fprintf(fileID, '%s\r\n', "*** MATERIALS ***");
fprintf(fileID, '%s\r\n', "*****");
fprintf(fileID, '%s\r\n', "**Material, Name=Mat1");
fprintf(fileID, '%s\r\n', "**Depvar");
fprintf(fileID, '%s\r\n', "      2,");
fprintf(fileID, '%s\r\n', "**Elastic, dependencies = 1");
fprintf(fileID, '%4d,%4d,%4d.,%4d.\r\n', [ShearAngle(:,4), ShearAngle(:,5),
Combined_Shear_Angle(:,2), Combined_Shear_Angle(:,1)].');
fprintf(fileID, '%s\r\n', "**Expansion");
fprintf(fileID, '%s\r\n', "6.5e-06");
fprintf(fileID, '%s\r\n', "**User Defined Field");
fprintf(fileID, '%s\r\n', "**Shell Section, ElSet=AllElements,
Material=Mat1, Thickness = 0.5, Orientation=A2AOrientations");
fprintf(fileID, '%s\r\n', "1.0,");
fprintf(fileID, '%s\r\n', "***");
fprintf(fileID, '%s\r\n', "***BOUNDARY CONDITIONS");
fprintf(fileID, '%s\r\n', "***");
fprintf(fileID, '%s\r\n', "*** Name: BC-1 Type:
Symmetry/Antisymmetry/Encastre");
fprintf(fileID, '%s\r\n', "**Boundary");
fprintf(fileID, '%s\r\n', "Set-2, ENCASTRE");
fprintf(fileID, '%s\r\n', "*** -----
-----");
fprintf(fileID, '%s\r\n', "***");
fprintf(fileID, '%s\r\n', "***STEP: Step-1");
fprintf(fileID, '%s\r\n', "***");
fprintf(fileID, '%s\r\n', "**Step, name=Step-1, nlgeom=NO");
fprintf(fileID, '%s\r\n', "**Static");
fprintf(fileID, '%s\r\n', "1., 1., 1e-05, 1.");
fprintf(fileID, '%s\r\n', "***");
fprintf(fileID, '%s\r\n', "***OUTPUT REQUESTS");
fprintf(fileID, '%s\r\n', "***");
fprintf(fileID, '%s\r\n', "**Restart, write, frequency=0");
fprintf(fileID, '%s\r\n', "***");
fprintf(fileID, '%s\r\n', "***FIELD OUTPUT: F-Output-1");
fprintf(fileID, '%s\r\n', "***");
fprintf(fileID, '%s\r\n', "**Output, field");
fprintf(fileID, '%s\r\n', "**Node Output");
fprintf(fileID, '%s\r\n', "CF, RF, U");

```



```

fprintf(fileID, '%s\r\n', "**Element Output, directions=YES");
fprintf(fileID, '%s\r\n', "FV, LE, PE, PEEQ, PEMAG, S, SDV, TEMP");
fprintf(fileID, '%s\r\n', "**Contact Output");
fprintf(fileID, '%s\r\n', "CDISP, CSTRESS");
fprintf(fileID, '%s\r\n', "***");
fprintf(fileID, '%s\r\n', "***HISTORY OUTPUT: H-Output-1");
fprintf(fileID, '%s\r\n', "***");
fprintf(fileID, '%s\r\n', "**Output, history, variable=PRESELECT");
fprintf(fileID, '%s\r\n', "**End Step");
fclose(fileID);

```

```

%
%Writing .ori file for lookup table of orientations
%

```

```

fileID = fopen('A2AOrientationVectors.ori', 'w');
fprintf(fileID, '%s\r\n', "*****");
fprintf(fileID, '%s\r\n', "**** ORIENTATIONS ****");
fprintf(fileID, '%s\r\n', "*****");
fprintf(fileID, '%s\r\n', "** Orientation vectors");
fprintf(fileID, '%s\r\n', "** 1st vector represents the fibre
direction");
fprintf(fileID, '%s\r\n', "** 2nd vector is an arbitrary vector
perpendicular to the first");
fprintf(fileID, '%s\r\n', ", 1.0, 0.0, 0.0, 0.0, 1.0, 0.0");
fprintf(fileID, '%4d,%4d,%4d,%4d,%4d,%4d,%4d\r\n',
[Orient(:,1),Orient(:,2),Orient(:,3),Orient(:,4),Orient(:,5),Orient(
(:,6),Orient(:,7)].');
fclose(fileID);

```

```

%
%Writing .f Subroutine for USDFLD
%

```

```

fileID = fopen('A2AFieldVariables.f', 'w');
fprintf(fileID, '%s\r\n', '!DEC$ ATTRIBUTES ALIAS:"usfld":USDFLD');
fprintf(fileID, '%s\r\n', "      SUBROUTINE
USDFLD (FIELD, STATEV, PNEWDT, DIRECT, T, CELENT, ");
fprintf(fileID, '%s\r\n', "          1
TIME, DTIME, CMNAME, ORNAME, NFIELD, NSTATV, NOEL, NPT, LAYER, ");
fprintf(fileID, '%s\r\n', "          2
KSPT, KSTEP, KINC, NDI, NSHR, COORD, JMAC, JMATYP, MATLAYO, LACCFLA ");
fprintf(fileID, '%s\r\n', "C");
fprintf(fileID, '%s\r\n', "          INCLUDE 'ABA_PARAM.INC');
fprintf(fileID, '%s\r\n', "C");
fprintf(fileID, '%s\r\n', "          CHARACTER*80 CMNAME,ORNAME");
fprintf(fileID, '%s\r\n', "          CHARACTER*3  FLGRAY(15)");
fprintf(fileID, '%s\r\n', "          DIMENSION
FIELD(NFIELD), STATEV(NSTATV), DIRECT(3,3), ");
fprintf(fileID, '%s\r\n', "          1 T(3,3), TIME(2)");
fprintf(fileID, '%s\r\n', "          DIMENSION
ARRAY(15), JARRAY(15), JMAC(*), JMATYP(*), COORD(*), ");
fprintf(fileID, '%4s %4d,%4s\r\n', "          1 matrix(", omesh.', "2)");
fprintf(fileID, '%s\r\n', '!DEC$ ATTRIBUTES
ALIAS:"getpartinfo":GETPARTINFO');
fprintf(fileID, '%s\r\n', "          FIELD(1) = NOEL");

```

```

fprintf(fileID, '%s\r\n', "          STATEV(1) = FIELD(1)");
fprintf(fileID, '%4s %4s %4s
%4s\r\n', [Substring(:,1), ShearAngle(:,3), Substring(:,2), Combined_She
ar_Angle(:,1)].');
fprintf(fileID, '%4s %4s %4s
%4s\r\n', [Substring(:,1), ShearAngle(:,3), Substring(:,3), Combined_She
ar_Angle(:,2)].');
fprintf(fileID, '%4s,%4d\r\n', "          DO i =1", omesh. ');
fprintf(fileID, '%s\r\n', "          IF (matrix(i,1) == FIELD(1))
then");
fprintf(fileID, '%s\r\n', "          STATEV(2) = matrix(i,2)");
fprintf(fileID, '%s\r\n', "          endif");
fprintf(fileID, '%s\r\n', "          enddo");
fprintf(fileID, '%s\r\n', "          RETURN");
fprintf(fileID, '%s\r\n', "          END SUBROUTINE");
fclose(fileID);

```

10 Appendix C

10.1 In-plane testing

10.1.1 Picture frame shear testing

The picture frame test is an in-plane shear testing methodology that fully constrains yarns between 4 pin-jointed arms with yarns at 45 degrees to the extension direction. Extension causes the arms to rotate, applying shear to the entire sample. When testing NCFs a set of assumptions must be met:

- Fibres rotate freely at the clamped boundary.
- Yarn crossover points provide zero slippage and allow rotation only.
- Fibres are inextensible.

The picture frame is susceptible to inconsistencies when testing woven fabrics with variable yarn tension across the sample. This is a lower concern for NCFs as the tensions in the yarn does not directly impact the frictional conditions at the yarn crossover point (in the same way that it affects the properties of a crimped fabric). The picture frame can therefore produce very repeatable data for NCFs as long as the assumptions above are met.

10.1.1.1 Picture frame sample preparation

Samples for the picture frame test are stamped using a standardised cutting form to improve shape consistency and fibre alignment. Each sample is a cruciform shape with a central 110mm x 110mm square region surrounded by 4 “arms” of 110mm by 40mm of which 20mm of each arm is clamped by the frame. The fibres are aligned at 45 degrees to the direction of extension so each biaxial layer has each end of its fibres clamped. For positively sheared samples the stitches were aligned in the direction of extension and for negatively shearing samples the stitches were aligned perpendicular to the displacement direction. A 1kN load cell was used and testing was conducted at 10mm/min to a final extension of 70mm. Force/displacement data was collected and converted into shear angle and shear force:

$$F_S = \frac{F_p}{2 * w * \cos \frac{\alpha}{2}} \quad \text{Equation 8}$$

$$\gamma = \frac{\pi}{2} - \alpha \quad \text{Equation 9}$$

The shear force was normalized so that comparisons could be drawn between picture frame and bias extension test results.

10.1.2 Bias extension shear testing

The bias extension test is an in-plane shear testing methodology that uses rectangular samples with fibres aligned at 45 degrees to the extension direction. When the sample is extended and a zone of pure shear (Zone C) is created in the centre of the sample, with two other zones (A and B) surrounding it. Region A appears at the clamped edge and is an area of zero deformation. Region B is a zone of material with multi-deformation modes that sits in between the pure shear region and Region A. The in-plane shear data outputted from the test is reliant on two relations holding true:

- The relationship between the length of Zone C and the shear angle
- The relationship between the shear moment and the load on the tensile machine.

The first of these relationships is questioned when the bias extension test is used for NCFs. This is due to the assumption that there is no slip between the warp and waft yarns (when testing a woven fabric). With FCIM739 the stitch provides sufficient links between the fibres to act as a point of rotation, meaning that the test can be considered, however zero slippage cannot be confirmed. There is also significant out of plane buckling that occurs in the central region. Further observation of the shear angle seen in zone C has been conducted in this section.

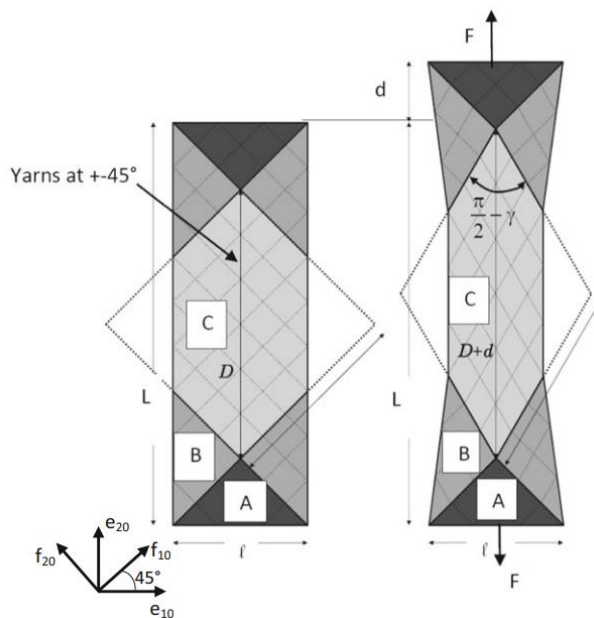
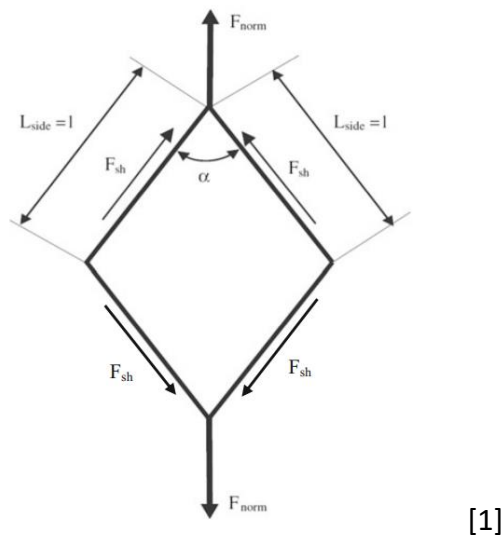


Figure 10-1 (a) bias extension pure shear regions diagram. (b) bias extension geometry diagram

10.1.2.1 Bias extension sample preparation

Samples for the bias extension test were cut to 320mm by 115mm rectangles. Each sample was made from FCIM739 and had the biaxial fibres aligned at 45 degrees. As FCIM739 is an NCF two different samples were needed for positive and negative shearing. For positively sheared samples the stitches were aligned in the direction of extension and for negatively shearing samples the stitches were aligned perpendicular to the displacement direction. Both positive and negatively shearing samples were tested in tension with the stitch direction defining the type of shear.

Each sample was clamped in a rubber padded jaw seated in an Instron tensile testing machine. 40mm of the samples was seated into each clamp to ensure zero slippage, so the final sample length was 240mm. A 1kn load cell was used and tests were conducted at 50mm/min with a final extension of 70mm. Force displacement data was collected and the shear angle in the pure shear zone was calculated using equation 10 [1]

$$\theta = \frac{\pi}{2} - 2 \cos^{-1} \left(\frac{D + d}{\sqrt{2}D} \right) \quad \text{Equation 10}$$

θ is the shear angle and D is the length of the central zone with d being the added extension to the central zone. The shear force was then calculated according to equation 11

$$F_{sh}(\theta) = \frac{F * D}{l(2D - l) \cos \theta} \left(\cos \frac{\theta}{2} - \sin \frac{\theta}{2} \right) - \frac{l \cos \frac{\theta}{2}}{(2D - l) \cos \theta} F_{sh} \left(\frac{\theta}{2} \right) \quad \text{Equation 11}$$

L and l are the original height and width of the sample respectively and F_{sh} is the shear force. $F_{sh} \left(\frac{\theta}{2} \right)$ is the shear force seen at half the current shear angle and its presence in the load calculation means that an iterative approach is needed? For this study an output range of 8000 values was used and $F_{sh} \left(\frac{\theta}{2} \right)$ was calculated from half of the previous value with an initial value for F_{sh} and $F_{sh} \left(\frac{\theta}{2} \right)$ of zero at $\theta = 0$. F_{sh} and θ are normalised for the sample size so can be directly compared between bias extension tests and to picture frame tests.

10.1.3 Tensile testing

10.1.3.1 Sample preparation

Tensile testing was used to measure the variations in tensile modulus between sheared and un-sheared fabrics. Each biaxial ply was sheared to the desired shear angle using an enlarged picture frame shear rig. Two sheared plies were stacked to create a laminate of: [0/+shear angle A, -shear angle A/0]. These were vacuum infused with Prime 20 epoxy resin. These were trimmed into tensile coupons of

250mm x 25mm with a nominal thickness of 1.5mm and epoxy resin was used to affix aluminium tabs of 50mm x 25mm to the sample ends in accordance with ASTM standard D3039/D3039M. Data was collected for shear angle values between -30 and 30 degrees, as larger positive shear angle values creates localised inconsistencies where stitch breakage can cause misalignment. This misalignment is not repeatable between tensile coupons. Testing was conducted on an Instron tensile testing machine at a standard rate of 2mm/minute. Force was measured using the crosshead force on the testing rig and strain was measured using video gauge strain measurements of the sample.

10.1.3.2 Single ply measurement

The contribution of the 0 degree fibre plies were separated from the rest of the laminate so the effect of fabric shearing on the tensile modulus of the ply could be measured. This was to remove the expected change in laminate modulus due to different values for shear angle A . A representative unit laminate was calculated with each ply treated as a separate UD layer and with the desired ply orientations. The orientation of plies 2 and 3 were rotated from -60 degrees to 60 degrees and the tensile modulus of the cell measured. This is captured in Figure 10-2 as the percentage change in tensile modulus as shear angle changes. This curve was removed from all data collected from the tensile testing. Data collection for a single sheared NCF biaxial ply that is separated from its partner ply is impossible without significant damage to the structure of the fabric.

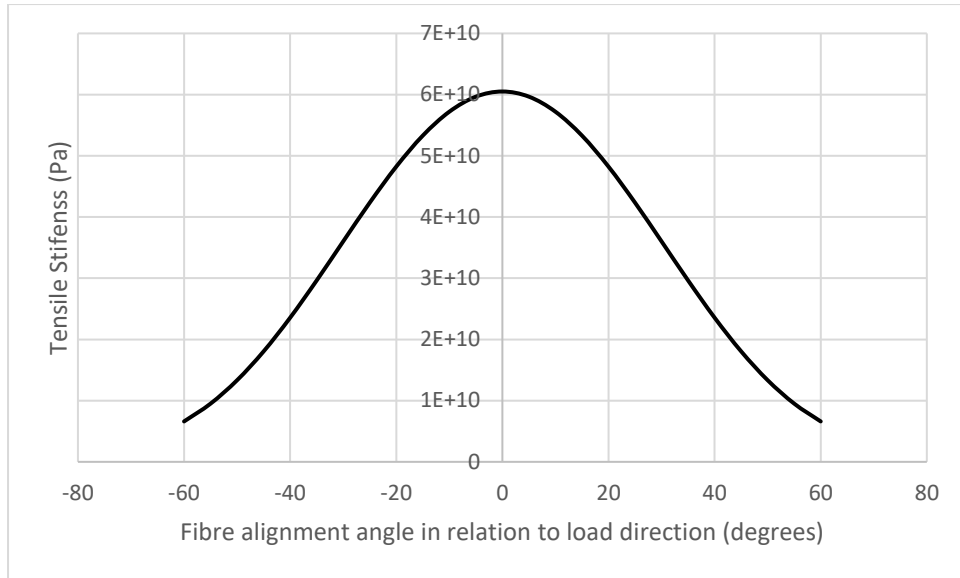


Figure 10-2 Change in tensile modulus of a fabric as fibre alignment changes in relation to the loading direction

11 Appendix D

11.1 Mutli-cycle picture frame testing

The multi-cyclic picture frame method described in previous chapters cycles a fabric to a set shear angle value before returning to 0 displacement and re extending to full extension. This only captures any hysteresis effects between the first and second cycle, so an extended study was conducted to observe any changes in the shear modulus over 5 cycles.

Aims:

- To observe the change in shear modulus of an NCF during multi cyclic in-plane shear testing of 2-5 cycles.
- To determine if the any hysteresis effects generated past cycle 2 are significant enough to be included in material modelling.

11.1.1 Extended multi-cyclic methodology

The Multi cyclic in-plane shear testing methodology was taken and extended. The extension used the same set values of A and B , however the test was repeatedly sheared to value A and back to zero displacement. The force and crosshead displacement were output, to calculate the shear angle and the shear force. The pre-extension feature of the Instron was used to implement the multiple cycles. This feature allows for a maximum and minimum displacement value to be set alongside a number of cycles. The pre extension is carried out before the actual test and all the data is collected together.

11.1.2 Results

FCIM 789 was used during this study as that is the material that was chosen for multi-cyclic modelling. The shear force and shear angle data has been plotted alongside the same data for the 2 cycle process used to generate data for the material model. The values for initial shear were set at 10, 20 and 30 degrees to match those from the

multi-cyclic material model. 4 sets of data were collected for each level of initial shear and the average was plotted.

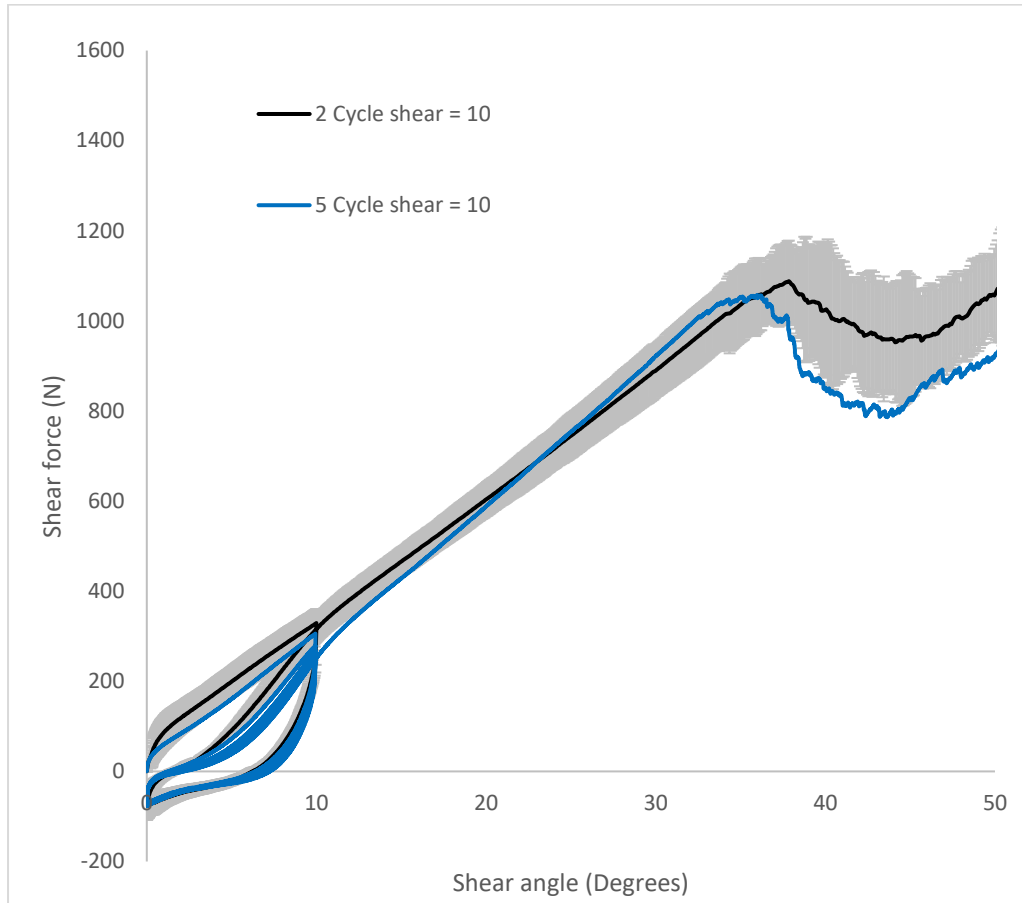


Figure 11-1 2 cycle and 5 cycle picture frame test. Initial shear angle set to 10 degrees

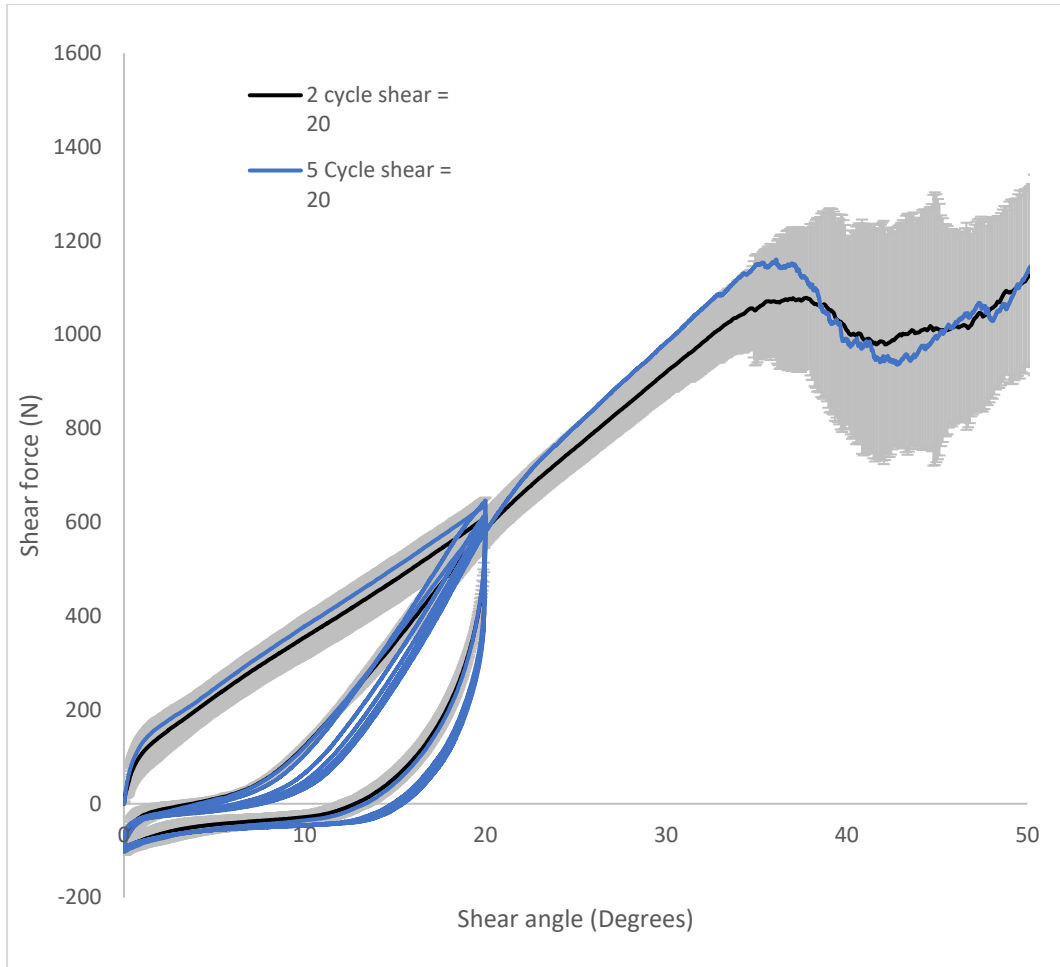


Figure 11-2 2 cycle and 5 cycle picture frame test. Initial shear angle set to 20 degrees

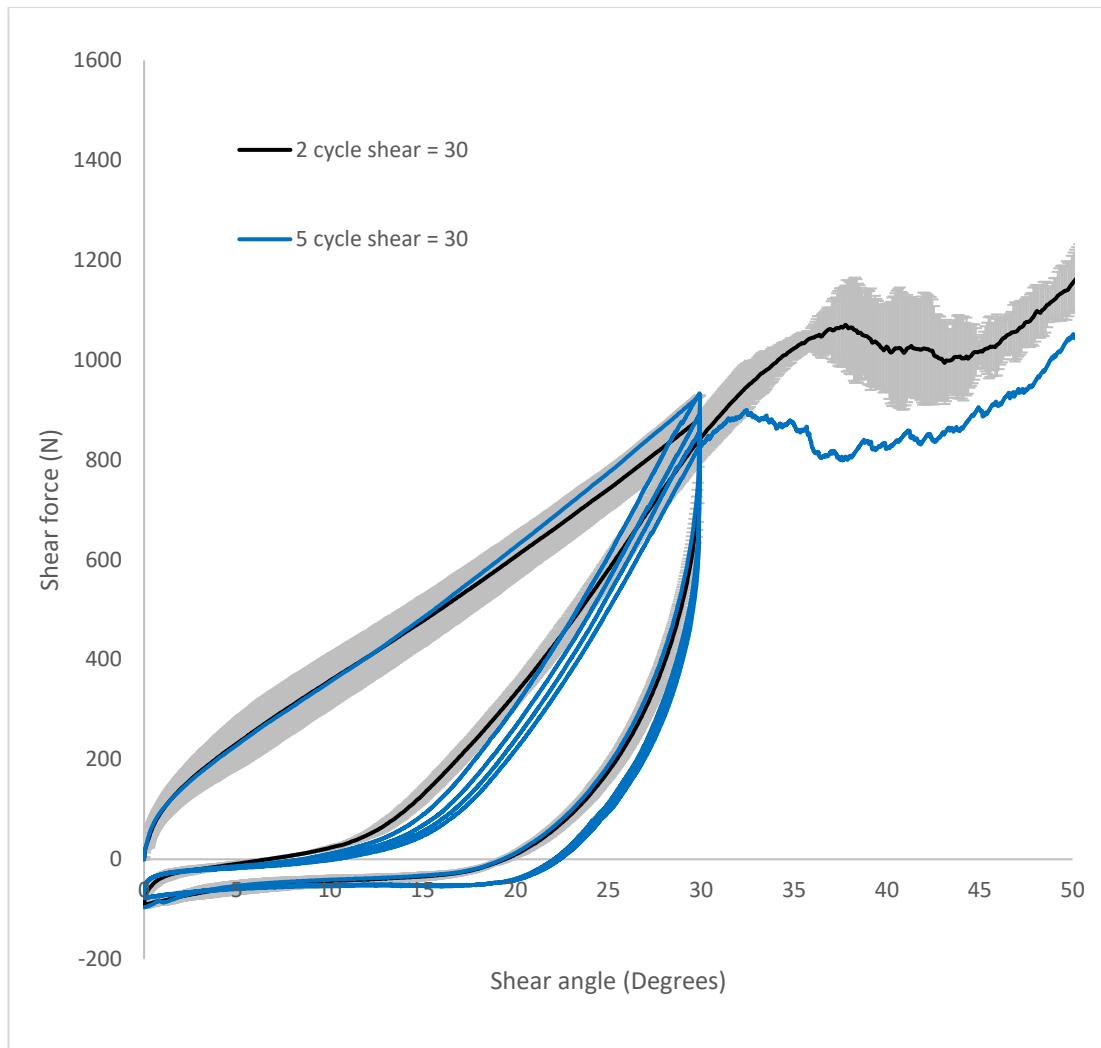


Figure 11-3 2 cycle and 5 cycle picture frame test. Initial shear angle set to 10 degrees

11.1.3 Discussion

Comparing results between 2 cycle and 5 cycle picture frame tests shows some generalised trends. The initial shear curve between 0 and value A is similar between both tests, with the values for the 5 cycle test falling within the error region of the 2 cycle test. The remaining data has been split into 2 section, 5 the unloading curves and the 5 re-loading curves. All values of the unloading curves remain within a 0.92 R^2 value of the 2nd cycle unloading curve, and do not exceed a difference of 3 degrees. The re-loading curve shows similar results with an R^2 value of 0.91 and a peak

difference of 4.3 degrees. Beyond the cycled region the shear angle shear force function is identical (within error) between the 2 and 5 cycle tests at values of A that are significantly below the stitch breakage point. At values close to the stitch breakage point, a phenomenon occurs where premature stitch breakage occurs during the cyclic process. This can be seen in Figure 11-3 where the shear force after cycling is consistently 150N lower than for the 2 cycle test and has a significantly lower negative modulus. Premature stitch breakage began to occur during re-loading after the 3rd cycle and continued through the 4th and 5th cycle.

11.1.4 Conclusion

The change in shear force/ shear angle curve for FCIM789 between the 2nd and 5th cycle is very small, having an average R^2 value between the two curves of 0.93. The shear modulus between the 2nd and 5th cycle can thus be concluded to be the same and the same function can be used to model the shear modulus, for all cycles following the 2nd. This assumption can't be used when there are multiple shear cycles that come close to the stitch breakage point, as premature stitch breakage occurs.

12 Appendix E

12.1 Fabric stabilisation and spring back

During the melting of the binder, the fabric will experience spring-back, which must be accounted for during the initial pre-shearing stage. The low shear stiffness of the fabric means that internal stresses caused during the shearing process are significant enough to partially return the fibres back towards the initial orthogonal orientation state when the shear force from the frame is removed (spring back). A method has been devised to stabilise the sheared fabric to facilitate single-ply double diaphragm forming.

The objective was to measure the spring back percentage seen when the binder stabilisation is removed through heating on a single ply in a pair of diaphragms.

12.1.1 Methodology

A picture frame shear test was setup with the same frame as Appendix (C). Samples were cut to fit the frame and then dusted with binder at 20g/sqm before being placed in the Instron 5581 testing machine. The applied shear angle was calculated using the method from Appendix (C) Equation 6-1. The mean full-field shear angle was computed via the optical scanning methodology, before the sample was heated to 75°C. This heating was done using a heat lamp facing the binder coated side of the sample to replicate the heating method seen in forming processes such as diaphragm forming. The temperature of the sample was measured in 5 locations, 3 on the front face and 2 on the back face. The heating was removed when all points reached 75-105°C which is the temperature range to set the binder into its first stage (where it can be re-melted). The sample was then left in the frame until all test points reached 30°C before being removed. The sample was then placed between a pair of Stretchlon diaphragms and reheated to 75-105 °C using the same method as above, before being left to cool. The samples were removed from the diaphragms and scanned using the optical scanning methodology. The change in fibre angle from the applied shear angle was measured to indicate the spring back of the material whilst being constrained within the diaphragms.

12.1.2 Fabric Spring Back Results

Fabric spring back has been recorded as a percentage of the intended pre-shear angle. The mean scanned fibre angle was compared to the applied shear angle and the results have been plotted in Figure 12-1 Spring back percentage seen when using a single ply double diaphragm methodology to stabilize pre-sheared fabrics once the binder stabilisation is removed through heating. This method measured a worst case scenario where the only constraint on the fabric was from highly deformable diaphragms. In all industrial diaphragm forming scenarios, more than one ply is used which will provide additional constraints due to inter-ply friction, however all forming in this study was conducted using a single ply. Figure 12-1 Spring back percentage seen when using a single ply double diaphragm methodology to stabilize pre-sheared fabrics once the binder stabilisation is removed through heating. and is divided into stitch tension (positive shear) and stitch compression (negative shear) regions. There is a linear trend between the spring back percentage and the initial shear angle applied to the sample in the negative shear direction and a polynomial response in the positive direction.

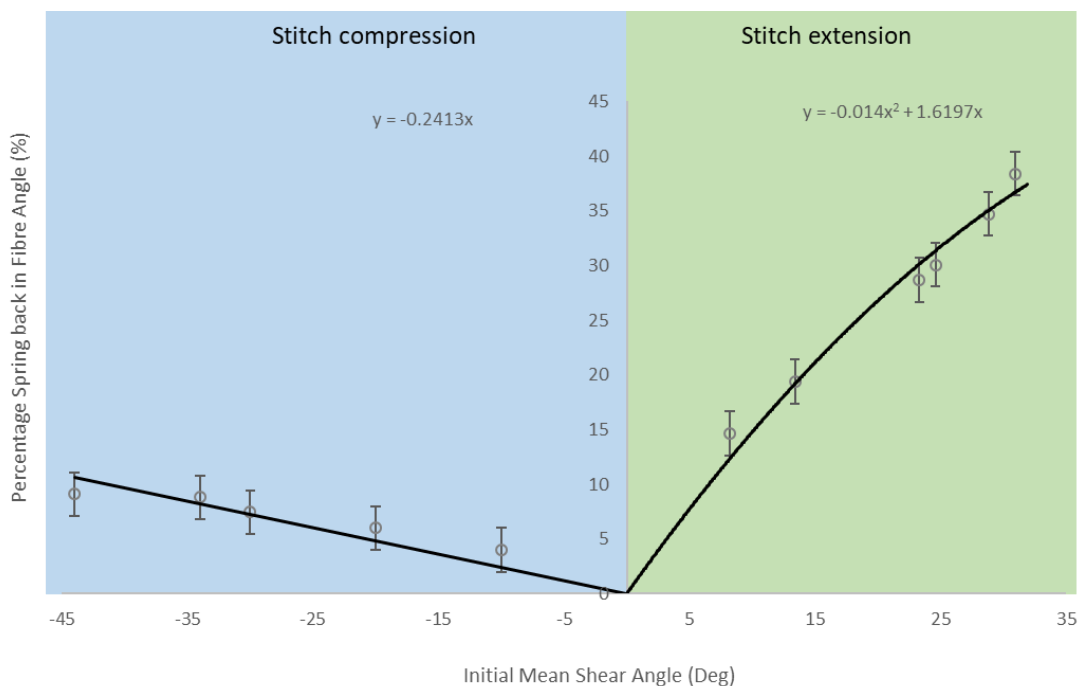


Figure 12-1 Spring back percentage seen when using a single ply double diaphragm methodology to stabilize pre-sheared fabrics once the binder stabilisation is removed through heating.

The level of spring back in the negative region is generally low and follows a linear trend, which remains below 12% up to 45° of applied shear angle. This spring back must be taken into account to ensure accurate fibre alignment in the final part. The fabric must therefore be over-sheared to compensate for this spring back when applying the initial shear.

The level of spring back in the positive direction is higher than the negative region for the same level of pre-shear. The spring back at 15° of applied shear is 3.1°, which is 15% higher than the spring back experienced at -15°. The fabric stitch breakage point is 42° and as such the maximum positive pre-shear that can be applied to a single ply via this method (once spring back is accounted for) is 20°. The increased spring back is due to the higher shear stiffness of the material in the positive direction, which is stitch dependent as shown by the literature [14]. The high shear stiffness is caused by the stitch going into tension shown in the results of the previous chapters. The stitch was shown to have a plastic nature where it returns to a similar but not initial state as the bundles contract when the tension is removed. This contraction has been shown in the previous chapters to generate a force that opposes the shear direction. (This contraction force during cyclic shear testing causes the shear force to dip into negative shear direction at 0 degrees after a cycle).

12.1.3 Conclusion

The results show a preference yarns shearing in the negative direction. During this studies the spring back can be managed with an increase in the initial pre-shearing angle, before forming. For practical applications there will be a higher constraint to the fabrics being formed, either from other plies or a matched tool. This will significantly reduce the spring back due to the increased frictional interaction between plies compared to between the ply and the diaphragm [37]. With this in mind, spring back is not seen as a major drawback for fabric pre-shearing studies.

13 Appendix F

Formed to mechanical mesh element mapping algorithm

```
% Searching pair elements

clear
clc
% -----
% -----
load 'Formed45Neg45_List.txt'
load 'Mechanical_Shape_2.txt'
Local1 = -45 ;
Local2 = 45 ;
struct_MP = Mechanical_Shape_2 ;
form_MP = Formed45Neg45_List ;

% (1) <struct_MP> -- integration points in structural mesh
% matrix with 4 columns:
% format: [ element_No, x-coord, y-coord, z-coord ]

% (2) <form_MP> -- integration points in forming mesh
% matrix with 14 columns:
% format: [ element_No,
% x-coord, y-coord, z-coord,
% f1_vect_x_comp, f1_vect_y_comp, f1_vect_z_comp,
% f2_vect_x_comp, f2_vect_y_comp, f2_vect_z_comp,
% f3_vect_x_comp, f3_vect_y_comp, f3_vect_z_comp,
% shear_angle_in_deg ]
% -----
% -----

% Total number of material points
N_struct_MP = length(struct_MP);
N_form_MP = length(form_MP);

% -----
% -----
% Initiate the element pair matrix
% -----
% -----
% <ele_pair> -- maxtrix with 2 columns saving element number for the
pair
% format: [ struct_ele_no, form_ele_no, pair_ele_dist
]
ele_pair = zeros(N_struct_MP,3);
% -----
% -----
% <struct_local_coord> -- matrix with 7 columns
% format:[ element_No,
% gn1_vect_x_comp, gn1_vect_y_comp,
gn1_vect_z_comp,
% gn2_vect_x_comp, gn2_vect_y_comp,
gn2_vect_z_comp]
struct_local_coord = zeros(N_struct_MP,7);
% -----
% -----
% <struct_local_ang> -- maxtrix with 2 columns
```

```

%                               format: [ struct_ele_no,
half_local_shear_angle ]
struct_local_ang = zeros(N_struct_MP,2);
% -----
-----

for n_struct_MP = 1:N_struct_MP
% -----
-----
% Calculate square distance between two points
SDist = (struct_MP(n_struct_MP,2)-form_MP(:,2)).^2 + ...
        (struct_MP(n_struct_MP,3)-form_MP(:,3)).^2 + ...
        (struct_MP(n_struct_MP,4)-form_MP(:,4)).^2;
[min_SDist,n_pair] = min(SDist);
% -----
-----
% Search and save element pairs
ele_pair(n_struct_MP,1) = struct_MP(n_struct_MP,1);
ele_pair(n_struct_MP,2) = form_MP(n_pair,1);
ele_pair(n_struct_MP,3) = sqrt(min_SDist);
% -----
-----
% Material card -- Distributed local coordinate system
struct_local_coord(n_struct_MP,1) = struct_MP(n_struct_MP,1);
struct_local_coord(n_struct_MP,2:7) = form_MP(n_pair,5:10);
vec2VertFibres(n_struct_MP,1) =
abs(atan(struct_local_coord(n_struct_MP,3)/struct_local_coord(n_struct_MP,2))) ;
vec1HoriFibres(n_struct_MP,1) =
abs(atan(struct_local_coord(n_struct_MP,6)/struct_local_coord(n_struct_MP,5)))- (pi/2) ;
% -----
-----
% Material card -- Distributed local 1st fibre angle w.r.t the
local
%                               coordinate system (half of the shear angle)
struct_local_ang(n_struct_MP,1) = struct_MP(n_struct_MP,1);
struct_local_ang(n_struct_MP,2) = form_MP(n_pair,14)/2;
% -----
-----
end
absAngle = (vec1HoriFibres - vec2VertFibres) * (180/pi) ;
Angle = struct_local_ang * 2 ;
NODEXYZSHEAR =
[struct_MP(:,1),struct_MP(:,2),struct_MP(:,3),struct_MP(:,4),Angle(:,2)] ;

% -----
-----
%vf and quality
nmax = size(NODEXYZSHEAR) ;
for n = 1:nmax(1,1)
    if NODEXYZSHEAR(n,5) > 37
        Etemp = 1.12E+7*(NODEXYZSHEAR(n,5))^2-
1.77E+9*(NODEXYZSHEAR(n,5))+1.36E+11 ;
    elseif NODEXYZSHEAR(n,5) <= 37 && NODEXYZSHEAR(n,5) > 0
        Etemp = 1.22E+7*(NODEXYZSHEAR(n,5))^2-
1.03E+8*(NODEXYZSHEAR(n,5))+7.45E+10 ;
    elseif NODEXYZSHEAR(n,5) <= 0

```

```

        Etemp =
3.55E+3*(NODEXYZSHEAR(n,5))^4+1.97E+5*(NODEXYZSHEAR(n,5))^3+1.42E+7*
(NODEXYZSHEAR(n,5)^2)+2.17E+8*(NODEXYZSHEAR(n,5))+7.45E+10 ;
    end
    E11(n,:) = Etemp ;
    E22(n,:) = 3.5E9 ;
    G12(n,:) = 5.2E9 ;
    G23(n,:) = 1.26E9 ;
    Nu12(n,:) = 0.28 ;
    Nu23(n,:) = 0.4 ;
    Field(n,:) = n ;
    LD1(n,:) = vec1HoriFibres(n,:) * (180/pi) + Local1 ;
    LD2(n,:) = vec2VertFibres(n,:) * (180/pi) + Local2;
end
format short
Elastic = [ E11,E22,E22,Nu12,Nu12,Nu23,G12,G12,G23,Field] ;
format short
AA_OUTPUT_Elastic = round(Elastic,4,'significant') ;
AA_OUTPUT_LD1 = [Field,LD1] ;
AA_OUTPUT_LD2 = [Field,LD2] ;

% -----
-----
fid = fopen('mapping_pair.txt','w');
fprintf(fid,'*Spring, elset=Springs/Dashpots-mapping-pair-
set\r\n');
fprintf(fid,'\r\n');
fprintf(fid,'1.\r\n');
fprintf(fid,'*Element, type=SpringA, elset=Springs/Dashpots-
mapping-pair-set\r\n');
for np = 1:N_struct_MP
    fprintf(fid,'%d, PUNCH-1-1.%d, QUATERSHEET-1-
1.%d\r\n',np,ele_pair(np,1),ele_pair(np,2));
end
%fclose(fid);

```



```

    Mesh(k,2) = X ;
    Mesh(k,3) = Y ;
    Mesh(k,4) = Z ;
end

ElementSize =
str2num(struct.root.Mesh.Elements.Attributes.nElements) ;
emesh = ElementSize ;
for e = 1:emesh
%Outputting element data (ID(Node 1 Node 2 Node 3)
    EID =
str2num(struct.root.Mesh.Elements.Element{1,e}.Attributes.ID) ;
    Nodes =
str2num(struct.root.Mesh.Elements.Element{1,e}.NodesID.Text) ;
    NODE1 = Nodes(1,1) ;
    NODE2 = Nodes(1,2) ;
    NODE3 = Nodes(1,3) ;
    Element(e,1) = EID ;
%"Element" is the element output
    Element(e,2) = NODE1 ;
    Element(e,3) = NODE2 ;
    Element(e,4) = NODE3 ;

end

OriSize = size(struct.root.DataSet.Element) ;
omesh = OriSize(1,2) ;
for o = 1:omesh
%Outputting Orientation data (ID,vector 1,2,3, perpendicular vector
1,2,3)
    OID = str2num(struct.root.DataSet.Element{1,o}.Attributes.ID) ;
    Orientation =
str2num(struct.root.DataSet.Element{1,o}.Layer.Data.Text) ;
    Ori1 = Orientation(1,1) ;
    Ori2 = Orientation(1,2) ;
    Ori3 = Orientation(1,3) ;
    fPerp = find_perp([Ori1,Ori2,Ori3]) ;
    Orient(o,1) = OID ;
%Orient is teh elemetn output
    Orient(o,2) = Ori1 ;
    Orient(o,3) = Ori2 ;
    Orient(o,4) = Ori3 ;
    Orient(o,5) = fPerp(1,1) ;
    Orient(o,6) = fPerp(1,2) ;
    Orient(o,7) = fPerp(1,3) ;
    Orient(o,8) = 3E+9 ;
%younghs modulus
    Orient(o,9) = 0.2 ;
%poisson ratio

end

    cn1 = 0 ;
%setting values for Loops
    cn2 = 0 ;
    cn3 = 0 ;
    cori1 = 0 ;
    cori2 = 0 ;
    cori3 = 0 ;
    cplx = 0 ;

```

```

        cp1y = 0 ;
        cp1z = 0;
        cp2x = 0 ;
        cp2y = 0 ;
        cp2z = 0;
        cp3x = 0 ;
        cp3y = 0 ;
        cp3z = 0;
for c = 1:omesh
%compiling all data into elemetn ID with orentaitons and nodal
positions
    for cb = 1:emesh
        if Orient(c,1) == Element(cb,1)
%(Elelment ID,Point1 XYZ,Point2 XYZ,Point3 XYZ,Orientation vector
XYZ)
            cn1 = Element(cb,2) ;
            cn2 = Element(cb,3) ;
            cn3 = Element(cb,4) ;
            cori1 = Orient(c,2) ;
            cori2 = Orient(c,3) ;
            cori3 = Orient(c,4) ;
        end
        ELOR(c,1) = Orient(c,1) ;
        ELOR(c,2) = cn1 ;
        ELOR(c,3) = cn2 ;
        ELOR(c,4) = cn3 ;
        ELOR(c,5) = cori1 ;
        ELOR(c,6) = cori2 ;
        ELOR(c,7) = cori3 ;
    end
for cc = 1:smesh
    if Mesh(cc,1) == ELOR(c,2)
        cp1x = Mesh(cc,2) ;
        cp1y = Mesh(cc,3) ;
        cp1z = Mesh(cc,4) ;
    end
    if Mesh(cc,1) == ELOR(c,3)
        cp2x = Mesh(cc,2) ;
        cp2y = Mesh(cc,3) ;
        cp2z = Mesh(cc,4) ;
    end
    if Mesh(cc,1) == ELOR(c,4)
        cp3x = Mesh(cc,2) ;
        cp3y = Mesh(cc,3) ;
        cp3z = Mesh(cc,4) ;
    end
    All_DATA(c,1) = Orient(c,1) ;
%All Data is output
    All_DATA(c,2) = cp1x ;
    All_DATA(c,3) = cp1y ;
    All_DATA(c,4) = cp1z ;
    All_DATA(c,5) = cp2x ;
    All_DATA(c,6) = cp2y ;
    All_DATA(c,7) = cp2z ;
    All_DATA(c,8) = cp3x ;
    All_DATA(c,9) = cp3y ;
    All_DATA(c,10) = cp3z ;
    All_DATA(c,11) = ELOR(c,5) ;
    All_DATA(c,12) = ELOR(c,6) ;
    All_DATA(c,13) = ELOR(c,7) ;
end

```

```

end

%
%
%

%Finding shear angle
OSA1 = 0 ;
OSA2 = 0 ;
OSA3 = 0 ;
OSA4 = 0 ;
OSA5 = 0 ;
OSA6 = 0 ;
OSA7 = 0 ;
OSA8 = 0 ;
OSA9 = 0 ;

for sa = 1:omesh
    OSA1 = Orient(sa,1) ; %element number
    OSA2 = Orient(sa,2) ;
    OSA3 = Orient(sa,3) ;
    OSA4 = Orient(sa,4) ;
    OSA8 = 3E+9 ;
    OSA9 = 0.2 ;

    FibreA = [OSA2,OSA3,OSA4] ; %fibre angle
    Dot = dot(FibreA,BaseOri) ;
    Dotabs =
sqrt(FibreA(1,1)^2+FibreA(1,2)^2+FibreA(1,3)^2)*(sqrt(BaseOri(1,1)^2
+BaseOri(1,2)^2+BaseOri(1,3)^2)) ; %vector calculation
    OriDifAngle = acos(Dot/Dotabs) ;
    ShearAngle(sa,1) = OSA1 ;
    SATEST = round(-((180/pi)*(((OriDifAngle)-(pi/4))+(0))*2));
%shear angle calculation
    ShearAngle(sa,2) = SATEST ;
    ShearAngle(sa,3) = sa ;
    ShearAngle(sa,4) = OSA8 ;
    ShearAngle(sa,5) = OSA9 ;
    m1 = " matrix(" ;
    m1s = string(m1) ;
    Substring(sa,1) = [m1s] ;
    m2 = ",1) =" ;
    m2s = string(m2) ;
    Substring(sa,2) = [m2s] ;
    m3 = ",2) =" ;
    m3s = string(m3) ;
    Substring(sa,3) = [m3s] ;

end
Superstring =
[Substring(:,1),ShearAngle(:,3),Substring(:,2),ShearAngle(:,2),Subst
ring(:,3)] ;

```

```

%
%
%
%Writing Abaqus Input file for comparison analysis
%
%
%

```

```

fileID = fopen('A2A.inp','w');
fprintf(fileID,'%s\r\n',"*Heading");
fprintf(fileID,'%s\r\n',"** Job name: Job-1 Model name: A2A");
fprintf(fileID,'%s\r\n',"File generated by Apodius 2 Abaqus
v1.1.1");
fprintf(fileID,'%s\r\n',"*Preprint, echo=NO, model=NO, history=NO,
contact=NO");
fprintf(fileID,'%s\r\n',"*Node");
fprintf(fileID,'%4d,%4d,%4d,%4d\r\n',
[Mesh(:,1),Mesh(:,2),Mesh(:,3),Mesh(:,4)].');
fprintf(fileID,'%s\r\n',"*Element, Type=S3R");
fprintf(fileID,'%4d,%4d,%4d,%4d\r\n',
[Element(:,1),Element(:,2),Element(:,3),Element(:,4)].');
fprintf(fileID,'%s\r\n',"*****");
fprintf(fileID,'%s\r\n',"*** ORIENTATIONS ***");
fprintf(fileID,'%s\r\n',"*****");
fprintf(fileID,'%s\r\n',"** Orientation vectors");
fprintf(fileID,'%s\r\n',"** 1st vector represents the fibre
direction");
fprintf(fileID,'%s\r\n',"** 2nd vector is an arbitrary vector
perpendicular to the first");
fprintf(fileID,'%s\r\n',"*Distribution Table,
Name=A2AOrientationVectors");
fprintf(fileID,'%s\r\n',"COORD3D,COORD3D");
fprintf(fileID,'%s\r\n',"*Distribution, Location=Element,
Table=A2AOrientationVectors, Name=A2AOrientationVectors,
Input=A2AOrientationVectors.ori");
fprintf(fileID,'%s\r\n',"*Orientation, Name=A2AOrientations,
Definition=coordinates");
fprintf(fileID,'%s\r\n',"A2AOrientationVectors");
fprintf(fileID,'%s\r\n',"1, 0");
fprintf(fileID,'%s\r\n',"*Orientation, name=Ori-PART-
1_A2AORIENTATIONVECTORS, system=RECTANGULAR");
fprintf(fileID,'%s\r\n',"PART-1_A2AORIENTATIONVECTORS");
fprintf(fileID,'%s\r\n',"3, 0.");
fprintf(fileID,'%s\r\n',"** Section: Section-1-ALLELEMENTS");
fprintf(fileID,'%s\r\n',"*Shell Section, elset=ALLELEMENTS,
material=MAT1, orientation=Ori-PART-1_A2AORIENTATIONVECTORS");
fprintf(fileID,'%s\r\n',"1., 5");
fprintf(fileID,'%s\r\n',"*****");
fprintf(fileID,'%s\r\n',"*** ELEMENT SETS ***");
fprintf(fileID,'%s\r\n',"*****");
fprintf(fileID,'%s\r\n',"** A2A generates a number of element
sets:");
fprintf(fileID,'%s\r\n',"** All - Contains all elements");
fprintf(fileID,'%s\r\n',"*ElSet, ElSet=AllElements, Generate");
fprintf(fileID,'%4s,%4d,%4s\r\n', "1",emesh.', "1");
fprintf(fileID,'%s\r\n',"*****");
fprintf(fileID,'%s\r\n',"*** NODE SETS ***");

```



```

fprintf(fileID, '%s\r\n', "*****");
fprintf(fileID, '%s\r\n', "*** A2A generates a number of node sets:");
fprintf(fileID, '%s\r\n', "*** AllNodes - Node set containing all
elements");
fprintf(fileID, '%s\r\n', "*NSet, NSet=AllNodes, Generate");
fprintf(fileID, '%4s,%4d,%4s\r\n', "1", smesh.', "1");
fprintf(fileID, '%s\r\n', "*Nset, nset=Set-2, Generate");
fprintf(fileID, '%4s,%4d,%4s\r\n', "1", smesh.', "1");
fprintf(fileID, '%s\r\n', "*****");
fprintf(fileID, '%s\r\n', "*** MATERIALS ***");
fprintf(fileID, '%s\r\n', "*****");
fprintf(fileID, '%s\r\n', "*Material, Name=Mat1");
fprintf(fileID, '%s\r\n', "*Depvar");
fprintf(fileID, '%s\r\n', "      2,");
fprintf(fileID, '%s\r\n', "*Elastic, dependencies = 1");
fprintf(fileID, '%4d,%4d,%4d,%4d.\r\n', [ShearAngle(:,4),ShearAngle(
,5),ShearAngle(:,2),ShearAngle(:,1)].');
fprintf(fileID, '%s\r\n', "*Expansion");
fprintf(fileID, '%s\r\n', "6.5e-06");
fprintf(fileID, '%s\r\n', "*User Defined Field");
fprintf(fileID, '%s\r\n', "*Shell Section, ElSet=AllElements,
Material=Mat1, Thickness = 0.5, Orientation=A2AOrientations");
fprintf(fileID, '%s\r\n', "1.0,");
fprintf(fileID, '%s\r\n', "***");
fprintf(fileID, '%s\r\n', "***BOUNDARY CONDITIONS");
fprintf(fileID, '%s\r\n', "***");
fprintf(fileID, '%s\r\n', "*** Name: BC-1 Type:
Symmetry/Antisymmetry/Encastre");
fprintf(fileID, '%s\r\n', "*Boundary");
fprintf(fileID, '%s\r\n', "Set-2, ENCASTRE");
fprintf(fileID, '%s\r\n', "*** -----
-----");
fprintf(fileID, '%s\r\n', "***");
fprintf(fileID, '%s\r\n', "***STEP: Step-1");
fprintf(fileID, '%s\r\n', "***");
fprintf(fileID, '%s\r\n', "*Step, name=Step-1, nlgeom=NO");
fprintf(fileID, '%s\r\n', "*Static");
fprintf(fileID, '%s\r\n', "1., 1., 1e-05, 1.");
fprintf(fileID, '%s\r\n', "***");
fprintf(fileID, '%s\r\n', "***OUTPUT REQUESTS");
fprintf(fileID, '%s\r\n', "***");
fprintf(fileID, '%s\r\n', "*Restart, write, frequency=0");
fprintf(fileID, '%s\r\n', "***");
fprintf(fileID, '%s\r\n', "***FIELD OUTPUT: F-Output-1");
fprintf(fileID, '%s\r\n', "***");
fprintf(fileID, '%s\r\n', "*Output, field");
fprintf(fileID, '%s\r\n', "*Node Output");
fprintf(fileID, '%s\r\n', "CF, RF, U");
fprintf(fileID, '%s\r\n', "*Element Output, directions=YES");
fprintf(fileID, '%s\r\n', "FV, LE, PE, PEEQ, PEMAG, S, SDV, TEMP");
fprintf(fileID, '%s\r\n', "*Contact Output");
fprintf(fileID, '%s\r\n', "CDISP, CSTRESS");
fprintf(fileID, '%s\r\n', "***");
fprintf(fileID, '%s\r\n', "***HISTORY OUTPUT: H-Output-1");
fprintf(fileID, '%s\r\n', "***");
fprintf(fileID, '%s\r\n', "*Output, history, variable=PRESELECT");
fprintf(fileID, '%s\r\n', "*End Step");
fclose(fileID);

```

%

```
%Writing .ori file for lookup table of orientations
```

```
%
```

```
fileID = fopen('A2AOrientationVectors.ori','w');
fprintf(fileID,'%s\r\n',"*****");
fprintf(fileID,'%s\r\n',"*** ORIENTATIONS ***");
fprintf(fileID,'%s\r\n',"*****");
fprintf(fileID,'%s\r\n',"** Orientation vectors");
fprintf(fileID,'%s\r\n',"** 1st vector represents the fibre
direction");
fprintf(fileID,'%s\r\n',"** 2nd vector is an arbitrary vector
perpendicular to the first");
fprintf(fileID,'%s\r\n'," 1.0, 0.0, 0.0, 0.0, 1.0, 0.0");
fprintf(fileID,'%4d,%4d,%4d,%4d,%4d,%4d\r\n',
[Orient(:,1),Orient(:,2),Orient(:,3),Orient(:,4),Orient(:,5),Orient(
(:,6),Orient(:,7)].');
fclose(fileID);
```

```
%
```

```
%Writing .f Subroutine for USDFLD
```

```
%
```

```
fileID = fopen('A2AFieldVariables.f','w');
fprintf(fileID,'%s\r\n','!DEC$ ATTRIBUTES ALIAS:"usfld":USDFLD');
fprintf(fileID,'%s\r\n',"      SUBROUTINE
USDFLD(FIELD,STATEV,PNEWDT,DIRECT,T,CELENT,");
fprintf(fileID,'%s\r\n',"      1
TIME,DTIME,CMNAME,ORNAME,NFIELD,NSTATV,NOEL,NPT,LAYER,");
fprintf(fileID,'%s\r\n',"      2
KSPT,KSTEP,KINC,NDI,NSHR,COORD,JMAC,JMATYP,MATLAYO,LACCFLA");
fprintf(fileID,'%s\r\n',"C");
fprintf(fileID,'%s\r\n',"      INCLUDE 'ABA_PARAM.INC");
fprintf(fileID,'%s\r\n',"C");
fprintf(fileID,'%s\r\n',"      CHARACTER*80 CMNAME,ORNAME");
fprintf(fileID,'%s\r\n',"      CHARACTER*3  FLGRAY(15)");
fprintf(fileID,'%s\r\n',"      DIMENSION
FIELD(NFIELD),STATEV(NSTATV),DIRECT(3,3,");
fprintf(fileID,'%s\r\n',"      1 T(3,3),TIME(2)");
fprintf(fileID,'%s\r\n',"      DIMENSION
ARRAY(15),JARRAY(15),JMAC(*),JMATYP(*),COORD(*,");
fprintf(fileID,'%s\r\n',"      1 matrix(9534,2)");
fprintf(fileID,'%s\r\n','!DEC$ ATTRIBUTES
ALIAS:"getpartinfo":GETPARTINFO');
fprintf(fileID,'%s\r\n',"      FIELD(1) = NOEL");
fprintf(fileID,'%s\r\n',"      STATEV(1) = FIELD(1)");
fprintf(fileID,'%4s %4s %4s
%4s\r\n',[Superstring(:,1),ShearAngle(:,3),Substring(:,2),ShearAngle
(:,1)].');
fprintf(fileID,'%4s %4s %4s
%4s\r\n',[Superstring(:,1),ShearAngle(:,3),Substring(:,3),ShearAngle
(:,2)].');
fprintf(fileID,'%s\r\n',"      DO i =1,9534");
fprintf(fileID,'%s\r\n',"      IF (matrix(i,1) == FIELD(1)
then");
fprintf(fileID,'%s\r\n',"      STATEV(2) = matrix(i,2)");
fprintf(fileID,'%s\r\n',"      endif");
fprintf(fileID,'%s\r\n',"      enddo");
fprintf(fileID,'%s\r\n',"      RETURN");
```

```
fprintf(fileID, '%s\r\n', "      END SUBROUTINE");  
fclose(fileID);
```

15 References

1. A. G. Prodromou, J. Chen., *Shear Testing To The Locking Angle Of Multiple Woven Fabrics. Altering Yarn Width And Spacing To Find A Way To Non-Experimentally Calculate Locking Angle.*, Composites Part A: Applied Science and Manufacturing, 1996. **28**(5): p. 491-503.
2. Riva, E. and G. Nicoletto, *Modeling and prediction of the mechanical properties of woven laminates by the finite element method*, in *Fracture and Damage of Composites*. 2005. p. 105-125.
3. P. Harrison, J.W., A.C. Long and C.D. Rudd, "*Constitutive Modelling Based On Meso And MicroKinematics For Woven And Stitched Dry Fabrics*", in *14th International Conference on Composite Materials*. 2006: San Diego, USA.
4. Farboodmanesh, S., et al., *Base fabrics and their interaction in coated fabrics*, in *Smart Textile Coatings and Laminates*. 2019. p. 47-95.
5. S. Kari, M.K., I.A. Jones, N.A. Warrior and A.C. Long, *Effect of yarn cross-sectional shapes and crimp on the mechanical properties of 3d woven composites*. University of Nottingham: University of Nottingham.
6. Pourtier, J., et al., *Two-way approach for deformation analysis of non-crimp fabrics in uniaxial bias extension tests based on pure and simple shear assumption*. International Journal of Material Forming, 2019.
7. Leif E. Asp, F.E.a.A.S., *Effects of stitch pattern on the mechanical properties of non-crimp fabric composites*, in *SICOMP*. Mölndal, Sweden.
8. Tan, K.T., et al., *Effect of stitch density and stitch thread thickness on damage progression and failure characteristics of stitched composites under out-of-plane loading*. Composites Science and Technology, 2013. **74**: p. 194–204.
9. Asp, L., F. Edgren, and A. Sjögren, *Effects of stitch pattern on the mechanical properties of non-crimp fabric composites*, in *European Conference on Composite Materials : 31/05/2004 - 03/06/2004*, G. Costas, Editor. 2004, European Society for Composite Materials: Rhodos.
10. A.A. Skordos, C.M.A., M.P.F. Sutcliffe, *A Simplified Rate Dependent Model Of Forming And Wrinkling Of Pre-Impregnated Woven Composites*. Composites Part A: Applied Science and Manufacturing 2006. **38**(5): p. 1318-1330.
11. KJLBY, W.F., *2-Planar Stress-Strain Relationships In Woven Fabrics*. Journal of the Textile Institute Transactions, 1963. **54**(1): p. T9-T27.
12. Wang, Y., et al., *An Analytical Model for the Tension-Shear Coupling of Woven Fabrics with Different Weave Patterns under Large Shear Deformation*. Applied Sciences, 2020. **10**(4): p. 1551.
13. P. Grosberg, B.J.P., *The Mechanical Properties of Woven Fabrics: Part V: The Initial Modulus and the Frictional Restraint in shearing of Plain Weave Fabrics*. Textile Research Journal, 1966. **36**(5): p. 420–431.
14. S.Chen*, O.M., LT Harper, NA Warrior, *Defect Formation During Preforming Of A Bi-Axial Non Crimp Fabric With A Pillar Stitch Pattern*. Composites: Part A, 2016. **91**: p. 156–167.
15. Albert S. Tam, T.G.G., *The kinematics for forming ideal aligned fibre composites into complex shapes*. Composites Manufacturing, 1990. **1**(4): p. 219-228.

16. E. de Bilbao*, D.S., G. Hivet, J. Launay, A. Gasse, *Bending Test Of Composite Reinforcements in Springer/ESAFORM 2008*. 2008. p. 835–838.
17. Boisse, P., N. Hamila, and A. Madeo, *Modelling the development of defects during composite reinforcements and prepreg forming*. Philos Trans A Math Phys Eng Sci, 2016. **374**(2071): p. 20150269.
18. Li, X., S. Shonkwiler, and S. McMains, *Detection of resin-rich areas for statistical analysis of fiber-reinforced polymer composites*. Composites Part B: Engineering, 2021. **225**: p. 109252.
19. Jurgita Domskienė, E.S., *Investigation of Fabric Shear Behaviour, in Fibres & Textiles*. 2005: Eastern Europe
20. P. Boisse, N.H., E. Guzman-Maldonado, Angela Madeo, G. Hivet, F. and Dell'Isola, *The bias-extension test for the analysis of in-plane shear properties of textile composite reinforcements and preregs a review*. International Journal of Material Forming, 2017. **10**(4): p. 19.
21. Harrison, P., M.J. Clifford, and A.C. Long, *Shear characterisation of viscous woven textile composites: a comparison between picture frame and bias extension experiments*. Composites Science and Technology, 2004. **64**(10-11): p. 1453-1465.
22. Gilbert Lebrun, M.N.B., Johanne Denault, *Evaluation Of Bias-Extension And Picture-Frame Test Methods For The Measurement Of Intraply Shear Properties Of PP/Glass Commingled Fabrics*. Composite Structures, 2003. **61**(4): p. 341-352.
23. Willems, An & Lomov, Stepan & Verpoest, I. & Vandepitte, Dirk. (2007). Picture frame shear tests on woven textile composite reinforcements with controlled pretension. AIP Conference Proceedings. 907. 999-1004. 10.1063/1.2729644.
24. J. Cao , R. Akkerman , P. Boisse ,1, J. Chen , H.S. Cheng , E.F. de Graaf , J.L. Gorczyca , P. Harrison , J.L., G. Hivet , W. Lee , L. Liud, S.V. Lomov , A. Long , E. de Luycker , F. Morestin , J. Padvoiskis , X.Q. Peng , Tz. Stoilova , X.M. Tao , I. Verpoest , A. Willems , J. Wiggers , T.X. Yu , B. Zhu , *Characterization of mechanical behavior of woven fabrics: Experimental methods and benchmark results*. Composites: Part A, 2008. **39**: p. 1037–1053.
25. S. V. Lomov, A.W., I. Verpoest and a.Y. Zhu", *Picture Frame Test of Woven Composite Reinforcements with a Full-Field Strain Registration*. Textile Research Journal, 2006. **76**(3): p. 243–252. .
26. Hivet, G. and A.V. Duong, *A contribution to the analysis of the intrinsic shear behavior of fabrics*. Journal of Composite Materials, 2010. **45**(6): p. 695-716.
27. Pasco, C., M. Khan, and K. Kendall, *A novel discrete method of shear angle measurement for in-plane shear properties of thermoset prepreg using a point-tracking algorithm*. Journal of Composite Materials, 2018. **53**(14): p. 2001-2013.
28. S. V. Lomov, A.V.T., And C. Cassidy, *A Predictive Model for the Fabric-to-Yarn Bending Stiffness Ratio of a Plain-Woven Set Fabric*. Textile Research Journal, 2000. **70**(12): p. 1088–1096.
29. Lecompte, D., et al., *Study and generation of optimal speckle patterns for DIC*. Vol. 3. 2007.

30. Yu, F., et al., *Simulating the effect of fabric bending stiffness on the wrinkling behaviour of biaxial fabrics during preforming*. Composites Part A Applied Science and Manufacturing, 2021.
31. Sutcliffe, M.P.F., S.L. Lemanski, and A.E. Scott, *Measurement of fibre waviness in industrial composite components*. Composites Science and Technology, 2012. **72**(16): p. 2016-2023.
32. Arumugam, V., et al., *In-plane shear behavior of 3D spacer knitted fabrics*. Journal of Industrial Textiles, 2016. **46**(3): p. 868-886.
33. Kim, S.-Y., et al., *Mechanical properties and production quality of hand-layup and vacuum infusion processed hybrid composite materials for GFRP marine structures*. International Journal of Naval Architecture and Ocean Engineering, 2014. **6**(3): p. 723-736.
34. Singh, P., et al., *Synthesis of Carbon Fiber Composites and Different Methods to Improve its Mechanical Properties: A Comprehensive Review*. IOP Conference Series: Earth and Environmental Science, 2021. **889**(1): p. 012013.
35. Hou, M. and K. Friedrich, *Stamp forming of continuous carbon fibre/polypropylene composites*. Composites Manufacturing, 1991. **2**(1): p. 3-9.
36. Harrison, P., R. Gomes, and N. Curado-Correia, *Press forming a 0/90 cross-ply advanced thermoplastic composite using the double-dome benchmark geometry*. Composites Part A: Applied Science and Manufacturing, 2013. **54**: p. 56-69.
37. S. Chen*, O.P.L.M., A. Endruweit, M. T. Elsmore, D. S. A. De Focatiis, L. T. Harper*, N. A. Warrior, *"Double diaphragm forming simulation for complex composite structures"*. Composites Part A Applied Science and Manufacturing · January 2017, 2017.
38. Smith, R., *Composite defects and their detection*. Materials Science and Engineering, 2009. **3**.
39. Kc, B., et al., *Green Composite Manufacturing via Compression Molding and Thermoforming*. 2015. p. 45-63.
40. S.Chen*, L.H., NA Warrior, *Formability Optimisation Of Fabric Preforms But Controlling Material Draw-In Through In-Plane Constraints*. Composites: Part A, 2015. **76**: p. 10–19.
41. J. Krebs’*, K.F.a.D.B., *A direct comparison of matched-die versus diaphragm forming*. Composites Part A: Applied Science and Manufacturing 1997. **29**(1–2): p. 183-188.
42. Hassan Alshahrani, M.H., *Influence of double-diaphragm vacuum compaction on deformation during forming of composite prepregs*. Journal of Science: Advanced Materials and Devices, 2016. **1**: p. 507-511.
43. H.E.N. Bersee*, S.L., G. Niño*,, *Diaphragm Forming Of Thermoset Composites*, in *16th International Conference On Composite Materials 2007*: Fellow Professor Doshisha Uuniversity, Kyoto, Japan.
44. Grimshaw, M.N.G., C. G. Diaz, J. M. L., *Advanced Technology Tape Laying For Affordable Manufacturing Of Large Composite Structures*. Society for the Advancement of Material and Process Engineering; 2001: a materials and processes odyssey 2001. **2**: p. 2484-2494.

45. Kropka, M., et al., *From UD-tape to Final Part – A Comprehensive Approach Yarnards Thermoplastic Composites*. Procedia CIRP, 2017. **66**: p. 96-100.
46. WEEEN, F.V.D., *Algorithms for draping fabrics on doubly-curved surfaces*. INTERNATIONAL JOURNAL FOR NUMERICAL METHODS IN ENGINEERING, 1991. **31**: p. 21.
47. Sanad, R., *Fabric and Garment Drape Measurement - Part 1*. Journal of Fiber Bioengineering and Informatics, 2012. **5**(4): p. 341-358.
48. Shuai Chen*, L.T.H., Andreas Endruweit and Nicholas A. Warrior, *Optimisation Of Forming Process For Highly Drapeable Fabrics*, in *20th International Conference on Composite Materials*. 2015: Copenhagen, .
49. Andrew Long*, A.S.P.H., Mike Clifford , Michael Sutcliffe, *"Optimisation Of Sheet Forming For Textile Composites Using Variable Peripheral Pressure "*, in *27th International Conference SAMPE EUROPE*. 2006: Paris, France
50. Boisse, Philippe & Aimene, Yamina & Dogui, Abdelwaheb & Dridi, S. & Gatouillat, Sébastien & Hamila, Nahiene & Khan, M. & Mabrouki, Tarek & Morestin, Fabrice & Vidal-Sallé, Emmanuelle. (2010). Hypoelastic, hyperelastic, discrete and semi-discrete approaches for textile composite reinforcement forming. International Journal of Material Forming. 3. 1229-1240. 10.1007/s12289-009-0664-9.
51. Pierce, R., *Improving the process modelling capability for manufacturing large composite structures used on passenger aircraft*. 2014.
52. Xiao, H., O.T. Bruhns, and A. Meyers, *On objective corotational rates and their defining spin tensors*. International Journal of Solids and Structures, 1998. **35**(30): p. 4001-4014.
53. Badel, P., et al., *Rate constitutive equations for computational analyses of textile composite reinforcement mechanical behaviour during forming*. Composites Part A: Applied Science and Manufacturing, 2009. **40**(8): p. 997-1007.
54. Hancock, S.G. and K.D. Potter, *The use of kinematic drape modelling to inform the hand lay-up of complex composite components using woven reinforcements*. Composites Part A: Applied Science and Manufacturing, 2006. **37**(3): p. 413-422.
55. Y. Aimene, B.H., F. Sidoroff, E.Vidal-Sallé, P. Boisse, S. Dridi *Hyperelastic Approach for Composite Reinforcement Forming Simulations* International Journal of Material Forming, 2008. **1**(1): p. 811–814.
56. Sharma, S.B. and M.P.F. Sutcliffe, *Draping of woven fabrics: Progressive drape model*. Plastics, Rubber and Composites, 2013. **32**(2): p. 57-64.
57. Hirsekorn, M., et al. *MESO-SCALE MODELING OF DAMAGE IN TEXTILE COMPOSITES WITH COMPACTED AND NESTED REINFORCEMENTS*. 2014.
58. Xiongqi Peng, J.C., *A Dual Homogenization And Finite Element Approach For Material Characterization Of Textile Composites*. Composites Part B: Engineering, 2001. **33**(1): p. 45-56.
59. De Luycker, E., et al., *Simulation of 3D interlock composite preforming*. Composite Structures, 2009. **88**(4): p. 615-623.
60. M. Nishi, T.H., *Approach For Dry Textile Composite Forming Simulation*, in *19th International Conference on Composite Materials*. 2013: Tokyo, Japan

61. Masato Nishi, T.K., Masashi Kurose, Tei Hirashima, Tetsusei Kurasiki, *Forming Simulation of Thermoplastic Pre-Impregnated Textile Composite*. International Journal of Materials and Textile Engineering, 2014. **80**(820): p. SMM0354.
62. Harrison, P., *Modelling the forming mechanics of engineering fabrics using a mutually constrained pantographic beam and membrane mesh*. Composites Part A: Applied Science and Manufacturing, 2016. **81**: p. 145-157.
63. Sencu, R.M., et al., *Generation of micro-scale finite element models from synchrotron X-ray CT images for multidirectional carbon fibre reinforced composites*. Composites Part A: Applied Science and Manufacturing, 2016. **91**: p. 85-95.
64. ten Thije, R.H.W. and R. Akkerman, *Solutions to intra-ply shear locking in finite element analyses of fibre reinforced materials*. Composites Part A: Applied Science and Manufacturing, 2008. **39**(7): p. 1167-1176.
65. Nguyen Dang, H., *Application of the duality in the finite element analysis of shell: self dual metis planar shell elements*. The Asia Pacific Journal of Computational Mechanics, 2014. **1**: p. 11.
66. S. Bel, N.H.a., P. Boisse a,† , F. Dumont, *Finite Element Model For Ncf Composite Reinforcement Preforming: Importance Of Inter-Ply Sliding*. Composites Part A: Applied Science and Manufacturing, 2012. **43**(12): p. 2269-2277.
67. W Najjar¹, C Pupin¹, et al., *Analysis of frictional behaviour of carbon dry woven reinforcement*. Journal of Reinforced Plastics and Composites, 2014. **33**(11): p. 10.
68. Cornelissen, B., B. Rietman, and R. Akkerman, *Frictional behaviour of high performance fibrous yarns: Friction experiments*. Composites Part A: Applied Science and Manufacturing, 2013. **44**: p. 95-104.
69. S. Allaoui, G.H., A. Wendling, P. Ouagne and D. Soulat, *Influence of the dry woven fabrics meso-structure on fabric fabric contact behaviour*. Journal of Composite Materials, 2012. **46**(6): p. 11.
70. Vanclooster, K., S.V.L. , and a.l. Verpoest, *Simulation of multi-layered composites forming*. Int J Mater Form, 2010. **3**(1): p. 3.
71. Dridi, S., et al., *Experimental analysis of Bias Extension and Picture Frame tests for woven fabric by Digital Image Correlation*. 2008.
72. Pierce, R.S., et al., *A Low-Cost Digital Image Correlation Technique for Characterising the Shear Deformation of Fabrics for Draping Studies*. Strain, 2015. **51**(3): p. 180-189.
73. Jauffret, M., et al., *Textile Composite Damage Analysis Taking into Account the Forming Process*. Materials (Basel, Switzerland), 2020. **13**(23): p. 5337.
74. P. Boisse, N.H., E. Vidal-Sallé, F. Dumont, *Simulation of wrinkling during textile composite reinforcement forming. Influence of tensile, in-plane shear and bending stiffness*. Composites Science and Technology, 2011. **71**(5).
75. Atkinson, G., O'Hara Nash, S., & Smith, L., *Precision fibre angle inspection for carbon fibre composite structures using polarisation vision*. . Electronics, 2021. **10**(22).
76. Potter, K., et al., *Variability, fibre waviness and misalignment in the determination of the properties of composite materials and structures*.

- Composites Part A: Applied Science and Manufacturing, 2008. **39**(9): p. 1343-1354.
77. Yurgartis, S.W., *Measurement of small angle fiber misalignments in continuous fiber composites*. Composites Science and Technology, 1987. **30**(4): p. 279-293.
 78. Jelf, P.M. and N.A. Fleck, *The failure of composite tubes due to combined compression and torsion*. Journal of Materials Science, 1994. **29**(11): p. 3080-3084.
 79. Hajebi, K., et al., *Fast Approximate Nearest-Neighbor Search with k-Nearest Neighbor Graph*. 2011. 1312-1317.
 80. Yu, F., et al., *A macroscale finite element approach for simulating the bending behaviour of biaxial fabrics*. Composites Science and Technology, 2020. **191**: p. 108078.
 81. I. Taha, Y.A.a.S.E., *Comparison of Picture Frame and Bias-extension Tests for the Characterization of Shear Behaviour in Natural Fibre Woven Fabrics*. Fibers and Polymers, 2013. **14**(2): p. 338-334.
 82. Vallons, K.J.R., et al., *Loading direction dependence of the tensile stiffness, strength and fatigue life of biaxial carbon/epoxy NCF composites*. Composites Part A-applied Science and Manufacturing, 2011. **42**: p. 16-21.
 83. Yang, X., et al., *Strength and Modulus Degradation of Carbon Fiber-Reinforced Polymer Laminates from Fiber Misalignment*. Journal of Materials in Civil Engineering - J MATER CIVIL ENG, 2002. **14**.
 84. Mandell, J., D. Samborsky, and L. Wang, *Effects of fiber waviness on composites for wind turbine blades*. 2003.
 85. Galkin, S., et al., *Experimental and Numerical Determination of the Local Fiber Volume Content of Unidirectional Non-Crimp Fabrics with Forming Effects*. Journal of Composites Science, 2019. **3**(1).
 86. Rudd, C.D., et al., *Modelling the processing and performance of preforms for liquid moulding processes*. Composites Manufacturing, 1994. **5**(3): p. 177-186.
 87. Hasan, K.M.F., P.G. Horváth, and T. Alpár, *Potential fabric-reinforced composites: a comprehensive review*. Journal of Materials Science, 2021. **56**(26): p. 14381-14415.
 88. Pinho, S.T., L. Iannucci, and P. Robinson, *Physically based failure models and criteria for laminated fibre-reinforced composites with emphasis on fibre kinking. Part II: FE implementation*. Composites Part A: Applied Science and Manufacturing, 2006. **37**(5): p. 766-777.
 89. Pinho, S.T., L. Iannucci, and P. Robinson, *Physically-based failure models and criteria for laminated fibre-reinforced composites with emphasis on fibre kinking: Part I: Development*. Composites Part A: Applied Science and Manufacturing, 2006. **37**(1): p. 63-73.
 90. Thwaite, M.J.P.E.G., *Elastic Compression of Spheres and Cylinders at Point and Line Contact*. National Standards Laboratory Technical Paper, 1969(No. 25).
 91. Aboudi, J. and R. Gilat, *Buckling analysis of fibers in composite materials by wave propagation analogy*. International Journal of Solids and Structures - INT J SOLIDS STRUCT, 2006. **43**: p. 5168-5181.
 92. K.Laws, *Texture energy Measures in Image Understanding Workshop 1979*: University of Southern California.

93. Kong, H., A.P. Mouritz, and R. Paton, *Tensile extension properties and deformation mechanisms of multiaxial non-crimp fabrics*. Composite Structures, 2004. **66**: p. 249-259.
94. Prodromou, A.G. and J. Chen, *On the relationship between shear angle and wrinkling of textile composite preforms*. Composites Part A: Applied Science and Manufacturing, 1997. **28**(5): p. 491-503.
95. Chakladar, N.D., P. Mandal, and P. Potluri, *Effects of inter-yarn angle and yarn size on carbon fibre friction*. Composites Part A: Applied Science and Manufacturing, 2014. **65**: p. 115-124.
96. Smerdova, O., O. Benchekroun, and N. Brunetiere, *Transversal friction of epoxy-lubricated and dry carbon yarns: From initial stages to stabilised state*. Composites Part A: Applied Science and Manufacturing, 2021. **143**: p. 106263.
97. Lomov, S.V., et al., *Carbon composites based on multiaxial multiply stitched preforms. Part 3: Biaxial tension, picture frame and compression tests of the preforms*. Composites Part A: Applied Science and Manufacturing, 2005. **36**(9): p. 1188-1206.
98. Lopes, C.S., Z. Gürdal, and P.P. Camanho, *Tailoring for strength of composite steered-fibre panels with cutouts*. Composites Part A: Applied Science and Manufacturing, 2010. **41**(12): p. 1760-1767.
99. Coutandin, S., et al., *Influence of punch sequence and prediction of wrinkling in textile forming with a multi-punch tool*. Production Engineering, 2018. **12**(6): p. 779-788.
100. Xiao, Z. and P. Harrison, *Fabric steering technology for variable stiffness panels: Manufacture and mechanical testing*. Composites Part B: Engineering, 2021. **223**: p. 109105.
101. Denis, Y., et al., *A dissipative model for deep-drawing simulations: Elastic springback prediction and incremental forming strategies*. Composites Part A: Applied Science and Manufacturing, 2021. **149**: p. 106547.
102. Sun, J., et al., *Effect of forming temperature on the quality of hot diaphragm formed C-shaped thermosetting composite laminates*. Journal of Reinforced Plastics and Composites, 2012. **31**(16): p. 1074-1087.
103. Thompson, A.J., J.P.H. Belnoue, and S.R. Hallett, *Modelling defect formation in textiles during the double diaphragm forming process*. Composites Part B: Engineering, 2020. **202**: p. 108357.
104. Krebs, J., D. Bhattacharyya, and K. Friedrich, *Production and evaluation of secondary composite aircraft components—a comprehensive case study*. Composites Part A: Applied Science and Manufacturing, 1997. **28**(5): p. 481-489.
105. Habboush, A., et al., *Characterization and Analysis of In-Plane Shear Behavior of Glass Warp-Knitted Non-Crimp Fabrics Based on Picture Frame Method*. Materials (Basel, Switzerland), 2018. **11**(9): p. 1550.
106. S. Chen, O.P.L.M., L.T. Harper, A. Endruweit and N.A. Warrior, *Optimisation of double diaphragm forming process through local adjustment of in-plane constraint*, in *21st International Conference on Composite Materials*. 2017: Xi'an.

107. Khan, M.A., *Numerical and Experimental Forming Analyses of Textile Composite Reinforcements Based on a Hypoelastic Behaviour*. 2009, The University of Warwick.
108. D'íaz-Urbe, M.F.G.a.-C.a.R., *An analysis on the inversion of polynomials*. REVISTA MEXICANA DE FÍSICA, 2006. **52**(2): p. 163-171.
109. Kazhdan, M.M. and H. Hoppe, *Screened poisson surface reconstruction*. ACM Trans. Graph., 2013. **32**: p. 29:1-29:13.
110. Blasques, J. and M. Stolpe, *Maximum stiffness and minimum weight optimization of laminated composite beams using continuous fiber angles*. Structural and Multidisciplinary Optimization, 2011. **43**: p. 573-588.
111. Schmit, L.A. and M. Mehrinfar, *Multilevel optimum design of structures with fiber-composite stiffened-panel components*. AIAA Journal, 1982. **20**: p. 138-147.
112. Liu, B., R.T. Haftka, and M.A. Akgün, *Two-level composite wing structural optimization using response surfaces*. Structural and Multidisciplinary Optimization, 2000. **20**(2): p. 87-96.
113. Liu, B. and R. Haftka, *Composite wing structural design optimization with continuity constraints*. 2001.
114. Kim, B.C., K. Potter, and P.M. Weaver, *Continuous yarn shearing for manufacturing variable angle yarn composites*. Composites Part A: Applied Science and Manufacturing, 2012. **43**(8): p. 1347-1356.
115. Capelle, E., et al., *Complex shape forming of flax woven fabrics: Design of specific blank-holder shapes to prevent defects*. Composites Part B: Engineering, 2014. **62**: p. 29-36.
116. K. Tanaka*, R.U., T. Katayama, S. Enoki & H. Sakamoto, *Formability Evaluation Of Carbon Fiber Ncf By A Non-Contact 3d Strain Measurement System And The Effects Of Blank Folder Force On Its Formability*. High Performance and Optimum Design of Structures and Materials 2014. **137**.
117. Farbod Nosrat Nezami a, T.G., Chokri Cherif, *Active Forming Manipulation Of Composite Reinforcements For The Suppression Of Forming Defects*. Composites Part A: Applied Science and Manufacturing, 2017. **99**: p. 94-101.
118. J.Wozney, M.A.P.D.D.E.B.M., *Fitting a Woven Cloth Model to a Curved Surface : Dart Insertion*. Computer Graphics in Textiles and Apparel, 1996.
119. Peng, X.Q., et al., *Experimental and numerical analysis on normalization of picture frame tests for composite materials*. Composites Science and Technology, 2004. **64**(1): p. 11-21.
120. Hermes, T., et al., *On Textures: A Sketch of a Texture-Based Image Segmentation Approach*. 2002.